Department of Chemistry

University College London

University of London

(UCL)

Title:

Computational study of de-NO_x reactions in Cu-exchanged zeolites

Thesis submitted for the degree of Master of Philosophy

By

Rupert Ting

2017

‘I, Rupert Ting, confirm that the work presented in this thesis is my own. Where information has been derived from other sources, I confirm that this has been indicated in the thesis.’

Abstract

Copper-exchanged zeolites have been widely studied as catalysts for NO_x emission control since the early 1980s. Over the last 40 years, there has been a growing search for a "de-NO_x" catalyst in order to reduce and control NO_x emissions. Selective catalytic reduction (SCR) is a commonly used method for NO_x removal, via catalytic reaction of the nitrogen oxides with ammonia or light hydrocarbons such as propane to produce N_2 as the only N-containing product. Cu-exchanged zeolite hosts SSZ-13 and SAPO-34, both belonging to the small-pore CHA framework have high activity in site-resolved de-NO_x SCR. The exact nature of the active Cu species and the atomic-level mechanism of the de-NO_x reaction are still subject to debate, and are of difficult characterisation by the application of experimental techniques alone. In this thesis the aim is to apply atomistic modelling techniques using both force-field and quantum chemical calculations, the following results has been observed: (i) site SI is the global energy minimum by on average 0.9eV, (ii) the proximity of dopant atoms has a pronounced effect on the equilibrium energy of the system, (iii) H_2O and NH_3 adsorption is preferable in site SIV and (iv) SAPO-34 is a more reactive system in terms of hosting small polar molecules.

Table of contents

Chapter 1 Introduction

1.1 NO_x abatement issue and SCR catalysis

The abatement of nitrogen oxides (NO_x) from exhaust gases is an interdisciplinary research area that spans across automotive engineering, materials and atmospheric chemistry. The central subject that sits in the crossroad of these disciplines is catalysis; the current issue of solving NO_x abatement is a challenging and dynamic area for the catalysis community.[1]

In Europe, around 60% of NO_x produced is from the combustion process in vehicle engines via thermal-NO_x – one of three pathways for NO_x formation (fuel- and prompt- NO_x are the other two).[7, 118, 119] Thermal NO_x is simply the oxidation of atmospheric nitrogen at very high temperatures, above 1600˚C, depicted by the following equation [118, 119]:

$$N_2 + O_2 \rightarrow 2NO \quad (1)$$

The decrease of nitrogen-containing compounds in petroleum and diesel fuels over the last two decades has resulted in a decline of NO_x formation via the oxidation of nitrogen directly from fuel (fuel-NO_x).[7] Diesel engines contribute around 75% of the NO_x production in road emissions.[119] Current methods involved in reducing NO_x emissions can be classified into pre-combustion modifications, combustion control and post-combustion abatement technologies.[51]

Future legislation as predicated from the Gothenburg Protocol[7] will result in stricter regulations of NO_x emissions limits by 2020. The current NO_x prevention technologies focused on fuel modifications by lowering of nitrogen content and engine management has been determined to be insufficient to meet these new changes [120,121,122]. Subsequently, in both research and industry, the treatment of exhaust gases via catalytic technology is presently the most viable solution, because, it can be a cheap and highly efficient process.[123]

The reverse of reaction (1) is thermodynamically unstable and kinetically difficult to achieve under the conditions observed in automobiles.[7]The three-way catalyst (TWC) is very efficient in reducing NO_x for a petroleum engine, but not in a diesel engine, because the TWC operates most effectively under stoichiometric conditions oscillating between rich (excess fuel) and lean (excess air) exhaust fumes composition. In a diesel engine the lean mode of operation results in high amounts of O_2 in the exhaust fumes means the TWC becomes ineffective in removing NO_x. [124, 125]

Researchers have attempted over the last 20 years to find a TWC that would be active under lean-burn conditions, but to no avail. Instead, three entirely new systems were developed during the 1990s with the aim of solving the NO_x problem in diesel and lean-burn engines. These are the NO_x storage reduction (NSR), selective NO_x recirculation (SNR) and the selective catalytic reduction (SCR) systems.

NSR was first introduced by Toyota and operates under a two-phase condition; an oxidative and reductive mode. In the former, under the presence of a lean-burn condition NO is oxidized to NO_2 over a precious metal support, and subsequently converted and stored as nitrates. Other pollutants including hydrocarbons (HCs), carbon monoxide (CO) and nitrogen are oxidized into water and carbon dioxide during this phase. For the latter, in a fuel-rich condition the stored nitrates are then released and reduced by CO, HCs and hydrogen via a sequence of reactions. This method has been deemed to be highly promising and does not require a reducing agent, however the nitrates storage materials are expensive due to

presence of alkaline-earth, alkaline and noble metals (platinum and rhodium). In addition, the reported susceptibility to sulphur poisoning and long-term thermal stability has diverted the industry's attention to other methods, with as SCR being most the prominent.

The SNR has been reported to be the least applied out of the three methods mentioned. Originally developed by Daimler-Chrysler, the operating procedure involve the thermal decomposition of NO_x via the combustion zone in the engine. The NO_x in diesel and lean-burn exhaust fumes are re-circulated and concentrated before being delivered into the engine for removal.

The final method is the SCR of NO_x with reductants (NH_3, hydrocarbons, CO and H_2) to form molecular N_2 and H_2O, and is currently regarded as the most effective method of converting NO_x into benign products in diesel and other lean-burn engines [2–4]. This thesis will be focused on the SCR method and the study of the materials that have been reported to be the leading technology within the field, as determined by industrial collaborators, Johnson Matthey. The NH_3-SCR reaction is the first and remains the pioneer in handling the NO_x problem, in both mobile and stationary emissions control [2, 5].

The NH_3-SCR reaction only requires a stoichiometric amount of ammonia for complete NO_x reduction. The SCR systems has been put into practice in stationary power plants since the first installation in 1978 [7, 126, 127]. The aim now for the catalysis community is to implement this existing technology into lean-burn engines found in automobiles and other vehicles.[7, 128 – 131]

One of the first catalytic materials used for the NH_3-SCR reaction are V_2O_5-based catalysts for the removal of NO_x in stationary sources [5, 6].Vanadium based catalyst are used in combination with other catalytic active metal oxides in the form of TiO_2 and WO_3 [5]. They have been used for diesel vehicles in Europe since 2005.[120] However, the toxicity of vanadium upon release at high temperatures, and the susceptibility to catalytic deactivation via sulphur poisoning (oxidation of SO_2) has been a concern,[5, 7] resulting in an unforeseeable future for commercial applications in next-generation automobile catalytic converters [7].

Consequently, other NO_x reduction technology has been developed and studied, including SCR (of de-NO_x reactions) over metal-exchanged zeolites as catalysts[7], which has shown to be promising. Yahiro and Iwamoto first demonstrated the catalytic activity of metal-exchanged zeolites for NH_3-SCR during the 1980s, with development focused on the MFI and FAU frameworks [7-10]. It has been generally agreed that it is the extra-framework metal cations which are the active sites, with Cu- and Fe- exchanged ions amongst the most active[5, 7]. Extra-framework ions in FAU and MFI zeolites, however, are subject to easy leaching that limits the lifetime and activity of the catalyst[7]. As of recently, zeolite frameworks with narrow-pore dimensions such as MOR, FER, BEA, ZSM-5 and CHA have shown high (SCR) activity and (hydrothermal) stability[7].

In general, the characteristics exhibited by metal-exchanged zeolites has made them particularly favourable as catalysts for SCR in vehicle applications. These are the non-toxicity, wider operation temperature range, thermal stability, excellent activity and selectivity[5, 7]. The discovery of Cu-SSZ-13, a Cu-exchanged zeolite in the CHA framework, and the (aluminophosphate) isostructural analogue Cu-SAPO-34 have proven to be the current state-in-the-art for mobile SCR technology[5, 11]. This is due to their superior NOx conversion, optimized performances in low and high extreme temperatures, in addition to high stability[5].

Despite numerous experimental and theoretical studies over the years[12-22], there has been an absence of a universally agreed structure-activity relationship[2]. This is because of the structural complexity of metal-exchanged zeolites, paired with the elusive nature of a precise

mechanistic understanding of SCR. In recent times, this has been considered the main impediment in developing commercially successful SCR zeolite catalysts in diesel engines, and referred to as a bottleneck problem by Mao et al[2].

The current strands of active research aimed at building a structure-activity relationship consist of: (i) discovering the nature of the active sites, (ii) determining the adsorption of SCR reactants and (iii) subsequent desorption of intermediates/products, in order for (iv) discovery of elementary reactions in the SCR de-NO_x catalytic cycle[12-22].

The range and variation of properties (parameters) in a metal-exchanged zeolite SCR system to be studied is vast. These include: (i) the different zeolite structures (MFI, CHA, BEA, MOR, FER etc.), (ii) the chemical framework composition, (iii) the choice of extra-framework metals used (Fe, Cu, Ni, Co, etc.) and (iv) can occupy different extra-framework sites[1].

The optimisation of the metal-exchanged zeolite catalysts employed in de-NO_x reactions is therefore a non-trivial task. In addition, even the most accurate experimental probes currently available are often unable to provide direct atomic level detail onto structures and mechanisms for a complex reaction scheme as the de-NO_x.

1.2 Aims

In close collaboration with industrial sponsors, Johnson Matthey, we aim to investigate the nature of copper-exchanged zeolites in de-NO_x reactions. Both mono- and poly-nuclear Cu clusters have been postulated in the literature as being responsible for the catalytic activity[24, 28-36]. The zeolite hosts to be investigated are the SSZ-13 and SAPO-34, both belonging to the small-pore CHA framework that show improved resistance to leaching of Cu, while retaining high activity in site-resolved de-NO_x SCR[11, 36-48].

The first step in elucidating the elusive and debated de-NO_x mechanism in a SCR reaction is to determine the nature of the active site. The exact nature of the active Cu species and the atomic-level mechanism of the de-NOx reaction are still subject to debate, and are of difficult to characterise by the application of experimental techniques alone. In the research, we aim to apply atomistic modelling techniques to complement the experimental results. In particular, we aim first to identify the location and mobility of the Cu ions in the zeolite; second to understand if the movement of these extra-framework Cu ions varies upon the addition of relevant adsorbates, such as H_2O and NO. The nature of transport mechanism and resulting final location and coordination of the Cu ions provide critical information for de-NO_x reaction mechanism, including the resistance to leaching.

From the outset, the aim of our research is to gain microscopic insights into Cu-exchanged SSZ-13 and SAPO-34, in order to build a structure-property and/or -performance relationships and to consolidate current theoretical understanding in zeolite heterogeneous catalysis. More specifically, our atomistic goals are to determine the: (i) oxidation state, (ii) location, (iii) nuclearity and (iv) redox properties of Cu ions in Cu- SSZ-13 and SAPO-34. This would be a significant step in understanding the nature of Cu ions and the active sites in these zeolite catalysts, subsequently the reported superior activity and selectivity for NOx conversion in SCR, and high stability. If possible, this will aid the building of a structure-property relationship, enabling a methodical procedure in improving the catalytic system.

In this report, we will be looking at the possible locations of an isolated Cu^{2+} ion, which has been observed most recently, as the active site in the SSZ-13 and SAPO-34 hosts[32, 42, 47]. The investigation will be carried out in two-folds, the first is to evaluate the energetic favourability of Cu^{2+} in the different environments of a CHA framework, as reported in literature, as a function of the different dopant configurations. This will be done with force field calculations which provide a simpler description of the forces between the atoms, with no explicit treatment of the electrons. As a result, this compromise in the level of theory enables fast computational time, therefore allows screening of Cu^{2+} locations as a function of a thousand of dopant configurations.

In the second part, among the Cu/dopant configurations from above, a select number of representative cases were performed with first-principles quantum mechanical (QM) methods. This was done at the density functional theory (DFT) level ensuring the electronic properties such as the spin state of a Cu^{2+}, and the structural properties of the bonding can be accurately predicted.

In addition to this, migration profiles were built showcasing the mobility of a Cu^{2+} inside the SSZ-13 and SAPO-34 hosts. This will give us an understanding of the energy barriers faced by a Cu^{2+} ion, and the changes in energy as a function of the different environments (cavities and channels) in SSZ-13 and SAPO-34. This was first done with force field methods, then repeated with QM methods.

After the equilibrium location(s) and respective energies of the Cu^{2+} is determined in SSZ-13 and SAPO-34, the final part of this thesis initiates adsorption studies of simple admolecules on the Cu sites, predominantly with H_2O molecules modelled via both force-field and QM calculations. NH_3 molecule – the active ingredient in performing the reduction of NOx in the NH_3-SCR cycle was comprehensively studied inside SSZ-13 and SAPO-34 as a function of adsorption geometry, location and energy via QM calculations,

1.3 Motivation for computational modelling

The study of the microporous solids with computational modelling techniques is a particularly dynamic and fast-paced field, especially concerning research in zeolites. This is because of the complexity and diversity of their structures. In addition to their importance in the technological and environmental fields[132].

The recent advances in computational processing power has resulted in the rise in significance of computational modelling methods as a tool in the study of materials, as observed in recent years[2]. Paired with the development and wide availability of QM techniques has meant the treatment of complex studies such as the NH_3-SCR process over metal-exchanged zeolites has become feasible[2]. From clusters to periodic boundary cell (PBC) conditions, the parameters in a computational model can be easily controlled and modified with precision, unlike in experiments. These can include, the composition of the solid, the location of the dopant and extra-framework atoms, the level of doping and the oxidation states.

Therefore, the atomic level of detail obtained from solutions to these methods can give information on the local environment of the exchanged-metal ions sitting in different extra-framework sites of the zeolite; the energies, coordination number, spin state and geometry of the occupation. The effect of dopant's proximity to the exchanged-metal ions can be understood in terms of energy and bonding, electronic properties of the neighbouring atoms and on the metal atom would be also be similarly known. The mode of interaction of adsorbates such as water molecules adsorbed onto the exchanged-metal would not be easily controlled in an experiment, thus calculations from both QM and force fields would provide insights valuable to the research field.

Yu *et al* and Wang *et al*[12, 21], for instance employed *in situ* diffuse reflectance infrared Fourier transform spectroscopy (DRIFTS), to identify chemical intermediates such as nitrite ions. However, the nitrite vibrational modes overlap with the signals from the zeolite framework resulting in large uncertainties. In addition, DRIFTS can only operate in the absence of water, and as such computational methods in this case would be useful to complement the experimental data.

Göltl and Hafner summarised that experimental characterization of the coordination and corresponding physiochemical properties of exchanged-metal ions in zeolites, is similarly challenging[23]. Mentzen and Bergeret described the limitation of X-ray diffraction (XRD), since it only yields average structure, regardless of occupation of the crystallographic sites in question[24].

Spectroscopic methods such as x-ray photoelectron and photoluminescence spectroscopy can provide information of the core and valence states of the metal cations, however, the correlation between energy levels and coordination environment is not unique, and interpretation of results is associated with large uncertainties[25-27]. The vibrational spectra of probe molecules, such as NO, can aid identifying the nature of active sites, but can only be performed ex situ in combination with theoretical calculations[23, 28].

It is becoming customary, therefore to perform computational studies of complex materials to determine the atomic level features, and de-NO_x catalysts are no exception as demonstrated by Mao *et al* and Göltl *et al*[1, 23]. This would enable the researchers to gain

microscopic insights that may not be experimentally feasible; to complement the experimental studies and even direct research towards the overall goal.

1.4 What are nitrogen oxides (NO_x)?

Nitrogen oxides are a family of seven oxides (NO, NO_2, NO_3, N_2O, N_2O_3, N_2O_4 and N_2O_5) globally indicated as NO_x that are found to occur in our atmosphere each with varying quantities[50, 51]. Their physical and infra-red spectroscopic properties are listed in Table 1. The definition of an 'air pollutant' is a substance that results in the damage to its surrounding environments (humans, animals, vegetation and materials) once released[51]. The major air pollutants are nitric oxide (NO) and nitrogen dioxide (NO2)[50, 51], indirect greenhouse gases[51], a cause of acid rain[50], photochemical smog[52], acidification and eutrophication of water and soils[51], and precursors in the formation of ozone in the troposphere[51, 53]. At high concentrations, both NO and NO_2 are toxic to humans and other living organisms[50], and their subsequent reactions with other pollutants in ambient air forms detrimental particulates[52].

Significant concentrations of NO and NO_2 (>500 µg/m^3 in urban areas) are mostly due to their production either directly or indirectly from combustion processes primarily from emissions in road transport and stationary power plants[50, 51]. Nitrous oxide (N_2O) is a powerful greenhouse gas with a global warming potential 298 times greater than that of CO_2 as per the United State of America's (USA) Environmental Protection Agency (EPA) and is produced mostly via anthropogenic activities. However, unlike NO and NO_2, the contribution of industrial sources including the burning of fossil fuels in internal combustion engines makes up less than 20% of N_2O emissions[51]. The main sink for NO_x are oxidation reactions with OH radicals and ozone to form HNO_3 and peroxy acetyl nitrate (PAN) both highly volatile products[51].

NO_x were first identified as major air pollutants in 1952 with the discovery as the principal cause of photochemical smog[52]. Since then, we now know NO_x is responsible for many environmental problems (above) along with the other major air pollutants such as sulphur oxides, particulate matter, carbon monoxide and unburned hydrocarbons. The escalation of NO_x emissions since 1952 has resulted in several protocols (Gothenburg and Kyoto) and subsequent regulations to clamp down on NO_x emissions[51].

Table 1[51]

Properties of the seven NO_x

Properties	**N_2O**	**NO**	**N_2O_3**	**NO_2**	**N_2O_4**	**N_2O_5**
Colour	Colourless	Colourless	Black	Red-brown	Transparent	White
Solubility in water g/dm^3	0.111	0.032	500.0	213.0	213.0	500.0
State of matter (ambient temperature)	Gas	Gas	Liquid	Gas	Liquid	Solid
Density (g/dm^3)	1.8	1.3402 (293K)	1447 (275K)	3.4	1492.7 (273K)	2050 (288K)
IR adsorbents peaks (cm^{-1})	1276.5 2200-2300	1876 1908	No data	3.4 749.7 1322.5 1600-1596 1617.75 1632-1629 2891 2917	808 1262 1379.6 1712 1748	722 743 824 1050 1247 1400 1413 2375

Chapter 2 SCR over metal-exchanged zeolites

2.1 Zeolites and their properties

Zeolites are compounds that forms extended frameworks with open structures. These frameworks are built from corner-sharing tetrahedral units, TO_4 also known as tetrahedra. Fig. 1a illustrates a SiO_4 tetrahedral unit linked to an AlO_4. The T-O-T bond angle is hugely flexible with a range between 120-180˚. Examples of the different elements represented by "T" includes Al, Si, P, Be, Ga, Ge and Zn. The most commonly known composition involves silicon and aluminium tetrahedra linked together, in an aluminium silicate framework. Depending on how these tetrahedra are connected in space, different zeolite structures can arise with frameworks that forms channels and cavities collectively known as pores.[133] Zeolites can be classified on the basis of their pore dimensions, shown in Table 2.

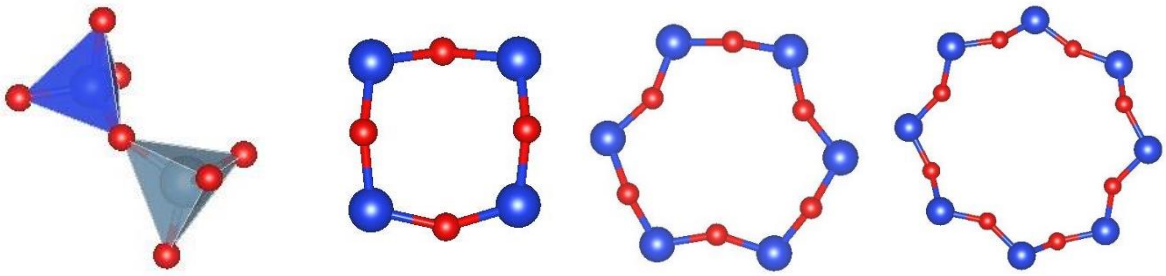

Figs. 1 (a – d): **(a)** TO_4 tetahedra, **(b)** 4MR, **(c)** 6MR and **(d)** 8MR. Red = O atom, Dark blue = Si atom and Pale blue = Al atom

Table 2

Porosity	Pore dimensions, *p* /nm
Micro-	$p < 2$
Meso-	$2 < p < 5$
Macro-	$p > 5$

As a result of the open structures of zeolites, small molecules such as CH_4, and inorganic species like transition metal cations can be hosted inside of the zeolites as extra-framework. Structural features common to many zeolites are referred to as secondary building units (SBUs). These are four (4MR), six (6MR) and eight membered rings (8MR) as shown in Figs. 1b – d which together form the 3-dimensional zeolite structures.[133] The different combinations of the SBUs in space results in 229 unique zeolite framework types (CHA, FAU, MFI etc.), each with different structural features subsequently belonging to different space groups.

The chemical composition formula for an aluminium silicate zeolite is[133]:

$$\{[M^{n+}]_{x/n}.[mH_2O]\}\ \{\ [AlO_2]_x\ [SiO_2]_{1-x}\}$$

Starting from just a pure silica material, the replacement of a $Si(IV)O_4$ tetrahedra with an $Al(III)O_4$ unit requires a charge balance compensation to ensure charge neutrality. This can be organic counter-cations such as H^+ or metal cations (Cu, Fe) as noted in the formula above coordinated with water adsorbates. This is known as a metal-exchanged zeolite. A typical zeolites synthesis involve the following steps: (1) silica and alumina containing reactants are mixed together in a basic solvent with a counter-cation and mineraliser present, (2) the mixture

is heated between 100 – 200˚C temperatures and 1 – 20 bar pressures in an autoclave, (3) an induction period follows where the reaction mixture remains amorphous and (4) after a period between hours – days, the amorphous materials is transformed into zeolite crystals. This is known as hydrothermal synthesis.[134] The counter-cation can act as a template or a structure-directing agent (SDA), and the mineraliser ensures solubility of the reagents.

Cu- SSZ-13 and SAPO-34 syntheses follows the same principles as above, however, post-synthetic treatments are commonly involved to introduce the Cu cations via ion-exchange. Fickel *et al* [38]performed Cu ion-exchange, by introducing a freshly prepared Na-SSZ-13 into a $CuSO_4$ solution at room temperature. Since, cations occupied extra-framework sites in cavities and pores, they are weakly-bounded to the framework walls (by physisorption) and may readily exchange via displacement. An ion-exchange reaction to describe the above is[133]:

$$\text{Na-SSZ-13} + 1/2Cu^{2+}\,(aq) \rightarrow Cu_{0.5}\text{-SSZ-13} + Na^{+}\,(aq) \quad (2)$$

In addition to ion-exchange, other useful properties of zeolites are absorption and catalysis. The open structures of zeolites mean small molecules can easily absorbed into the pores and cavities. Depending on the geometries of the pores (and cavities) different guest molecules based on size and shape selectivity can reside in the zeolites. The framework composition has a significant effect on determining the ease of molecules absorption. Zeolite A with a 1:1 silicon to aluminium ratio is hydrophilic, because of the high concentration of both Al atoms and charge-balancing cations, resulting in tendency to absorb water. Therefore, has been used as drying agents.[133]

Catalysis in zeolites are generally found in the Bronsted and Lewis acid sites. The former is introduced by exchange with ammonium cations, before heating to drive off NH_3.[133] The Bronsted acid sites are largely contributed by bridging Si – O*H – Al groups, but terminating groups are observed in Si-OH and P-OH in Cu-SAPO-34. Lewis acid sites can be formed by the dehydration of Bronsted acids, resulting in Si^{+} – O – Al forms. However, in metal-exchanged zeolites, the Lewis acid sites are mostly from transition metal centres that occupy extra-framework sites in the cavities and channels.[89] In the SCR de-NO_x reaction, it is the behaviour of the transition metal centre as a Lewis acid site that is pivotal for the SCR NO_x reduction reaction to proceed. A few authors have mentioned the ability of extra-framework Al in the zeolite surfaces to similarly behave as Lewis acids.[135-137] In both Cu –SSZ-13 and –SAPO-34, it is the extra-framework Cu that takes on the role of active sites for SCR NO_x reduction reaction. Cu and Fe cations compensate for the charge deficiency to ensure charge neutrality in the aluminium silicate (formula above) and aluminophosphate compositions, and subsequently behaves as active sites in SCR NO_x reduction reaction[22]. An atomistic illustration of this is depicted in Fig. 2. The rationale is the presence of transition metal cations acts as redox active centres in the large internal surface area of the zeolite host[22].

In general, zeolites have a close association with industrial catalysis, as described by Thomas *et al* and Li *et al*[76, 77]. They are for instance the basis of catalytic cracking and reforming in petroleum refinement, and the MTO process for the direct conversion of methanol to high-octane petroleum. In the chemical industry, they are of interest for their selectivity for instance in isomerization reactions. This is because, zeolites can behave like very strong acids and catalyse reactions commonly dehydrations and rearrangements[133].

In addition, the ability of zeolites to absorb small molecules into their open structures enable shape and size selectivity which makes them excellent materials for catalysis. There are reactant, product and transition state selectivity. Simply, in a reactant selectivity only a molecule of a specific size and shape can enter the zeolites' pores. In a product selectivity, a product formed within the zeolites' walls with dimensions that does not fit host's channels, would not be able to escape. An example is the isomerisation of dimethylbenzenes in ZSM-5 meant only the 1-4-dimethybenzene can rapidly escape the 10-ring channels[133]. Transition state selectivity ensures only intermediates that can fit the dimensions of the zeolites' cavities and/or channels can be formed, directing the reaction to a specific pathway[133].

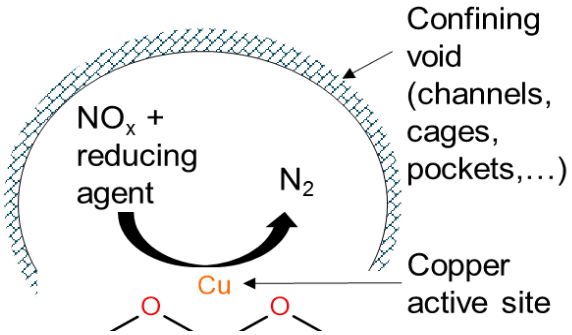

Fig. 2 A reproduced two-dimensional cartoon illustration of a zeolitic active site of SCR de-NO_x reaction; comprised of an extra-framework copper active site (ambiguous nuclearity and charge) and of the confining environments with varying size and topology.[88]

Because of zeolites' crystallinity, the active sites are identical in their environments, therefore, ensuring constancy in energy of interaction with reactants. The channels and cavities are of controlled geometry[76, 133]. This ensures the same products would be catalysed. Zeolites in industry are a success story and outside of heterogeneous catalysis, their ubiquitous-ness is overwhelming [76, 77].

Metal-exchanged zeolites for the SCR reaction has been studied for over 20 years[22, 77, 78]. The zeolites ZSM-5, Y, mordenite and Beta (MFI, FAU, MOR and BEA frameworks) have been the most studied, especially during the early years of SCR-zeolite catalysis research. This is because of their wide applications in related catalysis activities, wide availability and high thermal stabilities. The gradual progression in literature has shown a move from the large pore zeolites (Y, USY and Beta) to medium-sized pores zeolites (ZSM-5, ferrierite, mordenite) [22], and more recently towards zeolites with even smaller pore sizes, particularly the CHA structure[5, 22].

Metal-exchanged zeolites have been reported to show superior performance in the SCR de-NOx reactions with alkanes, alkenes or organic oxygenates compared to metal oxides. Li *et al* attempted to rationalize this observation via a mechanistic understanding by considering the three aspects of a metal-exchanged zeolite that are advantageous: (1) isolated oxo-ions of the extra-framework cations are favourable sites for selective oxidation, (2) the favoured dissociative chemisorption of intermediates in their cavities and (3) the nanopores of zeolites have high physisorption for many molecules[76].

In the case of Cu- SSZ-13 and SAPO-34, oxo-ions in the form of isolated mononuclear Cu^{2+} species located in the 6MR windows were found to be the active sites[22] and crucial for selective oxidation of the SCR reductants and intermediates. The complexity of electrostatics

in the zeolite structure is described as the main factor enhancing oxidation rates. The AlO_4 tetrahedra carries most the negative charge, with the positive charge provided by extra-framework cation. The compromised position of these mobile cations implies they are unable to compensate for the charge deficiency at all the unsaturated framework O atoms within their vicinity. As such, reactions within the zeolite pores that aid charge dissipation such as chemisorption and dissociation are favourable. Heat adsorption experiments have shown that physisorption energies are highly correlated with pore diameter size. Competitive adsorption occurs during a SCR process due to the presence of water vapour, therefore more hydrophobic zeolites tend to achieve higher N_2 yields with non-polar reductants (hydrocarbons)[46]. Zeolites with a high Al/Si ratio are more hydrophilic, consequently achieve higher NO_x conversion with more polar reductants such as ethanol[76].

Per Guan *et al*[5] current developments in SCR catalysts can be divided into vanadium-based and Fe- and Cu-exchanged zeolite catalysts. Cu- and Fe-zeolites are the automobile industry choice of catalyst, due to their high deNO_x activity along with excellent thermal durability. In addition, they can work at low temperatures and perform efficiently at high space velocities. Yet, their poor long term thermal stability is evident, with showing irreversible deterioration over time due to high temperature deactivation when undertaken in thermal aging experiments. The latter is vital for lifetime application in vehicles, this requires the Cu- or Fe-zeolite catalyst to be durable at high temperatures (around 670-900˚C) and in the presence of water vapour, a by-product of the NO_x reduction reaction and naturally occurring in the atmosphere. Therefore, thermal aging experiments involves the treatment of the catalyst under hydrothermal conditions – exposure to high temperatures at extended times (~64hrs) with a feed of air containing (4.5%) H_2O.

The discussion on Cu-ZSM-5 in 1986 by Iwamoto *et al* was the first appearance in the literature of the use of Cu-zeolites as catalysts for SCR de-NO_x reactions[8]. ZSM-5 is based on the MFI framework with 10-ring, medium-sized pore channels. The superior activity and selectivity of NO_x conversion showcased in Cu-ZSM-5 in both HC- and NH_3-SCR catalysis resulted in benchmark status[5]. Yet, Cu-ZSM-5 has poor hydrothermal stability resulting in catalyst deactivation via dealumination. Cu leaching has been observed at high temperatures that cause loss of structural integrity, and destruction of both Bronsted acid and redox sites[39]. A further issue found in ZSM-5 is the hydrocarbon adsorption (at low temperatures) and possible separate inhibition; the former causes damage to zeolite structure when the temperature is elevated as result of heat generated from hydrocarbons[82], and the latter is hydrocarbons entering the pore channels of the zeolite support inhibiting the SCR reaction via pore-blocking[40].

2.2 Properties of Cu -SSZ-13 and -SAPO-34

The use of Cu-SSZ-13 in de-NO_x by Bull et al was patented in 2009[79], Cu-SSZ-13 showed excellent catalytic activities including at low temperatures (90-100% NO_x conversion over a wide temperature window of 160-550°C) for the direct decomposition of NO, and importantly, paired with high hydrothermal stability[11]. Even after hydrothermal aging at 800°C, the NOx conversion was shown to be >80% [79]. Further studies, reported even greater hydrothermal stability and durability[40]. These excellent properties of Cu-SSZ-13 makes it the material of choice for the next generation automobile catalysts. However, the search for the nature of its active site is still controversial[36-48].

Cu-SSZ-13 catalyst has a chabazite (CHA) zeolite framework structure with narrow pore size of 8-atom rings large. A possible explanation for the superior hydrothermal stability of Cu-SSZ-13 is the significant effect of pore-size[38, 40]. The improved activity and selectivity observed for the Cu/CHA system in the conversion of NO via full reduction was first reported by Zones *et al*, in the form of SSZ-62[81]. SSZ-62 shares the same CHA framework topology as SSZ-13, but is a patented material which specifies a 10:1 Si: Al molar ratio in the chemical composition, and synthesised with a N,N,N-trimethyl-l-adamantamrnonium cation templating agent. The CHA SSZ-13 was first synthesized by Zones and Chevron[88] in 1985, a small pore zeolite with an AABBCC stacking sequence of double-6-rings (D6R). The D6Rs are adjoined to an 8MR framework to form a large cavity, the CHA cage enclosed, see Fig.3a[38]. It is a small-pore zeolite with dimensions ~3.8Å in the 8R[11, 37]. Kwak *et al* showed that even after extensive hydrothermal aging and HC fouling, the measured activity of NO decomposition exceeded 80% along with high selectivity for N_2 and less by-products such as N_2O formed[37].

Kwak *et al* made direct comparisons of Cu-SSZ-13's SCR activity and selectivity with Cu-ZSM-5. The results showed that the activity for NO_x conversion can be ranked as: Cu-SSZ-13 > Cu-ZSM-5 > Cu-beta, with both Cu-SSZ-13 and Cu-ZSM-5 achieving maximum conversions of >95% at temperatures of around 250°C, but Cu-SSZ-13 managed to maintain this high conversion (>90%) up to 500°C. Cu-ZSM-5 and Cu-beta begun to dramatically decline at around 300°C. At the highest temperature tested in the experiment, 550°C, Cu-SSZ-13 managed to achieve the highest conversion rate with 83%. Cu-SSZ-13 had the best performance between 200-500˚C for NO_x conversion[11].

In addition to the high activity, Cu-SSZ-13 demonstrated the highest selectivity with regards to N_2 formation over both NO_2 and N_2O in the oxidation of NH_3. At temperatures, above 300°C, both Cu-ZSM-5 and Cu-beta produced significant quantities of NO_2, more than Cu-SSZ-13. By 500°C, this gap widened, with the NO_2 production of Cu-ZSM-5 (30ppm) and Cu-beta (25ppm) more than twice that of Cu-SSZ-13 (<10ppm). NO_2 formation did perceptibly increase with temperature for Cu-SSZ-13, yet, N_2O production was consistently low at <5ppm, unlike ZSM-5 and Beta that showed large N_2O conversion peaks at round 200 and 500°C[11]. NO_2 formation has been identified as the rate-determining step in the SCR reaction, but is immediately consumed by the SSZ-13 catalyst by adsorption and not present in the gas-phase[89]. Kwak *et al*, postulated that the superior selectivity of Cu-SSZ-13 must be attributed to different reaction mechanisms, with a more selective pathway found in the production of N_2. Interestingly, the authors also unexpectedly speculated this observed difference in activity and selectivity is related to the structure of the zeolites, concerning the pore sizes and locations of the Cu active sites. The zeolite catalyst, Cu-beta, with the largest pore size (~7Å and ~5.5Å, 12-membered ring) had the lowest activity and selectivity. Cu-SSZ-13 with the smallest pore size out of the three (~4Å, 8MR) had the highest. This inverse relationship is an attractive finding between pore site and activity, but further studies are required, especially to aid the mechanistic understanding of the NO_x conversion pathway. A key understanding to this is the

ability of the zeolites catalysts to oxidize NH_3, with Cu-SSZ-13 attributed with the best NH_3 oxidation results over a wide temperature range[11].

The location of extra-framework ions in the CHA system was originally studied by Calligaris and Nardin in 1981 for hydrated Cd- and Ba- exchanged CHA. Based on Fourier maps, sites I, II, III and IV were postulated as locations for the framework atoms to reside in, with site I having the highest electron density peak, depicted in Fig. 3b.[83] Recent Rietveld analysis of X-ray diffraction patterns (XRD) of NH_4-CHA have shown that only site I is occupied significantly, located just outside the D6Rs in the top and bottom of the 8MR,[85] similarly electron spin resonance (ESR) on the isostructural Cu-SAPO-34 exhibited the same position for Cu[138]. Fickel and Lobo performed Rietveld refinements of synchrotron XRD data for NH_4-SSZ-13, Cu-SSZ13 and Cu-SSZ-16 zeolites. They found that the Cu cations in Cu-SSZ-13 are coordinated to three oxygen atoms just outside the plane of the six-membered rings (6MR). Interestingly, they also observed the off-centre shift of Cu from the origin of the 6MRs upon heating attributed to dehydration, and enhanced interaction of Cu with the electronegative framework oxygens in the 6MRs, evident in the shortening of the Cu-O bonds. The Cu-fractional occupancy in the 6MRs increases with temperature until 600°C, suggesting mobility of Cu ions before dehydration sets in "locking" the Cu ions more firmly in place[39].

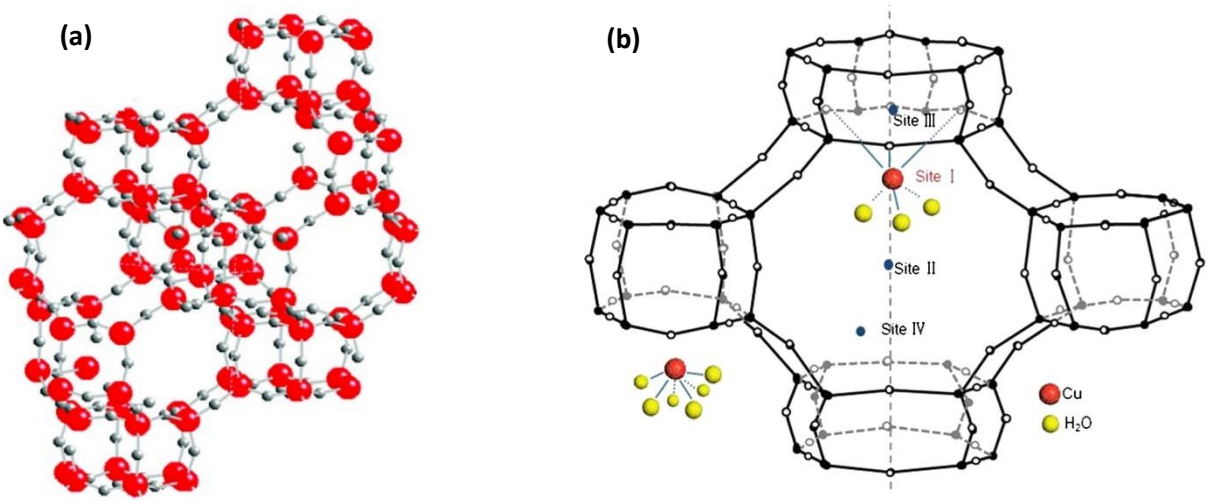

Fig. 3 (a) Zeolite framework structure of CHA SSZ-13, **(b)** skeleton structural diagram of the unit cell with the reported literature sites as taken from [38] and [19] respectively.

Based on H_2-temperature-programmed reduction (TPR) and Fourier transform infra-red spectroscopy (FTIR), Kwak *et al*, proposed the presence of two distinct copper species at different cationic positions in the SSZ-13 framework. At low exchange levels (<20%), the Cu ions firstly occupy the most stable site, this is the 6MRs which enables high-coordination of the Cu ions. On increasing exchange levels (>40%), upon saturation of the 6MRs, a new exchange-site is occupied, inside the large cages of the CHA structure[36]. Results for H_2-TPR on Cu-Y and Cu-FAU, by Dedecek *et al* also showed a similar peak at ~200°C have been attributed to the location of the Cu^{2+} ions in the large cages,[84] coinciding with Kwak *et al* results with large cage occupation at round 230°C[37]. Movement of the Cu^{2+} ions was deduced upon introducing H_2O into the H_2 gas stream; the respective H_2-TPR peaks were shifted and the overall spectra altered[36]. The same rationale as discussed by Fickel and Lobo, corresponding to H_2O adsorption enabling Cu^{2+} ions to move from their cationic positions was proposed[38].

FTIR of probe NO and CO molecules confirmed the autoreduction of Cu^{2+} ions to Cu^{+} ions during the pretreatment process, since CO only adsorbs on Cu^{+} ions, whilst NO adsorbs on both Cu^{+} and Cu^{2+}. Two different CO signals were shown on the FTIR spectra, implying

movement of some of the Cu^{+} ions from the original Cu^{2+} positions upon autoreduction into the 8MR (at 2135cm^{-1}). The NO probe showed two different cationic sites for the Cu^{2+} ions, both associated with 6MRs; either inside the 6MRs themselves or inside the large cages of the CHA structure in front of the 6MRs. These results contradict recent theoretical work, that concluded the only location of Cu ions is in the windows of the 6MRs. The nature of the reported Cu^{+} site at 2135cm^{-1} is a very small shift, compared to an isolated CO molecule[36]. Independently, Göltl *et al*[42] performed DFT calculations and managed to reproduce the vibrational spectrum of CO adsorption on Cu^{+} in good agreement with the experimental results of Kwak *et al* [36]. The experimental observation at 2135cm^{-1} is because of the gradual occupation of the cationic site corresponding to a specific 6MR configuration, where the details of the CO-Cu^{+} bonding (σ-donation from CO and π-back bonding from Cu^{+} d orbitals) is affected by the structural site, giving a distinct red-shifted peak. This was confirmed by charge analysis calculations[42].

Göltl's group[42] also managed to discern the nature of the active site for Cu-SSZ-13 SCR based on statistics that indicate Al distribution framework is not uniform[139], therefore in some cases two Al atoms can be present in the same unit cell. However, unit cells with three or more Al atoms were disregarded, because it was improbable for the high Si: Al ratio currently given in experiments. Majority of the distribution will have consisted of one Al atom per unit cell. In the preparation[140], Cu is introduced into a freshly prepared zeolite with post-modification methods, this is usually via ion-exchange with $CuSO_4$[141] or $Cu(NO_3)_2$. Since the zeolite framework is not charged during the ion-exchange, the formation of Cu^{2+} must be counterbalanced by two framework Al atoms. Thus, this affects the distribution of the Cu sites, with the first sites to be occupied associated with two Al atoms, but not necessarily from the same unit cell[42].

Due to the gradual lessening effect of increasing exchange level with respect to catalytic activity (experimental results from Kwak *et al* [36]) and with the assumption the most stable sites are occupied first[42]. Göltl *et al*[42] showed that the active sites are the Cu^{2+} cations in two different configurations, each with two Al atoms sitting in the same 6MR. This was first validated by calculating the energy and structure of Cu^{2+} occupation in different sites for a high Si/Al ratio (as per experiment) SSZ-13, constrained by statistics that in each unit cell there should be no more than two Al atoms present. This resulted in eight different, possible cationic sites for Cu^{2+}. They found the case where Cu^{2+} was in the 6MR with two Al atoms as the most stable configurations, and the 8MRs cationic positions are disfavoured. It is important to note the pivotal role that Si/Al ratio plays in forming highly active catalysts; at high Si: Al too few of the sites are created, while increasing Al content more than two Al atoms can occupy a single 6MR cationic position[42].

The hydrothermal stabilities of the Cu-SSZ-13 was investigated by Blakeman *et al* via in situ XRD hydrothermal studies. The comparison between Cu/CHA and Cu/Beta catalysts attributed highlighted the significant role played by pore size in hydrothermal stability. Upon hydrothermal exposure, for high temperatures at short time lengths (900°C/1hr), the small pore-sized Cu/CHA maintained NOx conversion efficiency of >90% within the operating window of 250-300°C (the temperature range found in a diesel engine), but the large pore-sized Cu/Beta suffered a significant drop to ~50-55% in NO reduction. When the two catalysts were treated at lower temperature, but for longer times (670°C/64hrs), a similar trend was observed. As such, the Cu/CHA showcases long-term hydrothermal durability and can cope with higher temperature extremities without significant effect on the catalyst's NO_x reduction performance, unlike the larger pore-sized Cu/Beta catalyst[40].

In situ XRD measurements were made during hydrothermal treatments within the temperature range 50-900°C. Prior to addition of Cu ions, the parent zeolites CHA and Beta were studied, both showed relatively good hydrothermal stabilities. However, both zeolites suffered from temperature-induced disordering upon reaching 900°C, but neither experienced a complete structural collapse. The framework was intact albeit slightly disordered. Upon the addition of Cu ions via ion-exchange, the Cu/CHA structure remained throughout the hydrothermal experiment, but the Cu/Beta framework collapsed at 900°C. At high temperatures, presence of Cu accelerated the collapse of the Beta zeolite framework, however the Cu/CHA structure only suffered from structural disordering. The differing hydrothermal stabilities of the Cu-zeolites cannot be predicated on the parent zeolite frameworks, since both showed good stabilities[40].

Blakeman *et al* hypothesized that the varying pore sizes is attributed to the different hydrothermal stabilities observed in Cu/CHA and Cu/Beta catalysts[40]. One of the main deactivation mechanisms in Cu/zeolite catalysts during hydrothermal aging is the dealumination process. Fickel *et al* suggested at high temperatures H_2O molecules attack the aluminium tetrahedral sites which forms $Al(OH)_3$ units. To cause framework collapse, these $Al(OH)_3$ units have to exit the zeolite by diffusion through the narrow pores. The kinetic diameter of $Al(OH)_3$ is bigger than an 8MR pore, therefore it is unlikely to pass through the pore system in a CHA zeolite[11]. The Blakeman group expanded on this theory by explaining for Cu-zeolites at high temperature above 800˚C, results in unfavourable Cu/Al_2O_3 interactions which initiates the framework collapse. This only affects the Cu/Beta catalyst, because for the Cu/Al_2O_3 interactions to cause structural damage, it has to involve Al- and Cu-moieties to diffuse through the pore channels. In the small-pore Cu/CHA catalyst, these Al- and Cu-related molecular intermediates would be too big to diffuse through the 8MR windows, however in the 12MR pore channels in Beta zeolite there would be minimal or no steric restriction. Thus, the pore sizes can affect hydrothermal stabilities [40]. This was verified by Göltl *et al* whom calculated the diffusion barriers for Cu through an 8MR pore and 12MR pore channels in CHA and FAU frameworks respectively, with a 100kJmol barrier found in the smaller pore-size compared to 40kJmol for the larger one[42].

The thermal stability of Cu-SSZ-13 was investigated within a temperature range of 100-900°C and showed that the catalyst can withstand temperatures up to ~800°C as observed from gradual weakening and decreased resolution of the XRD patterns. The thermal displacement parameters of Cu increased with temperature; the authors suggested this indicated Cu mobility and the transitioning of Cu in between identical sites in the framework[38]. UV/vis measurements showed no evidence for self-reduction of Cu^{2+} ions, as has been reported in Cu-ZSM-5[38] in contradiction with Kwak *et al*'s[36]. The ion-exchanged Cu ions increased the thermal stability of SSZ-13 compared to the acid form, and Cu-SSZ-13 was found to be more stable than Cu-SSZ-16[38]. Quantum chemical calculations indicate a very high stability of the Cu^{2+} sites in the 6MRs of SSZ-13. At high temperatures, the migration of Cu ions from one site to the next is unlikely, since the 6MR sites are not directly linked and the lowest-energy path requires diffusion via an 8MR (which per Göltl *et al* requires a barrier of 100kJ/mol[42]). As such, catalyst deactivation is less likely to occur in SSZ-13, since the active sites are well-separated in space and by high energy barriers (especially for diffusion of Cu between 6MR sites)[42].

XRD studies on the Cu-SAPO-34 showed that different methods of introducing Cu into SAPO-34 results in different forms of Cu species existing[47]. In the preparation of Cu-SAPO-34 via precipitation it is the CuO_x particles that are the dominant species, and mostly located on the external surfaces of the zeolite[47]. Isolated Cu ions inside the extra-framework sites are found when ion-exchange process was undertaken, unlike with the precipitation method, the

Cu is introduced uniformly over the zeolite and no aggregates of Cu species were observed from scanning tunnelling electron microscopy (STEM). Interestingly, the Cu ions in the ion-exchanged sample were more difficult to reduce during H_2 temperature programmed reduction (TPR), compared to the CuO_x species in the precipitation method. This confirms the stability of isolated Cu ions residing inside the extra-framework sites[47].

The SCR activity of both (precipitated and ion-exchanged) samples are vastly different. It is the ion-exchanged Cu-SAPO-34 which is the most active catalyst for NH_3-SCR reaction over a temperature range between 200-600˚C. This indicates that it is the isolated Cu ions in the extra-framework sites which are the active sites for SCR reaction. On the other hand, the precipitated sample shows a high NH_3 oxidation ability at temperatures above 350˚C, since the CuO species are found on the external surface with greater exposure and stronger Bronsted acidity inside the zeolite framework[47]. Similarly, Xue *et al* observed the same high NH_3 oxidation ability in Cu-SAPO-34 at temperatures greater than 350˚C.[46]

Liquid-ion-exchanged was performed by Xue *et al*[19] at four different % weight of Cu, from 0.98, 1.42, 1.89 and 2.89 weight % for preparation of Cu-SAPO-34. From H_2-TPR measurements, four types of Cu species were shown to co-exist in the Cu-SAPO-34 samples, these were; external surface CuO clusters, isolated Cu^{2+} ions, nanosize CuO and Cu^{+} ions. The presence of CuO clusters on the zeolite surface only occurred at high Cu loadings (2.89 weight %). The NH_3-SCR reaction rates showed a monotonic increased with the increased of Cu loading up to 1.89 weight %, within a temperature range between 100-200˚C. A decline in the reaction occurred with formation of CuO clusters. Both nanosize CuO and Cu^{+} ions located in the zeolite channels increased with copper content, and isolated Cu^{2+} ions found in the extra-framework sites similarly increased. However, only the change in amount of isolated Cu^{2+} calculated from EPR and H_2-TPR correlated with the change in NH_3-SCR reaction rates. Therefore, indicating isolated Cu^{2+} ions are the active sites at temperatures below 200˚C[19].

At temperatures, above 200˚C, the active sites for the NH_3-SCR reaction might involve other Cu species other than just isolated Cu^{2+}. Difference in activation energies were calculated for the NH_3-SCR reaction as a function of temperature, with 9.8 and 33.6kJ/mol at 220-350˚C[142] and 100-200˚C temperature ranges respectively. This difference in activation energy is postulated to be affected NH_3 adsorption coverage, and NH_3 migration between Bronsted and Lewis acid sites at higher temperatures[19]. A NH_3 migration reaction has been studied and confirmed by Wang *et al* with in situ-DRIFTS experiments[89]. Similarly, Bradenberger *et al*[143, 144] found change in active sites at different temperatures for Fe-ZSM-5, monomeric Fe species were the active sites at temperatures below 300˚C. However, at temperatures above 300˚C dimeric Fe species were found to be active in the NH_3-SCR.

2.3 Mechanism of de-NO_x SCR cycle

The NO_x content of exhaust fumes found in diesel engines are commonly in the form of NO, and only a fraction is NO_2[115]. As such, the basic SCR reaction is[7, 115, 116, 177]:

$$4NH_3 + 4NO + O_2 \rightarrow 4N_2 + 6H_2O \quad (3)$$

A fast SCR reaction is termed when there is a 1:1 mixture of NO and NO_2, this leads to an accelerated NOx reduction rate[7, 116, 117]:

$$4NH_3 + 2NO + 2NO_2 \rightarrow 4N_2 + 6H_2O \quad (4)$$

When the 1:1 ratio of NO:NO_2 is exceeded in favour of NO_2, the following SCR reaction occurs[7, 115, 117]:

$$4NH_3 + 3NO_2 \rightarrow 3.5N_2 + 6H_2O \quad (5)$$

From isotopic measurements on a Ba-Na-Y zeolite catalyst, it has been shown that the N_2 produced consists of N atom from a molecule of NO_x and another from the ammonia[145, 146], as indicated in reactions (3) and (4). The SCR reaction over zeolites requires that NO is oxidized into NO_2 and has been suggested as the rate-determining step of the mechanism[131, 147, 148-150]. As a result, reaction (5) can be regarded as the "true" SCR reaction[7]. NO oxidation into NO_2 has been noted[89] to be pivotal in the formation of surface nitrates[181-183]. The formation of NO_3^- species was observed and speculated to be the adsorption of NO_2 onto the bridging SiO*Si and FeO*Al groups for Fe-exchanged zeolites, silicalite and ZSM-5[90, 91, 92]. Wang et al conducted DRIFTS studies for Cu-SAPO-34 which showed characteristic peaks of adsorbed NO_2 species in the form of NO^{3-}, mono- or bi-dentately bounded between the range, 1625–1530cm^{-1}. These adsorbed species have been observed to have good stability on the zeolite surfaces. Surface nitrites could not be absolutely confirmed in the same study, due to overlap of peaks with the framework asymmetric signals. The group observed that the oxidation of NO would surface nitrates production, and that the presence of NO_2 would hinder this oxidation pathway, due to stability of nitrates[89]. This has been touted as the main reason for the poorer NO oxidation on Cu-SAPO-34[89, 93].

Evidence of the fact that NO_2 must be provided as the starting gas, or as NO to be oxidized into NO_2 for the SCR reaction to take place over a zeolite catalyst has been noted with an investigation using H-ZSM5[149, 151]. This experiment showed that H-ZSM5 produced negligible SCR activity with only NO, but then achieved high SCR activity when 50% NO_2 is added[7, 131, 147, 152]. Investigating the reactivity of NH_3 on Cu-SAPO-34, it was found that a feed of just pure NO led to very low N_2 production, but once 5% O2 was added to the starting, surface NH_3 concentration on the zeolite decreased and N_2 outlet increased. This confirms the above with regards to the pivotal role NO oxidation, and subsequent surface nitrates and nitrites formation[89].

It has mentioned by some authors that in metal-exchanged zeolites the NO_2 is produced at the metal centres, while the SCR reaction takes place within the zeolite matrix [131, 147]. The NO_2 is immediately adsorbed by the zeolite catalyst and it has been noted[89] that the presence of Fe-exchanged in ZSM-5 resulted in increased SCR activity compared to just H-ZSM-5, causing the authors to speculate that the Fe in this case does not only aid NO oxidation, but also accelerate the SCR reaction in the zeolite[131]. However, there is still debate

with the nature of active sites, as some investigation observed no changed in SCR activity between H-ZSM-5 and Fe-ZSM-5[150].

DRIFT spectroscopy has been used to study the adsorption of NO on Fe-ZSM-5. It showed that intermediate Fe^{n+} – NO intermediates along with $Fe^{2+}(NO)_2$ and NO^+ are formed [153-155]. The NO^+ can be formed either by metal ions on extra-framework sites acting as Lewis acids[154, 156]. Mechanistically this is shown as[7]:

$$NO + Fe^{3+} \rightarrow NO^+ + Fe^{2+} \quad (6)$$

By Bronsted acid sites, this is taken as[7, 155]:

$$2NO + 1/2O_2 + 2Olattice - H \rightarrow 2O\text{-}lattice - NO^+ + H_2O \quad (7)$$

NO in the form of mononitrosyl ligands on the Cu^{2+} species were detected at 1903cm^{-1} [189, 94]. Similarly, NO^+ in Cu-SAPO-34 were found in Bronsted acid sites at 3627, 2599 and 2145cm^{-1} [89, 95, 96]. It has been suggested that the rate of NO oxidation reaction is determined by desorption of NO_2 within the zeolite framework [7, 148], and subsequently traversing to another part of the matrix [7, 131, 147]. This fits relatively well to the current mechanistic understanding, since no NO_2 in the gas phase is observed as it assumed to be immediately consumed as adsorbed NO2[89].

The number of different metal centres that has been used in metal-exchanged zeolites has led to several proposals on what reactants regenerates the reduced metal sites. In vanadia based systems, it is the NO_2 that has been suggested to re-oxidized the V^{4+}, and similarly for Fe^{2+} SCR catalysts[42]. In Cu-FAU, it is O_2 instead of NO_2 that oxidizes Cu(I) back to Cu(II)[184]. Regardless of the precise species in regenerating the metal sites, under conditions absent of oxygen the SCR activity is minimal, since the catalytic cycle becomes incomplete and the metal centre remains in the reduced state[7, 148, 157].

DRIFTS studies by Wang *et al* have shown that the inclusion of O_2 in the feed is an important factor in the formation of surface nitrates and nitrites, therefore enhancing the reactivity of surface NH_3 [89]. The dimerization of gaseous NO_2 at low temperatures and the subsequent formation of reactive nitrates (NO^+, NO_3^-) has been suggested as key elementary steps in the fast SCR reaction [7, 89, 158, 159]. The dimerization of NO_2 forms N_2O_4, which disproportionate on the zeolite surface to form nitrates. The equations are [7, 131, 160, 161]:

$$2NO_2 \rightarrow N_2O_4 \quad (8)$$

$$N_2O_4 \rightarrow NO^+ + NO_3^- \quad (9)$$

The formation of NO_3^- is important in affecting the presence of NH_4NO_3 intermediate, before subsequent reductions by NO[89]. Whilst, NO^+ can be produced via oxidation of NO on Bronsted acid sites to form NO_3^-[100]. Interestingly, NO^+ has been confirmed via DFT calculations and EPR experiments to have the ability to react with framework O^{2-} atom to form NO_2^- [89, 97, 98, 99]:

$$NO^+ + O^{2-} \rightarrow NO_2^- \quad (10)$$

Another pathway NO^+ is the substitution of hydrogen proton on Bronstead acid sites in the presence of NO_3^- co-product from reaction (9) to give[89]:

$$NO_3^- + NO^+ \; Zeo - O - H \leftrightarrow Zeo - O - NO^+ + HNO_3 \quad (11)$$

The above reaction has been confirmed, due to the decreased in the OH bridging bonds when the NO, NO+O_2 and NO_2 was present[89]. Whilst, HNO_3 was observed by Rivallan *et al* in H-ZSM-5[89, 92.] In the presence of H_2O, HNO_3 can be formed by reduction of NO_2 [89, 101, 102]:

$$2NO_2 + H_2O \leftrightarrow HNO_3 + HNO_2 \quad (12)$$

As such, the nitrates produced in reaction (12) can generate more HNO_3 by reacting with NO_2, whilst the NO_2 can also pair with NO_2^- from reaction (10) to give NO_3^- [89, 101, 103, 104]:

$$NO_2 + NO_2^- \leftrightarrow NO + NO_3^- \quad (13)$$

$$NO_2 + HNO_2 \leftrightarrow NO + HNO_3 \quad (14)$$

This subset of nitrates and nitrites reaction will be ultimately determined by the ratios of NO_2 and NO_x in the feed[89]. The reverse reactions of both (13) and (14) is vital[89], since it results in the reduction of the nitrates (NO_3^- and HNO_3) into nitrites of the form NO_2^- and HNO_2 respectively, this can then react with NH_3 (at the Lewis acid sites) or activated NH_4^+ to form NH_4NO_2 intermediates [89, 105, 106, 107, 108, 109]. Reactions (15) and (16) illustrates this[89]:

$$NH_4^+ + NO_2^- \leftrightarrow NH_4NO_2 \quad (15)$$

$$NH_3 + HNO_2 \leftrightarrow NH_4NO_2 \quad (16)$$

The NH_4NO_2 intermediate then easily decomposes to N_2 and H_2O at relatively low temperatures of above 80˚C [89, 104, 110]:

$$NH_4NO_2 \leftrightarrow N_2 + 2H_2O \quad (17)$$

However, NH_4NO_2 can be oxidized into NH_4NO_3 a troublesome intermediate that can block the SCR active sites, due to its stability under low temperatures [89, 111, 114]. The nitrate intermediate has been observed in the ZSM-5, vanadium-based and BaNa-Y catalysts[89, 111, 112, 113].

Yeom *et al*[161] mentioned a feed with 1:1 ratio of NO:NO_2 can result in a direct reaction to form N_2O_3[7]:

$$NO + NO_2 \rightarrow N_2O_3 \quad (18)$$

N_2O_3 has been speculated as a reactive intermediate in both Cu-ZSM-5 and Fe-ZSM-5, and can result in the formation NH_4NO_2, see reaction (23) and subsequently reaction (24) achieving maximal SCR activity. The formation of N_2O_3 occurs with adsorbed NO and NO_2 on the surface of the zeolite catalyst implying a Langmuir-Hinshelwood mechanism[7, 89]:

$$NO_{ads} + NO_{2ads} \rightarrow N_2O_3 \quad (19)$$

The NO^+ in reaction (20) can react with H_2O to form HNO_2, additionally the oxidation of NO to NO^+ either from metal sites (reaction 6) or in Bronsted acid sites (reaction 7) can contribute to the formation of HNO_2[89]:

$$NO^+ + H_2O \rightarrow HNO_2 + H^+ \quad (20)$$

$$HNO_3 + NO \rightarrow HNO_2 + NO_2 \quad (21)$$

The reducing agent NH_3 either reacts with HNO_2 or N_2O_3 from reaction (9) to give the NH_4NO_2 via the following[89, 146, 159]:

$$HNO_2 + NH_3 \rightarrow NH_4NO_2 \text{ (22)}$$

$$N_2O_3 + 2NH_3 + H_2O \rightarrow 2NH_4NO_2 \text{ (23)}$$

The ammonium nitrite in reactions (22) and (23) decomposes quickly to give the SCR products N_2 and H_2O[89, 159, 162, 163]:

$$NH_4NO_2 \rightarrow N_2 + 2H_2O \text{ (24)}$$

Reaction (24) can be catalysed by protonation of the NH_4NO_2 intermediate by Bronsted acid sites, resulting in an intermediate that decomposes at room temperature[185]. Ammonium nitrate, NH_4NO_3 can be formed as such[89, 131, 164]:

$$2NO_2 + 2NH_3 \rightarrow NH_4NO3 + N_2 + H_2O \text{ (25)}$$

$$NO_3^- + NH_4^+ \rightarrow NH_4NO_3 \text{ (26)}$$

Alternatively, the NH_4NO_3 intermediate can be oxidized from the NH_4NO_2 species with NO_2 [89]:

$$NH_4NO_2 + NO_2 \leftarrow\rightarrow NH_4NO_3 + NO \text{ (27)}$$

In reaction (26), the NO_3^- is from a disproportionation product from in reaction (13) and the NH_4^+ ion is the activation of NH_3 on Bronsted acid sites. Upon NH_3-TPD experiments on Cu-SAPO-34, peaks at 1460 and 1617 were mentioned to be NH_4^+ ammonium ions on Bronsted acid sites, whilst NH_3 on Lewis acid sites (Cu centre) was observed at $1617cm^{-1}$[89]. From the studies, the authors deduced that both acid sites share similar strengths in acidity, in contrast from previous work.[89] This is a key factor in the effectiveness of Cu-SAPO-34, due to the ability to shuttle NH_3 between the acid sites, enabling an overload onto the Lewis acid sites which are mainly the transition metal centres for NO_x reduction. This was evident by the increased of NH_4^+ (in the NH_4NO_2 form), but no correlated change with the Bronsted acid sites was observed. Therefore, indicating, the transfer of NH_3 to Cu sites from the Bronsted sites, and the formation of NH_4NO_x on the Lewis acid sites. This procedure was facilitated by the presence of NO oxidation with O_2. NH_4NO_3 is a two-part problem, because (i) it forms deposits on the catalysts at low temperatures, causing active sites blockage and (ii) at temperatures above 200˚C it can decompose to nitrous oxide (N_2O) [7, 89, 131, 117, 159]. The two decomposition pathways are[89]:

$$NH_4NO_3 \rightarrow N_2O + 2H_2O \text{ (28)}$$

$$NH_4NO3 \rightarrow NH_3 + HNO_3 \text{ (29)}$$

Brandenberger *et al*[7] confirmed that the formation of N_2O is only when the NH_3NO_3 decomposition occurs in the absence of water, therefore, not in the standard SCR environment. This was further verified by Wang *et al*[89]. However, under increased temperature conditions, the oxidation activity of the metal centres increased, resulting in a tendency for metal-exchanged zeolites to form N_2O. This is especially valid for the strong oxidizing noble metals[165-167]. It has been observed that Cu-ZSM-5 is more susceptible to form N_2O compared to the Fe-exchanged. It has been reported that aggregates of CuO leads to formation of N_2O in Cu-FAU, and it is the presence of Cu that facilitates this formation[168, 169]. Nevertheless, N_2O is a highly undesirable product that would act as a greenhouse gas if escaped into the atmosphere, in addition it reacts with ozone in the troposphere[89].

Instead of the formation of N_2O under their SCR conditions, the group from Wang et al suggested that the NH_4NO_3 intermediate reacts with NO to give N_2, H_2O and NO_2. Since, no N_2O was observed in their outlet. This reaction is shown here[89]:

$$NO + NH_4NO3 \leftrightarrow N_2 + 2H_2O + NO_2 \quad (30)$$

N_2O can be decomposed into its elementary products at high temperatures when catalysed by a metal-exchanged zeolite[7]:

$$2N_2O \rightarrow 2N_2 + O_2 \quad (31)$$

Alternatively, ammonia can reduce N_2O to give N_2 and H_2O[7]:

$$3N_2O + 2NH_3 \rightarrow 4N_2 + 3H_2O \quad (32)$$

Because of reactions (31) + (32), N_2O can only be observed at low temperatures[131, 170-174], the presence of ammonia catalyses the decomposition of N_2O in reaction (32) which has been confirmed by TPR studies[89, 175].

Chapter 3 Computational techniques

3.1 Force field

Force field or interatomic potentials describes the forces between atoms, in a functional form and parameter sets. By evaluating these forces, the potential energy of a system can be calculated as function of the nuclear coordinates. For ionic materials, the potential energy function describes the interactions between all component species as[49]:

$$U = \sum_i^N \Phi_{ij}(r_i,\ r_j) + \sum_i^N \sum_j^N \sum_k^N \Phi_{ijk}\ (r_i,\ r_j,\ r_k) + \cdots \quad (33)$$

The potential energy function is expanded into two-body terms, which depends on the relative distance between pairs of atoms (r_i and r_j). Similarly, a three-body term depends on the positions of all three atoms (r_i, r_j and r_k). Higher body terms can be included, such as a four-body term when describing molecular organics. However, for inorganic crystalline materials, the expansion up to the three-body terms is sufficient. Potential energy function, U is the summation of all interactions between the atoms in a unit cell and the periodic replications within a finite cut-off distance. The interactions described in Φ_{ij} for expansion up to a two body-term are the electrostatic energy and intermolecular interactions between a pair of atoms. This can be decomposed into a long- and short- range potentials. The former is determined by the Coulomb's Law and the latter by interatomic potentials[49].

In force-fields, for most ionic materials the short-range interactions are described by the Buckingham potential[49] which consists of an exponential repulsive term and the inverse attractive term. The expression can be defined as:

$$\emptyset_{12} = Aexp(-Br) - \frac{C}{r^6} \quad (34)$$

The interatomic pair potential is given by $\emptyset_{12}$ for species 1 and 2 being described. *A*, *B* and *C* are constants. The term *r* is the absolute distance between particles 1 and 2. This effectively reproduces the Pauli repulsion energy and the van der Waals interactions (London, Keesom and Debye energies) within the limit of $r \rightarrow 0$. A three-body term is described using a harmonic angle-bending three body potential, this is described as[49]:

$$E_{ijk} = 1/2K\left(\theta_{ijk} - \theta_o\right)^2 \quad (35)$$

Where the θ_o is the equilibrium bond angle for which both zeolite and AlPO is at 109.47, around the pivot atom *j*[49]. The oxygen ions are modelled by the shell model of Dick and Overhauser [176] which aims to describe the effect of ion polarizability. The ions are partitioned into a massive charged core, q_{core} that bears the mass of the ion connected to a massless charged shell, q_{shell} via a harmonic spring constant. Q_{core} and q_{shell} are coulombically screened from each other. This gives the polarizability, α[49]:

$$\alpha = (q_{shell})^2/(f + K) \quad (36)$$

In equation (36), K is the core-shell spring constant and *f* is related to the sum of forces acting on the shell due to other ions[49].

The most important interaction in an ionic material is the electrostatic interaction as described simply by Coulomb's law which dominates the long-range potential. It can contribute

up to 90% of the total energy of the system[49], and is evaluated by calculating the Ewald summation since the electrostatic energy is conditionally convergent in real space[49]. The Coulomb form is given as:

$$U_{ij} = \frac{q_i q_j}{r_{ij}} + V_{ij}(r_i, r_j) \quad (37)$$

The Coulomb energy, U_{ij} and the formal charges for species *i* and *j* are q_i and q_j respectively. The term *r* is the absolute distance between the pair of species *i* and *j*.

3.2 First principles QM

First principles quantum mechanics (QM) methods attempt to solve the non-relativistic time-independent Schrodinger equation:

$$H\Psi = E\Psi \quad (38)$$

E is the energy of the state and Ψ is the wavefunction which carries all the information of the quantum state and *H* is the Hamiltonian operator (a functional) represents the total energy of a system. Invoking the Born-Oppenheimer approximation, we end up solving the electronic Schrodinger equation[177]:

$$H_{elec}\Psi_{elec} = E_{elec}\Psi_{elec} \quad (39)$$

Where H_{elec} consists of three terms[177]:

$$H_{elec} = -\frac{1}{2}\sum_1^N \nabla_i^2 + \hat{V}_{ext} + \sum_{i<j}^N \frac{1}{|r_i - r_j|} \quad (40)$$

The first term in equation (n) is the kinetic energy, the second is the interaction with external potential and the third is the electron-electron interaction. For materials modelling the external potential describes the interaction of electrons with the atomic nuclei[177].

In the case of Hartree-Fock theory (HF), we achieve a direct solution to the equation (n) by enabling us to solve the HF equations iteratively via the self-consistent field (SCF) procedure. Despite this, it completely neglects the electron correlation energy which describes the interaction between electrons of opposite spins. In addition, it requires significant computational expense, because it scales quickly with the number of electrons treated and the need of a large basis set to achieve realistic models of systems in solid-state materials[177].

However, density functional theory (DFT) which has been widely used in the study of materials such as zeolites, is able to avoid directly solving the Schrodinger equation[177]. This is on the basis of the Hohenburg-Kohn theorems which is firstly[177, 178]:

The electron density determines the external potential (to within an additive constant).

From equation n, this implies that the electron density uniquely determines the Hamiltonian operator, thus the wavefunctions of all states. This means all the properties of the material being computed can be gained. The second theorem establishes a variational principle[177, 178]:

For any positive definite trial density, ρ_t, such that $\int \rho_t(r)dr = N$ then $E[\rho_t] \geq E_o$

From the first theorem we know a trial density uniquely determines a trial Hamiltonian, however the second theorem establishes that DFT is only restricted only to studies of the ground state. The Kohn-Sham equations for a non-interacting uniform electron gas (UEG) enables the kinetic energy and electron density to be known exactly, reproducing the true ground density[177]. Both the Kohn-Sham and HF equations have identical structure, but in the case of Kohn-Sham equations, the non-local exchange potential is replaced by the local exchange-correlation potential[177, 179].

In the case of Local Density Approximation (LDA) the local exchange-correlation functional is taken as a simple function of the local charge density, and in Generalised Gradient Approximation (GGA), the energy functional depends on both the density and its gradient[177].

The GGA improves on the LDA in terms of the description of certain properties such as binding energy of molecules[177], an example of a GGA functional is the PBE. While hybrid functionals involve the mixing of DFT and HF formulations for the local exchange-correlation functional, such as B3LYP and PBE0 which has been widely used.

Chapter 4 Methodology

The aim of the current work is to investigate computationally the location of Cu ions in SSZ-13 and in the isostructural SAPO-34. Then to investigate the adsorption behaviour of small admolecules in the pre-determined equilibrium locations, see Chapters 6.1, 7.1 and 8.1 for the methodology of the force-field calculations of H_2O adsorption, QM calculations of H_2O and NH_3 molecules respectively. The energetically favourable locations of a Cu^{2+} ion in the CHA framework were determined by exploring the full energy landscape via force-field calculations. To this aim, we employed the General Utility Lattice Program (GULP) code[49] and a set of empirically-derived interatomic potentials[86, 180]. In doing so, we aim to gain microscopic insight in the Cu^{2+} behaviour within a zeolitic environment. This will aid the understanding, in how the electrostatic interactions interplay between both the Cu^{2+} and the different dopant configurations affect the energy and location of Cu in the CHA framework. Subsequently, the energetic pathways of Cu^{2+} migration in the CHA framework were studied. The calculations were performed on a standard (UNIX/LINUX) scientific desktop. Following this, quantum chemical calculations were performed with CRYSTAL on the UK National Supercomputing Service, ARCHER and University College London's (UCL) computing research clusters, Grace and Legion. This is because, the QM calculations are computationally very intensive requiring fives nodes per calulation, each running with 24 cores for 24 hours. Each CRYSTAL geometry optimisation was performed on 109 atoms supercells of Cu-SSZ-13 and Cu-SAPO-34. The electronic-structure calculations in CRYSTAL were performed, because the force-field calculations does not provide an explicit treatment of electrons, therefore, QM calculations enable the inclusion of crystal-field splitting.

4.1 Force field calculations

In the force-field calculations with periodic boundary conditions (PBC), unit cell dimensions of SSZ-13 and SAPO-34 structures, each consisting of 109 atoms including the Cu^{2+} extra-framework ion, with two dopant substitutions in the CHA framework for charge balance were computed. We were able to observe the general relocations of the Cu^{2+} ion from its initial positions in different sites (SI, SII, SIII and SIV including the symmetry equivalents: a, b, c, d, e, f, g, h and i) reported in literature[83] into energy minima.

In the force-field used, the short-range interactions are described by Buckingham potentials equation (34). This is in combination with the electrostatic potential energy given by Coulomb's Law to determine the long-range interactions. The interaction between three ions are described by a harmonic angle-bending three body potential. The O atoms are modelled using the Dick and Overhauser shell model[176]. The A, B and C constants were fitted empirically to the structure and physical properties of α-quartz and Al_2O_3, and Berlinite for the zeolite[86] and AlPO[180] interatomic potentials used respectively. The AlPO potential does not have a three-body O-P-O term, since upon empirical fitting, the authors realised the force constant went to zero[180]. Both set of potentials are shell model potentials, and the parameters to describe the zeolite and AlPO frameworks are listed in Table 3 and 4 respectively. The only exception to the potentials is the Buckingham potential for Cu^{2+} which was derived by Gale from a series of unpublished results, by utilizing non-zeolite potentials then relax fitted to structure and any available properties for the relevant binary oxide.

Table 3: Parameters of the Catlow and Jackson potential[86].

Buckingham Potentials	**A/ eV**	**ρ/ Å**	**C/ eV Å^6**
Si^{4+} - O^{2-}	1283.907	0.32052	10.66158
Al^{3+} - O^{2-}	1460.300	0.29912	0.00000
O^{2-} - O^{2-}	22764.000	0.14900	27.88000
Cu^{2+} - O^{2-}	712.800	0.32700	0.00000
Three-body potential	**K/eV rad^{-1}**		**Θ_o/degrees**
O-T-O*	2.09724		109.47
Core-shell-potential	**K/eV rad^{-1}**		
O^{2-}	74.92		

Coulombic charges	**Si^{4+}**	**Al^{3+}**	**O^{2-} (core)**	**O^{2-}(shell)**
	4+	3+	0.86902	-2.86902

Table 4: Parameters of the Gale and Henson potential[180].

Buckingham Potentials	**A/ eV**	**ρ/ Å**	**C/ eV Å^6**
P^{5+} - O^{2-}	877.340	0.35940	0.00000
Al^{3+} - O^{2-}	1460.300	0.29912	0.00000
O^{2-} - O^{2-}	22764.000	0.14900	27.88000
Cu^{2+} - O^{2-}	712.800	0.32700	0.00000
Three-body potential	**K/eV rad^{-1}**		**Θ_o/degrees**
O-T-O*	2.09724		109.47
Core-shell-potential	**K/eV rad^{-1}**		
O^{2-}	74.92		

Coulombic charges	**P^{5+}**	**Al^{3+}**	**O^{2-} (core)**	**O^{2-}(shell)**
	5+	3+	0.86902	-2.86902

*T = Al or Si

The rhombohedral Bravais lattice symmetry from the trigonal crystal system was defined for our unit cell, initially from a symmetric calculation with space group 166 set. The SSZ-13 and SAPO-34 structures were built from asymmetric unit cells derived from experimental X-ray diffraction crystallography[87]. An asymmetric CHA unit cell has 36 distinct atomic positons at the tetrahedral (T) sites. The four reported literature sites are site SI in the plane of the 6 ring windows (6R) with six symmetric equivalent sites, site SIII in the centre of the double-6-rings (D6R), site SII which is in the large cage directly below (or above) sites SI and SIII, consisting of three and two symmetric equivalent sites in each unit cell respectively. Then there is site SIVa in the plane of the 8-ring window (8R) situated in the origin of our unit cell with eight other symmetric equivalence around the unit cell boundary, Fig 4. In total, there are 20 extra-framework sites in a full CHA unit cell.

A comprehensive systematic investigation of the Cu^{2+} in all the reported sites was peformed at different Cu/dopant confiurations. This involved sampling two dopants per unit cell, and not higher than two dopants per unit cell. Since, experimentally the preparation of SSZ-13 involves a high Si:Al ratio of ~ 10:1, despite the non-uniformity of the distribution of Al atoms during hydrothermal synthesis, it is very unlikely to achieve more than two Al atoms in a unit cell. Therefore, two dopants per CHA unit cell was adopted for SSZ-13 and SAPO-34.

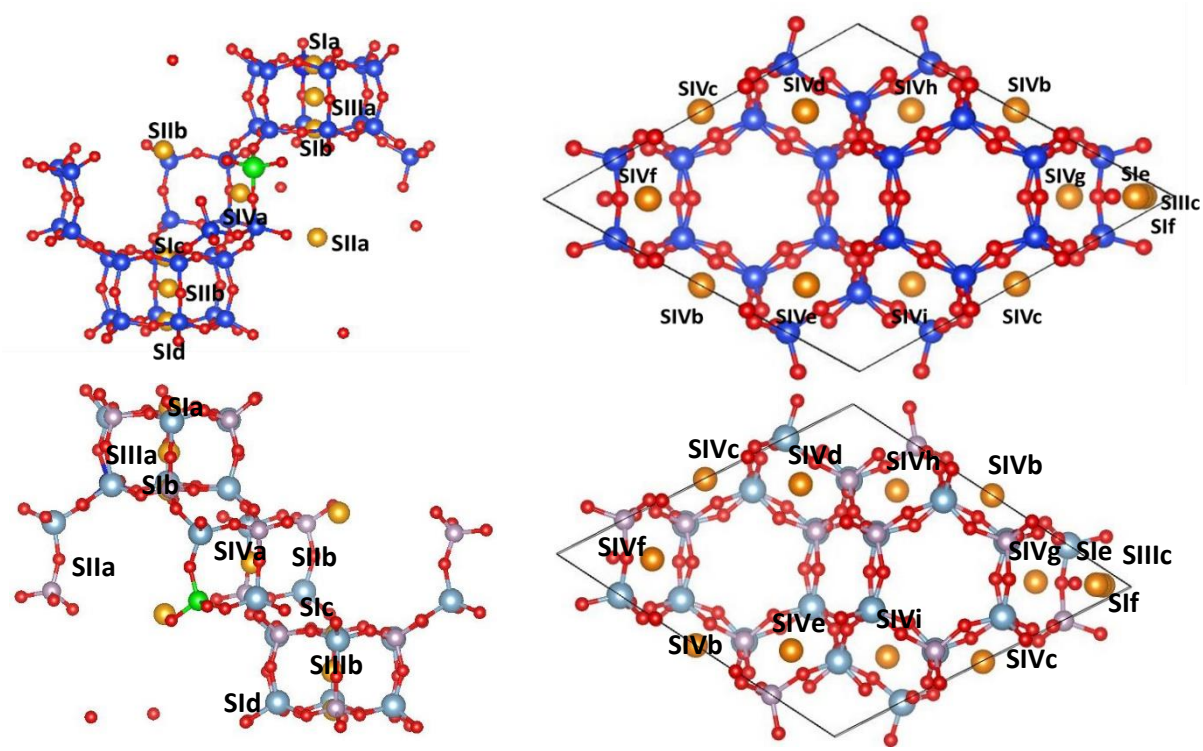

Fig. 4 Locations of the reported literature sites in the CHA unit cell. Orange atoms are Cu^{2+} found in sites SI, SII, SIII and SIV including symmetric equivalents. Red is framework O. Blue is framework Si. Light blue is framework Al. Green is stationary Al/Si. Purple is framework P. **Left**, shows the symmetric equivalent extra-framework sites for SIa, b, c, d, SIIa, b, SIIIa, b and SIVa. **Right**, shows a top eye view of the symmetric sites of SIVb, c, d, e, f, g, h and i in their topologically different locations. Site SIe is directly above site SIf, with SIIIc sandwiched in between.

The sampling of two dopants in a CHA unit cell which has 36 T sites would statistically have 630 different combinations. However, the 36 T sites in a CHA unit cell are all symmetrically equivalent, therefore in order to achieve representative sampling of the dopant/framework configuration, only the relative distance between the two dopants is important. This is because, the introduction of the first dopant atom into an CHA unit cell, would induce asymmetry in the other 35 T sites. The procedure developed for sampling is to keep the first dopant atom stationary, and systemtically move the other dopant atom through rest of the 35 T sites. Considering there are six different site SIs, two different site SIIs, three site SIIIs and 9 site SIVs for the Cu to occupy, we end with (35x6SI)+(35x2SII)+(35x3SIII)+(35x9SIV)= 700 different Cu/dopant configurations for SSZ-13. However, as observed later on in Chapter 5.1, 80 of these configurations disobey the Loweinstein rule and were excluded from the final result.

Similarly, for SAPO-34 the same procedure as above was repeated, with the exception that the in an AlPO framework, the number of T sites for a dopant subsitution is just less than a half. This is because, the 18 of the 36 T sites are occupied by Al atoms and the other 18 are occupied by P atoms. In order for a direct Si → P substitution, there are only 18 possibilites. Keeping the first Si dopant atom stationary and moving the secondary Si atom systematically through the remaining 17 T sites. This gives (17x6SI)+(17x2SII)+(17x3SIII)+(17x9SIV)= 340 different Cu/dopant configurations in our database. The location of the stationary Al and Si atoms in SSZ-13 and SAPO-34 structures respectively are shown in Fig. 4.

An semi-automatic procedure was designed to submit and maintain all 700 and 340 unique calculations for SSZ-13 and SAPO-34 respectively in GULP. This was done via Bash (UNIX shell) scripting by utizlizing the Sed and Awk languages, to manipulate muitiple files in a series, in order to simultaneuosly handle and modify large batches of files.

4.2 QM calculations

CRYSTAL calculations were performed with both hybrid and GGA functionals in the form of B3LYP and PBE respectively. The lack of exact exchange in PBE resulted in poor performance with regards to achieving self-consistent field (SCF) convergence. This is because of the self-interaction error in LDA. In LDA or GGA functionals, the implications of having averaged quantities of self-exchange term (U, Coulomb term) and the 'different orbital' exchange term (J, Exchange term) is that all electrons are described in the homogeneous electron gas's mean field. Therefore, an orbital-dependent potential is required to be able to describe the nodal behaviour of the orbitals. In LDA or GGA, the lack of orbital polarization means e_g and t_{2g} energies would not be accurately described, especially in Cu^{2+} with d^9 electrons; five spin ups and four spin downs electrons, and only the crystal field splitting to provide the orbital polarization.

As a result, hybrid functionals, PBE0 and B3LYP with HF exact exchange built in were better suited in our calculations. The importance of the exact exchange is depicted in Fig. 5. The increased in spin magnetic moment on Cu^{2+} is directly proportional to the HF exact change in the PBE functional used. Increasing the % of exact HF exchange energy in PBE from 0% to 35% showed a general tendency for spin polarization to be hosted on the Cu^{2+}. At lower % of exact exchange (0 and 10%), spin polarization is spread out towards neighbouring O atoms in the framework.

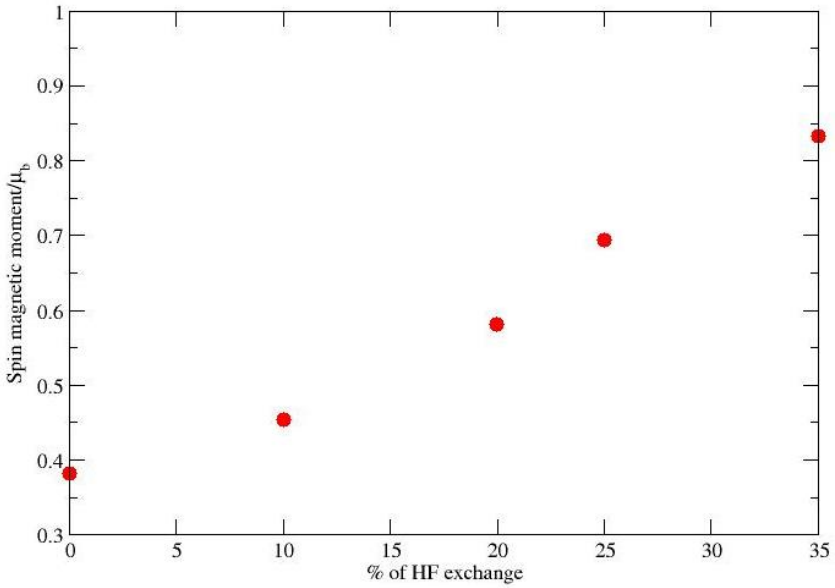

Fig. 5: A plot of spin magnetic moment on Cu^{2+} (in Bohr magneton units, μ_b) against the % of HF exchange implemented in the PBE functional from PBE (0%), PBE0-15%, PBE0 10%, PBE0-5%, PBE0 (20%), PBE0+5%, PBE0+10% and PBE0+15%

Chapter 5 Results and Discussion

5.1 GULP calculations

5.1.1 Statistical overview of Cu behaviour in SSZ-13 and SAPO-34

The Cu/dopant sampling procedure developed for SSZ-13 and SAPO-34 resulted in 700 and 340 calculations for SSZ-13 and SAPO-34 respectively. Taking into consideration Lowenstein's rule, Al-O-Al linkages in zeolitic frameworks are forbidden. This is evident with up to a 1.25eV energetic penalty for Lowenstein's forbidden extra-framework configurations, where Cu occupies identical topological sites with and without Al-O-Al links present, Table 6. The number of viable Cu-SSZ-13 configurations is reduced to 620. Similarly, in SAPO-34, the instability of Si-O-P bonds were not modelled in the calculations, as this was shown to be energetically unfavourable and not observed experimentally.

Described in this chapter is the equilibrium configurations and locations of Cu in the extra-framework sites inside both SSZ-13 and SAPO-34. The minimum energy barrier from the lowest energetic site (SI) in both zeolite and AlPO to the next energetically adjacent site is 0.68 and 1.21eV respectively. Considering under room temperature, the Boltzmann distribution is determined by the K_bT constant, which is a product of the Boltzmann constant, K_b and the temperature, T. The Boltzmann energy given under room temperature at 298K is 0.257eV, indicating that the Boltzmann distribution would be followed for the Cu distributions in both frameworks under room temperature.

However, it is noted during the high operating temperatures (>200˚C), this Boltzmann energy would increase to a minimum of 0.408eV and higher at greater temperatures, where the Boltzmann energy exceeds the energy barriers between the Cu sites. Under these conditions, the Boltzmann distribution might not be followed, instead there will greater lability between the Cu sites inside both frameworks. The thermodynamically most stable sites might not the most occupied in terms of population.

5.1.1.1 Cu-SSZ-13 calculations

After geometry optimisations with the GULP code, just over half of the calculations has Cu occupying sites SI at 50.16%. The other majority with 47.58% found Cu to occupy sites SIV. The remaining 2.10% has Cu occupying sites SII, sitting in the vacant large cages. See Table 5. However, the absence of zeolitic interactions for Cu in SII results in a large energy penalty of up to ~6eV compared with Cu in sites SI and SIV. Site SI is the lowest equilibrium location energetically, followed by SV and SIV, see Chapter 5.1.2 for a description of site SV. Cu in SII was observed, but the significant energy penalty shows that SII is not thermodynamically achievable as an equilibrium site. The standard deviation, σ and variance of the Cu locations within each site was calculated. Except for occupied site SII, the smallest σ and variance for Cu distances was in site SI by 0.13Å and 0.20 respectively against SIV. In addition to the Cu occupancy, this implies the size of the six-membered ring (6MR) in SI is suited for Cu(II) compared to eight-membered ring (8MR) in SIV. This is illustrated in Figs. 6(a – b).

Table 5: The 620 Cu-SSZ-13 configurations.

Occupied sites	Absolute occupancy	Fractional occupancy	Average energy (eV)	Average rel. energy (eV)	σ of distance (Å)	Variance of distance
SI	311	0.502	-4568.06	0.00	0.71	0.51
SII	13	0.021	-4561.79	6.28	0.26	0.07
SIII	0	0.000	-	-	-	-
SIV	295	0.476	-4567.03	1.03	0.84	0.71
SV	1	0.002	-4567.38	0.68	-	-

Table 6: The 80 configurations forbidden by the Lowenstein's rule in SSZ-13.

Occupied sites	Fractional occupancy	Average energy (eV)	Average rel. energy (eV)	σ of distance (Å)	Variance of distance
SI	0.513	-4566.81	1.25	-	-
SIII	0.013	-4564.63	-	-	-
SIV	0.475	-4565.96	1.07	-	-

Figs. 6(a – b): Illustration of the difference in spread of Cu positions as measured by σ within sites **(a)** SI and **(b)** SIV.

The ten lowest SSZ-13 Cu/dopant configurations are dominated by Cu in the SI site, see Table 7 and Figs. 7(a – j). The energy range within this group is 0.76eV, this is a relatively large energy gap highlighting the pronounced effect of different dopant configurations on the Cu-zeolite equilibrium energy. Two Al dopant atoms sitting in symmetric fashion in the SI site directly opposite each other, separated by two Si atoms on either side has the lowest energy observed in the CU-SSZ-13 system, see Fig. 7a. This is followed by two Al dopants in the SI site, but sitting in an asymmetric fashion. Losing the secondary Al dopant to the adjacent 6MR results in a huge energetic jump from 0.057 to 0.67eV. Interestingly, as the secondary Al shifts in the adjacent 6MR the energy increases from 0.67 to 0.71eV. As the secondary Al moves,

away from the Cu-occupied D6R, see Fig. 7g, the energy increases to 0.72eV indicating the long range effect of the location of secondary Al atom in the unit cell.

Table 7: The 10 lowest energy configurations in SSZ-13.

Al – Al configuration	Occupied site	Rel. energy/ eV	Figs. 3
1_34	SIe	0.00000	a
1_04	SIe	0.05176	b
1_07	SIe	0.05664	c
1_13	SIe	0.66650	d
1_19	SIf	0.71484	e
1_19	SIe	0.71484	f
1_11	SIe	0.72021	g
1_11	SIb	0.72021	h
1_26	SIb	0.75830	i
1_23	SIe	0.75830	j

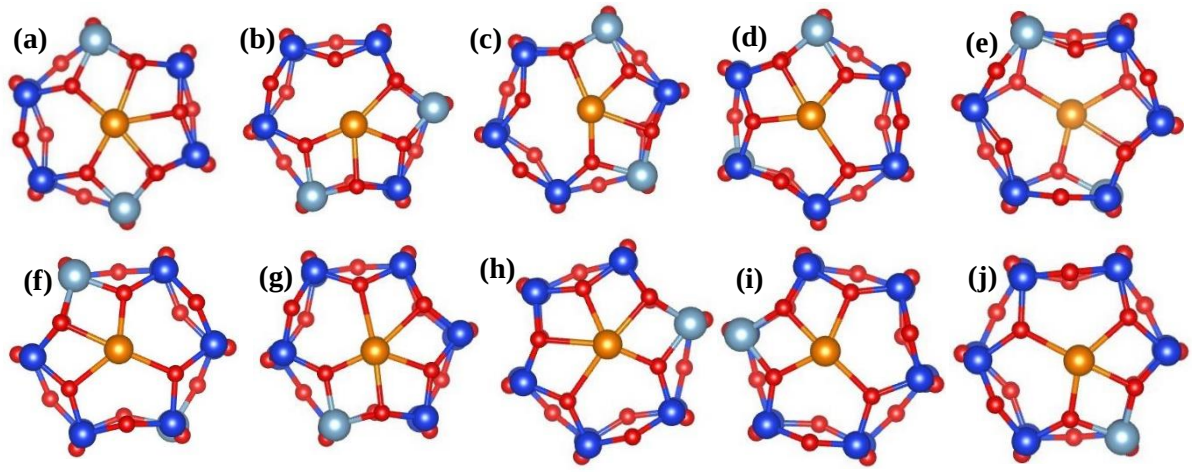

Figs. 7(a – j): The 10 lowest energy sites in Cu-SSZ-13 – all dominated by Cu in sites SI.

Aside from Cu in SI, the ten lowest energy SIV configurations are seen in Table 8 and Figs. 8(a – j). The four lowest structures have the same Al configurations with the two Al atoms at one Si atom away from each other at their nearest proximity, see Figs. 8(a – d). The Cu adopts the same bonding in each case between the Al dopants. This uniformity in the configurations is evident with the energy variation within 0.1eV. Unlike in SI, the big energetic jump from 0.097 to 0.34eV is not the removal of one Al atom away from SIV, but the movement of the Al atoms away from each at two Si atoms apart, see Fig. 8e. Interestingly, due to the large size of SIV as mentioned previously, the difference in Cu bonding configurations has a profound in the energy. In Figs. 8(h – i), the same Al configuration pattern is observed, but Cu

is bonded only to one of the Al dopant atoms instead of between the two, resulting in an increased in the equilibrium energy of ~0.07eV. Losing the secondary Al atom in SIV results in a ~0.06eV jump.

Table 8: The 10 lowest energy SIV configurations in SSZ-13.

Al – Al configuration	Occupied site	Rel. energy/ eV	Figs. 4
1_05	SIVf	0.00000	a
1_09	SIVa	0.02490	b
1_26	SIVa	0.09668	c
1_23	SIVf	0.09668	d
1_12	SIVf	0.33643	e
1_05	SIVa	0.39844	f
1_09	SIVj	0.39844	g
1_33	SIVa	0.40088	h
1_32	SIVf	0.40088	i
1_30	SIVj	0.40332	j

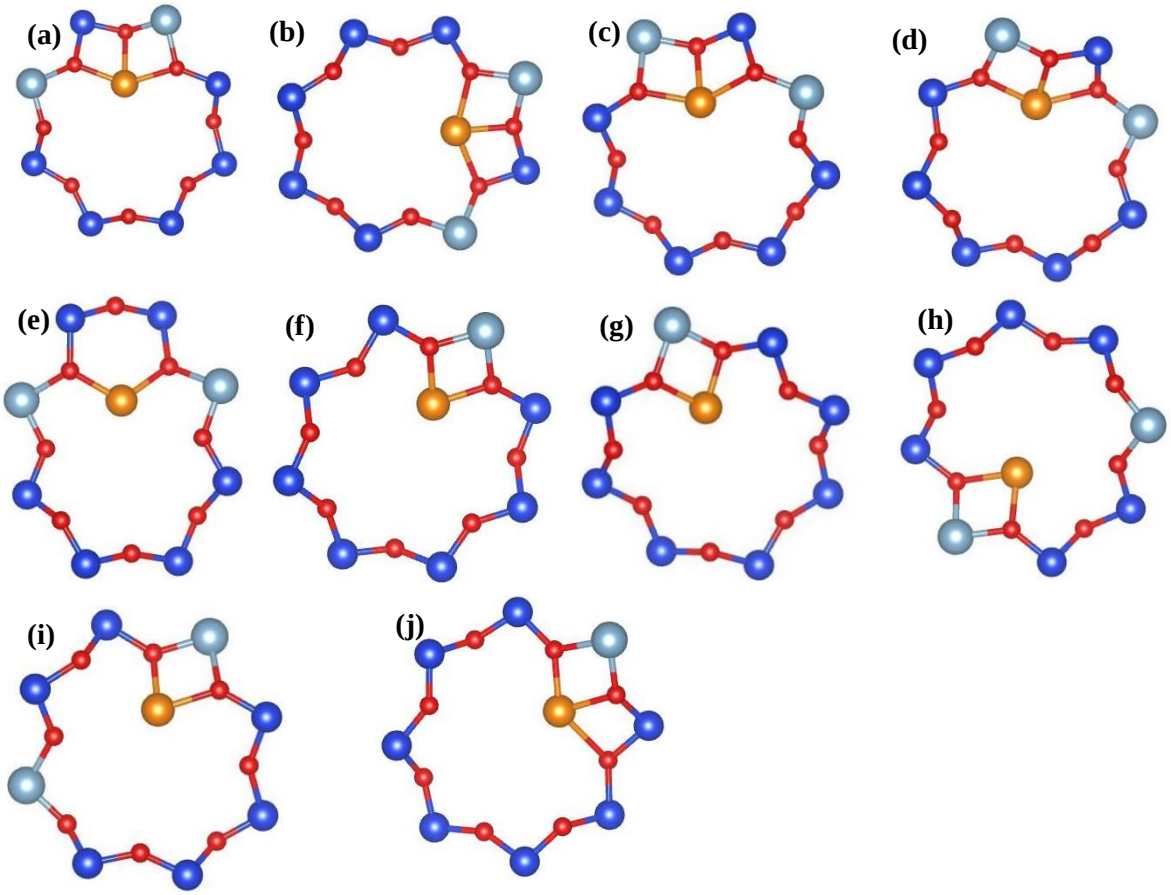

Figs. 8(a – j): The 10 lowest energy SIV sites in Cu-SSZ-13.

5.1.1.2 Cu-SAPO-34 calculations

The occupancy of sites in SAPO-34 is like SSZ-13 with majority of Cu residing in sites SI and SIV accounting for a combined 96.18% of the configurations. However, the ratio between SI and SIV is distinct in SAPO-34. In SSZ-13 this was 1.05: 1.00, but in SAPO-34 the ratio has reversed with 1.00: 1.44. Yet, the energy of SI is on average 1.21eV lower compared to SIV. In SSZ-13, the average energy difference between SI and SIV is slightly smaller at 1.03eV. This could indicate a shallower energy profile in the SAPO-34, despite the higher energy difference – more configurations accept Cu residing in a SIV site. Interestingly, more SV occupancy is observed in SAPO-34 relative to SSZ-13. Both this observation indicates a greater flux between sites in the AlPO situation. This is reinforced when looking at the occupancy of other sites which are not SI and SIV, in SSZ-13 these site occupancies attributed to 2.3% and in SAPO-34 this was 3.8%. However, it is important to observe that this could be because of twice the number of SSZ-13 configurations (620 against 340). A similar trend is observed with regards to the variation in the Cu position in each of the sites with SI < SIV as dictated by σ and variance. See Table 9.

Table 9: The 340 Cu-SAPO-34 configurations.

Occupied sites	Absolute occupancy	Fractional occupancy	Average energy (eV)	Average rel. energy (eV)	σ of distance (Å)	Variance of distance
SI	135	0.397	-4742.57	0.00	0.71	0.50
SII	0	-	-	-	-	-
SIII	1	0.003	-4739.78	2.80	-	-
SIV	192	0.565	-4741.36	1.21	0.87	0.75
SV	12	0.035	-4740.61	1.97	0.88	0.78

Inspecting the ten lowest energy configurations we observed that like the zeolite case, Cu in SI is overwhelmingly favoured with nine of the ten configurations. Interestingly, the trend for Si dopant sampling does not follow with respect to energy does not follow a discernible pattern as shown in SSZ-13. The lowest configurations have two Si atoms occupying the same 6MR, with one Si atom between them, Figs. 9(a – b). This is followed by only Si in the 6MR, Figs. 9(c – d) where the energy rises to 0.61eV. The sequence is then interrupted with an 8MR with two Si atoms, this resulted in a jump to 0.74eV. However, the effect of the secondary Si dopant atom, except when occupying the same site as the Cu has less of an effect on the equilibrium energy, this is evident with looking at 1_15 SIe, Fig. 9d and 1_10, SIe, Fig. 9f. See Table 10 and Figs. 9(a – j). Despite configuration 1_10, SIe possessing the secondary Si atom in the adjacent 6MR, the relative energy to 1_15, SIe with only one Si atom in the D6R is ~0.24eV higher. This contrasts with SSZ-13, where the secondary Al atom possess a higher degree of directionality on the equilibrium energy.

Table 10: The 10 lowest energy configurations in SAPO-34.

Si – Si configuration	Occupied site	Rel. energy/ eV	Figs. 6
1_04	SIf	0.00000	a
1_07	SIf	0.00000	b
1_18	SIc	0.60938	c
1_15	SIe	0.60938	d
1_18	SIVb	0.74414	e
1_10	SIe	0.83936	f
1_10	SIf	0.83936	g
1_12	SIf	0.87061	h
1_12	SIc	0.87598	i
1_16	SIf	0.88135	j

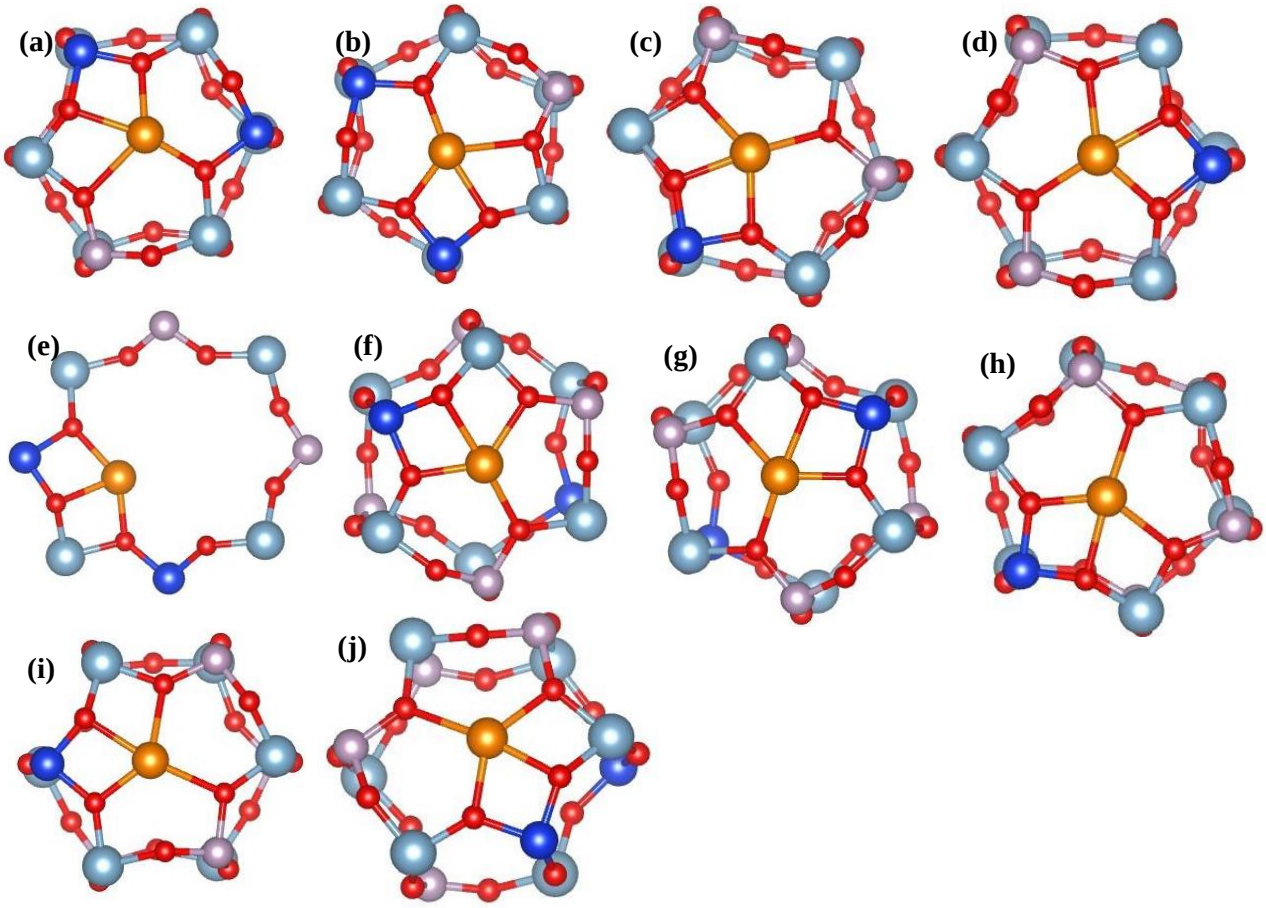

Figs. 9(a – j): The 10 lowest energy sites in Cu-SAPO-34.

5.1.2 Cu locations

The first property we have tried to address is the relative stability of Cu^{2+} in the isostructural SSZ-13 zeolite and SAPO-34, both doped with two ions (Al → Si or Si → P) per unit cell. To this aim, we have built all symmetry unique cells of both systems, and ran geometry optimisation for each using the force-fields method. As discussed in Chapter 4.1, the configurational sampling gives rise to 700 calculations for SSZ-13 (35 distinct Al distributions and 20 extra-framework sites) and 340 in SAPO-34 (17 distinct Si distributions and 20 extra-framework sites). Analysis of results will provide energetic information on stability and mobility of Cu in the two systems. We first note that in many of the calculations performed, Cu moves to an extra-framework site from the starting one, showing that several positions indicated in the literature as possible Cu sites are not minima in the potential energy surface. This is true for sites SII and SIII i.e. the centre of the D6R and CHA cages; Cu prefers therefore a close coordination with the framework O's in sites SI (6MR) and SIV (8MR window).

Figs. 10 (a) shows the occupancy of the 20 different extra-framework sites obtained in the 620 GULP calculations of SSZ-13. The overwhelming majority of the calculations has Cu residing in sites SI and SIV, whilst, sites SII and SIII are sparsely populated. This is in good agreement with the literature results from *ab initio* calculations[42] and experimental measurements[38], highlighting the 6MR window of site SI as the most stable Cu location, followed by 8MR window of site SIV. The occupation of sites SI contributed to just over half of the Cu final locations (311). Sites SIV are the second most occupied sites (295), the remaining 13 calculations are portioned between sites SII and SIII at 12 and 1 respectively as mentioned in Chapter 5.1.1.1. This gave a SI: SII: SIII: SIV ratio of 311: 12: 1: 295, see Table 5. In one calculation Cu was located nestled in between two 4MR structures inside the SII large cage, Fig. 10b. The Cu is adjacent to the secondary Al within a 2.77Å proximity, the shortest Cu-O framework bonds were at 1.88, 2.19, 2.50 and 2.09Å. This is an interesting observation, as of currently there has been no reported mentions of a 4-ring structure as a plausible extra-framework site for Cu in the literature. Further evidence of this site was found in the SAPO-34 calculations, which we herein labelled as site SV.

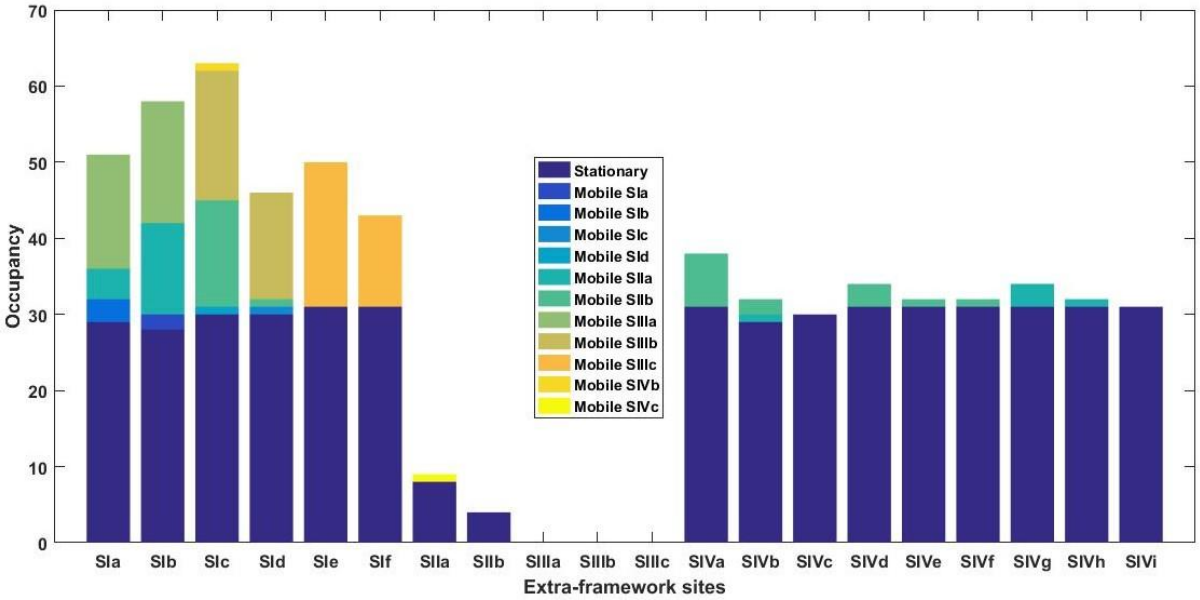

Fig. 10a: A coloured bar chart showing the occupancy of 620 Cu locations in SSZ-13 with exception of one Cu/dopant configuration. The bar chart is partitioned into different coloured sections depending on where the Cu has migrated.

The bars in Fig. 10a are partitioned into different colours corresponding to the contribution of different Cu locations in the initial configuration. All the bars for sites SI and SIV have consistent heights in the dark blue coloured section. This section corresponds to Cu ions that do not migrate to sites during the geometry optimisation. The significant contributions of the stationary sections in sites SI and SIV, indicates that the Cu are sitting inside favoured energy minima. The orange and two pale green sections belongs to Cu that had migrated from sites SIII (a, b and c) of the D6R, the majority of these Cu relocations ended up in sites SI. Sites SI and SIII are adjacent to each other and correspond to 6MR windows and central site of the D6R cage.

A similar relationship can be found between sites SII and SIV. The Cu ions relocating away from sites SII (a and b) are shown in the two shades of turquoise-blue coloured bars. The majority of these are found occupying sites SIV. In addition, a greater proportion of configuration were found with Cu in the newly discovered site, SIV, see Table 5. When Cu sits in the vacant centre of the large cage of sites SII, it migrates to the nearest framework sites which are made of five 8MR structures of the sites SIV. Interestingly, the large cage also consists of 10 4MR and two 6MR secondary building units. A significant fraction of Cu initially located in sites SII migrates to SI in the 6MR and one to the 4MR (33/62). On the whole amongst the SIV sites, there is not one particularly overwhelming favoured crystallographic site, since the heights of the nine bars (a, b, c, d, e, f, g, h, and i) are relatively similar. Considering site SIVa is where the stationary Al is located, this affects a minor influence with the most occupancy (38) in sites SIVs, indicating on a global scale all the sites are equally likely independent of the location of Al^{4+} tetrahedra. A similar uniformity in the occupancy of sites SI is observed, where the difference between the highest bar in site SIc and the lowest in site SIf is twenty occupancies.

Cu occupancy in SAPO-34 follows very similarly to that in SSZ-13. The majority of the Cu ions found in sites SI and SIV, which are the local energy minima in potential energy surface. However, the Cu is more labile in the AlPO than in SSZ-13 case as observed by the large fraction of Cu that migrates between different extra-framework sites. This is evident in Fig. 10(c), we observe in particular a more labile behaviour of the Cu ions initially in sites SI. Looking at the six symmetric SI sites (a, b, c, d, e and f), the stationary section (dark blue coloured) of the bars have lower heights compared to in SSZ-13. Considering the contributions of Cu relocations from other sites, there is a greater discrepancy between the symmetric sites in SI. Both sites SIc and SIf have approximately twice the Cu occupancy than that in site SId. This lopsided occupancy amongst the symmetric sites in SI, can be rationalised by the contribution of Cu relocations from sites SIII. For example, the occupancy of site SIc is largely favoured by relocations of Cu from site SIIIb. Similarly, for site SIf, relocation from site SIIIc is preferred over site SIe. This preference of Cu over one 6MR window is explained by the presence of a dopant in one of the windows, see Fig. 11. The tetrahedral Si atom present in one 6MR window, affects the final position of Cu, the subtle interplay between Cu and the framework environment is determined by the Coulomb's law of charge attractions as described in Chapter 3.1.

Cu inside the 8R window (SIV) is less prone to migrate compared to sites SI. Sites SI and SIV have 135 and 192 occupancies respectively, this is the reverse in comparison to SSZ-13, with sites SIV being the most occupied instead of sites SI in SAPO-34. This is explained by the increased mobility of Cu in sites SI compared to sites SIV. It also should be noted that sites SIV in SAPO-34 are more mobile than in SSZ-13, as shown by Cu migration away from the 8-ring windows. Twelve configurations that were observed adjacent to 4MRs, which were first mentioned in SSZ-13. This indicates, that the appearance of a Cu located in the 4MR structures is not an isolated event, and could be a plausible site for Cu when migrating between two energy minima.

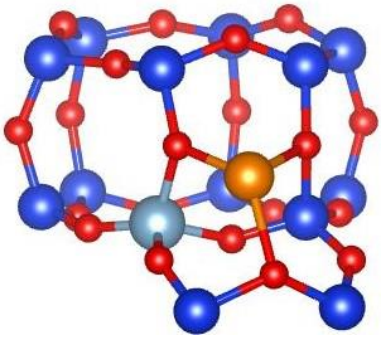

Fig. 10b: Site SV, Cu residing adjacent to a 4MR in SSZ-13 as observed in GULP.

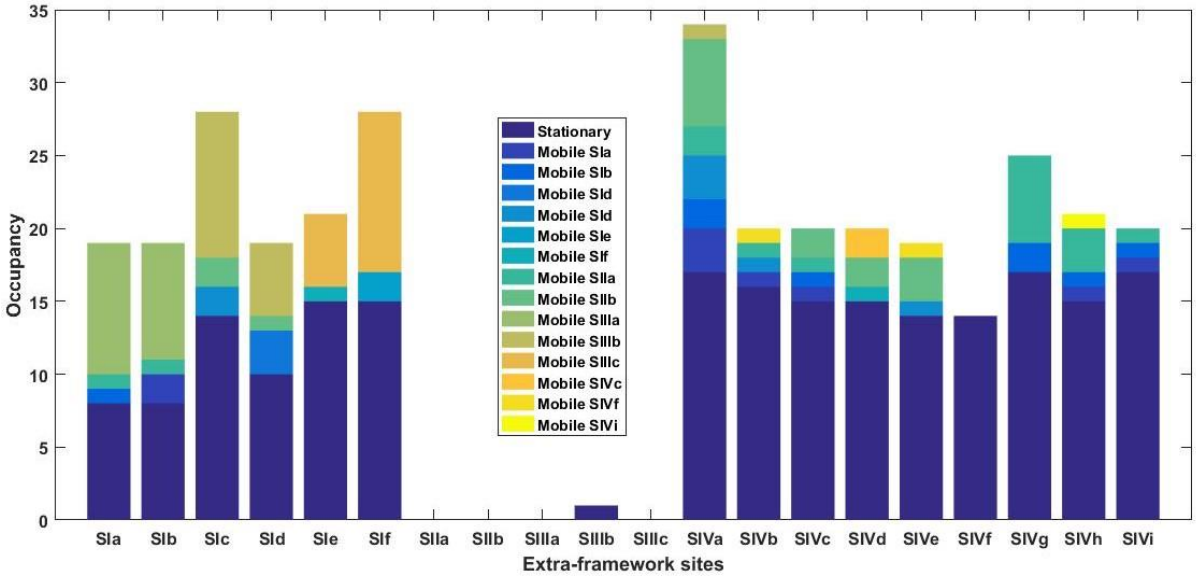

Fig. 10c: A coloured bar chart showing the occupancy of 340 Cu locations in SAPO-34 with exception of 12 configurations, which were observed to be in a newly found site named SV. The bar chart is partitioned into different coloured sections depending on where the Cu has migrated.

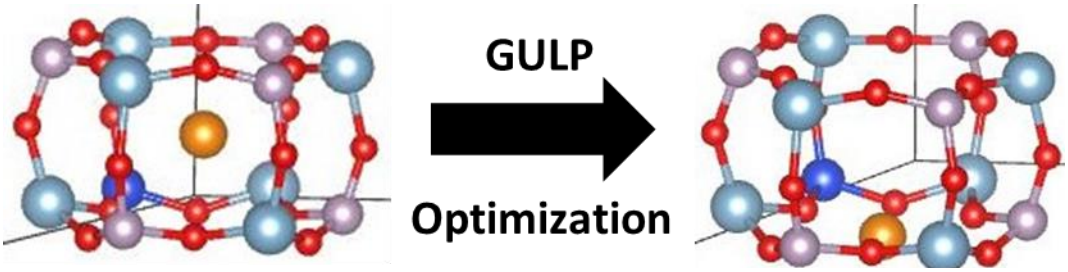

Fig. 11: An illustration of Cu migrating into a 6-ring window in the same plane as Si active site after GULP optimization.

Figs. 12 (a – d) illustrates a superposition of all the locations of Cu found in the CHA system for SSZ-13 and SAPO-34. It highlights that in both hosts, similar behaviour is found with regards to Cu residing in sites SI and SIV. In Figs. 12a and c we are able to witness the tendency for Cu to cluster in the centre of the 8-ring windows in sites SIV. Figs. 12b and d shows the 6MR windows with Cu sitting in the centres of locations of sites SI. The green arrows show where all the possible sites SI and SIV are in the unit cells of both SSZ-13 and SAPO-34. However, upon closer inspection of the Cu locations there is a small, but significant difference in the overall positions of the Cu inside the framework structure between SSZ-13 and SAPO-34. In the former, the Cu positions are more ordered and clustered together as can be seen in the 8MR and 6MR positions of Figs. 12a and b. In the latter, the Cu positions seems to be more disorganised and is especially evident in Fig. 12c, the Cu positions in the 8MR windows are more spread out and is never found in the central site. In Fig. 12d, the Cu positions inside the SAPO-34 framework structures around the 6MR windows are more disordered compared to that in SSZ-13 (Fig. 12b). This difference in Cu behaviour inside SSZ-13 and SAPO-34 confirms the greater mobility of Cu exhibited in the AlPO situation first observed in Figs. 10b and c.

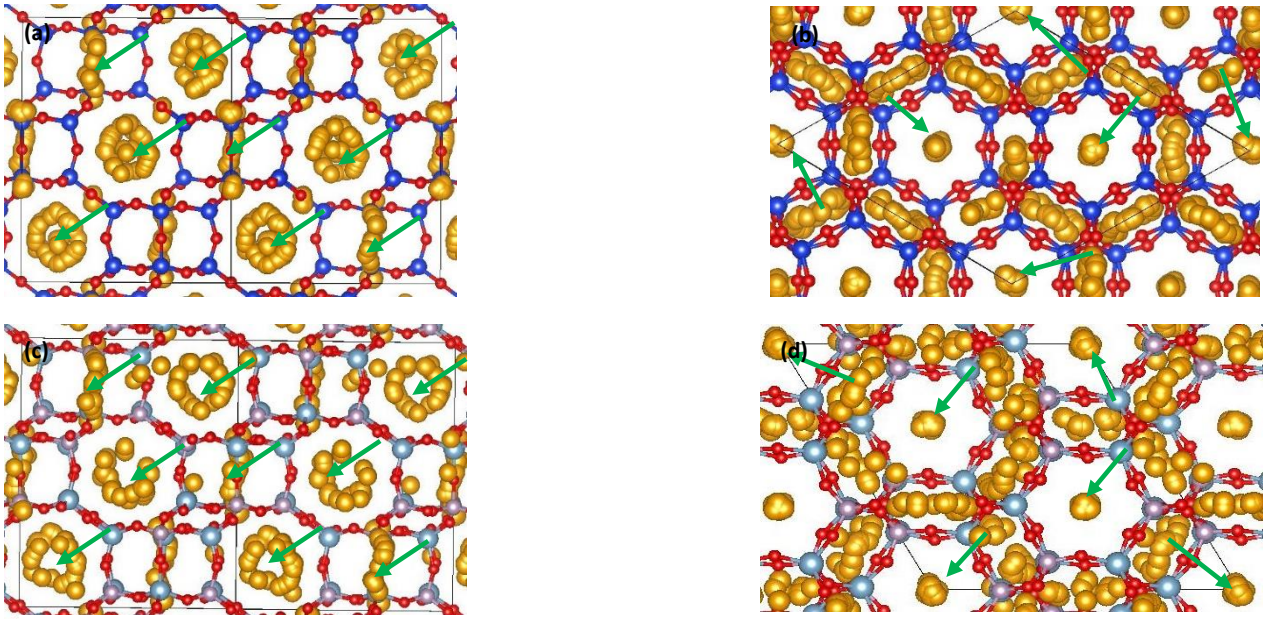

Figs. 12 (a – d): Superposition of all Cu locations identified in all geometry optimisation for SSZ-13 (**top**) and SAPO-34 (**bottom**). **Left** side-on views and **right** are top view (001) axis of the unit cells. Red is O atom, dark blue is Si atom, pale blue is Al atom, purple is P atom and orange is Cu atom. The occupation of sites SIV are indicated by green arrows in **(a)** and **(c)**. In **(b)** and **(d)**, the green arrows shows the Cu locations in sites SI.

5.1.3 Cu energies

Figs. 13 (a – b) shows the all the Cu locations for SSZ-13 colour-coded as a function of energy within the range of -4561 to -4570eV. The Cu sitting inside the 8-rings are coloured yellow which represents an energy value of -4566eV, while those sitting inside 6-rings of sites SI are mostly red which is attributed to -4570eV. In both cases, there are other colours present, for sites SIV there are green (-4565eV) and orange (-4569eV). Sites I are interspersed with green colour and a mixture of pale blue (-4564eV) and yellow. The navy blue (-4562eV) present belongs to Cu in the middle of the large cages of sites SII. Those that resided in the centre of

the large cages are located at a higher energy configuration of around -4562eV compared to the configurations which had Cu migrate across to the boundaries of the framework with an energy scale of between -4564 and -4569eV, resulting in a minimum threshold of 2eV difference between the two sets of configuration. This can be attributed to the favourable zeolitic interactions on the basis of electrostatics interplay between the Cu and the Si-O-Si framework.

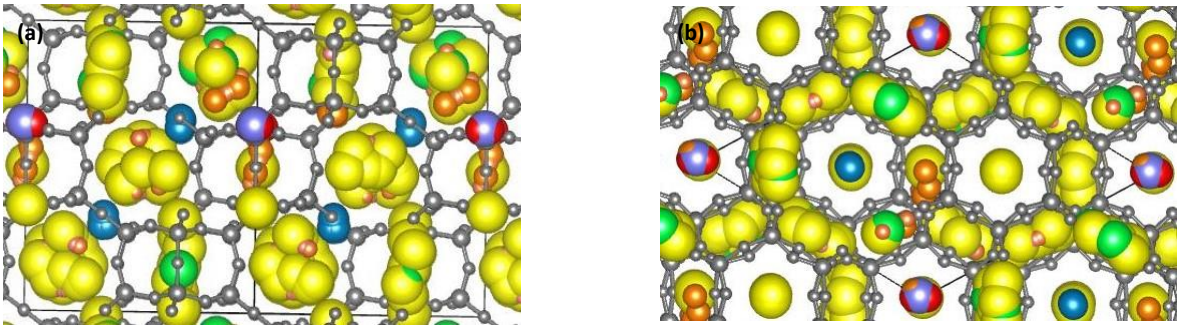

Figs. 13 (a – b): The grey atoms are the Si and O atoms of zeolite framework. Shows the Cu locations in the zeolite unit cell as a function of colours corresponding to different energies in the system. The energy range changes by 1eV increment from -4561 to -4570eV. Dark blue = -4561, navy blue = -4562, pale blue = -4564, green = -4565, yellow = -4566, pale pink = -4567, pale orange = -4568, orange = -4569 and red = -4570.

Figs. 14a and b is the corresponding representation of all Cu locations within the AlPO framework as a function of energy. In comparison to the zeolite case (SSZ-13), the energy range is smaller with a 5eV difference between the highest and lowest energy values in the system. In SSZ-13, the higher energy values are contributed by a few Cu sitting in the large cage, unlike in the SAPO-34 situation where no Cu were in the sites SII. The Cu sitting in sites SI are predominantly orange (-4743eV), while not observable in Figs. 10, the majority of the all reds (-4744eV) are hidden in the 6-rings of sites SI. A few yellows (-4742eV) can be seen in sites SI, and sites SIV are mostly green (-4741eV) and yellow with a few dark (-4739eV) and pale blues (-4740eV). The Cu locations found adjacent to the 4R structures are mostly dark and pale blues, in contrast, the 4-ring configuration in SSZ-13 was a pale pink (-4567eV) suggesting the 4-ring structure is a more energetically stable configuration with respect to the average in the SSZ-13 system.

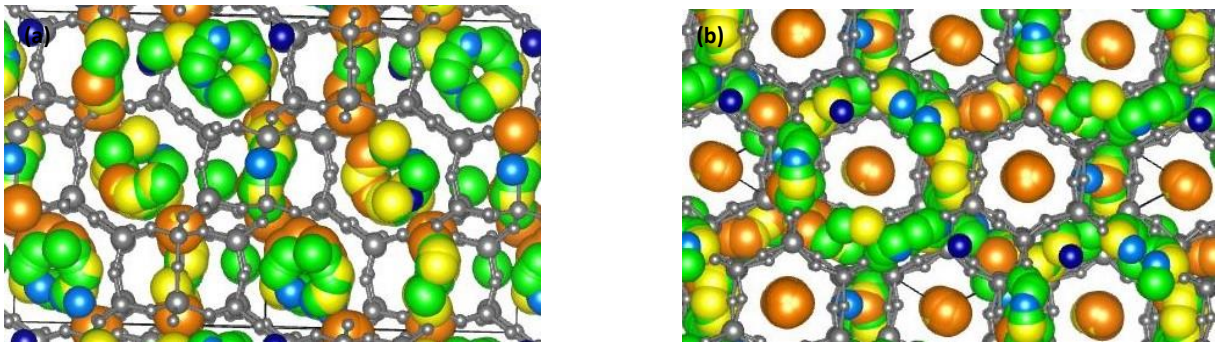

Figs. 14 (a – b): The grey atoms are the Al, P and O atoms of AlPO framework. Shows the Cu locations in the AlPO unit cell as a function of colours corresponding to different energies in the system. The energy range changes by 1eV increment from -4739 to -4744eV. Dark blue = -4739, pale blue = -4740, green = -4741, yellow = -4742, orange = -4743 and red = -4744.

In both the SSZ-13 and SAPO-34 cases, the lowest energy minimum was found when Cu is inside sites SI and then sites SIV is the second most stable. However, in certain

configurations there are cross overs in energetic stability between the two extra-framework sites.

5.1.4 Cu migration

Exploring the pathway for Cu^{2+} migration in the CHA framework for both SSZ-13 and SAPO-34 provides an interesting insight into how the Cu^{2+} behaves during the catalytic cycle. GULP calculations were performed, in which the Cu^{2+} ion was fixed at intermediary positions along the straight path between crystallographic sites I – IV, see Fig. 11e, and the rest of the lattice allowed to relax.

Fig. 15 (a)-(e) shows the energetic migration profile of Cu^{2+} in SSZ-13 from SIa → SIIIa → SIb → SIIa → SIV → SIIb → SIc → SIIIb → SId for different Al distributions in the framework configuration. In our previous analysis we deduced that sites SI and SIV are the energy minima, but not sites SII and SIII. The migration profiles confirm that both sites SI and SIV are energy minima. Sites SI have the lowest energy minima on our surface, whilst site SIV is a local minimum. Interestingly, from our relocation analysis when the Cu^{2+} was placed in the 8R of site SIV it never relocated away. This can be explained from our surface that the Cu^{2+} is sat between two significantly large energy barriers both in the region of ~4eV, as a result site SIV is a kinetic location for the Cu^{2+} since it is trapped in a deep minimum, unlike in sites SI which can be considered as thermodynamic configurations. Both sites SII and SIII can be considered to be maxima from our energy surface verifying our previous analysis that these are not favourable sites for the Cu^{2+}. We can now confirm the large cages in sites SII being the global maxima in good agreement with our relocation analysis and the energy of these systems as computed from GULP geometry optimizations.

The energy migration profiles were computed for five different Al distributions. We inspected the barriers for Cu^{2+} to the migration route when the secondary Al was in the sites of SIa, b, c, d and SIV. There are no significant changes in characteristics between the five profiles and as expected when the secondary Al is in the 6R of one of the sites in SIa, b, c and d, the respective site achieved the status of global minimum. These were -4568.45, -4567.46, -4567.13 and -4567.74eV for sites SIa, b, c and d respectively. When the secondary Al was positioned in the 8R, site SIc achieved the global minimum (-4568.11eV), this is not surprising since the secondary Al in the 8R was in the same plane as the SIc. The characteristics for each profile are not significantly affected by the framework configurations, indeed the expected induced asymmetry of having the secondary Al in each of the SI sites tip the global energy minimum to the respected site.

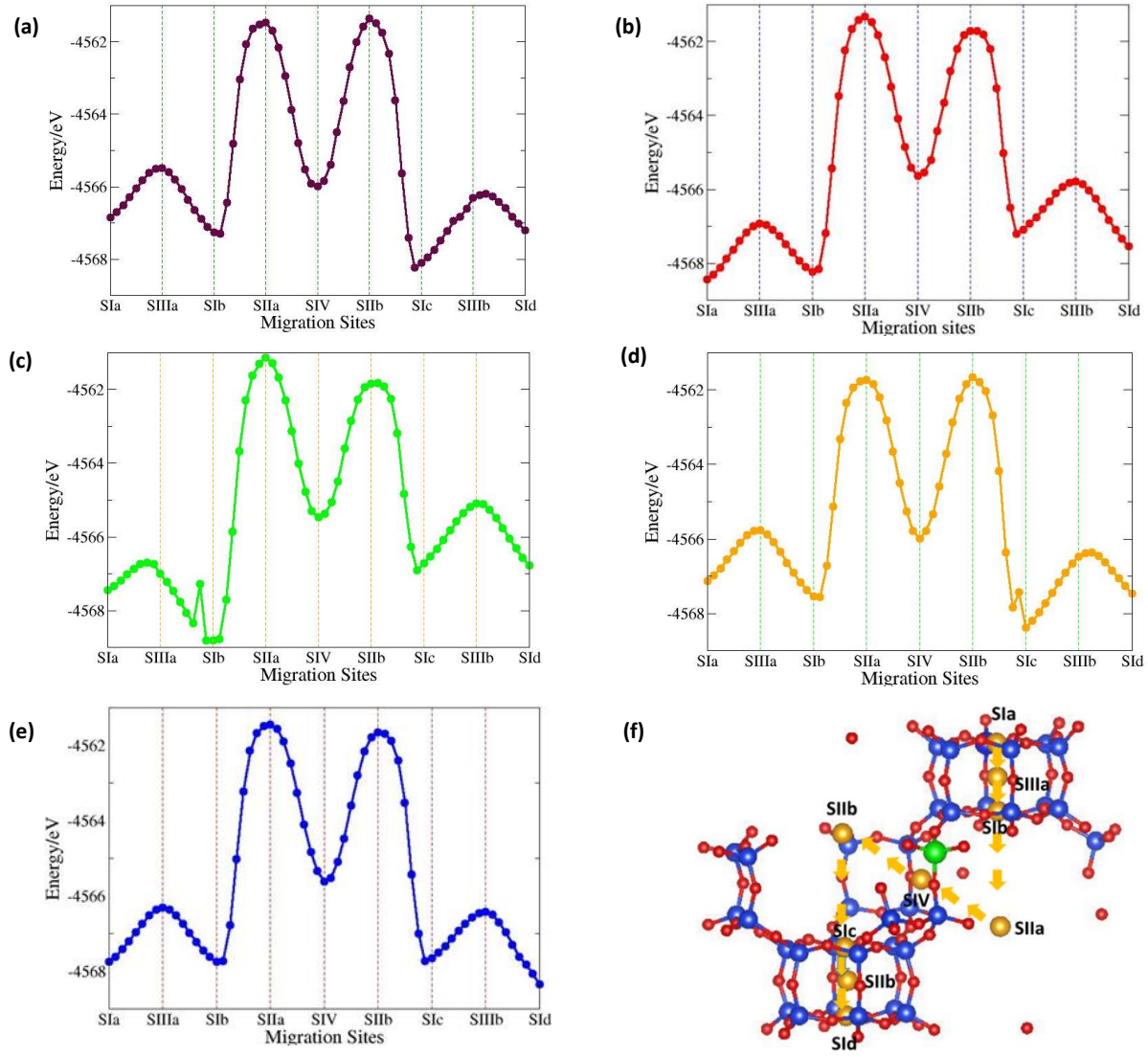

Fig. 15 (a)-(f) Energy migration profiles for Cu^{2+} in SSZ-13. **(a)** in the same 8R of SIV **(b)** in the 6MR of SIa, **(c)** in the 6MR of SIb, **(d)** in the 6MR of SIc and **(e)** in the 6MR of SId. **(f)** The migration path for Cu^{2+} from one D6R (SIa side) to the next (SId side) via the large cages (SIIa and SIIb).

In SAPO-34, the fixed calculations in order to build a migration profile as per for SSZ-13, see Fig.16c. However, this resulted in certain Cu configurations trapped in local minima. This manifested in sharp energetic peaks as shown in Fig. 16a, which are unable to be resolved via any stationary search methods attempted found in GULP, these include the Broyden-Fletcher-Goldfarb-Shanno (BFGS) algorithm, Davidon-Fletcher-Powell (DFP) formula or the Rational Function Optimisation (RFO) method. In an attempt to find the true minima for these trapped states, the optimized framework configurations of either side of these trapped states were borrowed and the new coordinates of the trapped Cu location were inserted, then optimized. This solution enabled the trapped states to eventually find the true optimized minima, and we were able to produce a relatively smooth migration profile, Fig. 16b. The migration path is illustrated in Fig. 16c, the secondary Si atom was located in site SId this is evident since the global minimum of the profile is when Cu sits in the plane of SId. Comparing the SSZ-13 and SAPO-34 migration profiles, both observed near-identical characteristics with a large barrier crossing the large cage at 6 and 7eV respectively. The trapped behaviour of Cu in the SAPO-34 migration profile shows that there are many local minima in the potential energy surface for an AlPO, compared to a zeolite.

The large barriers in crossing the large cages of sites SII in SSZ-13 and SAPO-34 in addition to results from chapters 5.1.1 and 5.1.2 indicates that the Cu would avoid migrating via the large cage. Instead, the Cu migration in both materials is highly likely to “roll around” the framework structures, moving from one minimum to the next. This ensures that the Cu is always in close contact with the framework O atoms.

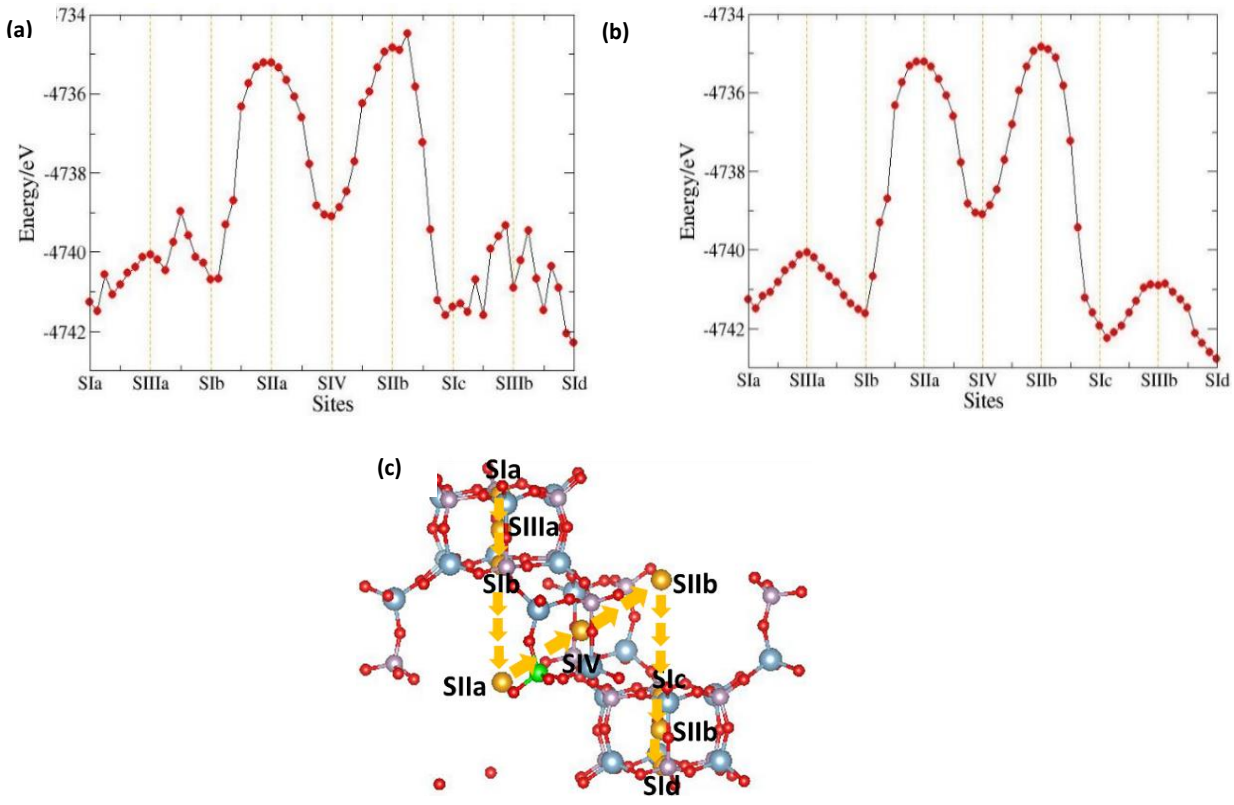

Figs. 16 (a)-(c) Energy migration profiles for Cu^{2+} in SAPO-34. The stationary Si adjacent to the centre 8R with secondary Si in the 6R of SId. **(a)** Migration profile with trapped minima and **(b)** with the high-energy states resolved. **(c)** The migration path for Cu^{2+} in the CHA framework from one D6R (SIa side) to the next (SId side) in the same unit cell via the large cages (SIIa and SIIb).

5.1.5 Effect of Al/Si dopant distributions

5.1.5.1 Al distributions in SSZ-13

The effect of dopant Al proximity to the extra-framework Cu^{2+} on the energy of Cu-SSZ-13 system is studied via statistical analysis. This will enable us to partition the effects that influence the energetics of a Cu exchanged location inside a dopant substituted framework into: (i) proximity to dopants and (ii) the local zeolite environment of the extra-framework sites (SI, SII, SIII and SIV). A series of simple functions are observed from the following:

$$f_1(r) = r_1(Al_1) + r_2(Al_2) \quad (\mathbf{41})$$

$$f_2(r) = r_1(Al_1) \times r_2(Al_2) \quad (\mathbf{42})$$

$$f_3(r) = r_3(Al_1 - Al_2) \quad (\mathbf{43})$$

$$f_4(r) = r_1(Al_1) + r_2(Al_2) - r_3(Al_1 - Al_2) \quad (\mathbf{44})$$

$$f_5(r) = \frac{r_1(Al_1) \times r_2(Al_2)}{r_3(Al_1 - Al_2)} \quad (\mathbf{45})$$

$$f_6(r) = \frac{r_1(Al_1) + r_2(Al_2)}{2} \quad (\mathbf{46})$$

$$f_7(r) = r_1(Al_1)^2 + r_2(Al_2)^2 \quad (\mathbf{47})$$

Seven equations (Eqs. 41 – 47) are proposed, all as a function of distances between Cu^{2+} and the two Al dopants (labelled as Al_1 and Al_2), r_1 and r_2 in the Cu-SSZ-13 system. r_3 is simply the difference between r_1 and r_2. The energy of the Cu-SSZ-13 system are plotted against seven of these functions, $f_n(r)$ for when Cu occupied the two most stable extra-framework sites in the 6MR and 8MR of sites SI and SIV respectively, see Figs. 17 (a – n).

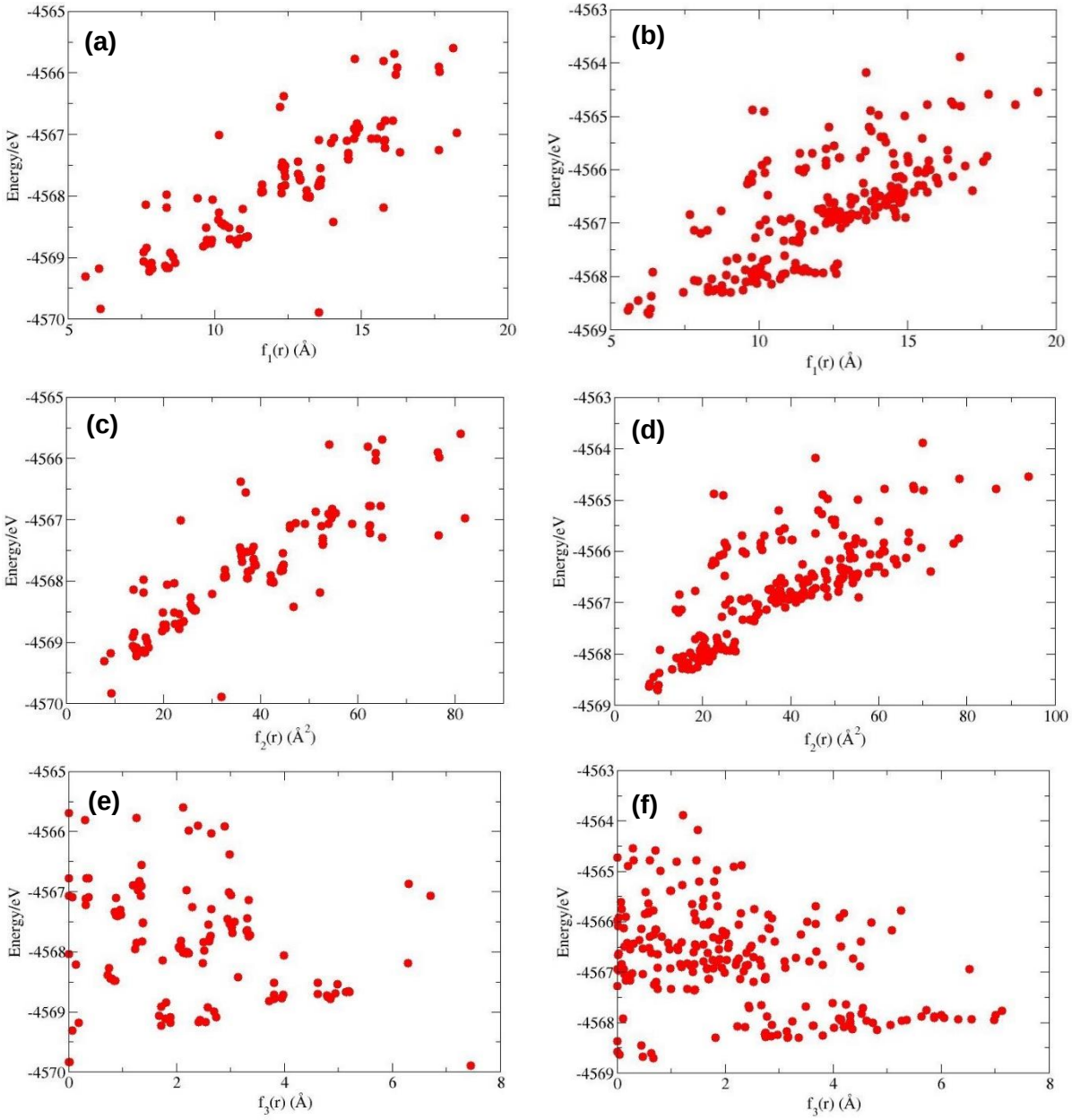

Figs. 17 (a – f): Plots of $f_n(r)$ against energy of Cu in sites SI on the **left**, and **right** in sites SIV.

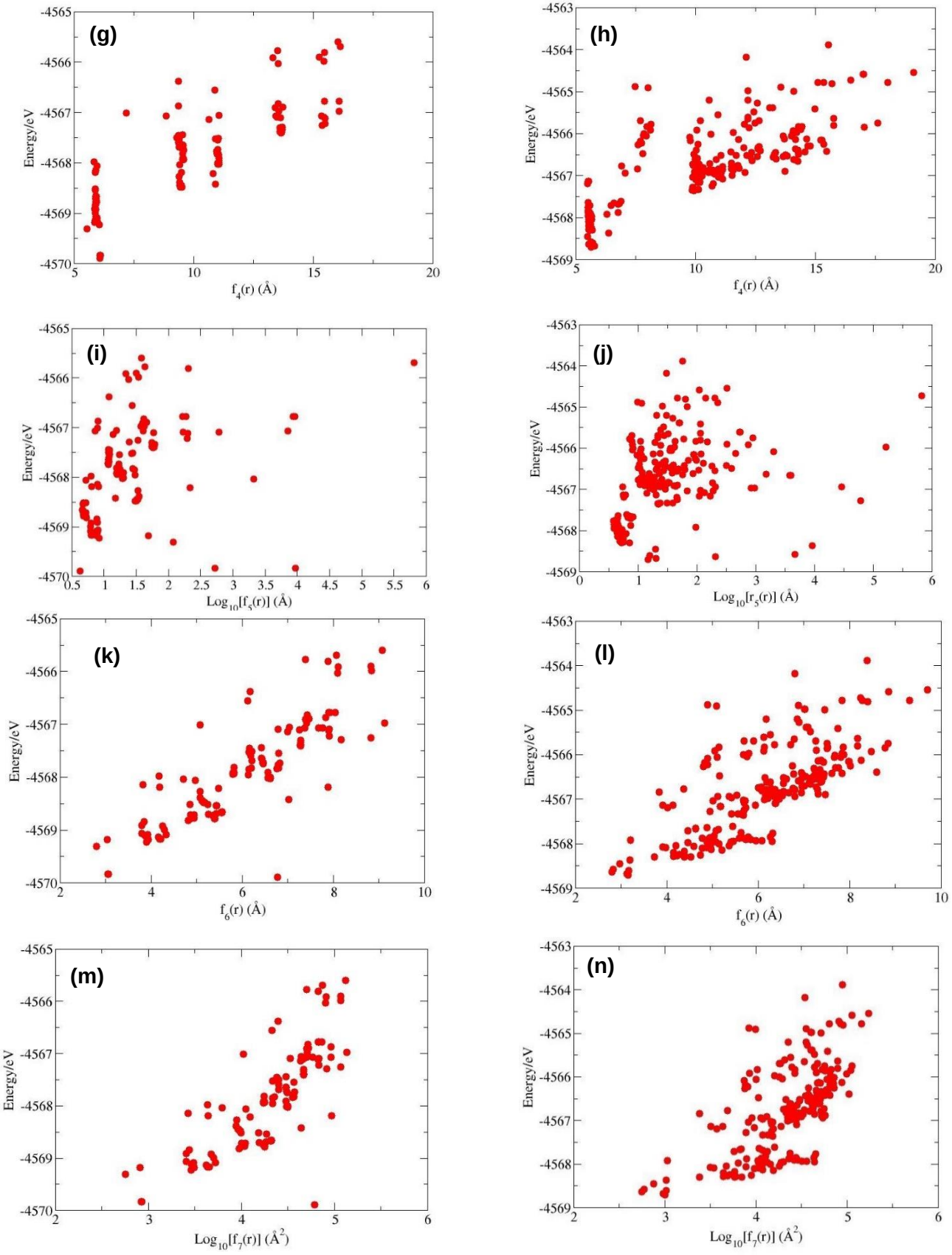

Figs. 17 (g – n): Plots of $f_n(r)$ against energy of Cu in sites SI on the **left**, and **right** in sites SIV.

Taking an intuitive approach by a first inspection, we can simply discern that functions $f_1(r)$, $f_2(r)$, $f_4(r)$, $f_6(r)$ and $f_7(r)$ shows a linear relationship with the energy of Cu-SSZ-13 system, see Figs. 17(a – d, g – h, k – n). These functions satisfy the charge-balancing principle that the proximity of Al dopants does affects the energy of extra-framework Cu in zeolite. On closer inspection, the energy range in sites SI scales between -4565.6 and -4569.9eV – a range of -4.3eV. Sites SIV, has a larger range of a 4.8eV scale. Comparing Cu in sites SI and SIV, Cu in the 6MR has the more favourable lower bound of energy values (-4565.60eV) and a slightly higher upper bound (-4569.89eV). Cu in sites SIV have greatest upper and lower bounds at -4568.70 and -4563.88eV respectively.

The slightly larger energy range for Cu in sites SIV can possibly be attributed to the larger geometrical size of an 8MR compared to a 6MR. The largest measured diameter from our calculations for the 8MR is ~7.85Å and the 6MR possesses a ~6.26Å diameter. The force-field calculations showed that the optimized geometry for Cu in sites SI, has the Cu sitting in the centre of the 6MR, see Fig. 18a. Cu in sites SIV, does not always occupy the centre of the 8MR, instead the Cu moves towards the framework, see Fig. 18b. There will be a greater range of energy values from Cu in sites SIV depending on the proximity of the Cu to the framework atoms. Indicating, the size of the 6MR is a better site for Cu location than the 8MR.

Figs. 18 (a – b): Cu in 6MR of site SI on the **left**, and **right** Cu in 8MR of site SIV.

$F_3(r)$ gives the difference in distance between two nearest Al dopant atoms from Cu, r_3, see Figs. 17(e – f). The lower and upper bounds for r_3 are ~0.0 and ~7.0Å respectively. The sampling of the two Al dopant atoms never took into account Al sittings in the same extra-framework sites, as a result the greatest lower bound is never 0.0Å. At r_3 values near to 0.0Å the Al dopant atoms are approximately in equidistant from the Cu atom. The energies of the Cu-zeolite system however, is unaffected and possesses a very large energy range (-4.3 and 4.8eV for sites SI and SIV) at very small r_3 values. At higher values of r_3, the energy range gradually decreases, this is more pronounced with Cu in sites SIV (Fig. 17f). This is an interesting observation, since $f_3(r)$ can be considered as an indirect measurement of the distance between the two nearest Al dopant atoms. Indicating that in order to prepare stable Cu extra-framework sites in a zeolite catalyst with relatively high Si: Al ratio, ensuring large distances from one Al dopant atom to the next could be a viable solution.

To compare the plots of $f_n(r)$ against energy where n = 1, 2, 4, 6 and 7, simple linear regression models are built in the form:

$$y = a.X + b \quad (\mathbf{48})$$

Linear regression models enable us to quantify the strength of relationship between the dependent and independent variables. In equation (48), y is the dependent variable in our case, the energy of the Cu-zeolite system. X is the independent variable – our predictor, which are the functions, $f_n(r)$. a and b can be considered as constants; the gradient and intercept of the regression line respectively. The plots of the simple regression model of the form in equation (8) are shown in Figs. 19(a – j). To ensure a sound basis for our models, we have to take in account the ratio of our fitting parameters and the sample size. In equations 1 – 7, each $f_n(r)$ consists of $r_1(Al_1)$, $r_2(Al_2)$ and/or $r_3(Al_1 - Al_2)$ parameters, however, since $r_3(Al_1 - Al_2)$ is mutually dependent on both $r_1(Al_1)$ and $r_2(Al_2)$, we can count only two independent variables. As an estimate, it is best to achieve one fitting parameter for every 10 data points – we have two parameters for 210 and 315 different Cu/dopant configurations for sites SI and SIV respectively, ensuring a good basis and avoiding overfitting.

By looking at three statistical variables we can determine which $f_n(r)$ behaves as the best regression model in terms of predictive power, considering the associated errors. These are: (i) calculated coefficient of determination, adjusted R^2, which is simply the measure of how close the data fits to the regression line, (ii) the sum of squared errors, SSE, the discrepancy of the actual data from the predicted values of the model and (iii) root mean squared error, RMSE, the standard deviation of the differences between our sample data and the predicted data. All three variables allow a measurement of the goodness of fit for the different $f_n(r)$, their values and those of a and b (of Eq. 48) for each $f_n(r)$ are listed in Table 11.

The adjusted R^2 factor by a linear regression fitting is used to determine and order the regression analysis, however, there are other regression techniques and instruments that are equally as effective, such as the Pearson correlation. Like adjusted R^2 factor, it is a measure of the linear correlation between two variables and is calculated by computing the covariance between the two variables, divided by the product of their standard deviations.

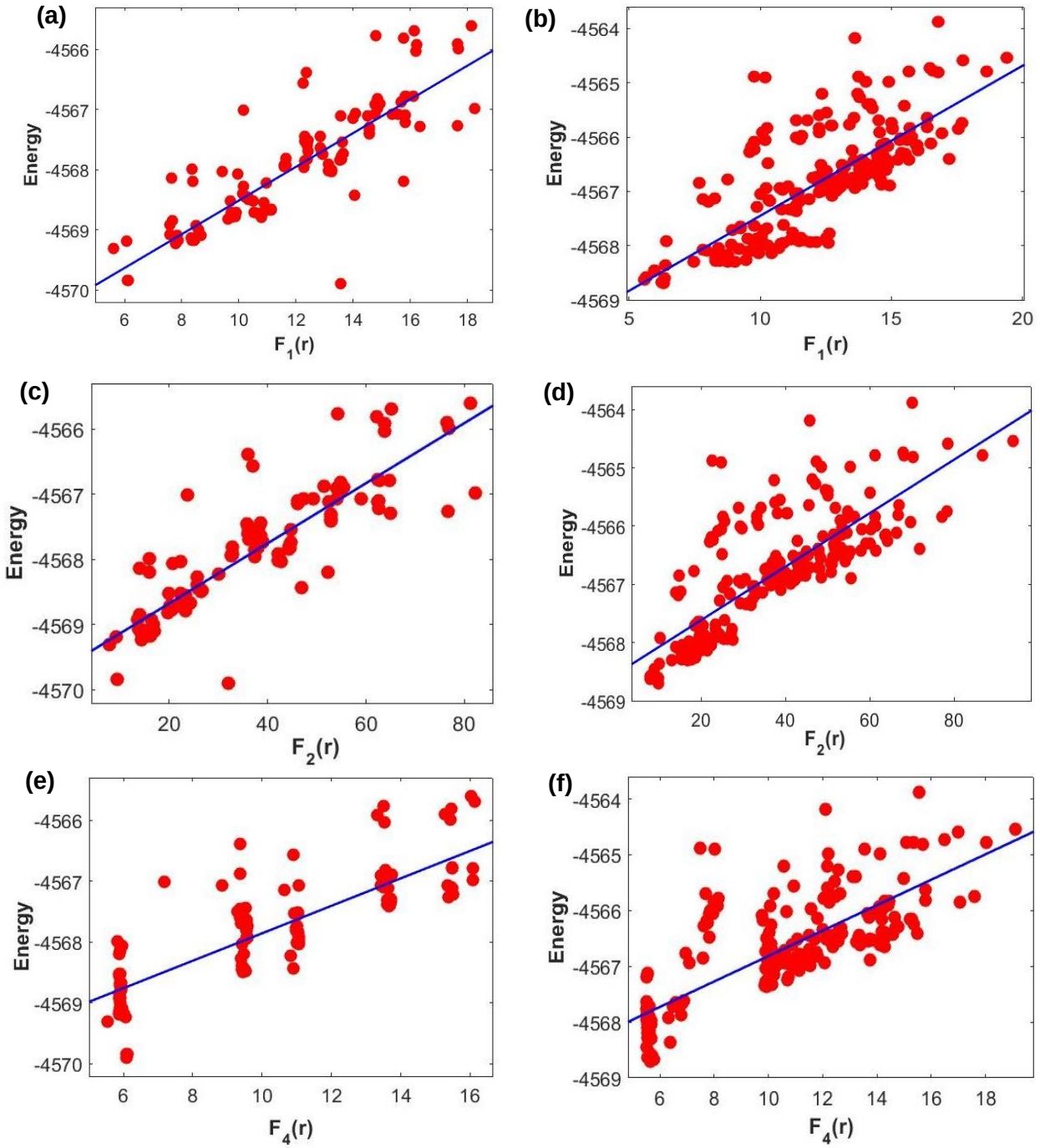

Figs. 19 (a – f): Plots of the linear regression models on **left**, for Cu in sites SI, and **right** for Cu in sites SIV. Regression line is coloured blue.

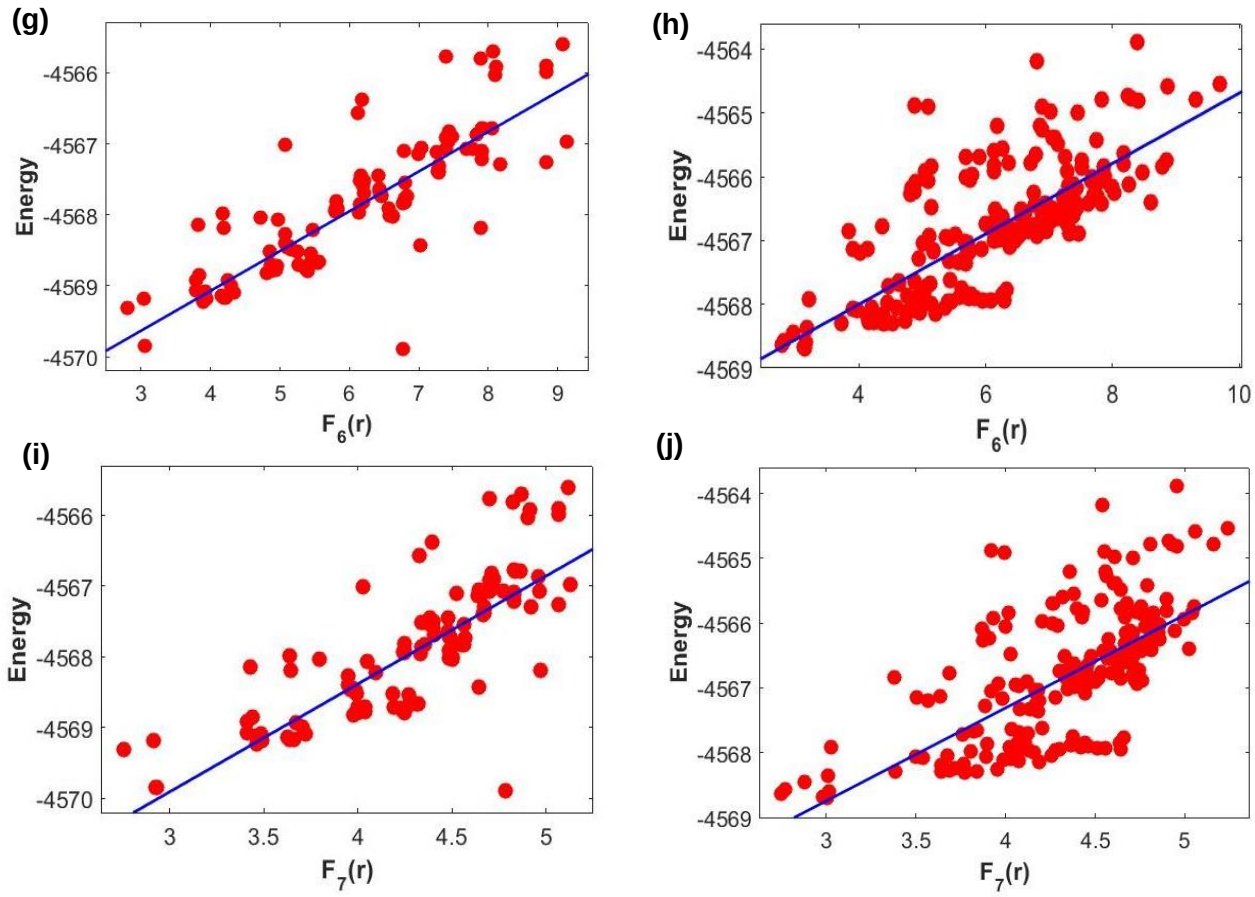

Figs. 19 (g – j): Plots of the linear regression models on **left**, for Cu in sites SI, and **right** for Cu in sites SIV. Regression line is coloured blue.

Table 11

$F_n(r)$	Adjusted R^2		SSE		RMSE		*a*		*b*	
	SI	SIV	SI	SIV	SI	SIV	SI	SIV	SI	SIV
1	0.7084	0.5416	46.71	142.1	0.4739	0.6749	0.2804	0.2764	-4571	-4570
2	0.7515	0.5965	39.80	125.1	0.4374	0.6332	0.0461	0.0460	-4570	-4569
4	0.7266	0.6221	43.79	117.2	0.4589	0.6128	0.2254	0.2280	-4570	-4569
6	0.7084	0.5416	46.71	142.1	0.4739	0.6749	0.5608	0.5527	-4571	-4570
7	0.5991	0.4272	64.22	177.6	0.5556	0.7545	1.5260	1.4370	-4574	-4573

Considering the plots in Figs. 19(a – j), $f_n(r)$ for both Cu in sites SI and SIV are relatively well described by the regression models. Table 11, enables us to directly compare which $f_n(r)$ best describes the effect of dopant distributions on the energy of Cu-zeolite systems for each sampled data (sites SI and SIV). Adjusted R^2 values is the lowest for $f_7(r)$ for both sites SI and SIV, indicating that a model based on $f_7(r)$ has greater errors associated with it upon prediction. This is evident in the RMSE values, which are at 0.5556 and 0.7545eV for sites SI and SIV within energy ranges of 4.3 and 4.8eV respectively. Considering thermal energy at room temperature is 0.013eV, these are perceptible errors and consistent for the other $f_n(r)$ (n =1, 2, 4 and 6). The SSE values highlights the discrepancy of the sampled data from the regression line, for sites SI these are in the range of 39.80 to 64.22 and for sites SIV it is greater by a magnitude in between 117.2 and 177.6.

Upon inspection of Table 11, it can be discerned that none of the $f_n(r)$ are good regression models for predicting the absolute outcome of energies in Cu/dopant zeolite systems. Comparing sites SI and SIV, the models describes with greater accuracy for Cu in sites SI, but the precision is lacking as highlighted by the values of RMSE and SSE. This difference between data with Cu from sites SI and SIV, indicates that in addition to dopant proximity, the effects of the extra-framework site environment similarly has an effect on the energy of these systems. The dopant proximity influences the overall energy of Cu/dopant zeolite system, but local environment Cu resides in affects the ordering of different Cu-zeolite configurations of the same dopant distributions, especially true concerning Cu in sites SIV as mentioned above.

Our aim was to choose the function which best accurately describes the effect of dopant distributions in sites SI and SIV. $F_2(r)$ for Cu in sites SI shows the least associated errors, and likewise $f_4(r)$ for the sites SIV. These two functions looks to best determine the energetic behaviour of Cu/dopant zeolite systems from the effects of dopant distributions.

5.1.5.2 Si distributions in SAPO-34

The effect of Si dopant distributions in the AlPO analogue on Cu-SAPO-34 was also considered, by establishing a series of plots of equations 41 – 47 against energy of the Cu/dopant-AlPO system, see Figs. 20(a – n). The same statistical modelling procedure was followed as from the Cu-SSZ-13 case, therefore, enabling direct comparisons on the effects of dopant distributions in both Cu-exchanged zeolite and AlPO.

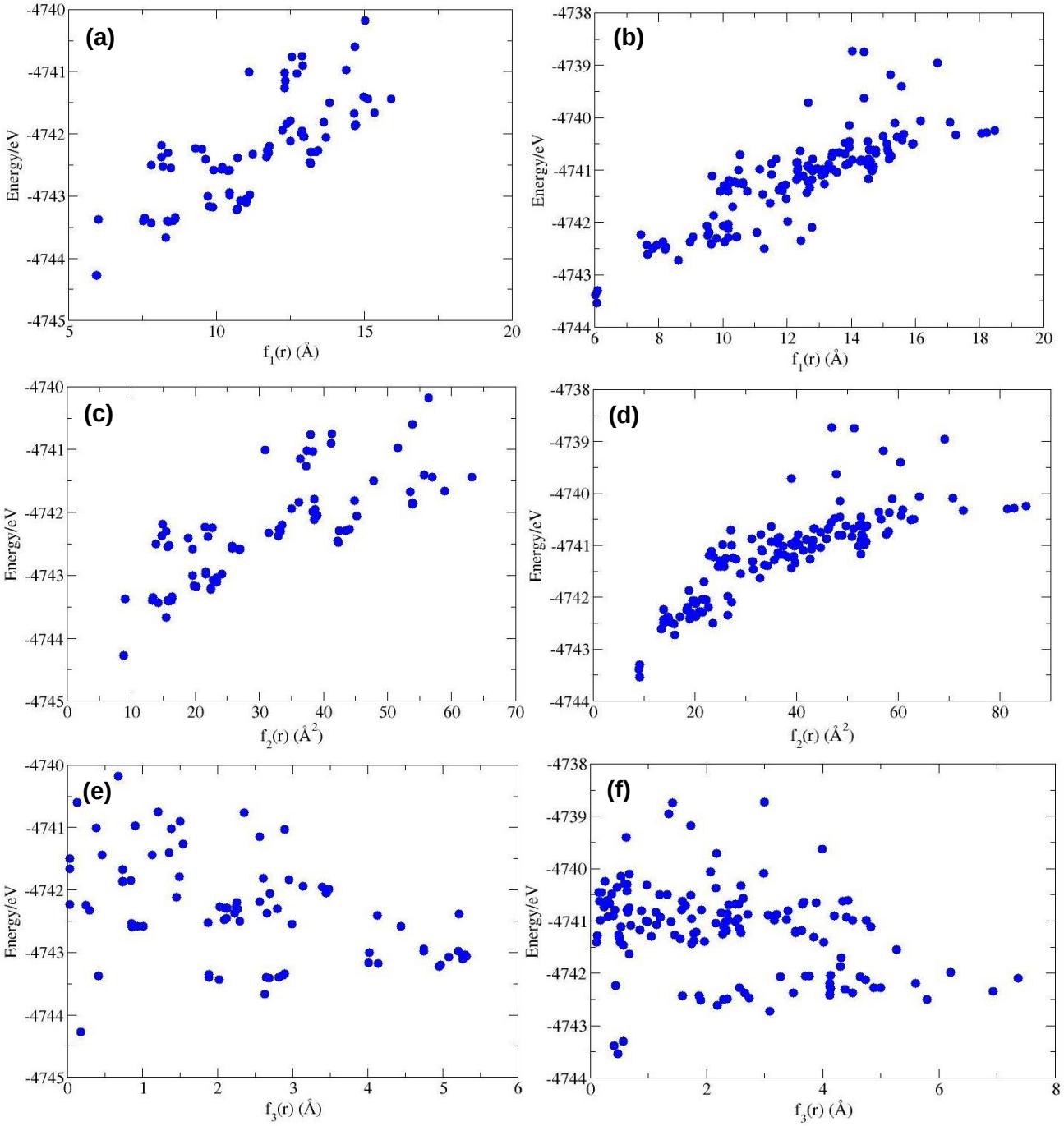

Figs. 20 (a – f): SAPO-34 plots of $f_n(r)$ against energy of Cu in sites SI on the **left**, and **right** in sites SIV.

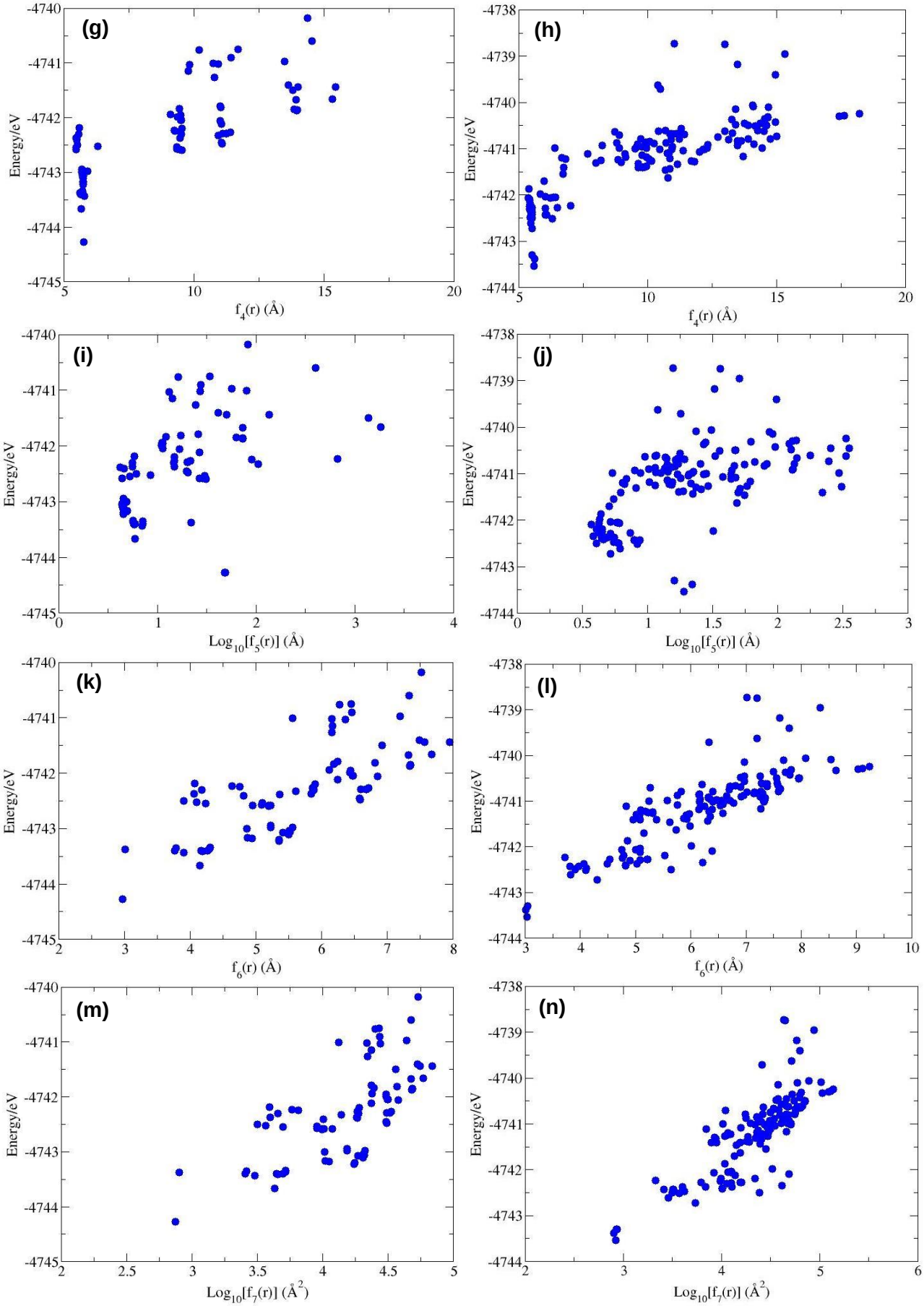

Figs. 20 (g – n): SAPO-34 plots of $f_n(r)$ against energy of Cu in sites SI on the **left**, and **right** in sites SIV.

As in the case for Cu-SSZ-13, the Cu-SAPO-34 plots of $f_n(r)$ where n = 1, 2, 4, 6 and 7 against energy all shows strong linear dependence, see Figs. 20(a – d, g – h, k – n). The greatest upper and lower bounds for Cu in sites SI is -4744.28 and -4740.18eV, giving an energy range of 4.1eV. In sites SIV, the limits are -4743.54 and -4738.74eV with a larger energy range of 4.8eV – in agreement with observation in the zeolite. Cu residing in sites SI, achieve an overall lower energy system in SAPO-34 compared to when in sites SIV. This observation is the same with the Cu-SSZ-13 case. The average energy for Cu-SAPO-34 is within the magnitude of -4741.85eV, and in Cu-SSZ-13 -4567.40eV, showing that the potential energy surface in the AlPO system is significantly deeper compared to the zeolite.

$F_3(r)$ provides the same insight as shown in the zeolite system; a general trend of more stable Cu/dopant SAPO-34 configurations with larger values of r_3, see Figs. 20(e – f). The agreement in observation from the AlPO case, confirms a secondary dopant distribution effect. The first is the linear dependence from energy of the Cu/dopant-host system. The secondary as shown from the results of $f_3(r)$, is the interplay between the two dopant atoms – in both zeolite and AlPO, the greater the difference in distance between the first dopant and secondary dopant atoms from the Cu results in a more stable Cu-configuration. Intuitively, this is an unexpected and not too perceptible effect of dopant ordering, but is impactful on the energy of the Cu configurations. The outcome from this observation is that having two dopant atoms in the same Cu (SI or SIV) site, does not necessarily equates to the most energetically stable Cu configuration. This is in contrast from Göltl *et al*, they performed DFT calculations showcasing that for a Cu^{2+} in the 6MR of site SI, the symmetrical ordering of a two dopants system in the same Cu site is most favourable.

$F_5(r)$ like that in the zeolite situation does not exhibit a strong linear relationship with the energy of the Cu/dopant AlPO system. To compare the different $f_n(r)$s that shows strong linear dependence from the energy, linear regression models are built as per previously for $f_n(r)$ where n = 1, 2, 4, 6 and 7, see Figs. 21(a – j). The statistical data are listed in Table 12.

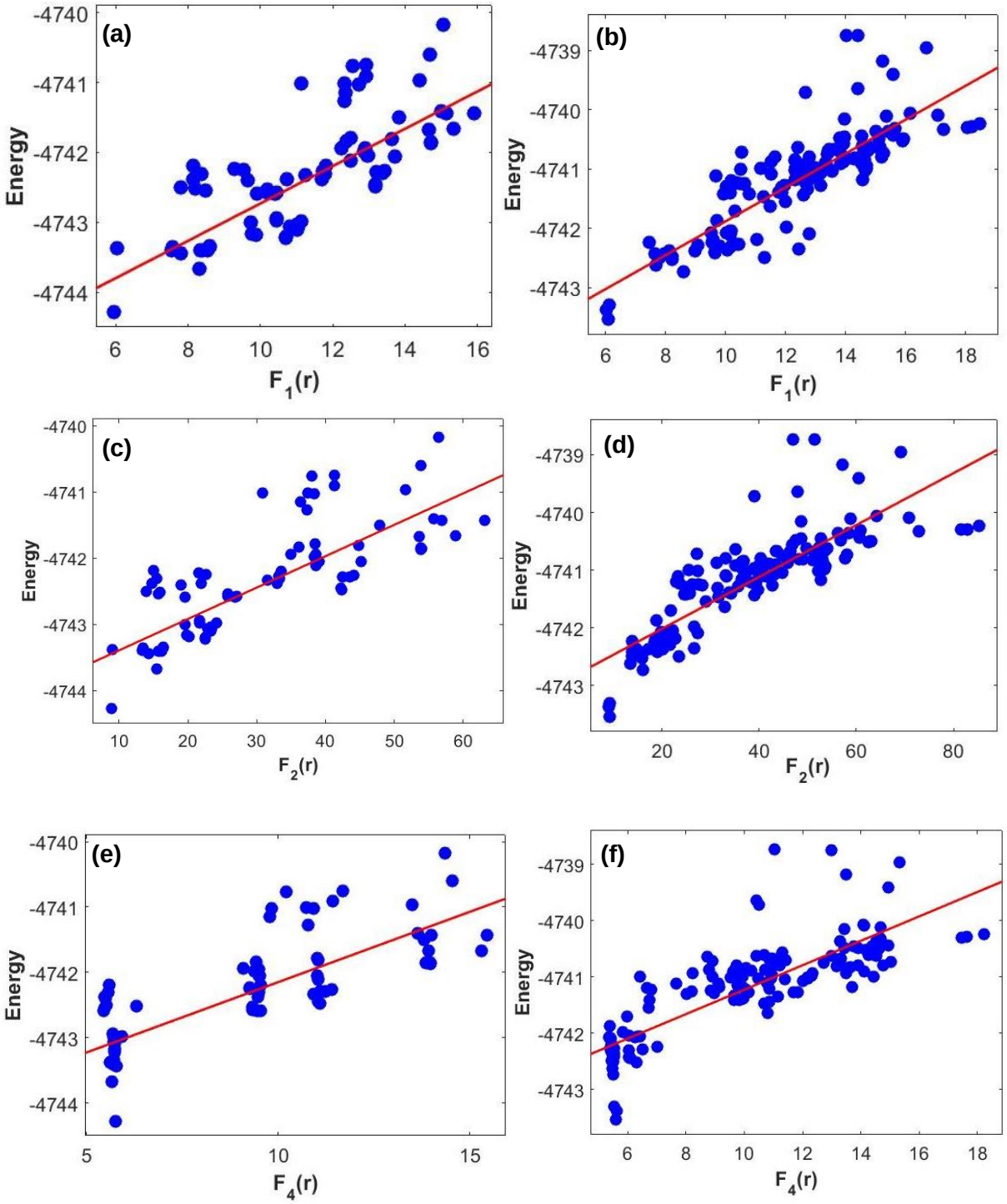

Figs. 21 (a – f): SAPO-34 plots of linear regression models of Cu in sites SI on the **left**, and **right** in sites SIV. Regression line is coloured red.

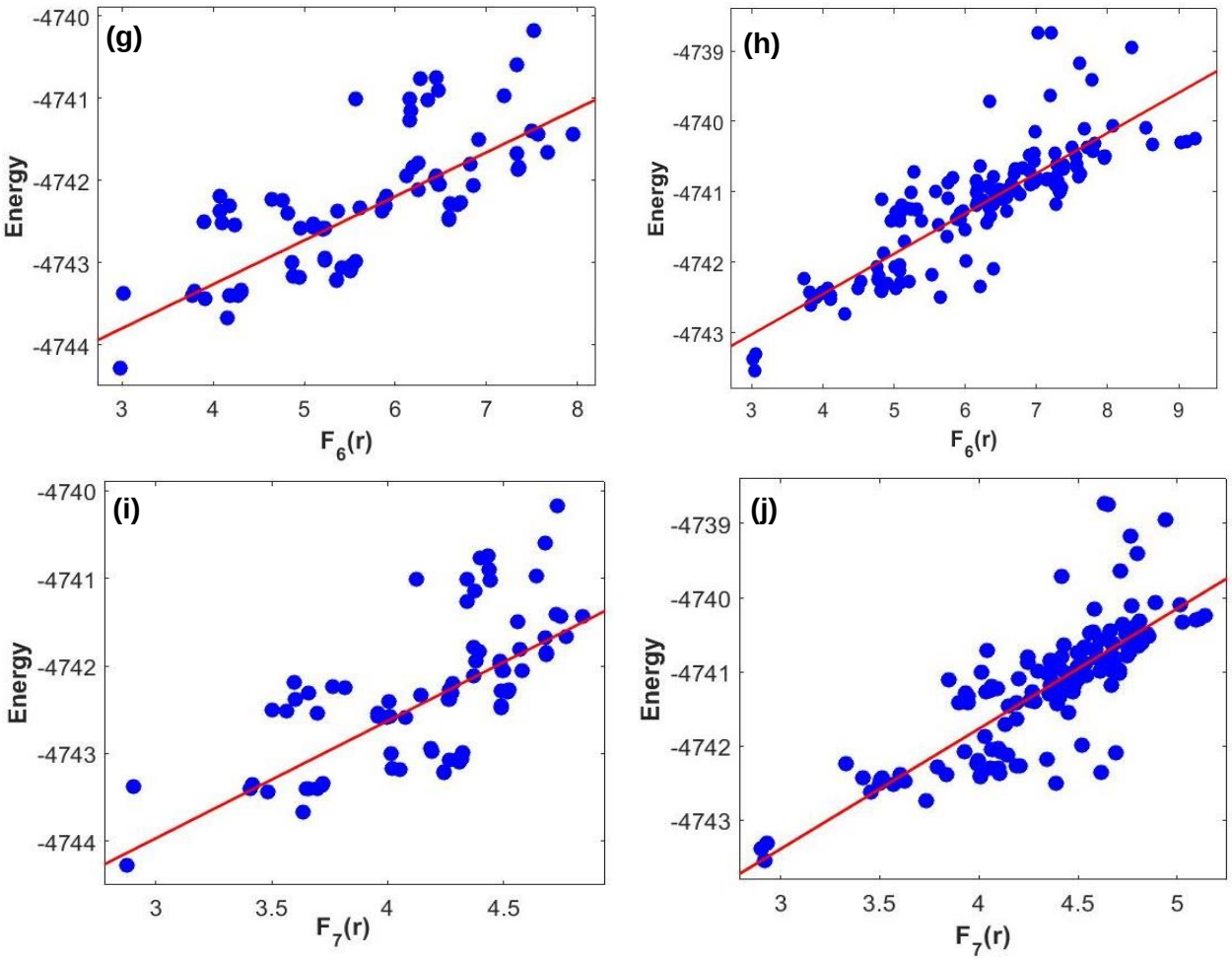

Figs. 21 (g – j): SAPO-34 plots of linear regression models of Cu in sites SI on the **left**, and **right** in sites SIV. Regression line is coloured red.

Looking at Table 12, $f_7(r)$ is show to be the least well-behaved model for both Cu in sites SI and SIV, with an attributed adjusted R^2 value of 0.4964 and 0.6674 respectively. Interestingly, Cu in sites SIV in the SAPO-34 case shows a better fit with the regression models, in contrast with SSZ-13 where it was Cu in sites SI that was shown to have the higher goodness of fit. $F_4(r)$ has the highest adjusted R_2 value for Cu in sites SI, while both $f_1(r)$ and $f_6(r)$ have equalled highest rank. This is expected, since functions $f_1(r)$ and $f_6(r)$ only differ by a constant, as $F_1(r)$ is the sum of $Al_1(r_1)$ and $Al_2(r_2)$ and $f_6(r)$ is simply the averaged of $Al_1(r_1)$ and $Al_2(r_2)$. The standard deviation error in the models (RMSE), is within the range 0.4736 – 0.5946eV, this is relatively high discrepancies considering the range in energy for is -4.1 and -4.8eV for Cu in sites SI and SIV respectively.

Based on adjusted R_2, SSE and RMSE values, $f_4(r)$ is the best model for Cu in sites SI, whilst either $f_1(r)$ or $f_6(r)$ best describe the behaviour of Cu in sites SIV. Inspecting equation 44, $f_4(r)$ considers the difference between the sum of the two Si dopant distances to Cu, and that of the difference in distances of the Si dopant atoms from Cu. Compared to SSZ-13, where the behaviour is best characterised by only $Al_1(r_1)$ and $Al_2(r_2)$. In the sites SIV, $f_1(r)$ or $f_6(r)$ is simply the linear dependence of the data on the sum of both $Al_1(r_1)$ and $Al_2(r_2)$.

Table 12

$F_n(r)$	Adjusted R^2		SSE		RMSE		*a*		*b*	
	SI	**SIV**	**SI**	**SIV**	**SI**	**SIV**	**SI**	**SIV**	**SI**	**SIV**
1	0.5919	0.7272	28.66	33.87	0.5353	0.4736	0.2674	0.286	-4745	-4745
2	0.6306	0.7087	26.2	36.18	0.5118	0.4895	0.0474	0.04495	-4744	-4743
4	0.6374	0.6743	25.72	40.45	0.5071	0.5176	0.2154	0.2171	-4744	-4743
6	0.5919	0.7272	28.66	33.87	0.5353	0.4736	0.5347	0.572	-4745	-4745
7	0.4964	0.6674	35.36	41.03	0.5946	0.5213	1.338	1.619	-4748	-4748

Summary 5.1: GULP calculations

From extensive geometry optimization calculations, inside the SSZ-13 and SAPO-34 frameworks we have observed the equilibrium locations of Cu^{2+} are the 6MR and 8MR windows in sites SI and SIV, with site SI the overall lowest energetic minimum. The average energy difference between the two extra-framework sites is found to be -1.03eV lower in energy for site SI compared to site SIV when in SSZ-13. Similarly, in SAPO-34 the average relative energy between sites SI and SIV is +1.21eV against SIV.

Neither the large cage in site SII or the vacancy inside the D6R of site SIII were shown to the energetically viable for both frameworks. This is because in the former, there was an absence of zeolitic interactions for stabilization of the Cu^{2+} electronic configuration, and in the latter, the combination of steric constraint inside the D6R and proximity to the 6MR windows of sites SI, ensure Cu^{2+} migration to the neighbouring site of SI. For SSZ-13, the energetic description of the above for site SII relative to SI is +6.28eV, whilst Cu^{2+} was not found in inside SIII out of the 620 calculations computed. Inside SAPO-34, site SII was not populated by Cu2+ out of 340 calculations, whilst site SIII was +2.80eV higher in energy relative to site SI.

The Cu migration profiles calculated in Chapter 5.1.4 was in good agreement with the geometry optimization calculations conducted. A hypothetical linear pathway was built through all the extra-framework sites reported in literature, and showed an energetic landscape with sites SI and SIV as the minima, whilst sites SII and SIII are the maxima. The migration profiles computed for SAPO-34 suffered from inconsistencies with respect to Cu^{2+} being trapped in local minima. This observation was not found in SSZ-13, indicating Cu^{2+} exhibits greater labile behaviour inside the AlPO framework, see Figs. 12(a – d). A plausible explanation for this distinct behaviour of the migration profiles, is the inherent flexibility of AlPO compared to a zeolite since the bonding inside an AlPO is more ionic.

A new site was discovered which as of writing was not reported in the literature; Cu^{2+} was observed inside a 4MR with a relative energy of +0.68eV against site SI in SSZ-13. This new site was labelled site SV. For SAPO-34, site SV was also observed with greater frequency, see Table 9. The average relative energy is +1.97eV against the site SI when found in SAPO-34, this is discernibly higher difference compared to inside SSZ-13.

A statistical approach to quantify the effect of dopant distribution on the overall energy of the system was built via linear regression, and deploying an R-squared analysis to determine the correlation between the energy of the Cu-framework system and proximity of Cu^{2+} to the pair of dopant atoms. Overall for both SSZ-13 and SAPO-34 a general trend can be confirmed for; the nearer the proximity between the pair of dopant atoms with Cu^{2+}, the lower the energy of the system. This is further confirmed by inspecting the individual Cu-dopant configurations with the lowest energy amongst the thousands of calculations performed for SSZ-13 and SAPO-34, see Figs. 8(a – j) and Figs. 9(a – j).

5.2 CRYSTAL calculations

The aim of the CRYSTAL calculations is to reproduce the results from the GULP work. Looking at the relative stabilities of the 6MR and 8MR windows in sites SI and sites SIV, compared to the vacant D6Rs and large cages of sites SIII and SII respectively. In addition, to investigate the plausibility of the 4MR structures as suitable Cu sites, which from here on we will name as site SV. Finally, to reproduce the migration profiles of Cu in the CHA system of SSZ-13 and SAPO-34. Firstly, three different hybrid functionals; B3LYP, PBE0 and PBE0+10% were investigated for their suitability in studying Cu^{2+} ion in a zeolite structure.

5.2.1 Comparing functionals

PBE0 performed comparably with B3LYP, both in conjunction with the Broyden algorithm implemented, which is a method for accelerating convergence in self-consistent calculations. In the absence of the Broyden algorithm, the calculations fails to achieve SCF convergence as a result of oscillations between a Cu(I) and Cu(II) state, this is particularly prominent when Cu^{2+} is not in the same site with any two of the active sites (Al or Si for zeolite and AlPO respectively). This slow convergence is partially rectified by Broyden, because it is able to "incorporate information from all previous iterations during the updating procedure"[187]. This enables the SCF to recall the first cycle in the SCF which has Cu as an absolute Cu(II) state and prevent the oscillations.

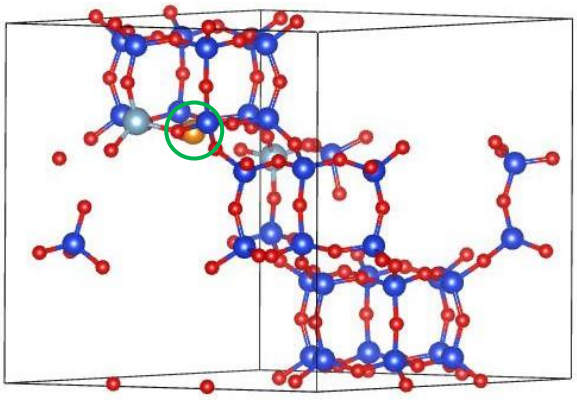

Fig. 22a: Zeolite SSZ-13, 1_23 as named in our database. This involves the secondary Al in the 6MR window of site SIb where Cu(II) occupies, circled green.

Table 13

Framework configuration	Functional	Broyden (B) or Level Shifting (L)	SCF convergence (cycles)	Force calculation	Spin on Cu^{2+} (4 s.f.)
1_23	B3LYP	B	21	Yes	0.653
1_23	PBE0	L	209	Yes	0.700
1_23	PBE0	B	18	Yes	0.700
1_23	PBE0+10%	B	19	Yes	0.768

Table 13 (above) shows the comparison of performance with the three different functionals that were studied with; B3LYP, PBE0 and PBE0+10% exact HF exchange for the same zeolite system, Fig. 22a (above). The Cu is in the 6MR window of site SIb, with an active site Al in the same place. In the cases where the functional was equipped with Broyden, this resulted in an accelerated SCF convergence by an order of a magnitude compared to the PBE0 (L), with only level shifting applied – where the highest occupied orbital, in this case the e_g orbitals are shifted by an addition of one hartree. A direct comparison of PBE0 (L) and PBE0 (B), excluding the number of cycles took to achieve SCF convergence, shows no significant difference is convergence upon energy. Whilst the spin magnetic moment on Cu^{2+} in both cases is 0.700 (4s.f.), this confirms that Broyden only affects an influence on the length of SCF convergence.

Except for the effect of Broyden, the biggest discrepancy among the three functionals is the spin magnetic moment on Cu^{2+}, which is ranked in descend: PBE0+10% (B) > PBE0 (L) = PBE0 (B) > B3LYP. B3LYP has the least spin on the Cu^{2+}, with the spin spread towards the framework O atoms. On the other hand, PBE0+10% which has the Cu^{2+} localized with the highest amount of spin at 0.768 as expected, due to the increased exact exchange. Both PBE0s (B) or (L) achieved the same spin on Cu^{2+}, because they are identical functionals and have the same amount of exact exchange in the formulation. The spin magnetic moment (M) indicates the nature of Cu, and therefore dictates the oxidation state of Cu in this situation either as Cu(I) or Cu(II). Similarly, Beato *et al* classified the oxidation states of Cu by assignment according to the spin magnetic moments of their DFT calculations where: $M(Cu^{2+}) > 0.45$ and $M(Cu^{+}) < 0.1$. The higher spin magnetic moment on Cu^{2+} observed with PBE0+10% is important, since the aim of the study is to investigate the nature of Cu^{2+} ions in these CHA frameworks. Subsequently, PBE0+10% would be the more rigorous functional to ensure the proceeding of the calculations as Cu^{2+}, in addition to accelerating the convergence of the SCF compared to the other three functionals.

Looking at the geometries of the Cu^{2+} in the 6MR window of site SIb, Fig. 23(b – e), we can conclude that the configuration of Cu^{2+} is relatively insensitive to the precise nature of the hybrid functionals used. All four configurations achieve a distorted square-planar, with the two shortest Cu-O bonds belonging to the framework O atoms adjacent to the secondary Al atom. The discrepancy in the Cu-O bond distances from the four functionals are on average within the range of 10^{-3} – 10^{-4}Å. Inspecting each Cu-O bond it is the PBE0+10% that achieves the shortest Cu-O bonds with the activated O atoms. In addition, the average Cu-O bond distances for each of the functionals are 1.956, 1.948, 1.953, 1.954Å for B3LYP, PBE0+10%, PBE0 (L) and PBE0 (B) respectively. This indicates that in the PBE0+10% functional, the Cu configuration is the most stable as evident by the strongest Cu-O bond coordination.

From first inspection, taking into consideration the above results, it can be fair to deduced that PBE0+10% gives results that are in line with a more stable Cu^{2+} system compared to PBE0 and B3LYP. Due to the higher exact exchange of 35% compared to 20% in PBE0 and B3LYP. This is in good agreement with the studies by Cora *et al*[186], where the optimum weight of HF exchange in a hybrid functional formulation was found to be greater than the 20% used in molecular studies, and indeed was nearer to a half-and-half hybrid of 50% for a solid-state[186]. As such, the CRYSTAL calculations to investigate Cu^{2+}-exchanged SSZ-13 and SAPO-34 was paired with PBE0+10% functional.

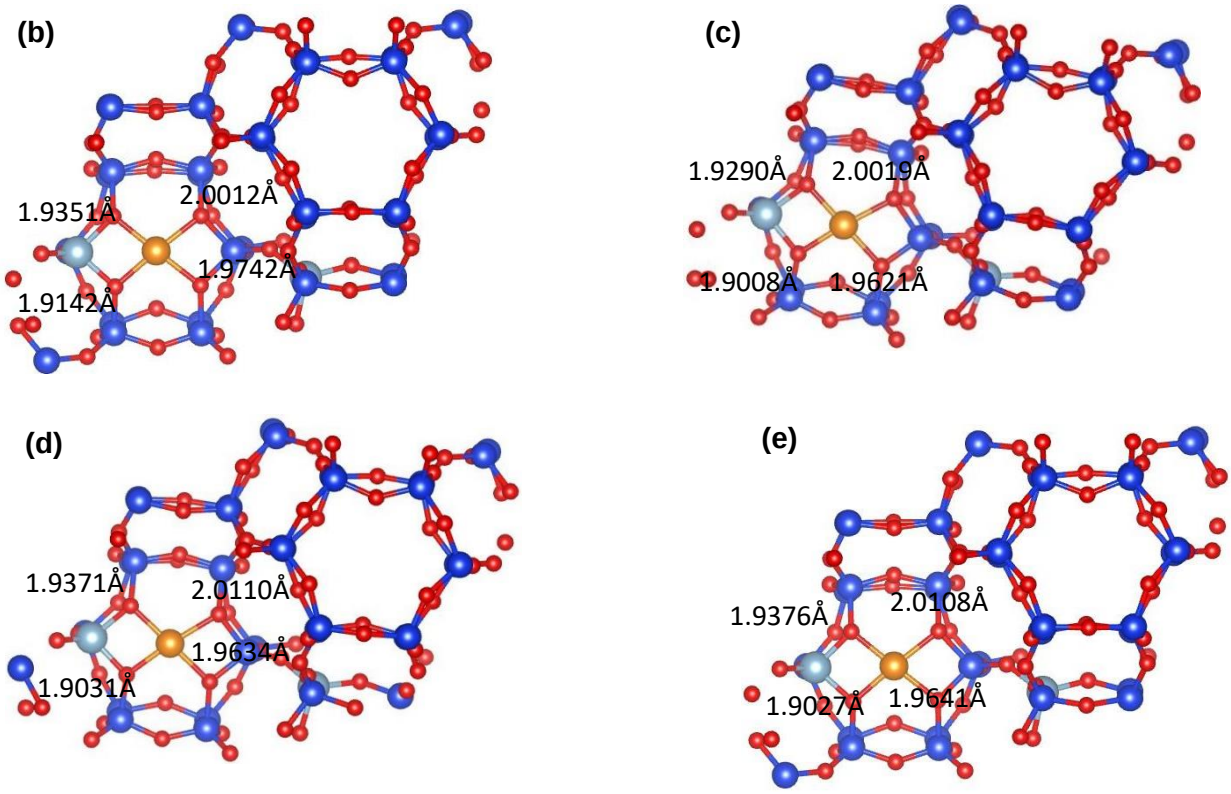

Fig. 23b – e: The 1_23 SSZ-13 configuration with Cu(II) in site SIb, the images are optimized with **(b)** B3LYP, **(c)** PBE0+35%, **(d)** PBE0 (L) and **(e)** PBE0 (B).

5.2.2 Extra-framework sites in SSZ-13

The extra-framework sites (SI, SII, SIII, SIV and SV) were investigated with regards to their energetic stability and the local environment of each of the sites. Geometry optimisation calculations in CRYSTAL were performed for each of the sites with and without an Al active site present. This gives an insight into the individual energetic stability of each sites, and the subsequent effect of an Al active site. Table 14 gives the comparisons for each of the investigated extra-framework site in the zeolite SSZ-13 with the 1_02 configuration, see Fig. 24. In this framework configuration, sites SIa, SIVa, SVa and SIIIa, are 6MR, 8MR, 4MR windows and D6R structure respectively with one Al active site present. Sites SIc, SIVb, SVb and SIIIb do not have an Al active site present. While, in site SIIa, the Cu sits in the centre of a large cage with an Al dopant present in the central 8MR (site SIVa) and the Al atom from in SIa from an adjacent unit cell in 001 direction.

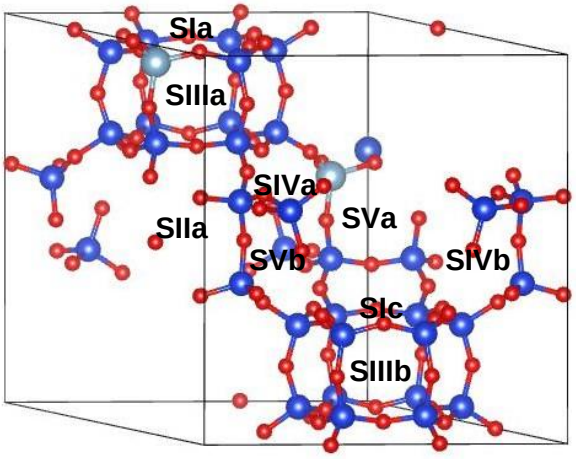

Fig. 24: Zeolite SSZ-13, 1_02. Stationary Al in the 8MR window of SIVa and secondary Al in the 6MR window of site SIa.

Table 14

Extra-framework site	Al active site present	Rel. energy (eV) (3 s.f.)	Spin on Cu^{2+} (4 s.f.)	Number of coordinations
SIa	One	0.000	0.76	4
SIVa	One	0.961	0.71	3
SIc	None	1.98	0.81	4
SIVb	None	2.19	0.68	3
SIIa	None	N/A	0.00	N/A
SIIIa	One	2.36	0.02	4
SIIIb	None	2.42	0.00	N/A
SVb	None	3.13	0.72	4
SVa	One	N/A	0.22	N/A

In Table 14 we are able to gather that sites SI is not always the most stable location for Cu to reside in, even though site SIa is the most stable overall and by 0.961eV against site SIVa which is the most second most favoured energetically. This is in relative good agreement with the average energetic insights gained from the GULP results, see Table 14. Looking at the sites, when no nearby Al atom is not present, in the case of SI, not in the plane of the 6MR window (SIc) and for SIV, not in the 8MR window (SIVb) we still observe site SI higher in stability against SIV. Here, SIc > SIVb in terms of stability by 0.21eV, however the energetic stability decreased between the two sites. This indicates the presence of the Al dopant atom accentuates the energetic difference between sites SI and SIV, this is particularly pronounced when inspecting sites SIa and SIc, both with Cu^{2+} inside a 6MR window, but the presence of an Al dopant in SIa is responsible for up to a 1.98eV difference. This is an interesting observation and indicates that the stability of sites is a function of both geometrical location of the site and the presence of nearby dopant atoms. The energetic difference between sites SIVb and SIa is great at 2.19eV; if Cu^{2+} is in site SIa it is thermodynamically unlikely that SIa will migrate to SIVb considering at room temperature (298K), the Boltzmann energy is 25.7meV – a fraction of the energy we observe between the profiles of SIVb and SIa.

Sites SII were a difficulty to calculate, since Cu^{2+} is situated inside the vacant large cages, there is no zeolitic interaction for stabilization and as such none of the calculations failed to achieve SCF convergence despite the inclusion of the Broyden algorithm. This is evident by the immediate reduction of Cu^{2+} to Cu^{+}, with the spin magnetic moment on Cu at 0.00, see Table 14. Similarly, for sites SIII, the Cu^{2+} is in the centre of the vacant double-6-ring subsequently no stabilization from the zeolite framework can be readily achieved. The closer proximity between the framework and Cu^{2+}, seems to enable convergence of the SCF cycle in both sites SIIIa and SIIIb. The situation with Al present in one of the 6MRs (SIIIa) resulted in a lower energy system compared to without (SIIIb) with a difference of 0.06eV. In both cases (SIIIa and SIIIb), the lack of zeolitic stabilization for the Cu^{2+} to enable crystal field splitting has resulted in reduction, Cu(II) → Cu(I) as evident by the spins on Cu of 0.02 and 0.00 for SIIIa and SIIIb respectively. Similar to both sites SII and SIII, the site SVa did not achieve SCF convergence, this is because the Cu(II) was reduced with a spin magnetic moment of 0.22 (see Table 14). After which, the SCF cycles oscillates wildly between high and low spins, unable to achieve a steady convergence. The Cu^{2+} in sites SIII is unable to form strong coordination Cu-O bonds, the average bond distance is 2.31Å, see Figs. 25(k – l).

In the GULP analysis, the proposed site of SV was on average 0.68eV higher in energy relative to sites SI. In the CRYSTAL calculations, we are able to show that for site SVb, with Cu^{2+} occupying the space opposite a 4MR with no nearby Al present, this was 3.13eV higher in energy compared to site SIa and 1.15eV less stable against site SIc. This discrepancy in the energetic description of Cu^{2+} in site SV between GULP and CRYSTAL, highlights the sensitivity of the Cu^{2+}'s electronic structure to the surrounding environment. In the GULP method, the Cu^{2+} forms three Cu-O coordination bonds to the 4MR, see Fig. 6a and the average bond distance was 2.0553Å. In CRYSTAL, four Cu-O bonds are formed, see Fig. 25(l – j), the average Cu-O bond length is 2.0450Å. Cu^{2+} in CRYSTAL adopts a strained square planar geometry, but in GULP a distorted trigonal planar is observed. This difference in the Cu^{2+} configuration achieved between the two methods, is because in CRYSTAL a square-planar arrangement gives the d-orbital splitting that is closest to that in a tetragonal distortion, which is preferable despite the strained square-planar around the small 4MR frameworks. However, in GULP, where the equilibrium energy is purely a function of the nuclear coordinates and not the electronic structure of the system, a trigonal planar is favoured, because the concern of d-orbital splitting is not required instead achieving a trigonal planar arrangement gives a relatively strain-free configuration.

It is plausible at high temperatures, with temperatures greater than the Boltzmann energy Cu^{2+} occupying site SV, in transient times. The 4MR structure is a strained square-planar because two of the O-Cu-O angles are on average 75˚, compared to a 90˚ angle in a regular square-planar arrangement. Whilst, the remaining two O-Cu-O angles are around 104˚. In terms of geometry, the 4MR configuration adopted is not too dissimilar from that found in sites SI, see Figs. 25(a – d). The O-Cu-O angles in sites SI are either round 108˚ or 73˚, whilst the average Cu-O bond inside the 6MR is 1.9825Å and in the 4MR this is longer at 2.0450Å. Despite the near-identical physical parameters in the configuration between sites SI and SIb, the discrepancy in equilibrium energy between the two is great. This is because, the 4MR aperture is around 3.3Å from one side to the opposite, but in the 6MR window this is 5.0Å. This is a significant difference, as the 4MR framework would be strained by the Cu^{2+} and suffer from repulsive energy due to the close proximity, this is evident with Cu^{2+} being projected outwards thereby resulting in a less stable system.

In terms of configuration geometry, sites SI and SIV in CRYSTAL, see Figs. 25(a – f), are identical to that observed in GULP. In GULP and CRYSTAL, the Cu^{2+} in sites SI achieves a distorted square planar geometry, whilst for SIV it is broadly a trigonal planar arrangement in GULP which is in good agreement with that observed from CRYSTAL. It can be safely deduced that the 0.96eV difference between sites SIa and SIVa is because, the size of the 8MR window is ill-fitted for Cu^{2+} to form four coordination bonds, in order to build a crystal field for d-orbital splitting. The 8MR is too large, unlike the 6MR which enables four coordination bond, each of relatively equidistant. Both sites SIa and SIVa have an Al dopant atom present in the site resulting in the shortest Cu-O bonds belonging to those coordinated to the activated O atoms. In SIa these are 1.9594 and 1.9074Å, for SIVa it is 1.8942 and 1.8705Å. Without the presence of an Al atom as in SIb and SIVb, the Cu-O bonds are more uniform since there is not one particularly strong ligand over another, such as the stronger σ-donors found in the activated O atoms.

On the whole, from our inspections and deductions we are able to say that the geometry of site SI is best-suited for occupation of Cu^{2+}, and the least-suited are sites SII and SIII, where the Cu^{2+} is unable to form strong coordination bonds to the framework for stabilization. In addition to this, the 8MR in site SIV is too big in size since, the Cu^{2+} is only able to form three coordination bonds in a trigonal-planar fashion, whilst the 4MR in site SV is too small since the Cu^{2+} does not sit readily in the 4MR and looks to exert a strain on the 4MR framework. However, the presence of dopant atoms exerts a significant effect on the equilibrium energy of the final configuration as evident between sites SIa and SIc or SIVa and SIVb, with and without an Al dopant in the site respectively.

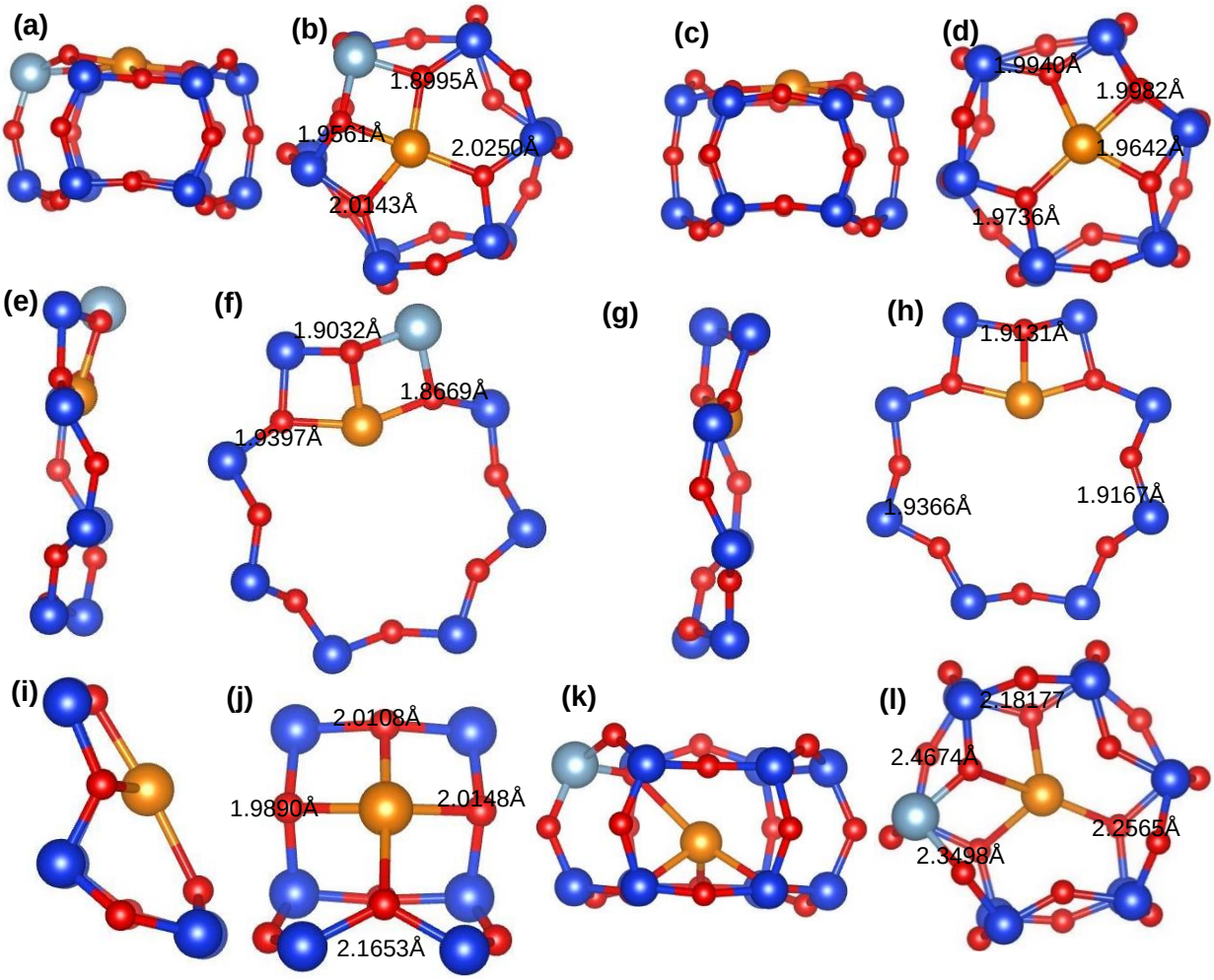

Figs. 25(a – l): Zeolite SSZ-13, 1_02. Optimized structures of **(a – b)** SIa, **(c – d)** SIc, **(e – f)** SIVa, **(g – h)** SIVb, **(I – j)** SIVb and **(k – l)** SIIIb in (001) and (100) views.

5.2.3 Extra-framework sites in SAPO-34

The same systematic investigation of the stability of the sites was repeated for SAPO-34 as shown in Table 15 with an identical dopant configuration as the 1_02 in SSZ-13, Fig. 26. Like in SSZ-13, site SIa with a (Si) dopant atom present in the 6MR window is the most stable configuration. The second most stable configuration is SIVa as in in SSZ-13 with a difference in energy compared to SIa of 0.92eV. This magnitude is similarly near-identical to that in SSZ-13, see Table 14. After, site SIVa, the next most energetically stable configuration is SIc followed by SIVb. This is trend is also reflected in the SSZ-13 energetic profile described, in SAPO-34 site SIc is 2.40eV less stable and in SSZ-13 this is substantially lower at 1.98eV. Likewise, site SIVb in SAPO-34 is much higher in energy relative to site SIa, compared to the situation in SSZ-13; 3.36 and 2.19eV respectively. This indicates that the absence of a dopant atom in the extra-framework has a more pronounced effect in SAPO-34, compared to in SSZ-13.

Just like in SSZ-13, the vacant confinements in sites SII and SIII were not favourable as Cu^{2+} locations. In both sites SIIIa and SIIIb, the Cu(II) was reduced to Cu(I) as evident by the spin magnetic moment. This reduction resulted in a failure for the calculations to achieve SCF convergence. Similarly, this was also observed in sites SIIa and SVa. In GULP, we were able to observe the relocation of the Cu^{2+} atom when in site SIII to the neighbouring sites SI. However, in CRYSTAL no relocation of Cu^{2+} towards the neighbouring 6-ring windows occurred. This is because, in such quantum chemical calculations, the first step in obtaining a geometry optimization is the SCF convergence, this iterative method enables an approximate determination of the wavefunction and energy of the system. After which, a force calculation is performed in order to obtain the first derivatives with respect to the nuclear atomic coordinates gives the forces acting on the atoms, this enables us to understand an accurate description of the equilibrium geometry. Consequently, in the site SIII calculations if the SCF convergence is not achieved with respect to a Cu^{2+} state, the resulting force calculation would not be able to determine a true equilibrium geometry.

Site SVb has an equilibrium energy of 3.69eV higher than site SIa, this highlights that the sites SV is unlikely to be an equilibrium site under thermodynamic conditions. For site SVa, the 4MR has a nearby Si dopant atom present and like in SSZ-13 did not achieve SCF convergence. A plausible rationale is the presence of the active Si atom actually leads to the Cu^{2+} to be reduced. This is probable, because the activated O atoms would have high energy sp-orbitals that reduces the Cu^{2+}. This would occur in geometrically unfavourable sites such as in SV, where the reduction of Cu^{2+} could compensate for the strained on the surrounding framework from the presence of the Cu^{2+} atom.

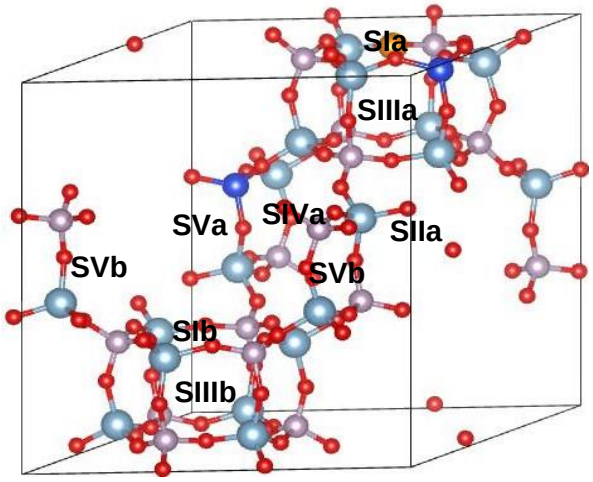

Fig. 26: SAPO-34, 34_35. Stationary Si in the 8MR window of SIVa and secondary Si in the 6MR window of site SIa.

Table 15

Extra-framework site	Si active site present	Rel. energy (eV) (3 s.f.)	Spin on Cu^{2+} (4 s.f.)	Number of coordinations
SIa	One	0.00	0.75	4
SIVa	One	0.923	0.69	3
SIc	None	2.40	0.82	4
SIVb	None	3.36	0.70	3
SIIa	None	N/A	0.00	N/A
SIIIa	One	N/A	0.01	N/A
SIIIb	None	N/A	0.00	N/A
SVb	None	3.69	0.78	3
SVa	One	N/A	0.00	N/A

Figs. 27(a – e) are images of the optimized structures that achieved successful force calculations belonging to Table 15. For sites SI, the same geometry is observed as in SSZ-13, but the Cu-O bond distances are shorter in SAPO-34, by on average of 0.018 and 0.013Å for sites SIa and SIc respectively. This is also observed in all the other structures (SIVb and SVb), this inherent ability for SAPO-34 to form shorter Cu-O bonds is as a result of the greater iconicity in the AlPO bonding compared to that of zeolite enabling the SAPO-34 framework to be more flexible.

The optimized Cu^{2+} in SIVb adopts a slight modified trigonal pyramidal geometry, see Fig. 27d, unlike that in SSZ-13 which has Cu^{2+} in a strained square-planar arrangement. This highlights that more than one 4MR configuration can be formed in site SV, and this can possibly explain the higher energy of site SVb relative to site SIa in SAPO-34, compared to the same pair of sites in SSZ-13. Since, the square-planar with four coordination bonds provides a stronger crystal-field splitting of the d-orbitals in Cu^{2+} compared to a trigonal pyramidal formation.

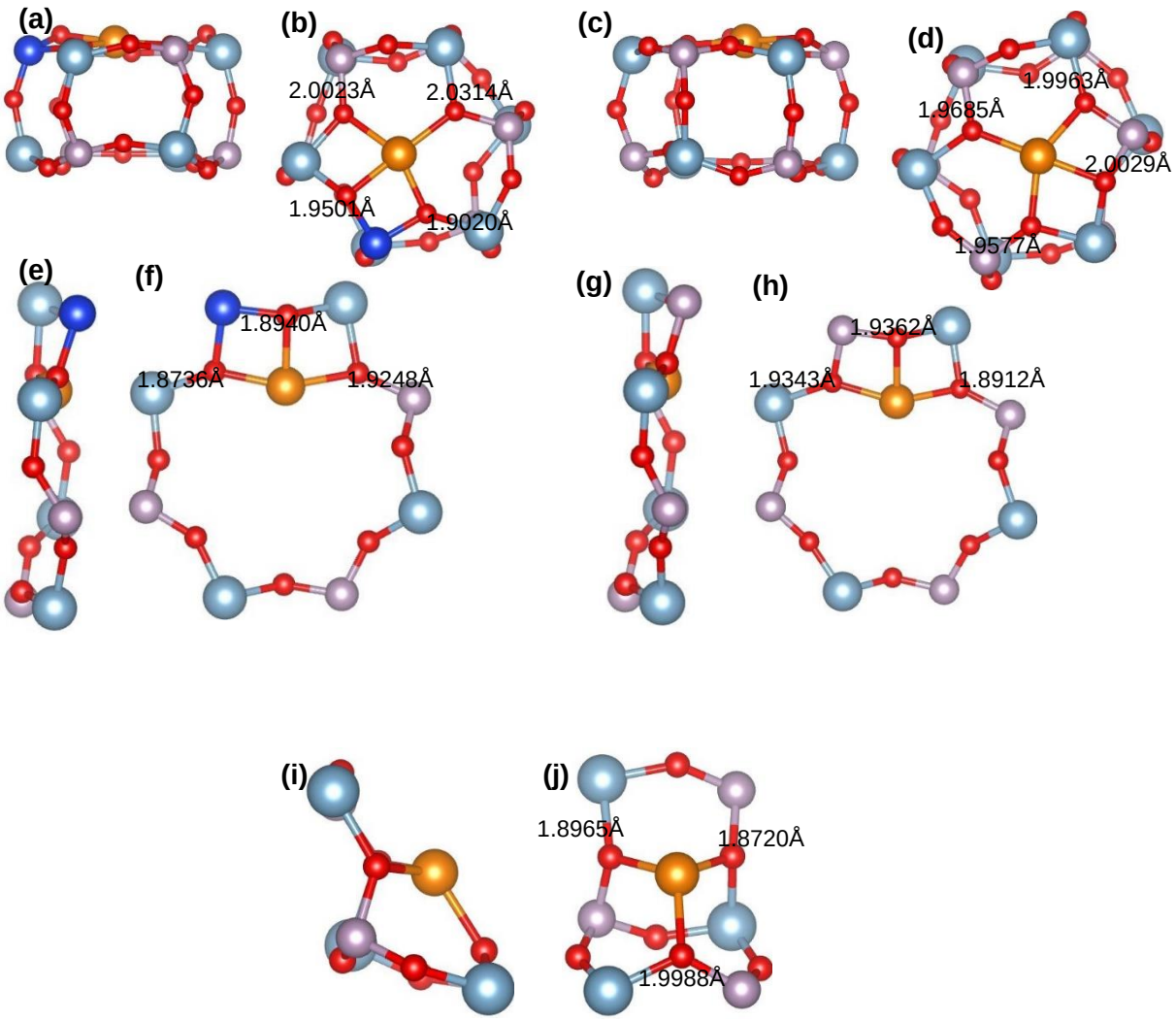

Figs. 27(a – j): SAPO-34, 34_35. Optimized structures of **(a - b)** SIa, **(c - d)** SIc, **(e - f)** SIVa, **(g - h)** SIVb and **(i - j)** SVb in (001) and (100) views.

5.2.4 Cu migration SIa → SIIIa → SIb

The migration profiles in GULP were reproduced for the pathway through SIa → SIIIa → SIb, the same procedure was followed with seven calculations between each site and an additional calculation per site, giving 17 energy points for the CRYSTAL profiles to be built on. Cu^{2+} is moved along a linear trajectory from one 6MR window to the next, via the centre of the D6R structure (SIIIa). The active sites (Al for zeolite and Si for AlPO) are placed above and below neighbouring 6MR windows, oppositely of each other, one in SIa and the other in SIb, Fig. 28a.

Fig. 28a: D6R structures. **Left**, SSZ-13 and **right** SAPO-34. Dark blue are Si atoms. Light blue are Al atoms. Purple are P atoms. Red are O atoms.

In our preliminary GULP calculations, a smooth trajectory is observed with a maximum at site SIIIa for both SSZ-13 and SAPO-34, Fig. 18b. The Cu^{2+} is migrating inside a relatively high energy environment within a 1.2eV scale.

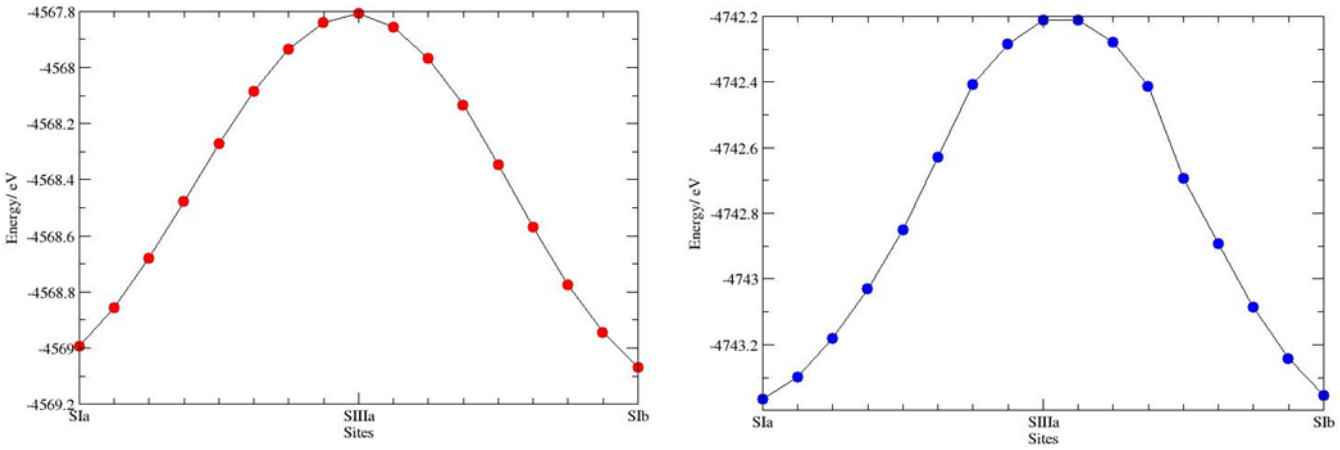

Fig. 28b: Cu2+ migration profile in GULP for SIa→ SIIIa→ SIb for SSZ-13 (red) and SAPO-34 (blue).

This is in contrast to the migration profiles as observed in CRYSTAL (Fig. 28c). Both profiles show a significantly smaller energy scale, at round a 0.4eV difference when moving the Cu^{2+} from one 6MR window to the next adjacent one in a linear path. This is due to the stabilization of Cu^{2+} in the SIIIa site, which are considered as minima in both SSZ-13 and SAPO-34. The observed SIIIa site in SSZ-13 is a shallow minimum in comparison to that in SAPO-34 which can be considered as a thermodynamic minimum – 0.068eV higher in energy than the profile's global minimum at site SIb.

In order to understand the presence of a minimum at site SIIIa, the changes in configuration around the Cu^{2+} were inspected. Table 16.1 shows the number of bonds and corresponding bond distances for each step in the Cu^{2+} SSZ-13 migration profile.

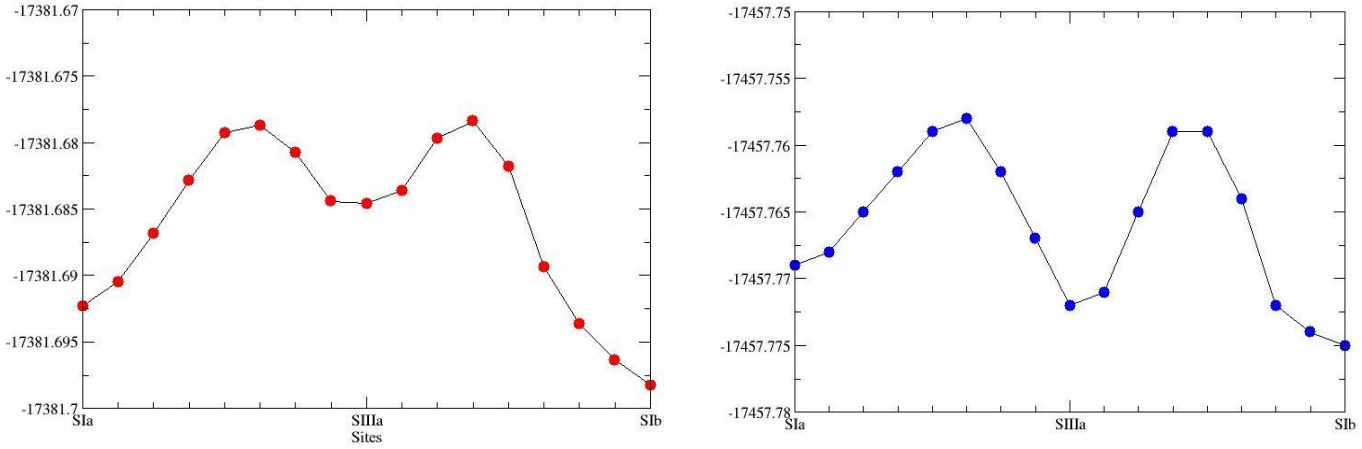

Fig. 28c: Cu^{2+} migration profile in CRYSTAL for SIa→ SIIIa→ SIb for SSZ-13 (**red**) and SAPO-34 (**blue**). The y-axes are energy in Hartree atomic units, au.

Table 16.1

Step	No. of bonds	Bond *a*	Bond *b*	Bond *c*	Bond *d*	Average bond length	Spin magnetic moment on Cu^{2+}
SIa	4	2.0505	1.9088	1.9217**	2.0587**	1.985	0.795844
SIa →SIIIa							
1	4	2.0467	1.9162	1.9170**	2.0716**	1.988	0.801883
2	4	2.0493	1.9278	1.9135**	2.0952**	1.996	0.808278
3	4	2.0551	1.9449	1.9075**	2.1606**	2.017	0.81603
4	3	2.0708	1.9726	1.9459**		1.996	0.825089
5	4	2.1423	2.1553*	2.0206	1.9708**	2.072	0.822404
6	3	2.0958*	2.0797		1.9942**	2.057	0.812523
7	3	2.0541*	2.1552		2.0234**	2.078	0.80409
SIIIa	2	2.0223*			2.0587**	2.041	0.801341
SIIIa → SIb							
1	3	1.9905*		2.1733	2.1064**	2.090	0.805885
2	3	2.1002	1.9656*		2.1631**	2.076	0.819541
3	3	1.9369*	2.0339	2.1268		2.033	0.82415
4	4	1.9156*	2.0268*	2.0218	2.0565	2.005	0.808127
5	4	1.9138*	2.0304*	2.0129	1.9977	1.989	0.791301
6	4	1.9135*	2.0144*	2.0091	1.9776	1.979	0.788391
7	4	1.9155*	2.0048*	2.0076	1.9655	1.973	0.787135
SIb	4	1.9933*	1.9309*	1.9414	2.0187	1.971	0.782875

Table 16.1: Number of bonds to Cu^{2+}, bond lengths and the spin magnetic moment for each step from SIa → SIIIa → SIb in SSZ-13. All bond lengths in angstrom, Å. Each successive step is increased by 0.0143Å increments in the z-direction.

* Cu-O bonds with O adjacent to Al in plane of SIb.

** Cu-O bonds with O adjacent to Al in plane of SIa.

Table 16.2

Step	No. of bonds	Bond *a*	Bond *b*	Bond *c*	Bond *d*	Average bond length	Spin magnetic moment on Cu^{2+}
SIa	4	1.9130*	1.9687*	2.0262	1.9687	1.969	0.7762032
SIa →SIIIa							
1	4	1.9291*	2.0317*	2.0221	1.9269	1.977	0.7873522
2	4	1.9289*	2.043*	2.0162	1.9293	1.979	0.800828
3	4	1.9291*	2.0634*	1.9374	2.0146	1.986	0.8136049
4	4	1.9309*	2.0988*	2.0189	1.9504	2.000	0.8243375
5	4	1.9026*	2.108	2.1642	1.9886	2.041	0.8229428
6	4	1.9281*	2.181	2.0869	2.0285	2.056	0.8098205
7	3	1.9541*		2.0406	2.0752	2.023	0.7991378
SIIIa	3	1.9865*		2.0090**	2.1382	2.045	0.7951692
SIIIa → SIb							
1	2	2.0282*		1.9828**		2.006	0.7985671
2	2	2.0799*		1.9567**		2.018	0.8023181
3	4	2.1526*	2.1297	1.9313**	2.1391	2.088	0.8171617
4	3	2.0515	2.0679	1.9046**		2.008	0.8233657
5	4	2.0288	1.9817	2.0255**	1.9311**	1.992	0.7994564
6	4	1.9993	1.9282	2.0037**	1.9765**	1.977	0.8015904
7	4	1.9815	1.9748	1.9284**	1.9917**	1.9691	0.7773449
SIb	4	1.9793	1.9734	1.9315**	1.9840**	1.967	0.770831

Table 16.2: Number of bonds to Cu^{2+}, bond lengths and the spin magnetic moment for each step from SIa → SIIIa → SIb in SAPO-34. All bond lengths in angstrom, Å. Each successive step is increased by 0.0150Å increments in the z-direction.

* Cu-O bonds with O adjacent to Al in plane of SIa.

** Cu-O bonds with O adjacent to Al in plane of SIb.

In the first four steps of the migration in SSZ-13, the coordination number on Cu^{2+} does not change and stays as a distorted square-planar geometry (Figs. 29a – d). The average Cu-O bond length increased upon each step from 1.984925 to 2.017025Å (Table 16.1), as the Cu^{2+} gradually moves further from the 6MR plane of SIa. Crossing the halfway point between SIa → SIIIa at step 4, we observed a loss in bond coordination to the Cu^{2+} (Fig. 29e). By step 5, a new bond coordinates with O adjacent to Al in the plane of SIb, Fig. 29f. The Cu^{2+} sitting in the enclosure of the D6R (Fig. 30b) can maintain the three bonds including the Cu-O bond d, in the plane of the SIa. In step 6 (Fig. 29g), a coordination from the plane of SIa is loss, but the Cu^{2+} is able to maintain bond *d*, whilst bond *a* decreases in length indicative of increasing bond strength – as expected. Step 7 follows the same pattern, with the coordination to site SIa weakening (including bond *d*) and bond *a* experiencing bond shortening (Fig. 29h). Fig. 29i and Fig. 30d, shows the occupation of Cu^{2+} in the centre of site SIIIa, only two coordination is remaining with bonds *a* and *d* in a diagonal fashion. Following this, is step 1 in SIIIa → SIb, resulting in the addition of a new bond coordination from site SIb (Fig. 29j). The previous three described steps correspond to the minimum showed in Fig. 28c. The location of Cu^{2+} within the vicinity of the centre in D6R for these three steps enables the Cu^{2+} to simultaneously form coordination with the activated O atoms adjacent to the Al atoms in the plane of SIa and SIb (bonds d and a respectively).

Step 2 in SIIIa → SIb has the same configuration as in step 1, but with increased bond *d* length and decreased lengths with coordination to SIb (Fig. 29k). As the Cu^{2+} gradually moves towards the plane of SIb, the remaining coordination with site SIa breaks – shown in Fig. 29l. During step 3, a trigonal planar coordination is formed in plane of site SIb. At step 4, a distorted square-planar geometry is formed with bonds *a* and *b* coordinated to the activated O atom (Fig. 29m). In the subsequent steps, this configuration is stabilized with bond lengths decreasing from step 5 to the final step with Cu^{2+} sitting in the plane of SIb (Figs. 29n – q).

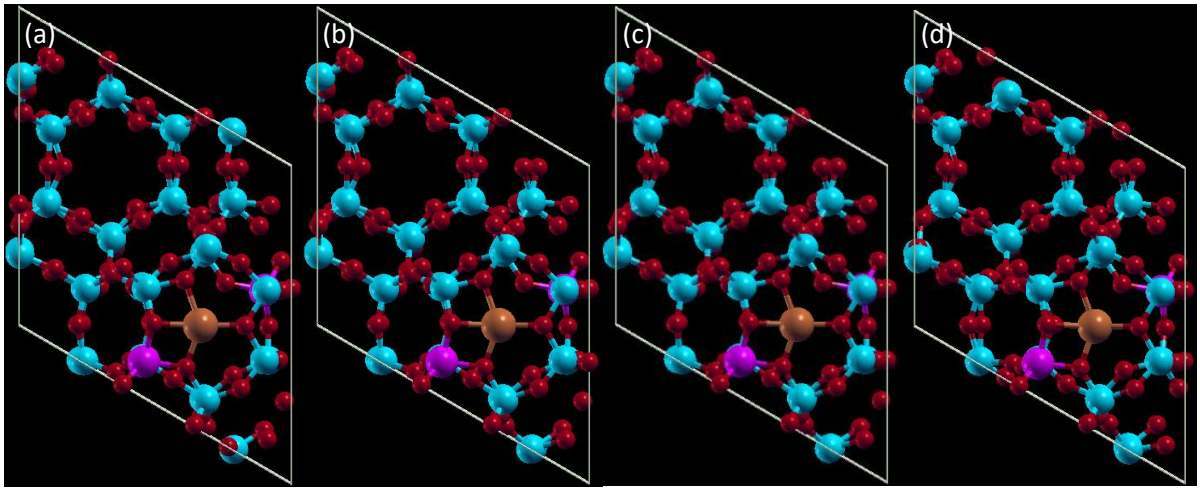

Figs. 29a – d: Top-view images from XCrysDen of the successive steps for Cu^{2+} migration in SSZ-13 for SIa → SIIIa → SIb.

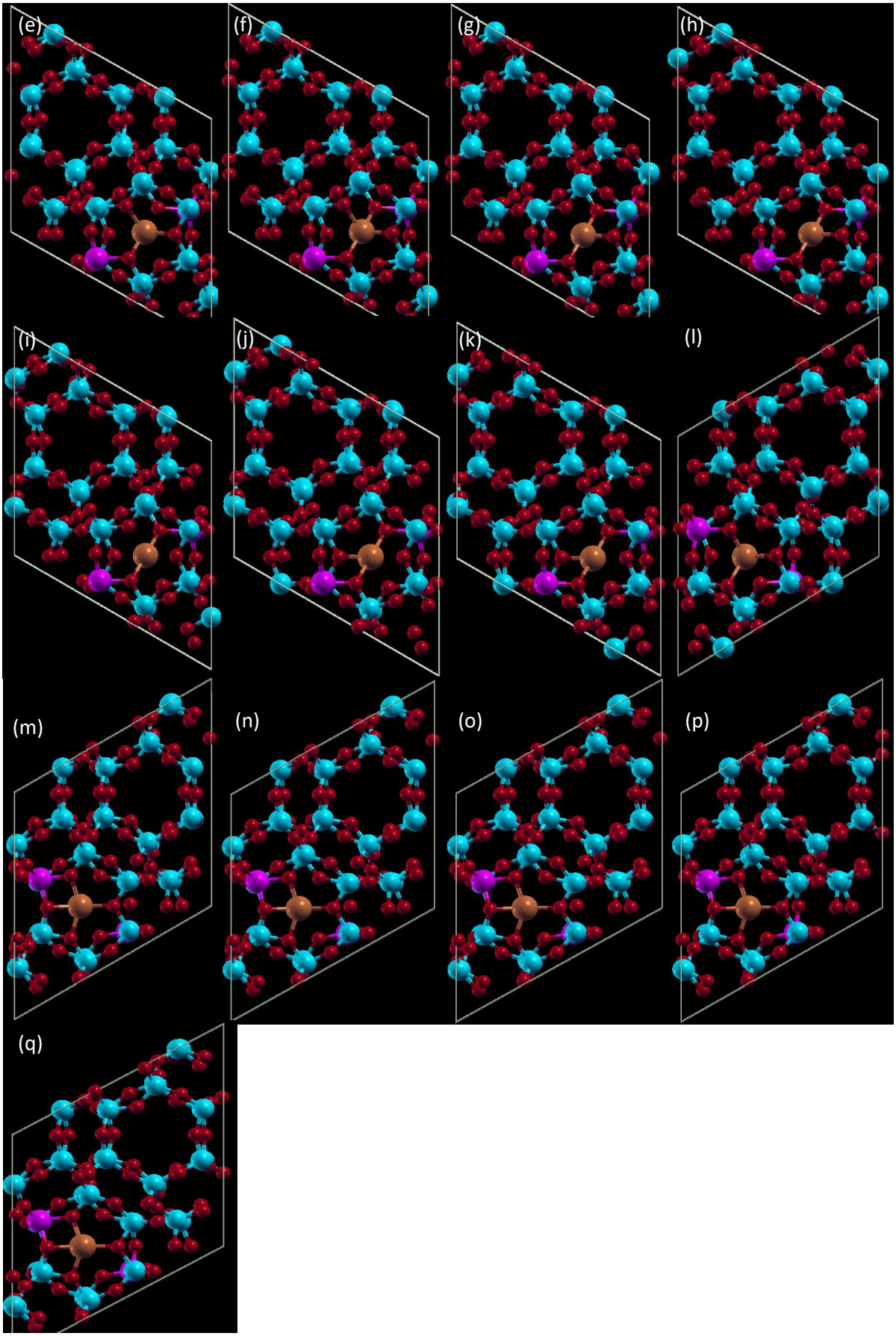

Figs. 29e – q: Top-view images from XCrysDen of the successive steps for Cu^{2+} migration in SSZ-13 for SIa → SIIIa → SIb.

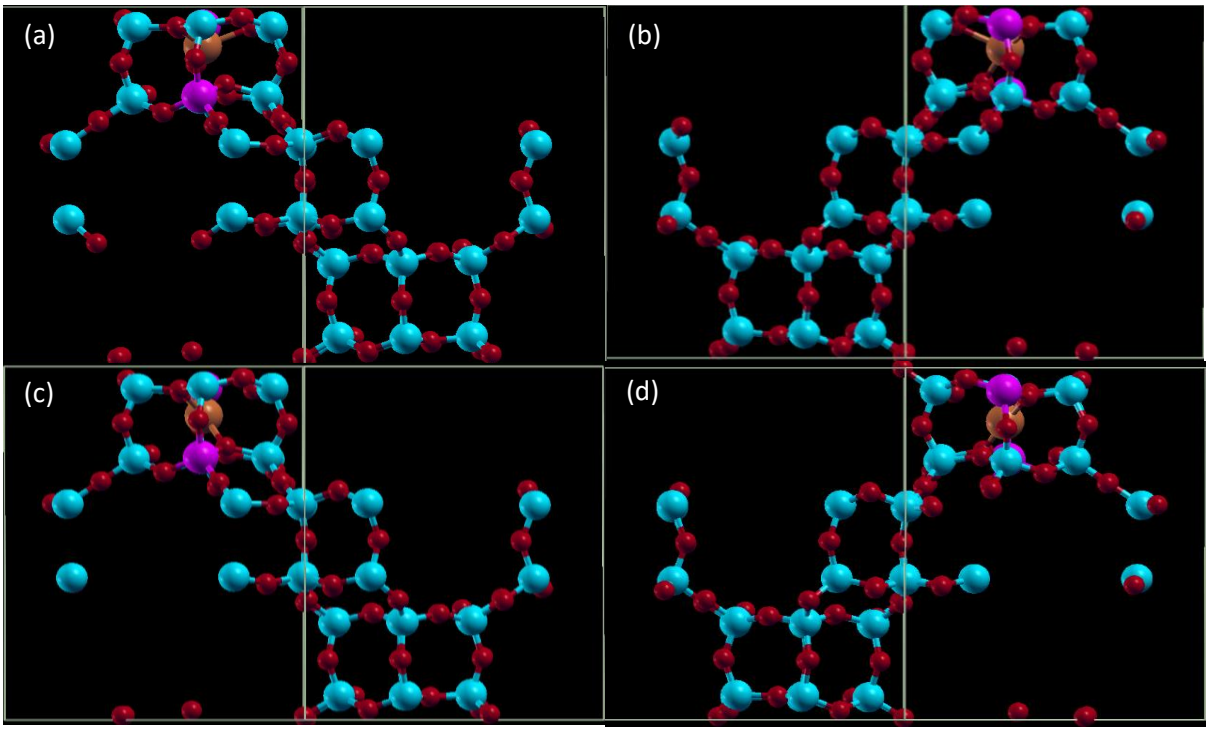

Figs. 30a – d: Side-on-view images built in XCrysDen of the successive steps for Cu^{2+} migration in SSZ-13 from step 4 in SIa → SIIIa to step 7 in SIIIa → SIb.

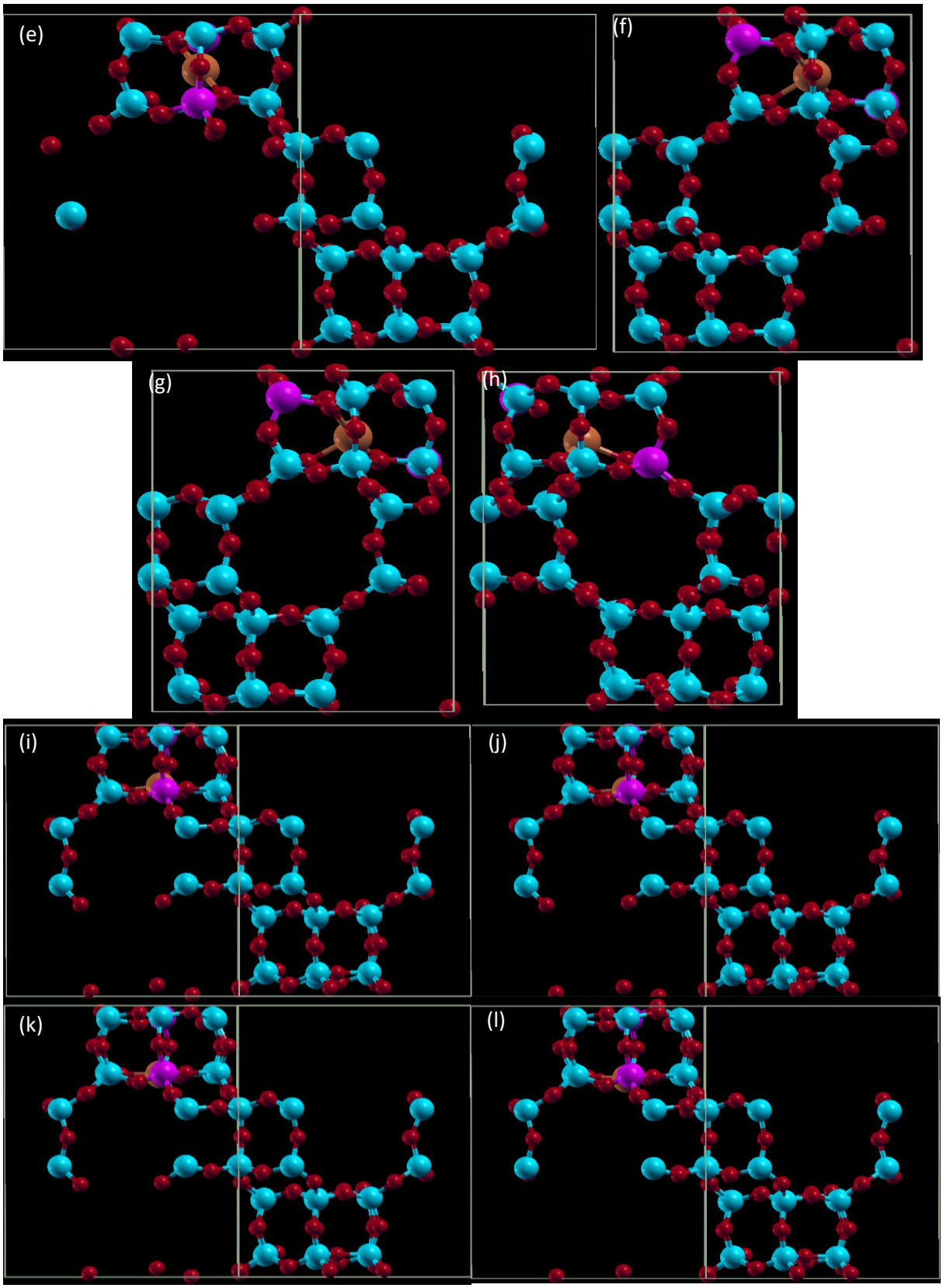

Figs. 30e – l: Side-on-view images built in XCrysDen of the successive steps for Cu^{2+} migration in SSZ-13 from step 4 in SIa → SIIIa to step 7 in SIIIa → SIb.

The SAPO-34 migration's first five steps showed an average increased in bond lengths for coordination towards SIa, in addition to this, a change in bond coordination during step 1, SIa → SIIIa (Figs. 31a – d). By step 5, SIa → SIIIa, the Cu^{2+} sits deep enough in the D6R cavity to form a bond with an activated O atom in the plane of SIb, Fig. 31e. The next two steps gradually shows successive increased in average bond lengths, as the Cu^{2+} moves further away from the plane of site SIa (Figs. 31f – g). Step 7, results in three bond coordination as Cu^{2+} loses one bond attached to plane of SIa (Fig. 31g). In step SIIIa, occupation of the centre of site SIIIa is shown. The average bond length shows a decreased as the two bond coordination to plane of SIb decreases, with the exception of the last remaining bond (bond a) to the plane of SIa which increased to 1.9865Å length.

The next seven steps in SIIIa → SIb shows Cu^{2+} descending into the plane of site SIb (Figs. 31h – l). By step 3, Cu^{2+} is able to form three bonds to the plane of site SIb and in step 4, the remaining bond to plane of SIa is lost. Step 5, shows Cu^{2+} with a distorted square planar geometry as the Cu^{2+} is able to form four coordination within plane of SIb, with all bond lengths less than 2.05Å. In general, the bond lengths gradually shortens as the Cu^{2+} reaches the plane of SIb, as evident with averaged bond lengths. The final structure, Fig. 31n, shows Cu^{2+} inside the plane of SIb with all bond lengths less than 2.00Å, with two of these bonds (c and d) satisfying the activated O atoms adjacent to the Si atom in the 6R plane.

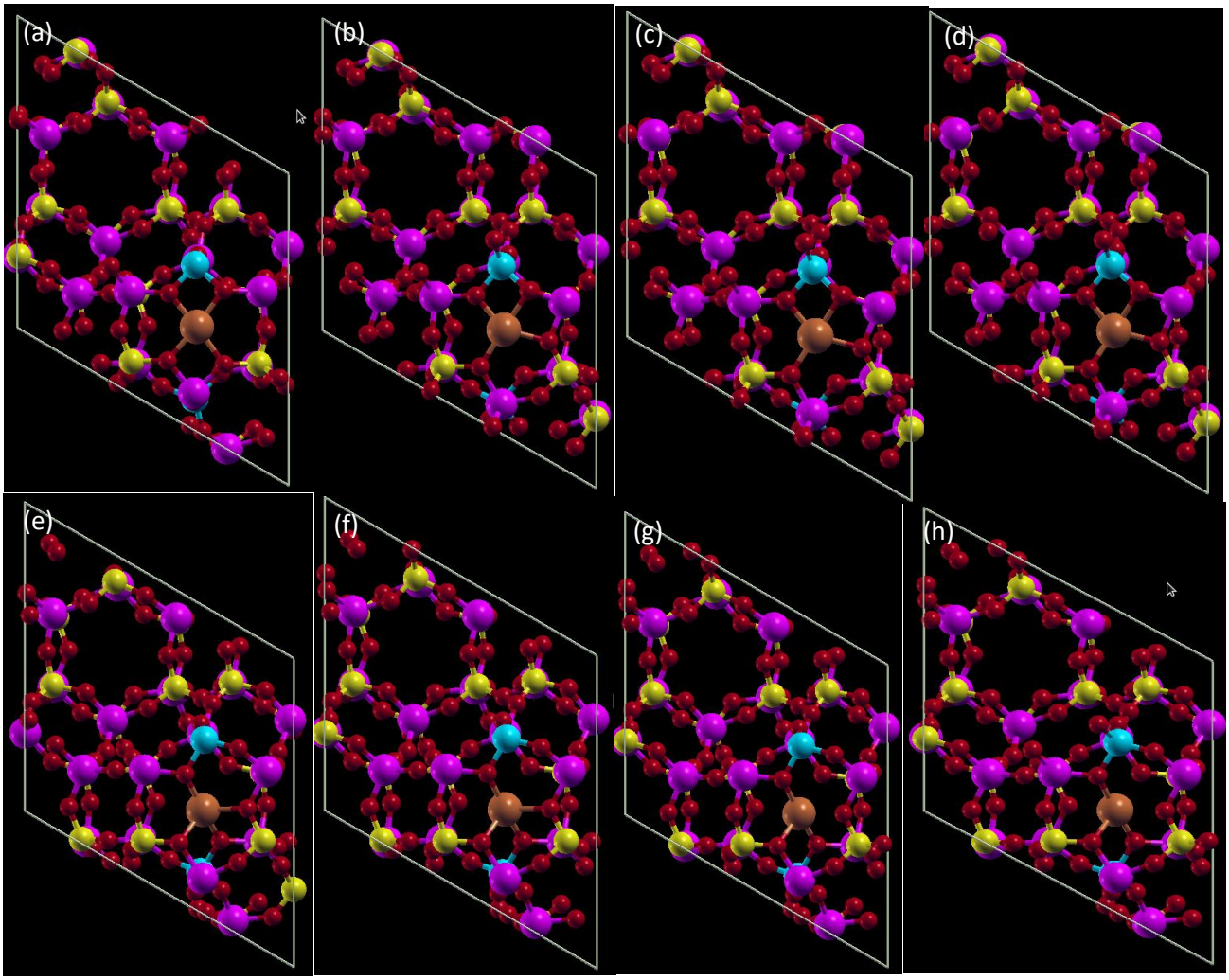

Figs. 31a – l: Top-view images of the successive steps for Cu^{2+} migration in SAPO-34 for SIa → SIIIa → SIb.

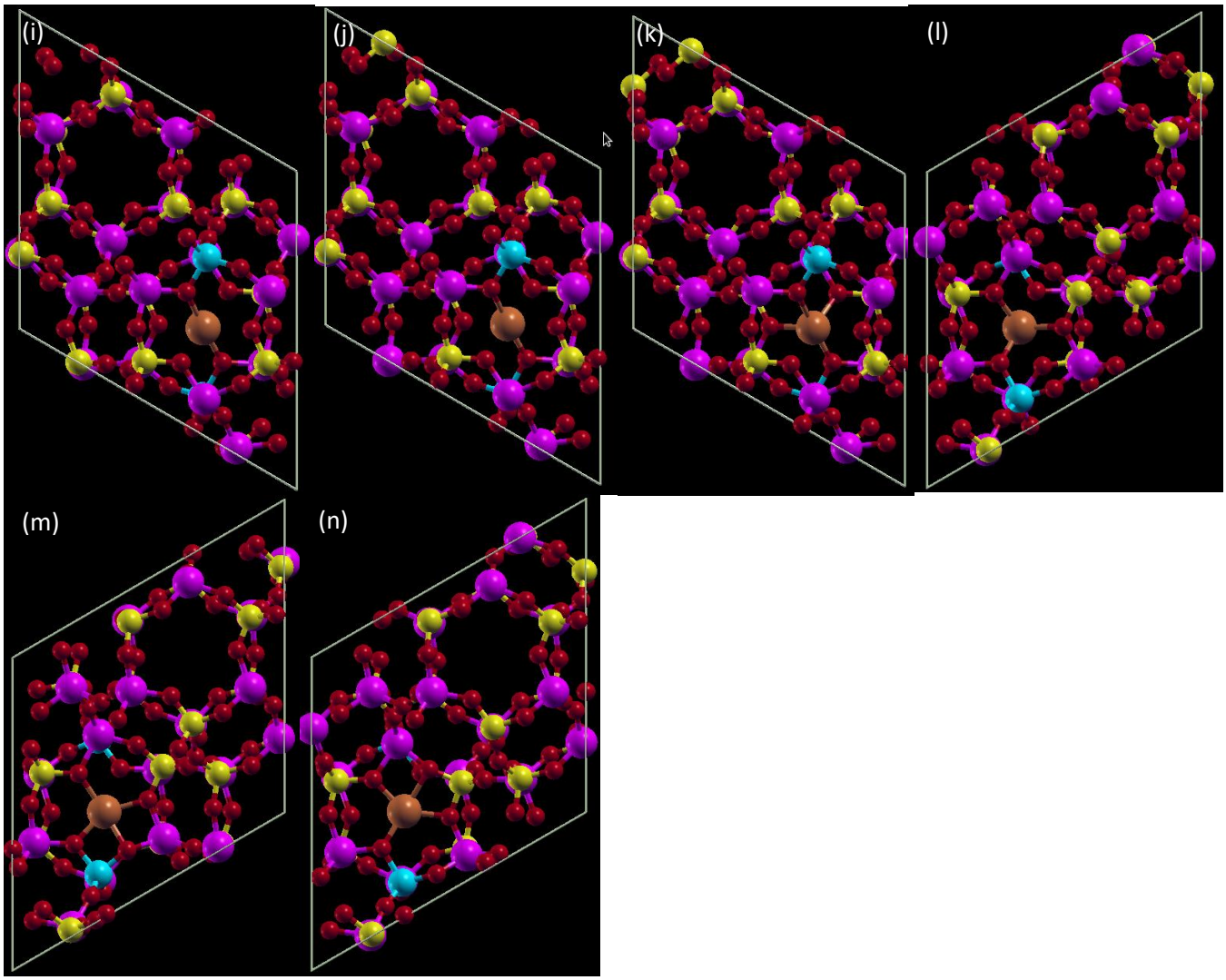

Figs. 31i – n: Top-view images of the successive steps for Cu^{2+} migration in SAPO-34 for SIa → SIIIa → SIb.

Summary 5.2: CRYSTAL calculations

The CRYSTAL calculation were performed with the PBE0 hybrid functional and an additional 10% exact exchange, this is to ensure during the SCF convergence the spin polarization is maintained on Cu^{2+} as a d^9 electronic configuration. The aim of the CRYSTAL calculation was to verify the GULP results, and to observe the effects upon inclusion of the electronic energy such as crystal-field splitting.

In general, for both frameworks the Cu^{2+} in sites SI adopt a slightly distorted square-planar geometry and in sites SIV a trigonal planar is observed. As deduced from the geometries, it is site SI which is overall lowest energy in the system. Since, a square-planar geometry to able to maintain a crystal-field splitting, therefore the crystal-field stabilization energy. For SSZ-13, the relative energy between SI and SIV both with an Al dopant atom inside the site is 0.961eV. However, a Cu^{2+} residing in site SI without a neighbouring Al dopant atom is 1.98eV higher compared to a site SI with an Al dopant atom. This highlights the important influence of dopant configurations with respect to the Cu^{2+} atom inside a framework. Interestingly, this shows that in certain scenarios Cu^{2+} residing in site SIV (with an Al dopant present) is energetically more favoured compared to a site SI (without an Al dopant).

For SAPO-34, a similar observation was observed with near-identical relative energies, see Table 15. Sites SII and SIII like in the GULP calculations were disfavoured sites for Cu^{2+}, in both frameworks site SII failed to achieved SCF convergence. Site SIII resulted in the reduction of Cu^{2+} to Cu^{+} from the background negative charge on the framework localised on the framework oxygen atoms. The discovered site SV from the GULP calculations possessed a high relative energy compared to site SI of 3.13 and 3.69eV for SSZ-13 and SAPO-34 respectively. This indicates site SV is a highly unlikely equilibrium site for Cu^{2+}, however, under operating conditions where the temperatures are high, the Boltzmann energy might make site SV a feasible site especially as an intermediate migration site for Cu^{2+} to hop on and off from.

The GULP migration profiles showed that site SIII is an energetic maximum for both frameworks, however, the CRYSTAL calculations highlighted that site SIII is local minima for certain dopant configurations. This is when the dopant atoms are symmetrically placed on opposite 6MR windows, this enables the maximum number of activated oxygen atoms to coordinate with the Cu^{2+} in an octahedral fashion fostering the crystal-field splitting, see Fig. 28c.

5.3 GULP water calculations

The metal-exchanged zeolite and AlPO catalyst under operating conditions would be working in the presence of exhaust fumes – and the significant part of these combustion gases would consist of N_2, O_2, water vapour and CO_2, accounting for approximately 99.7% of the total fumes in a diesel engine. The remaining 0.3% would be trace elements in the form of NO_x, CO, HCs and particulate matter. The composition of water in an idling diesel engine is found to be around 11%, but this would increase in a running engine.

Subsequently, it is important to consider the effect of water on the atomistic behaviour of the Cu-exchanged zeolite and AlPO, especially considering the hydrothermal stability is one of the key parameters that these catalysts are measured and reported against. In addition, as of writing, no explicit calculations either force-field or quantum mechanical based for the treatment of water in the Cu -SSZ-13 and –SAPO-34 systems have been reported. Or in determining the role water plays in the de-NOx mechanism for the said systems.

GULP calculations were performed for both Cu-SSZ-13 and Cu-SAPO-34. A systematic method was devised to investigate and quantify the effects of: (i) water on Cu(II) in each of the reported extra-framework site, SI, SII, SIII and SIV, (ii) increasing the number of water molecules on each site and (iii) difference in behaviour of water in zeolite and AlPO. The effects of water would be characterised by the adsorption energy and the adsorption geometry before and after water is introduced.

The water pair potentials were taken from the work developed by Lewis *et al*[188], modified from De Leeuw *et al*[189] original work. This was achieved by the authors, by taking the short-range parameters as described by the Buckingham potential between the cations and lattice oxygen ions, then implemented for use in the interactions between cations and water oxygen ions, see Tables 17.1 and 17.2. The core-shell charge for lattice oxygen ions is -2.0 as prior, whilst that for water oxygen ions is -0.8. The core-shell interactions for the water oxygen ions is near three times that for the lattice oxygen ions. This ensures differences in charges between the two types of oxygen ions, thereby the Coulombic forces experienced by the cations would differ.

Table 17.1: Pair potential parameters and charges for water molecules

Species	**Charge/e**	**Core-shell interactions/ eV*Å^{-2}**
H	0.40000	
Ow (core)	1.25000	
Ow (shell)	-2.05000	209.449602
Ion pair	A/eV*Å-2	B/eV*Å-2
Ow-Ow	39344.98	42.15

Ion pair	***A*/eV**	***ρ*/Å**	***C*/eV*Å^6**
H-Ow	396.270	0.25000	10.00000
	***D*/eV**	***a*/Å^{-1}**	***r$_o$*/Å**
H-Ow	6.203713	2.22003	0.92376

	k/eV rad^{-2}	**Θ$_0$/deg**
H-Ow-H	4.19980	108.69

Table 17.2: Parameters to describe interactions between framework and the extra-framework cations and the water molecules

Ion pair	A/eV	ρ/Å	C/eV*Å^6
Si-Ow	1283.907	0.32052	10.66158
Al-Ow	1460.300	0.29912	0.00000
O-Ow	22764.000	0.14900	28.920000

5.3.1 Computational procedure

Water molecules were manually built in the *Materials Studio* software package, then a preliminary geometry optimization was performed on the water molecules with the Universal Force Field (UFF) in *Forcite*. After which, the optimized zeolite and AlPO *GULP* structure calculations were imported into *Materials Studio*.

Optimized water molecules were docked into the desired sites (SI, SII, SIII and SIV), "interacting" with the Cu^{2+}. The initial Cu-O distances are in the range of 1.4 – 2.8Å. The procedure that was followed for obtaining the *GULP* water calculations was to ensure that the primary (Coulombic) effect on the Cu(II) was exerted by the water molecules within the vicinity. Subsequently, the SSZ-13 and SAPO-34 configurations that were modelled did not involve an Al or Si dopant in the occupied extra-framework site. The calculations would enable atomistic observations of how the topologically distinct extra-framework sites affect Cu's interactions with the water molecules.

The numerical parameters that were measured for the water adsorption calculations are relative and adsorption energy. These are calculated as such:

$$(i)\ E_{rel} = E_{Zeol+nH_2O} - E_{nH_2O} \quad \textbf{(49)}$$

$$(ii)\ E_{Ads} = E_{Zeol+nH_2O} - \left(E_{Zeol} + E_{nH_2O}\right) \quad \textbf{(50)}$$

5.3.2 Results

5.3.2.1 Site SI energy

5.3.2.1.1 SAPO-34

As consecutive H_2O molecules are added into the vicinity of site SI, the adsorption energies increased by approximately a magnitude of two, see Table 18. This is expected, since the water calculation increases by approximately 22eV per inclusion of H_2O molecule, see $E_{AlPO+nH_2O}$ values. As a result of the direct proportionality with the number of H_2O molecules, as reflected by the EH_2O values. The adsorption energy per H_2O molecule remains relatively constant between one and three H_2O molecules; -0.50, -0.51 and -0.57eV. Interestingly, the addition of a fourth H_2O molecule results in a -0.86eV averaged contribution per H_2O. This can be explained by observing the structural orientations of the H_2O molecules, Figs. 32(a – j).

Table 18: Energies of the H_2O configurations in site SI of Cu-SAPO-34.

No. of H_2O **molecules**	$E_{AlPO+nH_2O}$	$E_{Cu\text{-}AlPO}$	**Rel. E**	**Ads. E**	**Ads. E per** H_2O **molecule**	**E**H_2O
1	-4764.48	-4742.45	-4742.95	-0.50	-0.50	-21.53
2	-4786.52	"	-4743.46	-1.02	-0.51	-43.06
3	-4808.74	"	-4744.15	-1.71	-0.57	-64.59
4	-4832.01	"	-4745.89	-3.44	-0.86	-86.12

5.3.2.1.2 SSZ-13

Unlike in the SAPO-34 case, the adsorption energy for each successive addition of H_2O molecule does not follow a linear trend, see Table 19. As the number of H_2O molecules increases the adsorption energy changes inconsistently. As a result, the constancy in adsorption energy per H_2O molecule observed in the SAPO-34 is not evident in the SSZ-13 calculations. The absolute energies of each calculation, $E_{Zeol+nH_2O}$ increases inconsistently; increasing by approximately -25, then -20, and finally -27eV. Considering, the energy of a discrete H_2O molecule is -21.53eV, this indicates other factors are affecting and skewing the energy profile of the H_2O calculations. Similar to SAPO-34, inspection of the H_2O molecules configurations relative to the SSZ-13 framework would give an insight into the energetic behaviour observed here. See Figs. 33(a – j).

Table 19: Energies of the H_2O configurations in site SI of Cu-SSZ-13.

No. of H_2O **molecules**	$E_{Zeol+nH_2O}$	$E_{Cu\text{-}Zeol}$	**Rel. E**	**Ads. E**	**Ads. E per** H_2O **molecule**	**E**H_2O
1	-4589.42	-4566.91	-4567.89	-0.98	-0.98	-21.53
2	-4614.30	"	-4571.23	-4.33	-2.16	-43.06
3	-4633.93	"	-4569.34	-2.43	-0.81	-64.59
4	-4661.02	"	-4574.90	-7.99	-2.00	-86.12

5.3.2.2 Site SI configuration

5.3.2.2.1 SAPO-34

The addition of discrete H_2O molecules in close proximity with the Cu(II)-SI site does not definitively result in H_2O coordination with the Cu. Instead, for the calculations with 1 and 2 H_2O molecules, the H_2O molecules coordinated with the AlPO framework in the large cage forming hydrogen bonds within distances of 1.66 – 2.46Å, see Figs. 32(c – f). Cu coordination with the framework oxygen atoms in the SI site does change after inclusion of H_2O molecules. The Cu bond distances with the framework oxygen atoms shows an averaged increased of the Cu-O bond lengths after inclusion of the H_2O molecules, see Table 21. Indicating the weakening of the Cu to framework oxygen atoms due to the presence of surrounding H_2O molecules, despite the lack of strong Cu-OH_2 interactions, as 60% of the H_2O coordination were between 3.18 – 5.07Å. In our analysis, Cu-OH_2 distances within a 3.00Å is defined as a Cu-OH_2 coordination present.

The calculations with equilibrium configurations that meets the criteria for Cu-OH_2 coordination are the three and four H_2O molecules calculations as observed in Figs. 31(i – j). In the calculation with three H_2O molecules, a H_2O coordination to Cu(II) was observed with coordination distance of 2.63 and 2.95Å. Four H_2O molecules calculation has two individual Cu-OH_2 coordination at 2.46 and 2.78Å, see Table 22. Taking bond lengths as indication of bond strengths, this implies a relatively weak Cu-OH_2 coordination especially compared to the hydrogen bond lengths with framework oxygen atoms and between H_2O molecules. As a result, the contribution of the Cu-OH_2 coordination to the overall energy would be minor.

In Table 18, the adsorption energy increases from -0.50 to -1.02eV as the number of H_2O molecules in the SAPO-34 increased from one to two. This is expected, since the calculation with one H_2O molecule present involves an equilibrium configuration where the H_2O detaches away from the Cu(II) and forms hydrogen bonds inside an 8MR in the large cage. Similarly, the two H_2O molecules calculation has a near-identical equilibrium structure with respect to the H_2O molecular orientations, with both H_2O molecules sitting in separate 8MRs. See Figs. 31(c – f). In both calculations, the hydrogen bonds formed with the framework oxygen atoms are within the same range of 1.66 – 1.99Å. Considering both calculations has H_2O molecules interacting in the same fashion with 8MRs in the large cage, but the second calculation has twice the number of H_2O molecules this would be reflected in the adsorption energy with a simple linear proportionality relationship as: 2(-0.50eV) = -1.00eV which is in good agreement with the actual adsorption energy.

As the number of H_2O molecules increases from two to three, the adsorption energy increased by -0.69eV. This is -0.19eV more than expected, however, this is because upon inspection of Figs. 31(g – h), the H_2O molecular orientations is different to the previous two calculations. In the three H_2O molecules calculation, all three H_2O molecules are not sitting inside the surrounding framework of the large cage. One H_2O molecules sits outside an 8MR forming one hydrogen bond to framework oxygen atom at 2.03Å. The second H_2O is situated adjacent to a 4MR forming a single hydrogen bond at 1.97Å and Cu coordination at 2.95Å. The lack of hydrogen bonds to the framework is compensated by weak hydrogen bonding with each other at 2.30Å. The third H_2O sits off-centre in the large cage without any hydrogen bonds to the framework oxygen atoms, but with weak coordination to the Cu(II) of bond distance of 2.63Å, see Table 22. Compared to the prior calculation with two H_2O molecules, all three H_2O molecules interacts more weakly with the SAPO-34 framework.

In order to quantify the effect of hydrogen bonding between H_2O molecules has on the overall energy of our calculations, a numerical approach was used, see Fig. 32. An individual H_2O molecule in vacuum was optimized and compared with a calculation consisting of two H_2O molecules in vacuum, but in close proximity, enabling hydrogen bonds to be formed. By doubling the equilibrium energy of an individual H_2O molecule in vacuum, the difference in energy with the calculated equilibrium structure of two H_2O would provide a solution of the hydrogen bonding energy between H_2O molecules. The derived energy provided from two H_2O molecules hydrogen bonded to each other is -2.51eV, with hydrogen bonding at 1.28Å, see Table 20.

The hydrogen bonding between H_2O molecules provides a very large energy contribution, however, this is not observed in the calculations with one to three H_2O molecules present. In both one and two H_2O molecules calculations, no H_2O-H_2O interactions were present, whilst in the three H_2O molecules calculation, a weak H_2O-H_2O interaction is observed with hydrogen bond lengths of 2.30 and not 1.28Å. Thus, only a fraction of the -2.51eV energy would contribute to the adsorption energy for the three H_2O molecules calculation. Therefore, considering only two of the three H_2O molecules are adsorbed on the framework and weakly coordinated to Cu(II) an adsorption energy of: 3(-0.5eV) = -1.5eV is deduced, not including the energetic contribution from a weak H_2O-H_2O interaction. The actual adsorption energy is -1.71eV with a -0.21eV difference compared to the deduced value, which can reasonably attribute to the energy provided from the weak H_2O-H_2O interaction and Cu coordination. Subsequently, the adsorption energy can be deciphered and partitioned into the number of H_2O molecules, interaction with the framework and the presence of H_2O-H_2O bonding.

For the four H_2O molecules calculation, a significantly large adsorption energy is observed at -3.44eV, see Table 18. Looking at Figs. 31(i – j), only one H_2O molecule is interacting with the SAPO-34 framework via a single hydrogen bond adjacent to a 4MR at 2.08Å. The other three H_2O molecules are interacting with each other, however, with differing strengths. Two of which are adsorbed onto the Cu(II) with a coordination distance of 2.46 and 2.78Å, see Table 22, and forms a hydrogen bond with the third H_2O at 2.06Å and with each other at 1.30Å. In total, three of the four H_2O molecules are either adsorbed onto the SAPO-34 framework or the Cu(II). Considering the one strong H_2O-H_2O interaction present, an adsorption energy of: 2(-0.50eV) + (-2.51eV) = -3.51eV. This gives a -0.07eV difference with the observed value. Due to the lack of interactions with the framework and the weak Cu-OH_2 coordination, the strong hydrogen bonding between two of the water molecules accounts for approximately 73% of the adsorption energy.

This seems to indicate the adsorption energy in the water calculations for site SI are dictated by the number of H_2O-H_2O interactions present, and more importantly the strength of these hydrogen bonds.

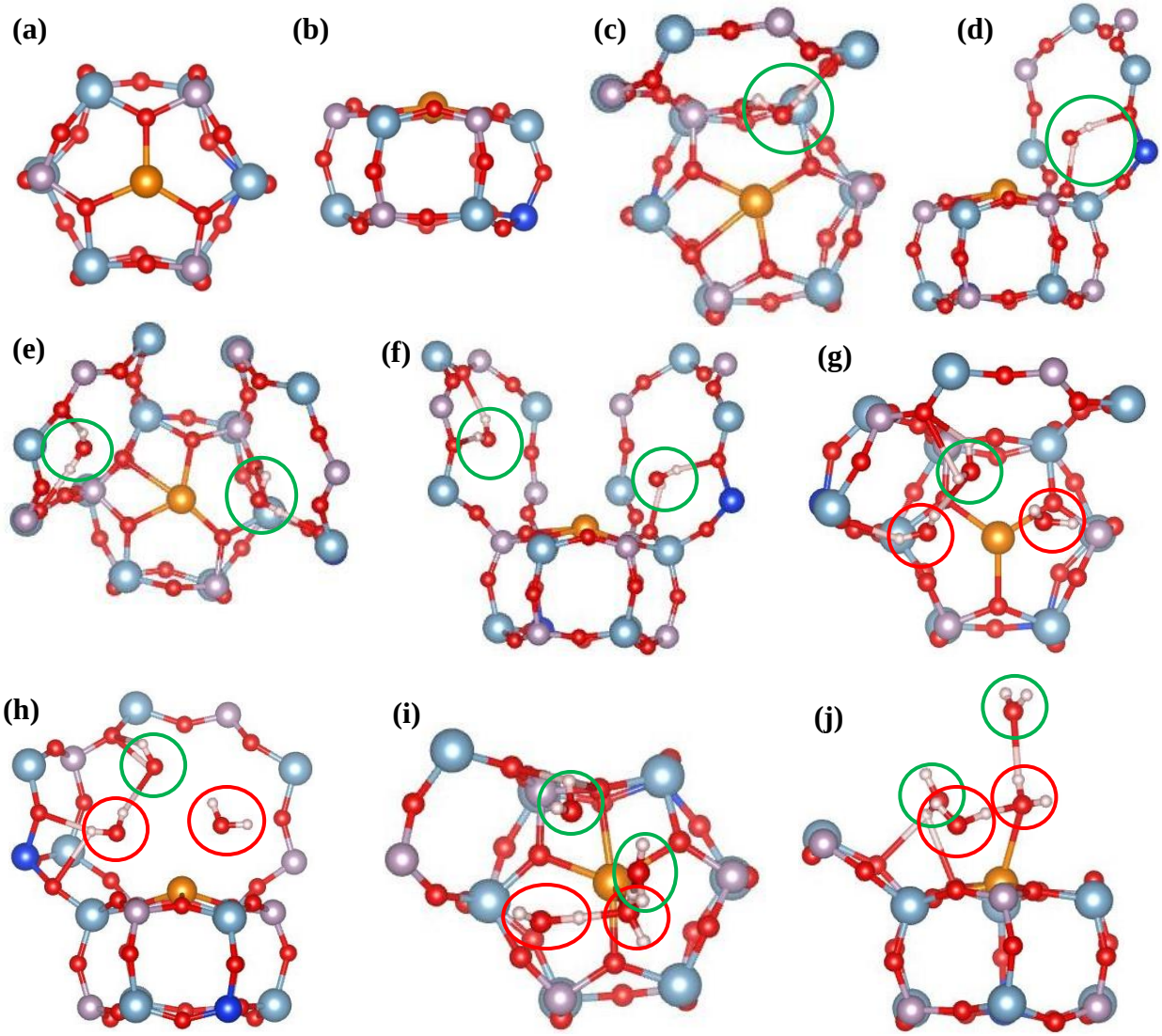

Figs. 31(a – j): **(a – b)**, Optimized structure of Cu(II) in site SI before inclusion of H_2O molecules, top and side views of; **(c – d)**, one H_2O molecule after *GULP* optimization when docked within the vicinity of Cu in site SI, **(e –f)**, with two H_2O molecules, **(g – h)**, with three H_2O molecules, **(i – j)**, with four H_2O molecules. Circled red and green are the H_2O molecules coordinated and not to Cu(II) respectively. All bond lengths within 2.50Å

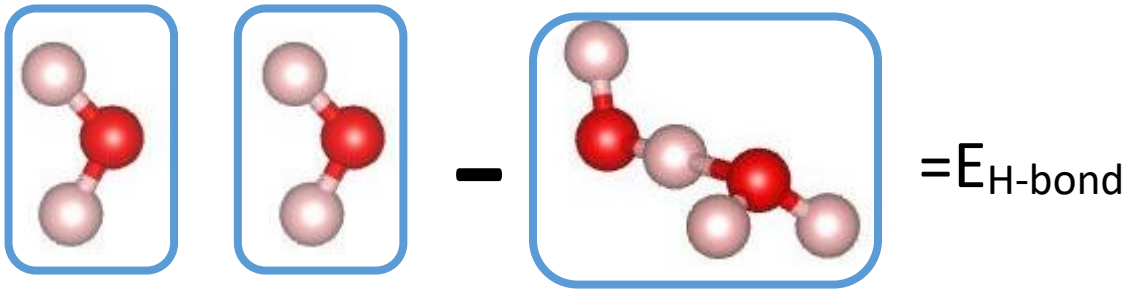

Fig. 32: Schematic of the numerical approach to derive the energy provided by hydrogen bonding from a single H_2O-H_2O interaction, $E_{H\text{-}bond}$.

Table 20: Difference in energy attributed to hydrogen bonding between two H_2O molecules.

Type of H_2O calculation	**Energy**	**Difference**
Individual	-43.06	-2.51
Pair	-45.57	

Table 21: List of Cu-O bond distances before and after for each water calculation in SAPO-34.

No. of H_2O molecules	**Before**					**After**				
	Cu-O1	Cu-O2	Cu-O3	Cu-O4	Average	Cu-O1	Cu-O2	Cu-O3	Cu-O4	Average
1	2.0229	1.9666	2.0498	N/A	2.0131	2.0532	2.4768	2.0961	1.9794	2.1514
2	"	"	"	"	"	2.0500	2.4577	2.1090	1.9906	2.1518
3	"	"	"	"	"	2.0645	N/A	2.1276	2.0396	2.0772
4	"	"	"	"	"	2.0503	2.4287	2.0519	2.0850	2.1540

Table 22: H_2O coordination to Cu(II) in SI and corresponding bond distance in SAPO-34.

No. of H_2O molecules	**H_2O coordination**	**Cu-O1H_2**	**Cu-O2H_2**	**Cu-O3H_2**	**Cu-O4H_2**
1	No	3.20	N/A	N/A	N/A
2	No	3.18	4.96	N/A	N/A
3	Yes	2.63	2.95	4.75	N/A
4	Yes	2.46	2.78	3.23	5.07

5.3.2.2.2 SSZ-13

The four H_2O molecules calculations have two H_2O molecules weakly adsorbed onto the Cu(II), see Table 23 and as observed in SAPO-34, the H_2O molecules forms hydrogen bonds with the framework. These hydrogen bonds are attached to the 4MR and 8MR rings within a range of 1.44 – 1.91Å, indicating very strong interactions with the zeolitic framework. Compared to SAPO-34, the H_2O molecules in SSZ-13 favours forming stronger hydrogen bonds with the framework. Studying Figs. 33(c – d), a one H_2O molecule calculation has the H_2O adsorbed to the 4MR forming two hydrogen bonds at lengths of 1.59 and 1.84Å. This corresponds to an adsorption energy of -0.98eV, see Table 19.

The two H_2O molecules calculation has both H_2O molecules fitted just out of the plane of an 8MR, forming three strong hydrogen bonds at 1.84, 1.80 and 1.62Å with the framework oxygen atoms, see Figs. 33(e – f). In addition, H_2O-H_2O interaction is present due to the close proximity of the H_2O molecules. The hydrogen bond lengths from this interaction is at 1.14Å indicating a very strong H_2O-H_2O interaction. The nearest H_2O molecule to the Cu has a shorter coordination distance of 2.55Å, compared to 3.21Å in the one H_2O molecule calculation. Since the adsorption energy of a single H_2O molecule calculation is -0.98eV, a two H_2O molecule calculation with both molecules adsorbed onto the framework would be twice of this at -1.96eV. Including the strong H_2O-H_2O interaction observed which according to the described numerical approach (Fig. 32 and Table 20), this would contribute an additional -2.51eV – giving an approximate adsorption energy of: 2(-0.98eV) + (-2.51eV) = -4.47eV. This is in good agreement with the calculated adsorption energy of -4.33eV in Table 19.

A three H_2O molecules calculations has two H_2O molecules sharing the same 8MR and the other in an adjacent 8MR, see Figs. 33(g – h). Strong interactions with the framework are observed with hydrogen bond lengths of 1.64, 1.91, 1.73 and 1.66Å. A weak H_2O-H_2O interaction is present between two of the H_2O molecules occupying the same 8MR with a hydrogen bond distance of 2.17Å. Cu coordination was observed for two of the H_2O molecules at 2.85 and 2.87Å. Despite the weak H_2O-H_2O interaction, an adsorption energy of: 3(-0.98eV) = -2.94eV is expected, which would be smaller than the two H_2O molecules calculation. An adsorption energy of -2.43eV was obtained, see Table 19, which is smaller than expected. The relative energy for the three H_2O molecules calculation was -4569eV which is smaller than for the two H_2O molecules calculation by 6eV. This indicates that the H_2O configurations within the framework is less favoured compared to that in the two H_2O molecular calculation.

A possible explanation is the effect of nearby Al dopant atoms in the large cage. In the one and two H_2O molecules calculation, one of the H_2O molecule is coordinated to two of the oxygen atoms adjacent to the dopant Al in the 8MR, see Figs. 33(c – f), but in the three H_2O molecules calculation only one of the activated oxygen atom is coordinated to a H_2O molecule. This will have a significant effect on the overall energy of the system as evident by looking at the relative and the adsorption energies. This gives an added dimension in determining the energies of water calculations, since in addition to the strength of H_2O-H_2O interactions, the influence of nearby dopant atoms have to be considered.

The equilibrium structure of four H_2O molecules calculation has similar H_2O configurations to that of the three H_2O molecules calculation with weak coordination to the Cu from two of the H_2O molecules, see Figs. 33(i – j). A H_2O molecule is adsorbed onto an 8MR with hydrogen bond lengths of 1.89Å. The other three H_2O molecules are interacting with each other, with hydrogen bond distances of 1.20 and 1.15Å. However, only two of these H_2O molecules are adsorbed onto an adjacent 8MR with bond distances of 1.59, 1.65 and 1.75Å, coordinated to both of the activated oxygen atoms (nearby Al dopant). The fourth H_2O molecule acts as a bridge between the two H_2O molecules sharing the same 8MR. On the

whole, three of the four H_2O molecules are adsorbed onto the framework, including two strong H_2O-H_2O interactions – an expected adsorption energy of: 3(-0.98eV) + 2(-2.51eV) = -7.96eV. The observed adsorption energy was -7.99eV which is in good agreement with the deduced value by inspection of the H_2O configurations.

Like in SAPO-34, the Cu-O bond distances increases upon inclusion of H_2O molecules. In general, the averaged Cu-O bond lengths is larger as the number of H_2O molecules added into the SSZ-13 increases, see Table 23. This is expected since a direct H_2O coordination to the Cu in the SI could weaken the Cu-O bonds, however the Cu-OH_2 bond distances in these calculations are long within the range of 2.55 – 5.31Å. Despite the weak H_2O coordination, the negative dipole on the H_2O molecules manages a pull on the Cu, and becomes greater with collective H_2O molecules in the surrounding environment.

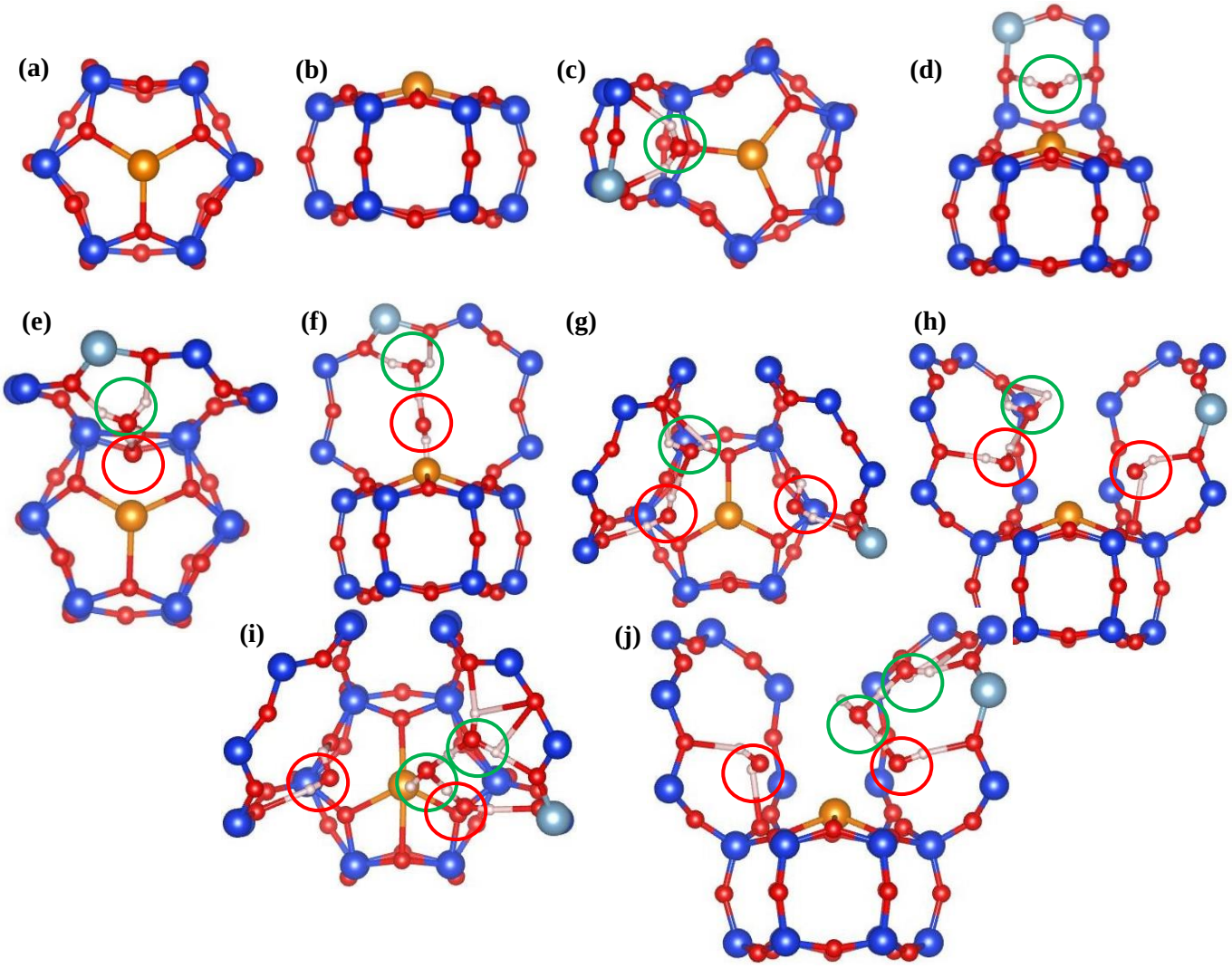

Figs. 33(a – j): **(a – b)**, Optimized structure of Cu(II) in site SI before inclusion of H_2O molecules, top and side views of; **(c – d)**, one H_2O molecule after *GULP* optimization when docked within the vicinity of Cu in site SI, **(e –f)**, with two H_2O molecules, **(g – h)**, with three H_2O molecules, **(i – j)**, with four H_2O molecules. Circled red and green are the H_2O molecules coordinated and not to Cu(II) respectively as defined in the text.

Table 23: List of Cu-O bond distances before and after for each water calculation in SSZ-13.

No. of H_2O molecules	**Before**					**After**				
	Cu-O1	Cu-O2	Cu-O3	Cu-O4	Average	Cu-O1	Cu-O2	Cu-O3	Cu-O4	Average
1	2.1496	2.1512	2.0985	N/A	2.1331	2.2081	2.2017	2.0644	N/A	2.1581
2	"	"	"	"	"	2.1874	2.3065	2.1070	N/A	2.2003
3	"	"	"	"	"	2.1849	2.2531	2.1527	N/A	2.1969
4	"	"	"	"	"	2.2413	2.2529	2.1367	2.4700	2.3181

Table 24: H_2O coordination to Cu(II) in SI and corresponding bond distance in SSZ-13.

No. of H_2O molecules	**H_2O coordination**	**Cu-O1H_2**	**Cu-O2H_2**	**Cu-O3H_2**	**Cu-O4H_2**
1	No	3.21	N/A	N/A	N/A
2	Yes	2.55	4.72	N/A	N/A
3	Yes	2.85	2.87	4.52	N/A
4	Yes	2.65	2.89	3.28	5.31

5.3.2.3 Site SII energy

5.3.2.3.1 SAPO-34

In our results from investigating the favoured extra-framework sites of Cu(II) in both SSZ-13 and SAPO-34, it was observed that sites SII in the centre of the large cage is an energetically unfavourable location. The Cu(II) would migrate away from SII into the adjacent 8MRs (SIVs) in the framework of the large cage. A key understanding to be gained from these set of water calculations is whether the H_2O molecules would stabilize the Cu(II) in the large cage by providing coordination. However, as observed in Figs. 34(a – j) the Cu(II) migrates away from site SII despite the presence of H_2O within a coordinative distance. The number of H_2O molecules successfully investigated was two. This is because, the Hessian matrices were poorly built when performing these water calculations, in combination with the sensitivity of the calculations to the initial coordinates of the Cu and H_2O molecules.

These sub-set of water calculations are dynamic because, the Cu(II) and H_2O molecules would migrate into the framework of the large cage. Due to the presence of the dopant atoms in the large cage and the different SBUs present – the final location of the Cu(II) differed between the water calculations in terms of topology and energy.

The energies for site SII calculations are shown in Table 25. The $E_{Cu\text{-}AlPO}$ calculated are specific to the final location of the Cu(II) in each of the H_2O calculations. In addition, the "Before" Cu-O bond distances in Tables 27 and 19 are taken from reference calculations where the Cu location is in the same sites as observed in the "After" water calculations, but without the presence of H_2O molecules. The adsorption energy of a one H_2O molecule calculation is -0.03eV, significantly smaller than a two H_2O molecules calculation with an

adsorption energy of -1.09eV. Considering the ECu-AlPO in the two H_2O molecules calculation is only -0.09eV lowered in energy compared to that in the one H_2O molecule calculation, this indicates other factors must be affecting the adsorption energy. The presence of a Cu-OH_2 coordination for the two H_2O molecules could be a significant contribution, see Table 28. Despite the difference in adsorption energies, the relative energies are very similar, this is because the Cu(II) equilibrium configuration are near-identical in both cases with the Cu(II) sitting inside a 8MR framework and coordinated to two of the activated oxygen atoms adjacent to an Si atom, see Figs. 34(c – d) and Figs. 35(c – d).

Table 25: Energies of the H_2O configurations in site SII of Cu-SAPO-34.

No. of H_2O molecules	**$E_{AlPO+nH_2O}$**	**$E_{Cu\text{-}AlPO}$**	**Rel. E**	**Ads. E**	**Ads. E per H_2O molecule**	**EH_2O**
1	-4763.80	-4742.24	-4742.27	-0.03	-0.03	-21.53
2	-4786.48	-4742.33	-4743.42	-1.09	-0.54	-43.06

5.3.2.3.2 SSZ-13

The adsorption energy for the one H_2O molecule calculation is -0.79eV, see Table 26, considering the absence of a H_2O-H_2O interaction in the two H_2O molecules calculation and similar Cu-OH_2 distances, see Table 30 – the adsorption energy is expected to be: 2(-0.79) = -1.58eV. The actual value is -1.36eV; a 0.22eV higher in energy. This implies another factor is in effect, looking at Figs. 36(c – d) and Figs. 37(c – d) no H_2O-H_2O interaction is present for the two H_2O molecule calculation, but the equilibrium location for Cu(II) in both the calculations differed. The one H_2O molecule calculation has Cu(II) in the 6MR, but two H_2O molecules calculation is found with Cu(II) sitting in an 8MR. Prior investigation for the preferred site of Cu(II) found on average site SI are 1.0eV lowered in energy compared to sites SIV.

For this specific dopant configuration, the difference in energy between sites SI and SIV is found to be 0.49eV, see $E_{Cu\text{-}Zeol}$ in Table 26. In both one and two H_2O molecules calculations, a weak Cu-OH_2 coordination can be observed, see Figs. 36(c – d), Figs. 37(c – d) and Table 30. But in the two H_2O molecules calculation, only one of the H_2O is at close proximity to the Cu(II) to coordinate. The original deduction is based on the one H_2O molecule calculation where all the H_2O molecules present forms a (weak) coordination to the Cu(II). Since the two H_2O molecules calculation only has half the H_2O molecules present coordinated to Cu(II), this and the different Cu locations could compensate for the additional -0.22eV difference in adsorption energy between the observed and expected.

Table 26: Energies of the H_2O configurations in site SII of Cu-SSZ-13.

No. of H_2O molecules	$E_{Zeol+nH_2O}$	$E_{Cu\text{-}Zeol}$	Rel. E	Ads. E	Ads. E per H_2O molecule	EH_2O
1	-4590.14	-4567.83	-4568.61	-0.79	-0.79	-21.53
2	-4611.76	-4567.34	-4568.70	-1.36	-0.68	-43.06

5.3.2.4 Site SII configuration

5.3.2.4.1 SAPO-34

The Cu-O bond distances before and after the inclusion of H_2O molecules resulted in an averaged shortening of the bond lengths. This is interesting, since it is expected the presence of a H_2O coordination would weaken the Cu(II)'s bond to the SAPO-34 framework, however as observed with the two H_2O molecules calculation a H_2O coordination resulted in a more significant shortening of the Cu-O bonds from 2.15 to 1.90Å, see Table 27.

Subsequently, this implies the H_2O coordination to the Cu(II) is weak compared to the Cu-O framework bonds as evident with a bond length of 2.47Å compared to an averaged of 1.90Å. In order to understand the difference in adsorption energies between the two calculations, in two H_2O molecule calculations, the equilibrium structure found had one H_2O molecule coordinated to the Cu and the second H_2O adsorbed onto the framework of an 8MR with hydrogen bond lengths of 1.72 and 1.70Å, indicating a strong adsorption, see Figs. 35(c – d).

However, for the one H_2O molecule calculation, the H_2O molecule does not adsorbed onto Cu or the framework of the large cage indeed the nearest framework oxygen atom for hydrogen bonding is at 3.40Å away. See Figs. 34(c – d). This explains the minor adsorption energy we observed in Table 25, in contrast with the two H_2O molecules calculation. For the latter, the H_2O molecules are able to coordinate to the Cu and the framework providing the stabilization energy resulting in a -1.09eV adsorption energy.

Figs. 34(a – d) and Figs. 35(a – d) shows the before and after locations of the H_2O molecules and Cu(II) upon performing geometry optimizations. The H_2O molecules are shown initially coordinated to the Cu(II), circled red in Figs. 34(a – b) and Figs. 35(a – b). Despite the coordination of the H_2O molecules in the centre of the large cage, the Cu(II) is favoured in the surrounding 8MR framework with energetic stabilizations provided from the AlPO interactions, see Figs. 34(c – d) and Figs. 35(c – d). In both cases, the Cu(II) equilibrium forms three Cu-O bonds (Table 27), but the two H_2O molecules calculation has one of the Cu-O bond replaced with a H_2O coordination.

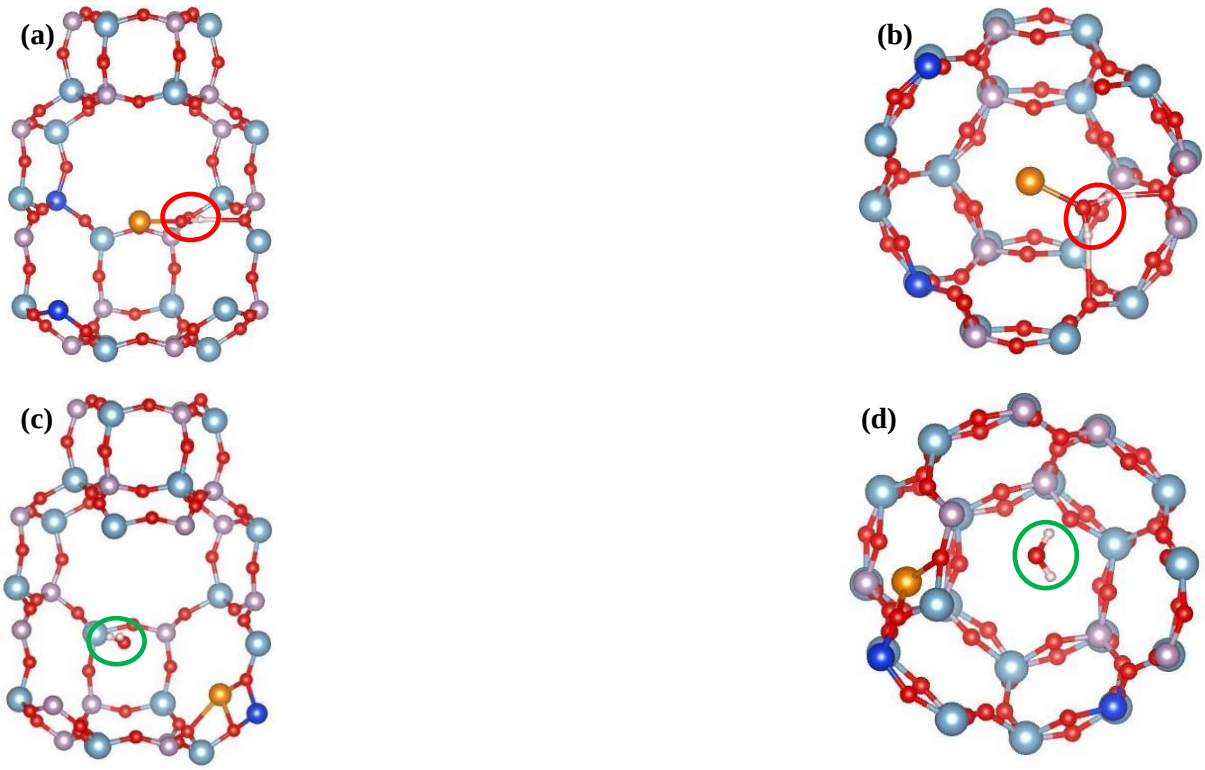

Figs. 34(a – d): (110) and (001) views of; **(a – b)** the initial positions of Cu(II) and a H_2O molecule inside the large cage, **(c – d)** the final equilibrium positions.

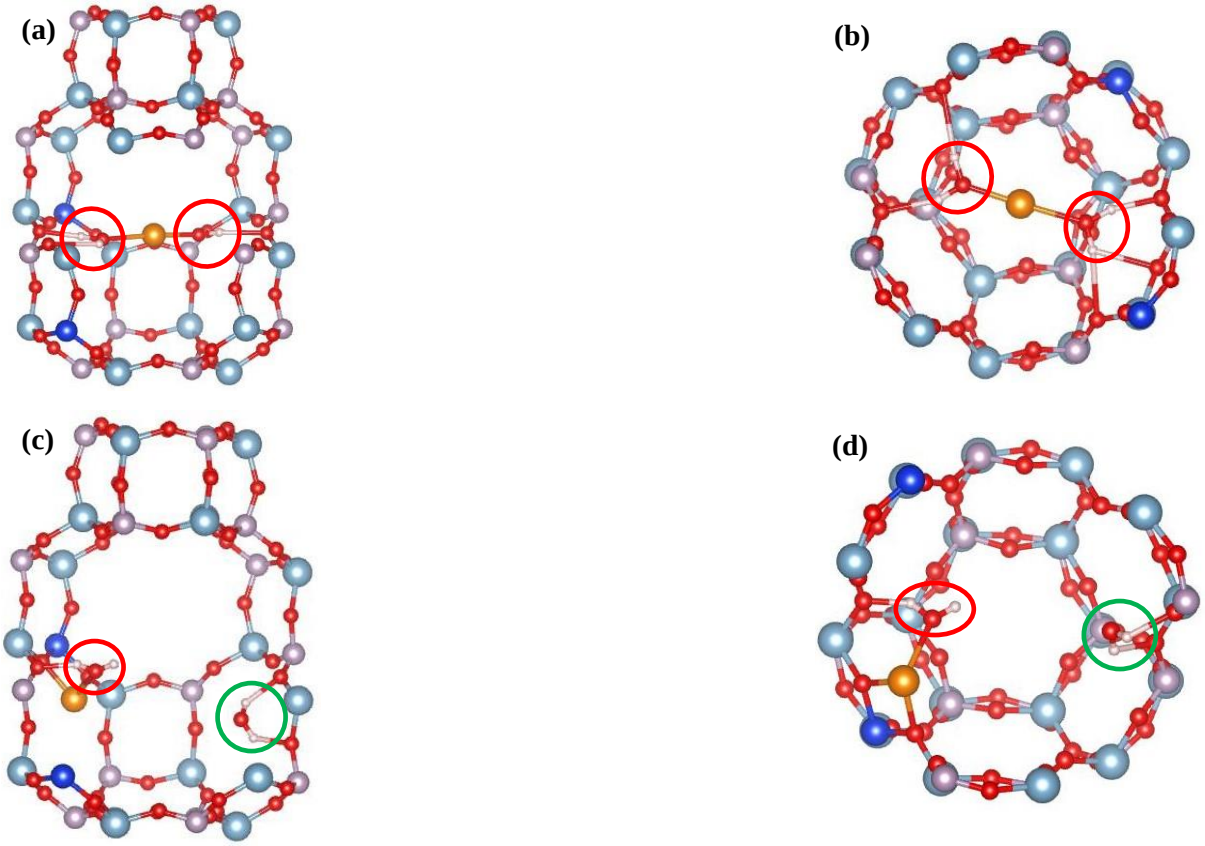

Figs. 35(a – d): (110) and (001) views of; **(a – b)** the initial positions of Cu(II) and two H_2O molecules inside the large cage, **(c – d)** the final equilibrium positions.

Table 27: List of Cu-O bond distances before and after for each water calculation in SAPO-34.

No. of H_2O molecules	Before					After				
	Cu-O1	Cu-O2	Cu-O3	Cu-O4	Average	Cu-O1	Cu-O2	Cu-O3	Cu-O4	Average
1	2.0203	1.8759	2.2065	N/A	2.0342	1.9760	1.9092	2.2067	N/A	2.0306
2	2.0607	1.8818	2.1517	N/A	2.0314	1.8934	1.9020	N/A	N/A	1.8977

Table 28: H_2O coordination to Cu(II) in SII and corresponding bond distance in SAPO-34.

No. of H_2O molecules	H_2O coordination	Cu-O1H_2	Cu-O1H_2
1	No	4.88	N/A
2	Yes	2.47	6.79

5.3.2.4.2 SSZ-13

Figs. 36(a – d) and Figs. 37(a – d) shows the before and after Cu and H_2O configurations inside the large cage. In the one and two H_2O molecules calculations, the initial distances between Cu(II) and H_2O were in the range of 2.30 – 2.49Å, with the negatively charged oxygen atom in the H_2O pointed towards the Cu(II), see Figs. 36(a – b) and Figs. 37(a – b). As observed in SAPO-34, after optimization despite H_2O coordination in the centre of SII, the Cu(II) moves into the surrounding framework of the large cage. In the one and two H_2O molecules calculation, the Cu(II) moves into the 6MR, SI and 8MR, SIV respectively, see Figs. 36(c – d) and Figs. 37(c – d). In the one H_2O molecule calculation, the H_2O molecule "follows" the Cu(II) and sits outside of the 6MR Cu site. The Cu-OH_2 distance is 2.53Å, see Table 30, in addition the H_2O is coordinated to the 6MR framework via a single hydrogen bond of 1.64Å, Fig. 36c.

The behaviour of H_2O molecules in the two H_2O molecules calculation follows a similar behaviour to that in the one H_2O molecule calculation. One of the H_2O molecules is found adjacent to the Cu(II) with a coordinative distance of 2.61Å, see Table 30. It forms two hydrogen bonds to the framework at 1.87 and 2.46Å. Yet, the second H_2O molecules is not near the Cu, instead it is 7.18Å distance away across the large cage. However, this H_2O molecule forms strong hydrogen bonds with the framework at 1.79 and 1.82Å. See Figs. 37(c – d).

In contrast to SAPO-34, the Cu relocation in SSZ-13 are not found coordinated to the activated oxygen atoms in the surrounding framework of the large cage. It is possible, the described pronounced iconicity of the bonding in an AlPO could have a more profound influence here compared to the zeolite.

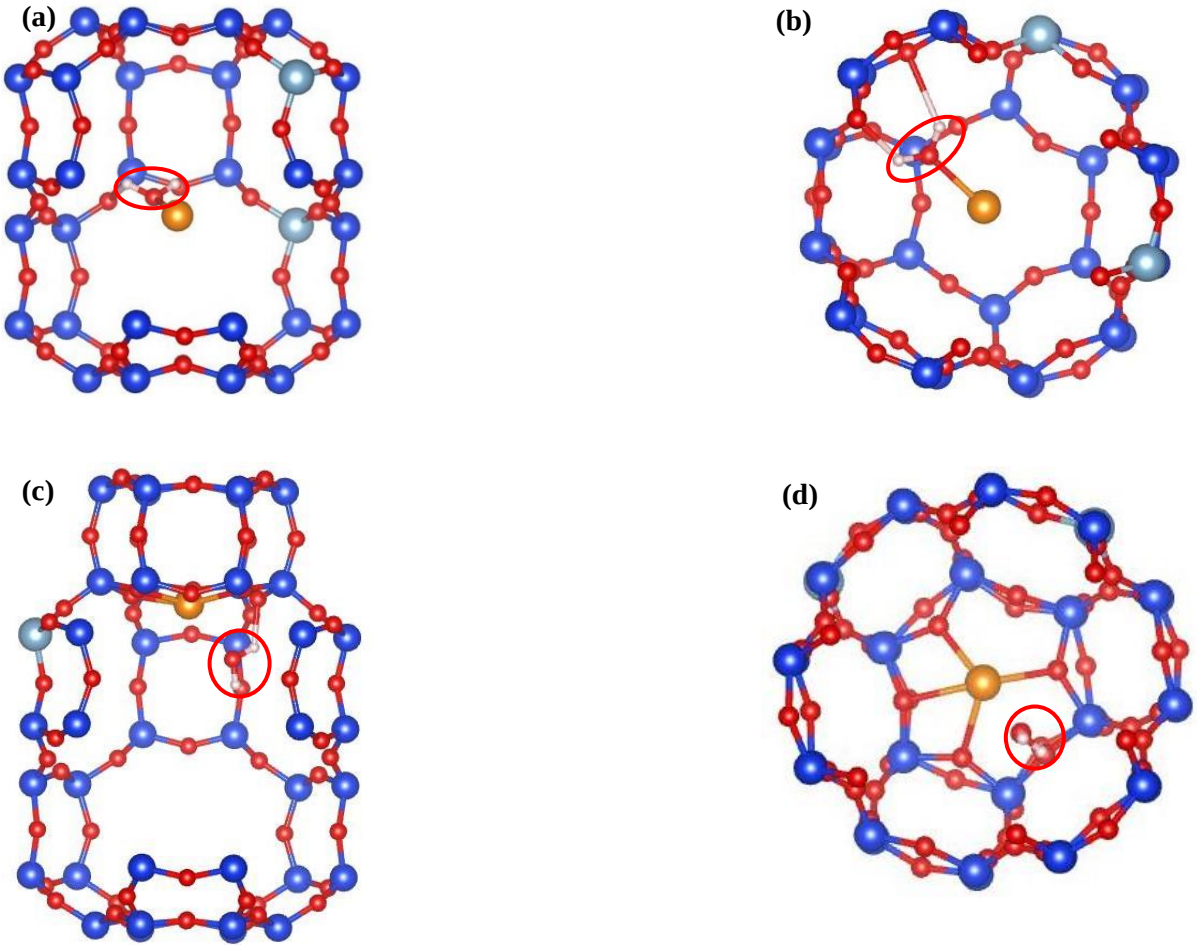

Figs. 36(a – d): (110) and (001) views of; **(a – b)** the initial positions of Cu(II) and a H_2O molecule inside the large cage, **(c – d)** the final equilibrium positions.

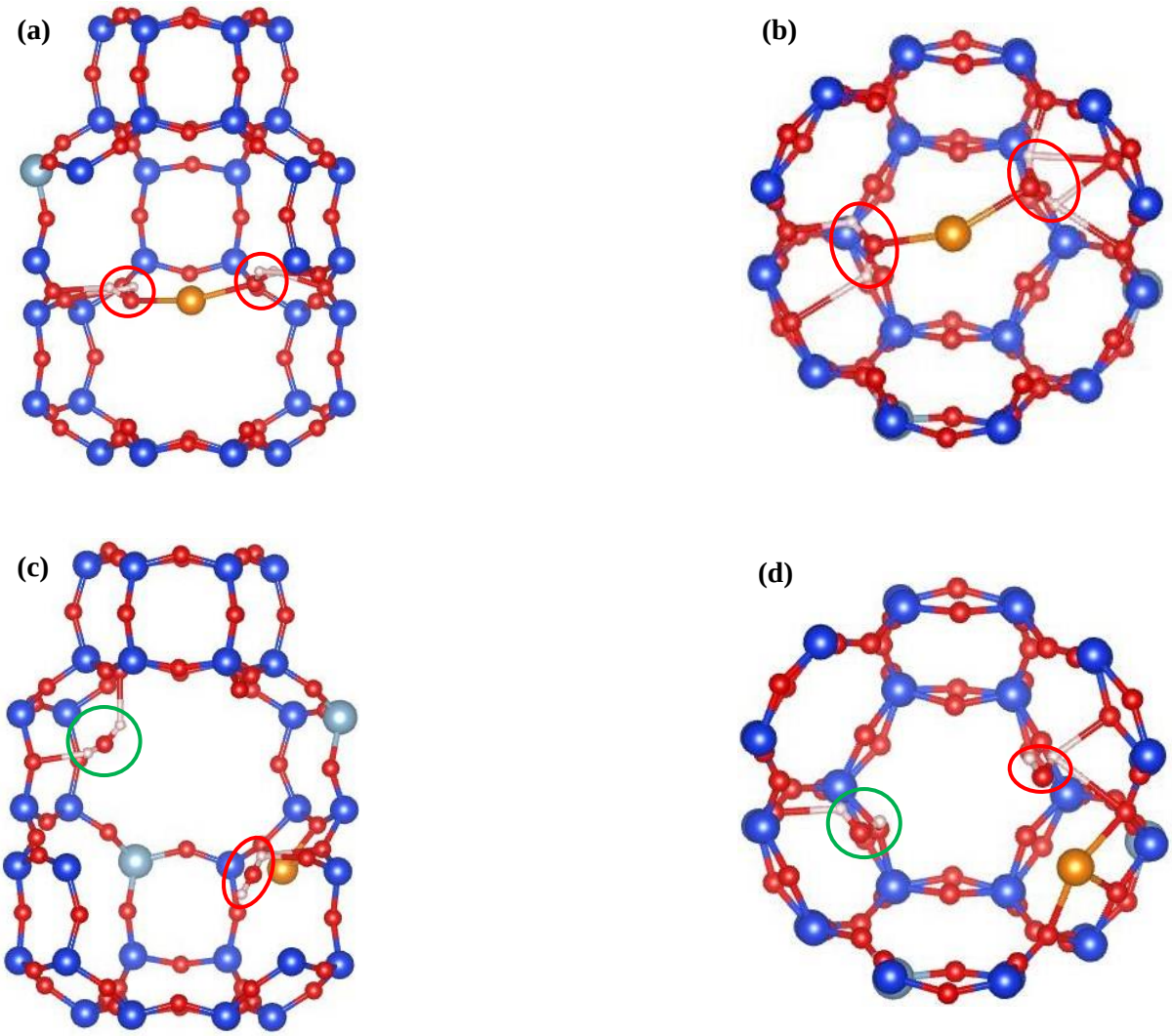

Figs. 37(a – d): (110) and (001) views of; **(a – b)** the initial positions of Cu(II) and two H_2O molecules inside the large cage, **(c – d)** the final equilibrium positions.

Table 29: List of Cu-O bond distances before and after for each water calculation in SSZ-13.

No. of H_2O molecules	Before					After				
	Cu-O1	Cu-O2	Cu-O3	Cu-O4	Average	Cu-O1	Cu-O2	Cu-O3	Cu-O4	Average
1	2.0821	2.3156	2.2166	2.4803	2.2736	2.0863	2.3113	2.2575	2.1712	2.2006
2	2.1138	1.9267	2.0917	N/A	2.0441	2.1323	1.9407	2.1232	N/A	2.0654

Table 30: H_2O coordination to Cu(II) in SII and corresponding bond distance in SSZ-13.

No. of H_2O molecules	H_2O coordination	Cu-O1H_2	Cu-O1H_2
1	Yes	2.53	N/A
2	Yes	2.61	7.18

5.3.2.5 Site SIII energy

5.3.2.5.1 SAPO-34

The Cu was placed in site SIII, a space inside the D6R between two 6MRs, labelled sites SIa and SIb. In these sub-set of calculations after optimization, the Cu would move inside the planes of either sites SIa and SIb. The presence of H_2O molecules does not seem to alter the Cu preference for sites SI over SIII. This is not surprising considering the energetic stabilization gained from the AlPO framework interactions in the 6MR. The H_2O molecules with its permanent dipole would move in relation with the Cu(II) and orient such that the negatively charged oxygen atoms are pointed towards the cation. In addition, the H_2O molecules would form hydrogen bonds with the nearby framework oxygen atoms. See Figs. 38 – 42 (a – d).

Table 31 lists the energies for up to two H_2O molecules inside site SIII, but with different starting H_2O configurations. The vertical and horizontal placements of the two H_2O molecules inside SIII around the Cu, noted (V) and (H) respectively in the table, see Figs. 39 – 40 (a – d). The reference energy for a bare Cu-SAPO-34, $E_{Cu\text{-}AlPO}$ is calculated as a function of the final location of the Cu(II) either in sites SIa or SIb. These two sites differ by 0.16eV. The adsorption energies per H_2O molecule are relatively consistent in the range of -0.73 – -0.98eV with the exception of the two H_2O molecules calculation placed in a horizontal arrangement. This has an adsorption energy of 0.45eV indicating a highly unfavourable arrangement of H_2O configurations which would not be observed, because of the confinement of two H_2O molecules inside the D6R, see Figs. 39(a – d).

Comparing the adsorption energies of a one H_2O molecule calculation with that of the two H_2O molecules calculation (V), the difference in adsorption energy per molecule is: -0.84--0.78= -0.06eV. In both calculations, the final configurations has the H_2O molecules coordinated to the Cu(II) within a distance of 2.57 – 2.90Å, see Table 33 and Figs. 38, 40(a – d). Therefore, the -0.06eV discrepancy does not stem from the difference or lack of (proportional) Cu-OH_2 coordination in the two calculations. Instead, looking at Fig. 38c the H_2O molecule is situated deeper inside of the D6R unlike in Figs. 40(c – d) of the two H_2O molecules calculation (V), where the H_2O molecules are sitting nearer to the planes of a 6MR and 8MRs. The closer proximity of the H_2O molecules to the AlPO framework in the two H_2O molecules calculation (V) results in stronger hydrogen bonds formed. The one H_2O molecule calculation forms (weak) hydrogen bonds within a range of 2.05 – 2.47Å, but the two H_2O

molecules calculation (V) is able to form three strong bonds with distances of: 1.56, 1.62 and 1.76Å. In addition, steric effects could have an influence in the one H_2O molecule calculation configuration since the H_2O sits inside the D6R.

In order to understand the difference in energies of the two H_2O locations observed in the two H_2O molecules calculation (V) final configuration, two separate one H_2O molecule calculations were undertaken: one with a H_2O molecule inside the 6MR and another with the H_2O molecule inside the 8MR. Interestingly, the H_2O location in the 6MR is -0.26 lower in energy compared to the 8MR configuration. In terms of adsorption energy, the 6MR is -0.25eV lower in energy. The H_2O molecule in the 6MR is able to form two strong hydrogen bonds to the framework with distances of 1.58 and 1.59Å, unlike in the 8MR with only one strong hydrogen bond at 1.78Å. In addition, the H_2O molecule in the 6MR is closer to the Cu compared to when inside the 8MR indicating stronger Cu-OH_2 coordination; 2.58 against 2.91Å, see Figs. 41 – 42 (a – d).

Table 31: Energies of the H_2O configurations in site SIII of Cu-SAPO-34.

No. of H_2O molecules	**$E_{AlPO+nH_2O}$**	**$E_{Cu\text{-}AlPO}$**	**Rel. E**	**Ads. E**	**Ads. E per H_2O molecule**	**EH_2O**
1	-4763.73	-4741.42	-4742.20	-0.78	-0.78	-21.53
2 (H)	-4784.19	-4741.58	-4741.13	0.45	0.23	-43.06
2 (V)	-4786.16	-4741.42	-4743.10	-1.68	-0.84	-43.06
1*	-4763.93	-4741.42	-4742.40	-0.98	-0.98	-21.53
1**	-4763.67	-4741.42	-4742.14	-0.73	-0.73	-21.53

(H) = horizontal placements

(V) = vertical placements

*Inside the 6MR

** Inside the 8MR

5.3.2.5.2 SSZ-13

Similarly, in SSZ-13 the Cu(II) does not reside inside the space of the D6R of site SIII. Instead, the Cu will migrate in to the nearby 6MRs despite the presence of up to two H_2O molecules within coordinative distances, see Figs. 43 – 47 (a – d). However, like in SAPO-34 the final locations of the H_2O molecules are tightly correlated with the movement of the Cu(II) in the zeolite framework.

The most favoured calculation on the basis of adsorption energy was the two H_2O molecules calculation (V) with an adsorption energy of -2.12eV, see Table 32 and Figs. 45(a – d). This is followed by the one H_2O molecule calculations where the H_2O molecules interact strongly with the 6MR frameworks, see Figs. 43(a – d) and Figs. 46(a – d), both at -1.27 eV adsorption energies. The next lowest adsorption energy is -0.90eV; the one H_2O molecule calculation with the H_2O residing just outside of the plane of the 8MR, see Figs. 17(a – d). The least favoured is the two H_2O molecules calculation (H) with both the H_2O molecules sitting inside site SIII; -0.39eV, Figs. 44(a – d). This energetic trend is observed in SAPO-34, but the adsorption energies of the H_2O molecules in SSZ-13 is significantly more favoured. Each calculation in SSZ-13 is at least -0.23eV lower in energy compared to the SAPO-34 counterpart.

Despite the permanent dipoles of H_2O molecules, the relative iconicity of an AlPO framework compared to that in a zeolite as described previously is less favourable for interactions with H_2O molecules. In general, the energetic discrepancies in H_2O molecules adsorption between the frameworks is observed for all calculations including in sites SI and SII.

The adsorption energy of a one H_2O molecule calculation is -1.27eV, and that of the two H_2O molecules calculation (V) is -2.12eV. The absence of a direct proportionality in the adsorption energies is due to the difference in the equilibrium location for the second H_2O molecule in the two H_2O molecules calculation (V). As in SAPO-34, the vertical placements of two H_2O molecules around Cu in the D6R resulted in two different H_2O locations, one sitting inside the D6R but coordinated to a 6MR in an identical fashion to the one H_2O molecule calculation, and the second molecule is sat outside of the D6R and adjacent to the plane of a 8MR, see Figs. 45(a – d).

The difference in energies between the two H_2O locations were investigated, and the H_2O molecule sitting inside the D6R is -0.37eV lower in energy, see Table 32 “Inside the D6R” and “Outside the D6R”. The sum of these two separate calculations are: -0.90 + -1.27 = -2.17eV, which is -0.05eV lower in energy compared to the two H_2O molecules (V) calculation. This discrepancy is due to the re-orientation of the H_2O molecule for outside of the D6R calculation; decreasing the Cu-OH_2 distance from 3.00 to 2.90Å, see Figs. 46(a – d).

This large difference is as a result of stronger hydrogen bonds to the zeolite framework when in the 6MR. The H_2O molecule forms two strong hydrogen bonds of distances at 1.78 and 1.91Å to the 8MR when outside of the D6R, but the H_2O molecule inside the D6R forms two stronger hydrogen bonds at 1.57 and 1.59Å. In addition, the Cu-OH_2 distance is shorter when inside the D6R at 2.58 compared to outside between 2.90 – 3.00Å, see Table 36.

Like in SAPO-34, the two H_2O molecules calculation (H) is the least favoured configuration adopted for these particular subset of calculations, as evident by the adsorption energy. Despite the presence of four strong hydrogen bonds with the range of 1.56 – 1.93Å, and relatively short Cu-OH_2 coordinative distances (2.53Å), this is an energetically unfavourable configuration. This is attributed to steric effects, as two H_2O molecules are

confined inside the D6R and a Cu(II) inside the plane of the adjacent 6MR, see Figs. 44(a – d).

Table 32: Energies of the H_2O configurations in site SIII of Cu-SSZ-13.

No. of H_2O molecules	**$E_{Zeol+nH_2O}$**	**$E_{Cu\text{-}Zeol}$**	**Rel. E**	**Ads. E**	**Ads. E per H_2O molecule**	**EH_2O**
1	-4590.15	-4567.35	-4568.62	-1.27	-1.27	-21.53
2 (H)	-4610.81	-4567.35	-4567.75	-0.39	-0.20	-43.06
2 (V)	-4612.54	-4567.35	-4569.48	-2.12	-1.06	-43.06
1*	-4590.15	-4567.35	-4568.62	-1.27	-1.27	-21.53
1**	-4589.79	-4567.35	-4568.25	-0.90	-0.90	-21.53

(H) = horizontal placements

(V) = vertical placements

*Inside the D6R

** Outside the D6R

5.3.2.6 Site SIII configuration

5.3.2.6.1 SAPO-34

Like the SII calculations, sites SIII calculations results in the movement of the Cu away from the initial position. Subsequently, the Cu-O "Before" distances are based on the final locations of the Cu as observed in these water calculations, but without the presence of the H_2O molecules. Figs. 38(a – d), shows the before and after configurations for the one H_2O molecule calculation. The before configuration has Cu sitting in mid-distance between the two 6MR planes inside the D6R, and the H_2O molecule is coordinated to the Cu(II) sideways with a coordinative Cu-OH_2 length of 1.54Å. After optimization, this configuration changes with Cu(II) moving inside an adjacent 6MR and the H_2O molecule residing inside the D6R, but just out of the plane of the opposite 6MR. The H_2O molecule coordinates to the 6MR with hydrogen bond lengths within 2.05 – 2.47Å, whilst the Cu(II) sits in the 6MR with Cu-O bond lengths between 2.01 and 2.08Å, see Table 33. A Cu-OH_2 coordination is present at 2.56Å, see Table 34.

Unsurprisingly, the final configuration for the two H_2O molecules calculation (H) is very similar to the one H_2O molecule calculation, see Figs. 39(a – d). Since, the starting positions of the H_2O molecules in both calculations are horizontal with respect to the Cu and the D6R framework. The Cu(II) sits in the plane of the 6MR framework with four Cu-O bonds, unlike in the one H_2O molecule calculation with three Cu-O bonds, see Table 33. However, both H_2O molecules reside in the D6R like in the one H_2O molecule calculation, but the H_2O molecules in the former are situated more in the centre of the D6R, as evident by closer proximity to the Cu, see Table 34.

The locations of H_2O molecules between the initial vertical and horizontal placements of the two H_2O molecules is vastly different which profoundly affects the energetics as observed in Table 31 and the final configurations, see Figs. 39 – 40(a – d). In the horizontal configurations, both the H_2O molecules reside in the D6R and follows the Cu(II) as the latter migrates into the 6MR plane. It can be considered; the H_2O molecules "pushes" the Cu(II) outwards into the 6MR as the H_2O molecules are situated in the centre of the D6R. However, this is unlikely as prior GULP calculations of Cu(II) in site SIII results in the Cu occupying the adjacent 6MRs regardless of dopant distributions (see Chapters 5.1.2) or the presence of H_2O molecules.

For the vertical configuration, the initial positions of the two H_2O molecules are inside opposite 6MR planes and the Cu(II) occupies site SIII. The final configuration has Cu(II) sitting inside an adjacent 6MR, but the H_2O molecules due to the different starting positions compared with the horizontal configuration behaves markedly different. One of the H_2O molecule stays relatively in the same position in the plane of the 6MR, but further inside the D6R to decrease the Cu-OH_2 distance as the Cu moves away from site SIII into SI. The second H_2O molecule leaves the plane of the 6MR into the large cage, occupying opposite an 8MR plane. See Figs. 40(a – d).

The calculation for Cu and H_2O molecule configurations derived from the two H_2O molecules calculation (V) shows subtle changes in the Cu(II) and the H_2O molecule occupying the 6MR. Without the presence of the second H_2O adjacent to the 8MR, the Cu-OH_2 distance between Cu and the H_2O molecule in the opposite 6MR decreased from 2.63 to 2.58Å, see Table 34. This is akin to the final configuration obtained for the one H_2O molecule calculation. However, the H_2O molecule's hydrogen bond lengths to the 6MR framework differ. In the one H_2O molecule calculation as mentioned previously, the H_2O forms relatively weak hydrogen bonds to the 6MR framework within the range of 2.05 – 2.47Å. For the H_2O molecule 6MR calculation, there are two strong hydrogen bonds at 1.58 and 1.59Å, with a weaker one at

2.42Å. In the vertical calculation, the hydrogen bonds to identical framework oxygen atoms were 1.56, 1.62 and 2.45Å. The lack of change in the lengths indicate that either the Cu(II) has moved closer to the remaining H_2O or the H_2O has managed to re-orient to decrease the Cu-OH_2 distance whilst keeping the strong hydrogen bonds. Comparing the final Cu-O bonds for the two calculations, the 6MR calculation is on averaged 0.029Å longer, see Table 33, indicating that the Cu(II) movement closer to the H_2O is only weakly perceptible.

The combination of both Cu and H_2O slight movements is probable in achieving the decreased Cu-OH_2 distance. Close inspection of configurations between the original one H_2O molecule and 6MR calculation shows a difference in orientation of the H_2O molecule, see Figs. 38(c) and 41(c). The former is at an obtuse angle relative to the plane of the 6MR, whilst the latter is perpendicular. This slight difference in H_2O orientation could affect the H_2O's ability to form strong bonds to the framework and the Cu-OH_2 distance. Whilst the 8MR calculation did not show any perceptible changes in Cu and H_2O configurations, see Figs. 42(a – d).

Figs. 38(a – d): Top and side views of one H_2O molecule calculation before **(a)** – **(b)** and after **(c)** – **(d)**.

Figs. 39(a – d): Top and side views of two H_2O molecules calculation (H) before **(a)** – **(b)** and after **(c)** – **(d)**.

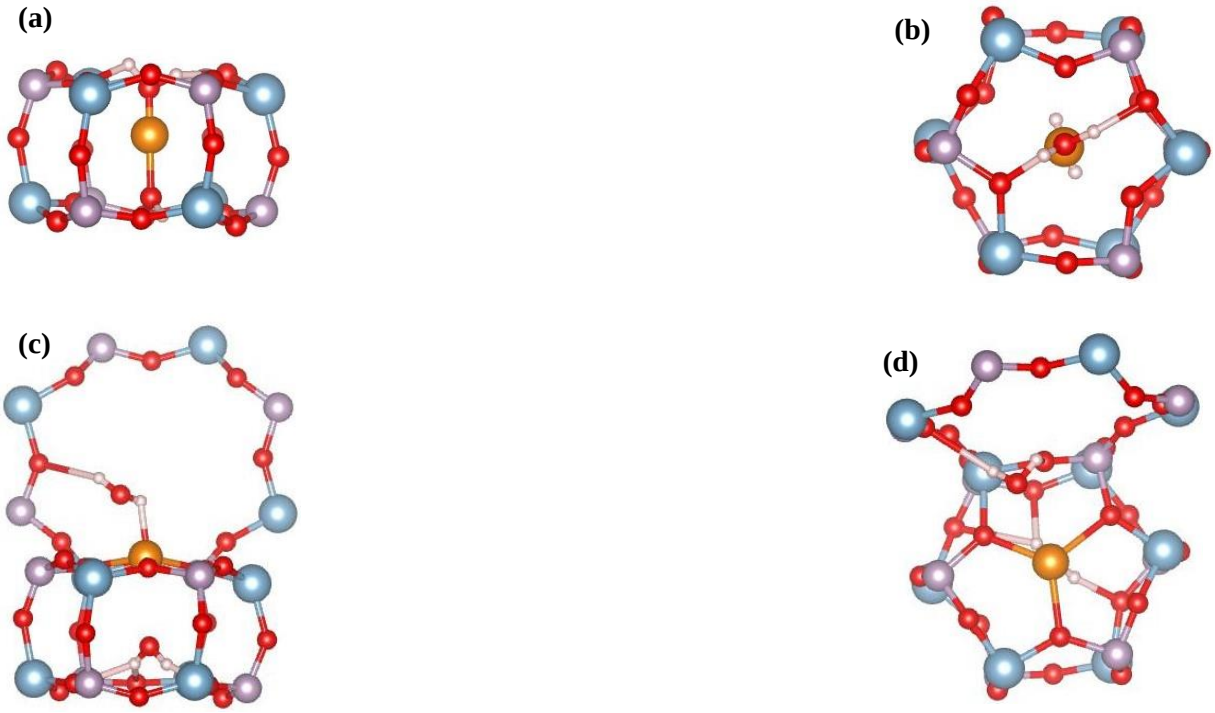

Figs. 40(a – d): Top and side views of two H_2O molecules calculation (V) before **(a)** – **(b)** and after **(c)** – **(d)**.

Figs. 41(a – d): Top and side views of one H_2O molecule calculation in the 6MR before **(a)** – **(b)** and after **(c)** – **(d)**.

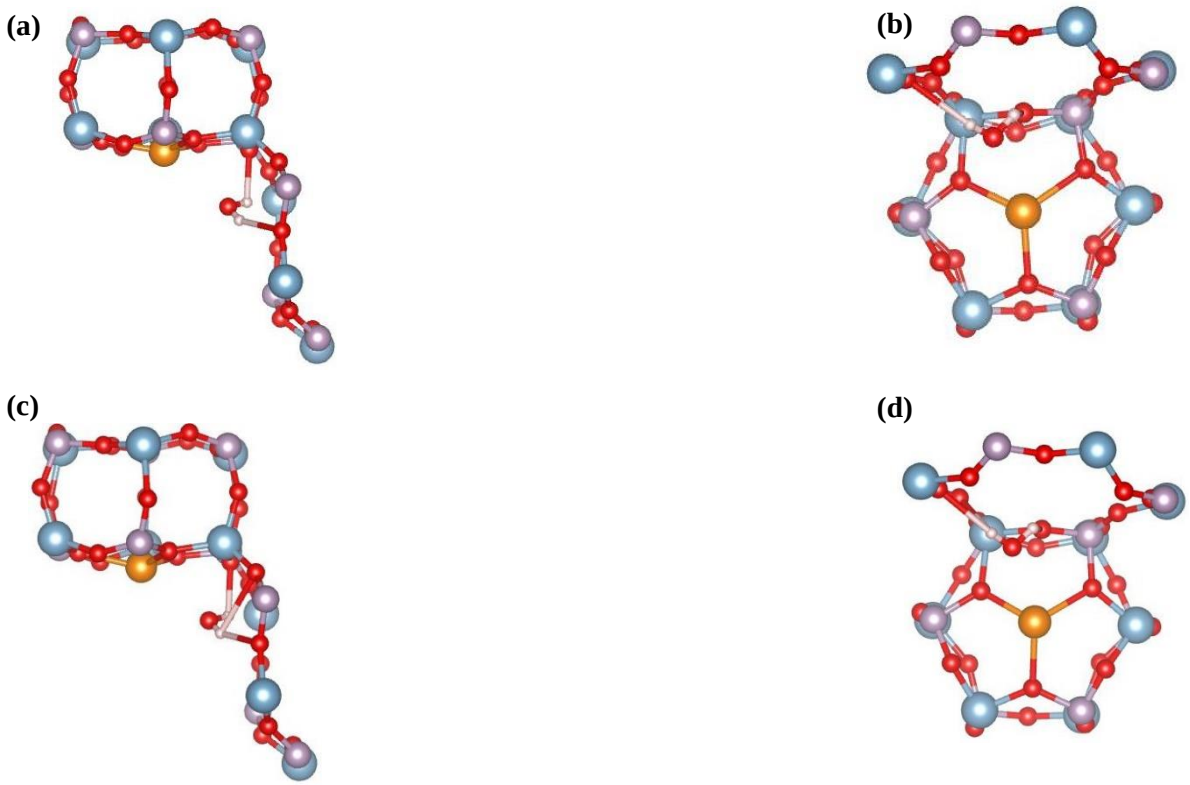

Figs. 42(a – d): Top and side views of one H_2O molecule calculation in the 8MR before **(a)** – **(b)** and after **(c)** – **(d)**.

Table 33: List of Cu-O bond distances before and after for each SIII water calculation SAPO-34.

No. of H_2O molecules	**Before**					**After**				
	Cu-O1	Cu-O2	Cu-O3	Cu-O4	Average	Cu-O1	Cu-O2	Cu-O3	Cu-O4	Average
1	1.9739	2.0370	2.0316	N/A	2.0142	2.0106	2.0765	2.0632	N/A	2.0501
2 (H)	1.9731	2.0218	2.0559	N/A	2.0169	2.1139	2.0857	2.2253	2.2985	2.1809
2 (V)	1.9739	2.0370	2.0316	N/A	2.0142	2.0774	2.0170	2.1507	N/A	2.0817
1*	1.9739	2.0370	2.0316	N/A	2.0142	2.0536	2.0211	2.0843	N/A	2.0530
1**	1.9739	2.0370	2.0316	N/A	2.0142	2.1059	1.9702	2.0655	N/A	2.0472

Table 34: H_2O coordination to Cu(II) in SIII and corresponding bond distance in SAPO-34.

No. of H_2O molecules	**H_2O coordination(s)**	**Cu-O1H_2**	**Cu-O2H_2**
1	Yes	2.57	N/A
2 (H)	Yes	2.48	2.50
2(V)	Yes	2.63	2.90
1*	Yes	2.58	N/A
1**	Yes	N/A	2.91

(H) = horizontal placements

(V) = vertical placements

*Inside the 6MR

** Inside the 8MR

5.3.2.6.2 SSZ-13

These calculations like in SAPO-34 the Cu did not stay in site SIII and migrates inside the 6MR frameworks. The equilibrium configurations and locations of the Cu(II) had no perceptible difference between SSZ-13 and SAPO-34, but the energetics for H_2O adsorption is favoured for the zeolite as observed previously. However, the behaviour of the H_2O molecules in sites SIII for both frameworks are distinct compared to other sites, because the orientation and movement of the H_2O molecules follows more closely the Cu(II) behaviour. This is evident by the negatively charge oxygen atoms in H_2O molecules pointed towards the Cu(II) in the equilibrium configurations, and the distances between Cu and H_2O molecules were never more than 3.00Å apart. The initial positioning of the H_2O molecules in close proximity with Cu(II), in combination with the confinement of H_2O and Cu(II) inside the D6R most possibly affected a more pronounced Cu and H_2O interaction.

Due to the uniformity in behaviour of the Cu and H_2O molecules in the SIII calculations in both zeolite and AlPO frameworks, we are able to observe the strengths of the H_2O adsorption as a function of the hydrogen bond lengths. In Tables 31 and 32, the energetic behaviour of the H_2O interaction with the frameworks showed consistently, adsorption on the SSZ-13 is more favoured. As a result, this was reflected in the lengths of the hydrogen bonds formed for each H_2O configuration.

In the one H_2O molecule calculation as in SAPO-34, the H_2O molecule is initially coordinated to the Cu inside the D6R with a coordinative distance of 1.68Å. The final configuration Cu sits in the 6MR and the H_2O molecule inside the D6R but adjacent to the plane of the opposite 6MR. The Cu-OH_2 distance is 2.58 Å, see Table 36, as a result the increased Cu-OH_2 distance is compensated by the location of Cu inside the 6MR and removal of a possible steric constraint. This is similarly observed in SAPO-34. In SSZ-13, the hydrogen bond lengths for the H_2O molecule with the 6MR framework were 1.57 and 1.59Å, but for SAPO-34 the distances were in the range of 2.05 – 2.47Å. Indicating stronger hydrogen bonds between the H_2O molecule and the SSZ-13 framework, in good agreement with the more favourable adsorption energy compared to SAPO-34. See Figs. 38(a – d) and Figs. 43(a – d).

Both the two H_2O molecules calculations; vertical and horizontal placements the Cu and H_2O behaviour were reproduced as in SAPO-34. Interestingly, in the horizontal calculation the equilibrium configurations of the H_2O molecules have the oxygen atoms pointed towards the Cu in the 6MR, but the orientation of the H_2O molecules are tilted away from each other, due to the close proximity of the negative dipoles, see Figs. 44(a – d). In SSZ-13 and SAPO-34 the horizontal configuration of H_2O molecules is the least energetically favoured, and in the case of the latter heavily disfavoured due to the confinement of two H_2O molecules in the D6R. The hydrogen bond lengths between the H_2O and framework would not be indicative of strength of adsorption, because of the energetic penalty of steric effects.

In the case of the vertical calculation, one H_2O molecule occupies inside the D6R but just out of the plane of a 6MR. Whilst, the second H_2O molecule sits in the large cage adjacent to an 8MR, see Figs. 45(a – d). The same configuration was observed in SAPO-34, but the difference is the strengths of the hydrogen bonds between the H_2O molecules and the 6MR and 8MR frameworks. For the former, two hydrogen bonds were observed with lengths of 1.57 and 1.59Å, in the 8MR the lengths were 1.77 and 1.98Å. In SAPO-34, the H_2O molecules were observed in identical locations and configurations, yet the hydrogen bond lengths are on average perceptibly longer. For the 6MR, the hydrogen bond lengths were 1.56, 1.62 and 2.45Å. In the 8MR the hydrogen bond distances were 1.76 and 2.27Å, this indicates a stronger H_2O – zeolitic framework interaction as reflected in the energetic behaviour.

A comparison of the before and after of 6MR calculation shows a decreased in the Cu-OH_2 distance of 0.06Å for the latter as observed in SAPO-34, see Tables 34 and 36. There is a slight perceptible difference in the H_2O's hydrogen bonding to the 6MR between the two configurations. In the before configuration, two hydrogen bonds were measured at 1.57 and 1.59Å. For the after, there are two hydrogen bonds with the same lengths to identical framework oxygen atoms, and an additional measured at 2.45Å previously 2.52Å since only bond lengths within 2.50Å are visible in the configurations. The Cu-O bonds before and after are on average the same both at 2.23Å, see Table 35. This indicates the slight change in the H_2O orientation resulted in a decreased in the Cu-OH_2 distance. See Figs. 46(a – d).

Similarly, in the 8MR calculation the Cu-OH_2 distance decreased in the after configuration by 0.11Å, whilst the H_2O hydrogen bond lengths to the 8MR framework decreased on average. In the before configuration, the average hydrogen bond lengths was 1.88Å and after the average distance was 1.84Å. See Figs. 47(a – d). The H_2O molecule formed both stronger interactions to the Cu(II) and the SSZ-13 framework in the 8MR, resulting in a high adsorption energy of -0.90eV, see Table 32.

Table 35 shows the changes in the Cu-O bond lengths after the inclusion of H_2O molecules. The Cu-O bond lengths shows the expected increased upon addition of H_2O molecules with respect to the bare Cu site, as was observed in SAPO-34, Table 33. The Cu-OH_2 distances in the SIII calculations are all relatively consistent in both SSZ-13 and SAPO-34, this is because of the compact arrangement of the H_2O molecules and Cu(II) being confined inside the D6R.

Figs. 43(a – d): Top and side views of one H_2O molecule calculation before **(a)** – **(b)** and after **(c)** – **(d)**.

Figs. 44(a – d): Top and side views of two H_2O molecules calculation (H) before **(a)** – **(b)** and after **(c)** – **(d)**.

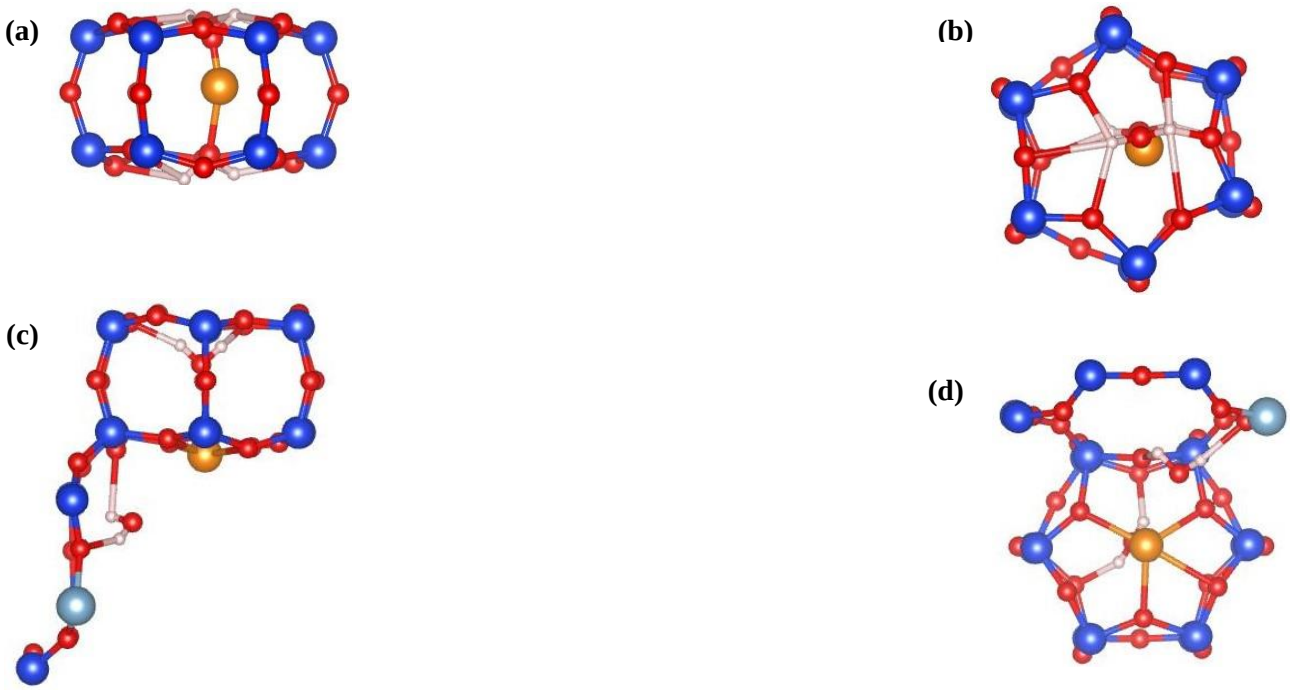

Figs. 45(a – d): Top and side views of two H_2O molecules calculation (V) before **(a)** – **(b)** and after **(c)** – **(d)**.

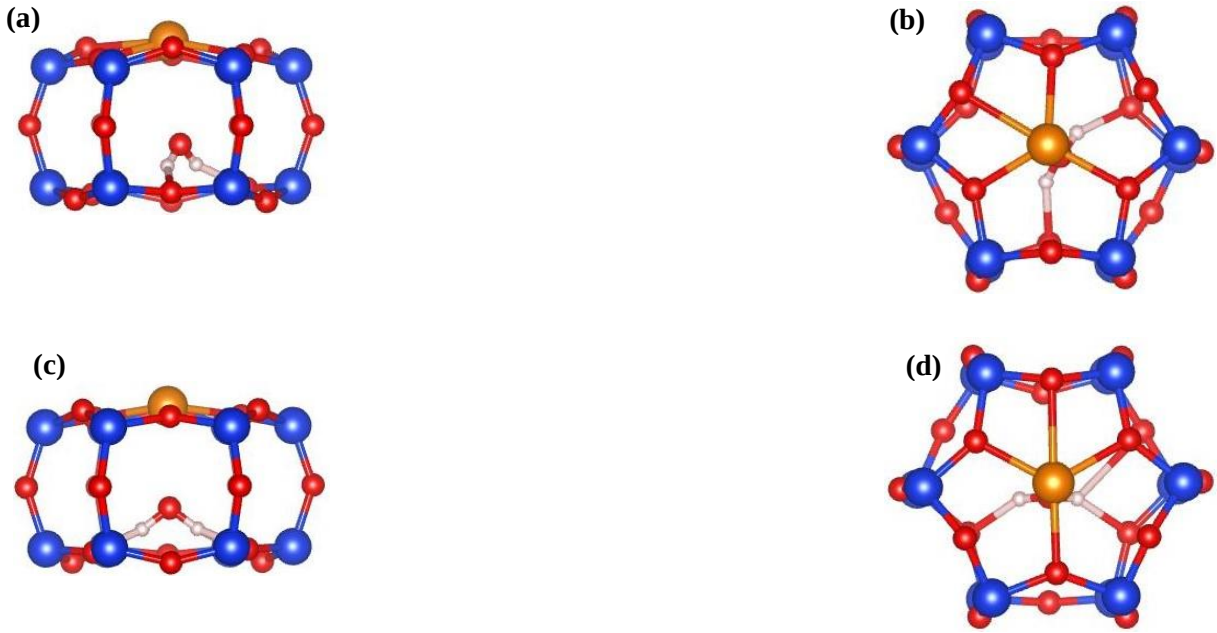

Figs. 46(a – d): Top and side views of one H_2O molecule calculation in the D6R before **(a)** – **(b)** and after **(c)** – **(d)**.

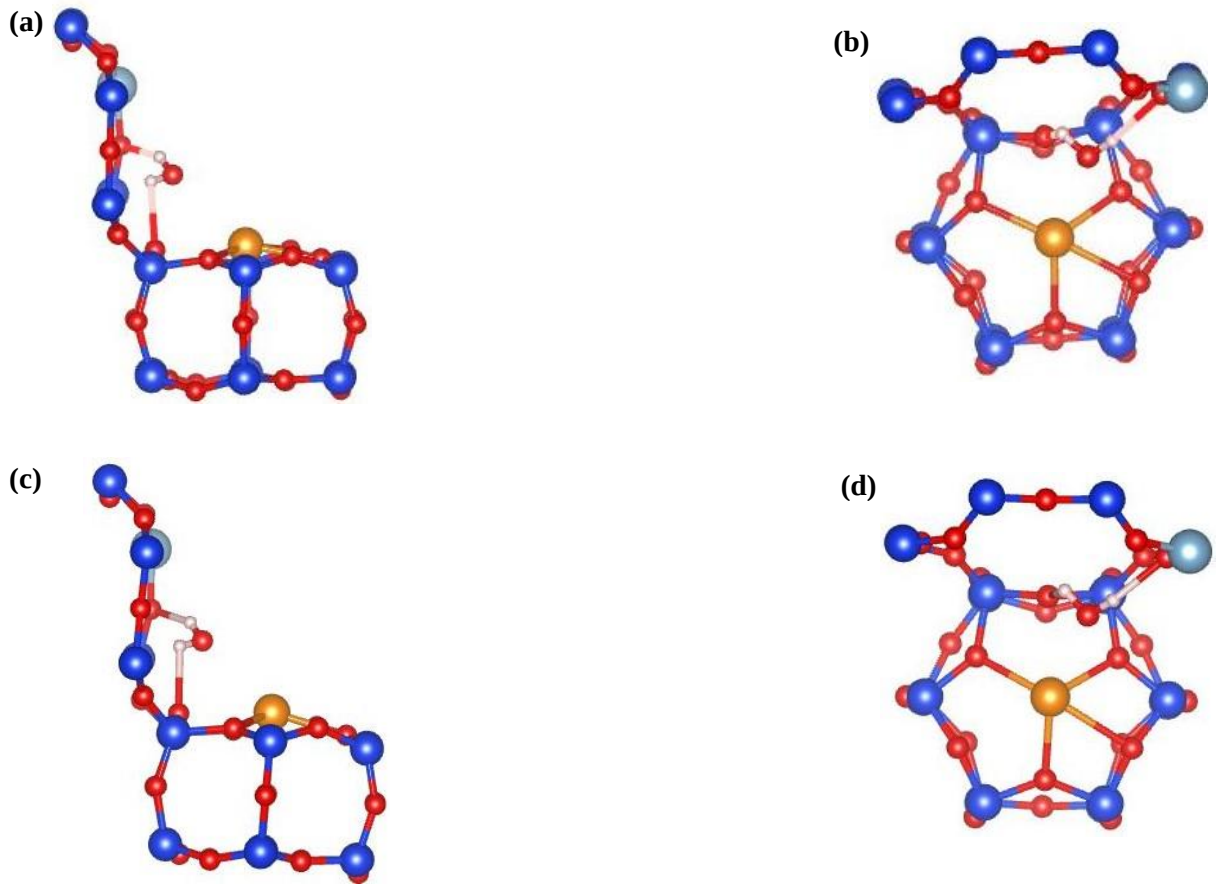

Figs. 47(a – d): Top and side views of one H_2O molecule calculation outside the D6R before **(a)** – **(b)** and after **(c)** – **(d)**.

Table 35: List of Cu-O bond distances before and after for each SIII water calculation in SSZ-13.

No. of H_2O molecules	Before					After				
	Cu-O1	Cu-O2	Cu-O3	Cu-O4	Average	Cu-O1	Cu-O2	Cu-O3	Cu-O4	Average
1	2.1103	2.1710	2.4976	2.1126	2.2229	2.1774	2.1288	2.4739	2.1288	2.2272
2 (H)	2.1103	2.1710	2.4976	2.1126	2.2229	2.3459	2.3142	2.2109	2.0480	2.2298
2 (V)	2.1103	2.1710	2.4976	2.1126	2.2229	2.2039	2.1133	2.4397	2.1731	2.2325
1*	2.1103	2.1710	2.4976	2.1126	2.2229	2.1287	2.4739	2.1289	2.1774	2.2272
1**	2.1103	2.1710	2.4976	2.1126	2.2229	2.2108	2.0961	2.4796	2.1627	2.2373

Table 36: H_2O coordination to Cu(II) in SIII and corresponding bond distance in SSZ-13.

No. of H_2O molecules	H_2O coordination(s)	Cu-O1H_2	Cu-O2H_2
1	Yes	2.58	N/A
2 (H)	Yes	2.53	2.53
2(V)	Yes	2.65	3.01
1*	Yes	2.58	N/A
1**	Yes	N/A	2.90

(H) = horizontal placements

(V) = vertical placements

*Inside the D6R

** Outside the D6R

5.3.2.7 Site SIV energy

5.3.2.7.1 SAPO-34

In these calculations Cu(II) sits in site SIV and the H_2O molecules are docked in the large cage, but facing with the molecules oriented such that the negatively charged oxygen atoms are pointed towards the Cu. The initial Cu-OH_2 distances are within the range of 2.37 – 3.02 Å in order to ensure the close proximity between Cu and the H_2O molecules, this will aid understanding the behaviour of Cu(II) with water in site SIV and if there is a perceptible difference in Cu(II) configuration after the addition of H_2O molecules.

Subsequent addition of H_2O molecules from one to three; the energy of the system increases by 22.65 and 22.40eV, see Table 37. This consistent increase upon each addition of H_2O is reflected by the energy of a H_2O molecule in vacuum at -21.53eV. The adsorption energy per H_2O molecule increased from -0.77 to -0.82 then to -0.92eV. This steady increase shows the influence of both the different H_2O orientations with respect to the framework and the presence of H_2O-H_2O interactions.

In the one H_2O molecule calculation, the H_2O molecule is stabilized by framework interactions in the large cage. Two hydrogen bonds are formed to adjacent 4MRs with distances of 1.70 and 2.39Å. The Cu sits in site SIV in an off-centre fashion and is coordinated to the 8MR framework via two Cu-O bonds. A third Cu bond is observed as a Cu-OH_2 coordination with a distance of 2.59Å. See Figs. 48(c – d). This configuration accounts for a -0.77eV adsorption energy.

A two H_2O molecules calculation has a similar equilibrium configuration, but with the second H_2O molecule on the other side of the large cage. Both H_2O molecules are coordinated to the Cu with similar bond lengths of 2.66 and 2.62Å. One of the H_2O molecule has a near-identical configuration as the one H_2O molecule calculation, but is stabilized by a single hydrogen bond instead of two with a distance of 1.57Å. The other H_2O molecule forms hydrogen bonds with the 6MR framework within distances of 1.70 – 2.08Å. The H_2O molecules are far apart from each other with the nearest proximity for hydrogen bonding at 3.25Å. This indicates an absence of H_2O-H_2O interaction or a very weak one. The Cu sits in SIV and has two Cu-O bonds to the 8MR framework, like in the previous calculation, the absence of additional Cu-O bonds is compensated by Cu-OH_2 coordination. See Figs. 49(c – d). The difference in adsorption energy per H_2O molecule at -0.77 and -0.82 between the one and two H_2O molecules calculation respectively, could be due to the presence of (weak) H_2O-H_2O interaction. Since, the H_2O molecules adsorption to the framework is of similar strengths in both calculations, and the Cu-OH_2 coordination is perceptibly stronger in the former.

The addition of a third H_2O molecule resulted in a H_2O molecule moving into the plane of the 8MR, and the other two H_2O molecules residing in the large cage adopting a similar configuration as the one and two H_2O molecules calculations. The two H_2O molecules in the large cage are adsorbed onto the 4MR and the 6MR with hydrogen bond lengths of 1.58Å for the former, and 1.70, 2.18, 2.38Å for the latter. The nearest distance for H_2O-H_2O interaction between these two molecules is at 3.06Å. Both are coordinated to the Cu with Cu-OH_2 distances of 2.67 and 2.73Å. The H_2O molecule inside the 8MR has a shorter Cu-OH_2 coordination distance of 2.41Å, and forms two strong hydrogen bonds in the 8MR framework with distances of 1.62 and 1.64Å in addition with two weaker ones at 2.25 and 2.35Å. The nearest H_2O-H_2O molecule between the H_2O molecule inside the 8MR and the two inside the large cage is 3.16Å. This indicates H_2O-H_2O interaction is weak in this configuration, but the overall coordination to the Cu and adsorption to the framework is strong, especially concerning the location of the H_2O molecule inside the 8MR. See Figs. 50(c – d). This can explain the high adsorption energy per H_2O molecule of -0.92eV.

The energies between H_2O adsorption in SIV and SI are comparable, however due to the presence of different H_2O orientations and the presence of hydrogen bonding between H_2O molecules this skews the adsorption energies. A fair comparison is to investigate the adsorption energies of the one molecule calculation in sites SI and SIV, since this removes the presence of H_2O-H_2O interaction and only takes into account the ability of the H_2O molecule to interact with the Cu(II) and the surrounding topology of sites SI and SIV within the host framework. In site SI, the adsorption energy was -0.50eV compared to -0.77eV, indicating that Cu in site SIV is possible a more energetically favourable location for H_2O adsorption. This can be extended to other smaller molecules with a similar permanent dipole to H_2O, like nitrogen monoxide (NO) and it is possible that in order to achieve optimised Cu exposure to small molecules like H_2O and NO inside SAPO-34, having Cu in site SIV would be preferable.

Table 37: Energies of the H_2O configurations in site SIV of Cu-SAPO-34.

No. of H_2O molecules	$E_{AlPO+nH_2O}$	$E_{Cu\text{-}AlPO}$	Rel. E	Ads. E	Ads. E per H_2O molecule	EH_2O
1	-4763.02	-4740.71	-4741.49	-0.77	-0.77	-21.53
2	-4785.42	-4740.71	-4742.36	-1.64	-0.82	-43.06
3	-4808.07	-4740.71	-4743.48	-2.76	-0.92	-64.59

5.3.2.7.2 SSZ-13

The energies for docking the H_2O molecules directly above Cu(II) in site SIV shows a similar trend to that in SAPO-34, see Table 38. In contrast to the previous calculations in site SIII, we do not observe more favoured adsorption energies in SSZ-13 compared to SAPO-34. This could be due to the different orientations adopted by the H_2O molecules around site SIV in the large cage between the two frameworks.

Like in SAPO-34, the energy of the system increases by approximately 22eV per inclusion of a H_2O molecule in each calculation, in good agreement with the energy of an individual H_2O molecule in vacuum, -21.53eV. The adsorption energy of a one H_2O molecule calculation is -1.10eV, which is -0.33eV lower in energy compare to the SAPO-34 counterpart. The SSZ-13 equilibrium configuration has the H_2O molecule sitting inside the 8MR with Cu(II), a Cu-OH_2 coordination distance of 2.41Å. Adsorption of the H_2O molecule onto the 8MR framework was observed with strong hydrogen bonds in the range of 1.56, 1.80 and 2.36Å. The significant difference in adsorption energy between the two frameworks is due to the more favoured configuration of the H_2O molecule in SSZ-13, resulting in a stronger adsorption on the framework and coordination to the Cu(II). See Figs. 51(c – d). This favoured H_2O configuration – inside the 8MR was observed in the three H_2O molecule calculation for one of the H_2O molecules inside the SAPO-34 framework.

The two H_2O molecules calculation has H_2Os attached to the 4MR frameworks either side of the Cu inside the 8MR, see Figs. 52(c – d). The Cu is relatively equidistant to both H_2O molecules with Cu-OH_2 distances at 2.59 and 2.61Å. This is shorter compared to the SAPO-34 configuration with distances of 2.62 and 2.66Å, however the hydrogen bonding to the 4MR frameworks in SSZ-13 is on average longer at 2.22Å compared to 1.88Å. In addition, hydrogen bonding between the H_2O molecules is weak due to the distance between the H_2O molecules – the nearest proximity for a hydrogen bond is at 3.27Å similar to in SAPO-34. As a result, both equilibrium configurations shared very similar adsorption energies (-1.64 and -1.65 for SAPO-34 and SSZ-13 respectively) despite the different H_2O locations occupied.

In the three H_2O molecules calculation all H_2Os reside inside the large cage just opposite the Cu in site SIV, see Figs. 53(c – d). In contrast to SAPO-34 where one of the H_2O molecules sits inside site SIV. This could explain the more favoured adsorption energy in SAPO-34 compared to SSZ-13, since the H_2O molecule seems to be more stabilized occupying the 8MR with stronger Cu coordination and adsorption to the framework as described above. While, hydrogen bonding within the three H_2O molecule in the large cage of SSZ-13 are weak as they are far apart and the nearest proximity for H_2O-H_2O interaction is 2.80 and 3.25Å.

In SSZ-13 the adsorption energy of a single H_2O molecule onto Cu in site SIV is -1.10eV compared to -0.91eV in site SI. This is a smaller difference compared to in the SAPO-34 case, however, it is important to note the Al dopant effect in the SI situation since the H_2O molecule is attached to two of the activated oxygen atoms. On the whole taking into account the dopant effect, the larger dimensions of the 8MR enables H_2O molecules to fit inside ensuring a more compact coordination to the Cu and adsorption to the framework. Indicating, that similar to SAPO-34, site SIV is a more preferable adsorption site in terms of topology for H_2O molecules compared to site SI.

Table 38: Energies of the H_2O configurations in site SIV of Cu-SSZ-13.

No. of H_2O molecules	**$E_{Zeol+nH_2O}$**	**$E_{Cu\text{-}Zeol}$**	**Rel. E**	**Ads. E**	**Ads. E per H_2O molecule**	**EH_2O**
1	-4589.64	-4567.01	-4568.11	-1.10	-1.10	-21.53
2	-4611.72	-4567.01	-4568.66	-1.65	-0.82	-43.06
3	-4634.17	-4567.01	-4569.58	-2.56	-0.85	-64.59

5.3.2.8 Site SIV configuration

5.3.2.8.1 SAPO-34

The Cu does not leave the plane of the 8MR framework in site SIV, whilst the original positions of the H_2O molecules in the large cage directly opposite the Cu are re-positioned into more viable locations near 4MR, 6MR and 8MR frameworks to gain stabilization via hydrogen bonding to the framework oxygen atoms, see Figs. 48 – 50(a – d). This is observed in all the site SIV calculations, in some cases like in the two H_2O molecules calculation the H_2O molecule moves to a framework edge at the expense of increasing the Cu-OH_2 distance. Indicating for the H_2O molecules an equilibrium should be achieved between Cu-OH_2 distance and forming interactions with framework for adsorption. The ability of the H_2O molecule to fit inside the plane of the 8MR was observed to be an optimum location, since the adsorption energies for these configurations are the most favoured between the SSZ-13 and SAPO-34 frameworks studied.

Looking at the Cu-O bonds distances we observed a reduction in the number of Cu-O bonds from three before the addition of H_2O molecules to two after, see Table 39. It was observed the longest Cu-O bond breaks measured at 2.3412Å to enable the formation of a Cu-OH_2 coordination, see Figs. 48 – 50(a – d). The H_2O configuration inside the 8MR achieves the shortest Cu-OH_2 coordination distance due to the proximity of the H_2O, see Table 40.

Table 39: List of Cu-O bond distances before and after for each SIV water calculation in SAPO-34.

No. of H_2O molecules	**Before**					**After**				
	Cu-O1	Cu-O2	Cu-O3	Cu-O4	Average	Cu-O1	Cu-O2	Cu-O3	Cu-O4	Average
1	1.9123	2.3412	1.9925	N/A	2.0821	1.9305	1.9270	N/A	N/A	1.9287
2	"	"	"	"	"	1.9490	1.9348	N/A	N/A	1.9419
3	"	"	"	"	"	1.9855	1.9535	N/A	N/A	1.9695

Table 40: H_2O coordination to Cu(II) in SIV and corresponding bond distance in SAPO-34.

No. of H_2O molecules	**H_2O coordination(s)**	**Cu-O1H_2**	**Cu-O2H_2**	**Cu-O3H_2**
1	Yes	2.59	N/A	N/A
2	Yes	2.62	2.66	N/A
3	Yes	2.41	2.67	2.73

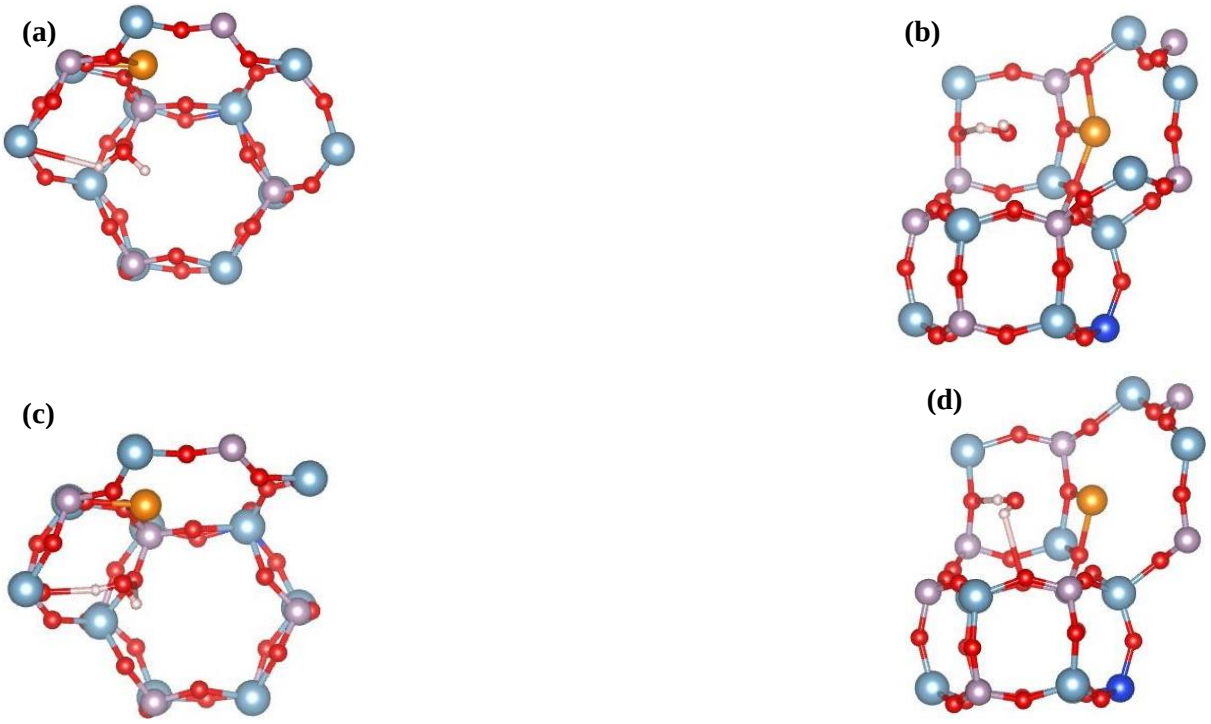

Figs. 48(a – d): Top and side views of one H_2O molecule calculation opposite Cu in site SIV before **(a)** – **(b)** and after **(c)** – **(d)**.

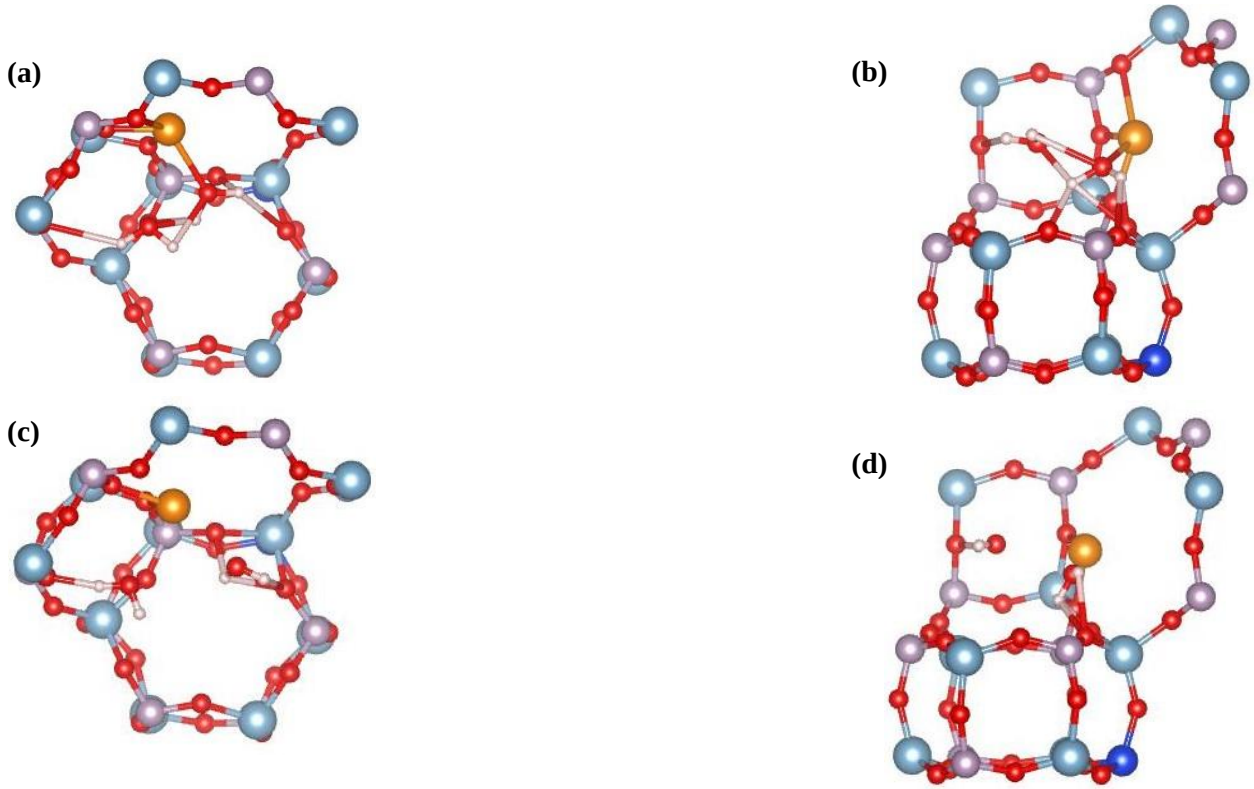

Figs. 49(a – d): Top and side views of two H_2O molecules calculation opposite Cu in site SIV before **(a)** – **(b)** and after **(c)** – **(d)**.

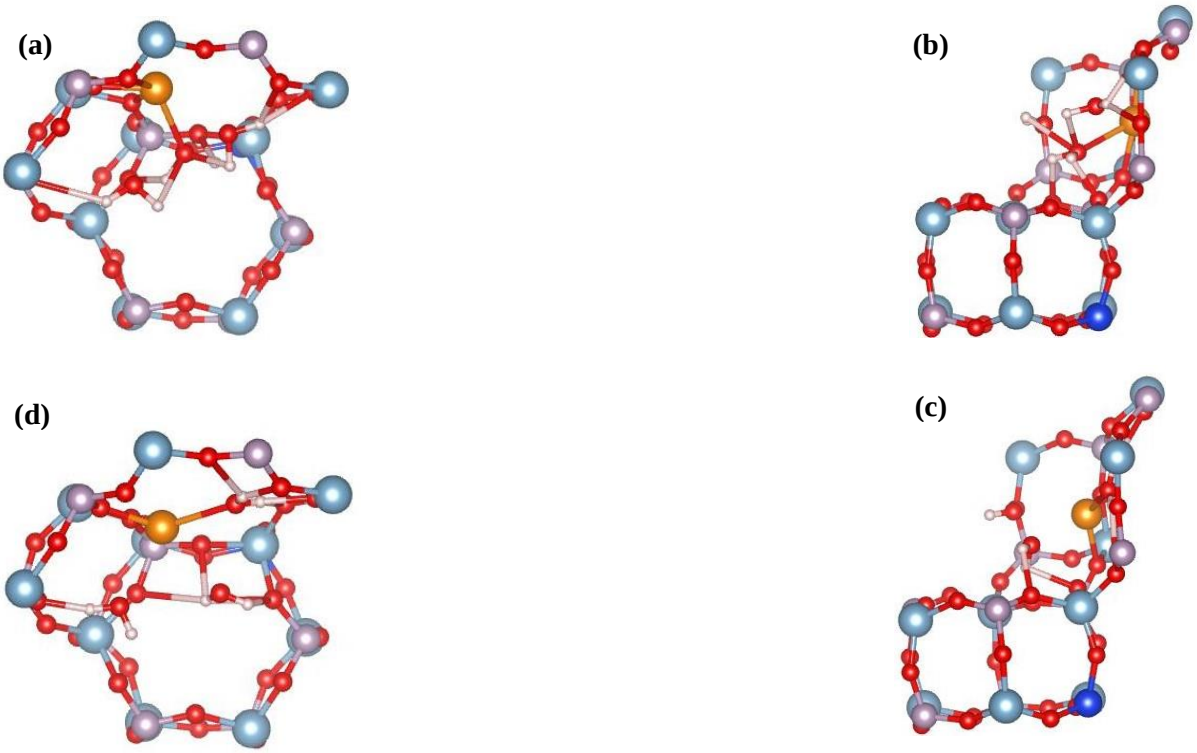

Figs. 50(a – d): Top and side views of three H_2O molecules calculation opposite Cu in site SIV before **(a)** – **(b)** and after **(c)** – **(d)**.

5.3.2.8.2 SSZ-13

The Cu and H_2O molecules behaviour in site SIV is very similar to that in SAPO-34, the Cu stays in the 8MR and the H_2O molecules are positioned adjacent to the framework in order to achieve zeolitic stabilization. However, the Cu(II) remained unaffected by the H_2O coordination unlike in SAPO-34 where we witnessed a Cu-O bond breaking. In SSZ-13, all three Cu-O bonds remained intact in addition to coordination to a H_2O molecule, see Figs. 51 – 53(a – d). Despite the absence of a Cu-O bond, we do observe an averaged increase in the Cu-O bond lengths in each of the calculation. The Cu-O bond increased is greater as the number of H_2O molecules added increases, see Table 41.

Like in SAPO-34, the H_2O molecule inside the 8MR plane has the shortest Cu-OH_2 bond, this bond coordination distance is the same as that in SAPO-34 at 2.41Å, see Table 42. The Cu-OH_2 distances in both SSZ-13 and SAPO-34 are all relatively consistent within the range of 2.41 to 3.51Å, indicating a strong Cu-OH_2 interaction. This seems to indicate that Cu(II) inside site SIV is a more accessible location for H_2O interaction compared to site SI where the Cu-OH_2 range is larger between 2.46 and 5.31Å. In addition to the more favourable adsorption energies for H_2O molecules around the SIV framework topology, it is possible to predict Cu in site SIV as a more accessible and reactive location for H_2O adsorption and other similar small permanent dipole molecules.

Table 41: List of Cu-O bond distances before and after for each SIV water calculation in SSZ-13.

No. of H_2O molecules	**Before**					**After**				
	Cu-O1	Cu-O2	Cu-O3	Cu-O4	Average	Cu-O1	Cu-O2	Cu-O3	Cu-O4	Average
1	2.1411	1.9597	2.1393	N/A	2.0800	2.1873	1.9701	2.1403	N/A	2.0992
2	“	“	“	“	“	2.1962	1.9981	2.1638	N/A	2.1194
3	“	“	“	“	“	2.2632	2.0156	2.1718	N/A	2.1502

Table 42: H_2O coordination to Cu(II) in SIV and corresponding bond distance in SSZ-13.

No. of H_2O molecules	**H_2O coordination(s)**	**Cu-O1H_2**	**Cu-O2H_2**	**Cu-O3H_2**
1	Yes	2.41	N/A	N/A
2	Yes	2.59	2.61	N/A
3	Yes	2.56	2.59	3.51

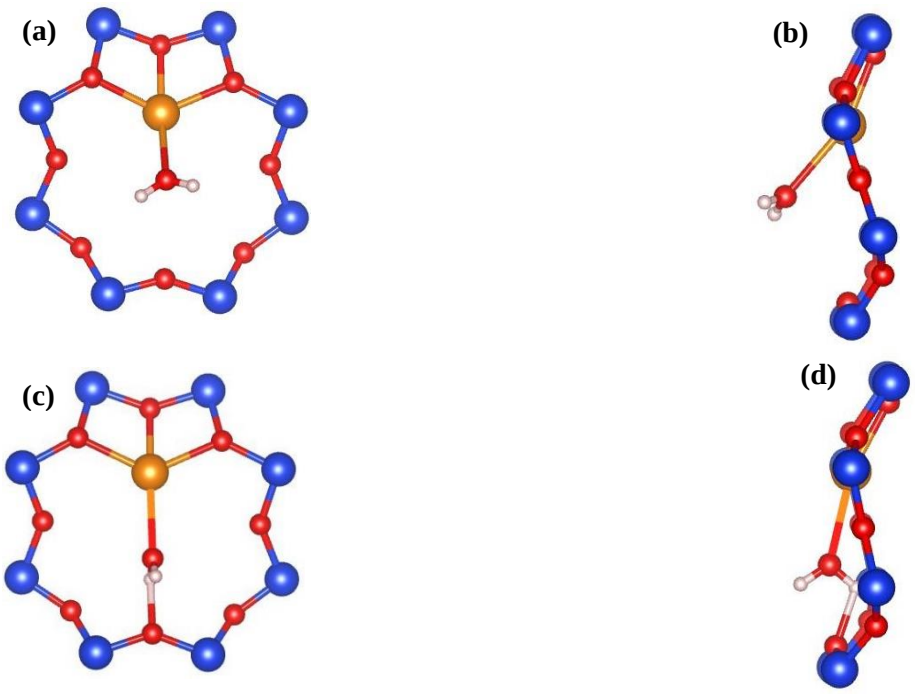

Figs. 51(a – d): Top and side views of one H_2O molecule calculation opposite Cu in site SIV before **(a)** – **(b)** and after **(c)** – **(d)**.

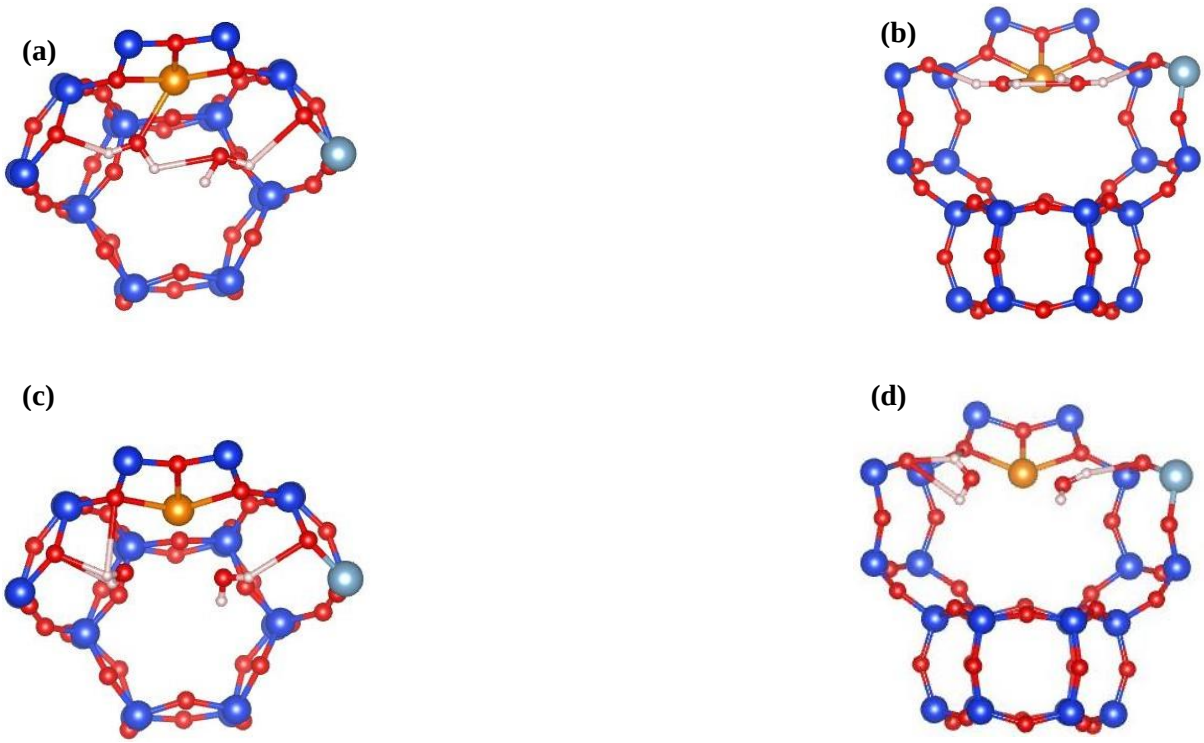

Figs. 52(a – d): Top and side views of two H_2O molecules calculation opposite Cu in site SIV before **(a)** – **(b)** and after **(c)** – **(d)**.

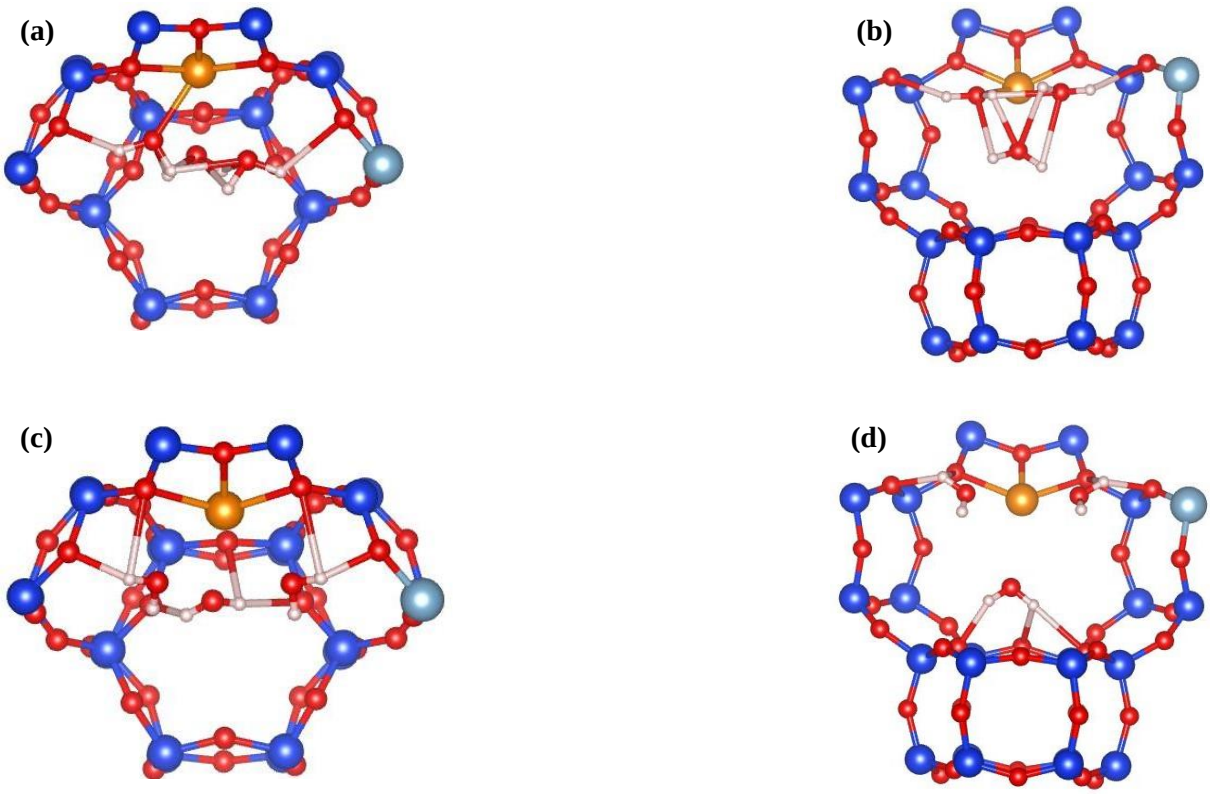

Figs. 53(a – d): Top and side views of three H_2O molecules calculation opposite Cu in site SIV before **(a)** – **(b)** and after **(c)** – **(d)**.

Summary 5.3: GULP water calculations

On the whole GULP calculations with H_2O molecules did not show a strong preference for one extra-framework site over another, within sites SI, SII, SIII and SIV. This is due to the large variations in adsorption geometries between the H_2O molecules with each other, and with the Cu^{2+}-framework, whilst the presence of hydrogen bonding skews the adsorption energies for determining the acidity of each site for H_2O molecular adsorption. In addition, H_2O coordination to the Cu^{2+} was not perceptibly observed in the calculations, therefore stabilization of Cu^{2+} inside the vacant areas of sites SII and SIII was not evident in the GULP calculations.

However, we observe in general that H_2O adsorption is favoured inside the SSZ-13 framework compared to the SAPO-34 by close inspection and deductions of the adsorption energies, see Tables 18, 19, 25, 26, 31, 32, 37 and 38.

5.4 CRYSTAL water calculations

In the GULP calculations with H_2O molecules within each of the extra-framework site (SI, SII, SIII and SIV), we observed that in general H_2O adsorption is favoured inside the SSZ-13 framework compared to the SAPO-34. This was determined by the adsorption energies and is an indication of the acidity of each site with respect to the H_2O molecules. In both SSZ-13 and SAPO-34, the ability of the H_2O molecules to stabilized Cu^{2+} inside the vacant spaces of the large cage and D6R of sites SII and SIII was not possible.

However, this is because in GULP when treating ionic materials like the case here, the Coulomb term is the dominant factor and can represent up to 90% of the total energy. Despite, the modified Buckingham potential used to describe the dispersion interaction between H_2O molecules and the framework oxygen atoms, as taken from Lewis *et al* work. The Buckingham potentials were modified from De Leeuw's results, since the *A* constant of the interaction between the framework T atom and oxygen atoms on water in the original result was approximately half that of the interaction between the T atom and framework oxygen atoms (Si – Ow *A* = 562.032eV, ρ = 0.32052Å and *C* = 10.66158eVÅ^6 and Al – Ow *A* = 584.1107eV, ρ = 0.29912Å and *C* = 0.0eVÅ^6). Lewis *et al* reverted to the same values as the T atom to the framework oxygen atom potentials, see Table n in Chapter n. This ensures avoidance of the "Buckingham catastrophe" at short distances, because during the minimization procedure the water can moves at unfeasible proximity to the T atoms.

Lewis *et al* increased the *A* constant to ensure a higher repulsive term between the water and the framework T atoms. In SSZ-13, the *A* constant terms used are 1283.907 and 1460.30eV for Si and Al respectively. Whilst, in SAPO-34, the *A* constant terms are the same for both Si and Al, in addition to 877.340eV for P. Taking into account two dopant substitution inside 36 T sites, in SSZ-13 the average *A* term is [(1283.907 x 34) + (1460.3 x 2)]/36 = 1293.71eV. While, in SAPO-34 the average *A* term felt is [(1460.3 x 18) + (877.34 x 16) + (1283.907 x 2)]/36 = 1191.41eV. If water molecules on average feels less of a repulsive force in SAPO-34, it should interact more strongly with the framework and result in a lower adsorption energy, but we observe otherwise.

It is very possible that since the Coulombic electrostatic force is a significant factor in determining the energy of a system in GULP as mentioned prior, the more ionic framework in SAPO-34 (Si^{4+}, Al^{3+} and P^{5+}) compared to the more covalent nature in the zeolite SSZ-13 means that H_2O adsorption as modelled by GULP calculations is less favoured in SAPO-34. This is because, despite the permanent dipole in a H_2O molecule it is still a neutral entity.

By employing CRYSTAL we aim to verify the accuracy of the GULP results, since quantum chemical calculations will enable the computation of the electronic structure of the framework system and interaction with water molecules, in addition to inclusion of the crystal-field splitting effect as observed in d^9 of Cu(II). To this aim we will investigate the following: (i) the effect of H_2O adsorption on Cu configuration in sites SI and SIV, (ii) how the difference in framework chemical composition affects H_2O adsorption in SSZ-13 and SAPO-34, (iii) the effect of number of dopants in sites SI and SIV on adsorption and (iv) whether H_2O molecules can stabilize Cu^{2+} inside sites SII and SIII.

5.4.1 Computational procedure

Like in the original quantum chemical calculations of Chapter 5.2, the hybrid DFT functional PBE0 including an additional 10% exact HF exact exchange was used in a PBC method. Geometry optimization calculations were performed to find the lowest energy equilibrium structures of H_2O adsorption in the frameworks of Cu-SSZ-13 and –SAPO-34. This was done via an atom only directive, where by only the atomic coordinates of all the atoms in the system was optimized.

The following procedure was developed for CRYSTAL calculations of water adsorption; firstly the bare SSZ-13 and SAPO-34 frameworks were optimized in GULP, then GULP optimized output coordinates were optimized in CRYSTAL via an atom only geometry optimization, subsequently H_2O molecules were docked inside the fully optimized SSZ-13 and SAPO-34 frameworks in *Moldraw* in order to be computed. Prior to docking the H_2O molecules were optimized in CRYSTAL with the same functional.

The dopant effect was included by building different dopant framework configurations labelled as single and paired. In the single configuration, only one dopant atom is present in the Cu occupied location of sites SI and SIV. But in the paired configuration, two dopant atoms are present. This enables to study how the number of dopant atoms in a site affects the Cu's interaction with the H_2O molecules in sites SI and SIV.

5.4.2 Results

5.4.2.1 Site SI configuration

5.4.2.1.1 Single Si/Al atoms

Upon adsorption of H_2O molecules in sites SI, the H_2O coordinates to the Cu(II) with relative differing strengths in SSZ-13 and SAPO-34, 2.0522 and 1.9148Å respectively. The difference in coordination strengths could be as a result of the different angle of H_2O approach to the Cu, in SAPO-34 the H_2O molecule is coordinated to the Cu at a 61.7˚ angle against the 6MR plane. This acute angle enables H_2O molecule to tilt away from the framework's background negative charge centred around the Si dopant atom, in order to avoid electrostatic repulsion between the lone pairs on the H_2O's oxygen atoms and the excess electronegativity from the different valences in a Si → P substitution.

However, for SSZ-13 this approach is less pronounced since the H_2O molecule is at 89.4˚ angle with respect to the plane of 6MR. The H_2O molecule is marginally tilted away from the Al dopant atom, but to a lesser extent than in SAPO-34. This can explain the weaker Cu-OH_2 bond, as the electrostatic repulsion felt by the H_2O molecule is greater when coordinated to Cu at a near-perpendicular fashion compared to the acute angle observed in SAPO-34.

The average Cu-O bond lengths prior H_2O adsorption are 1.9672 and 1.9658 in SSZ-13 and SAPO-34 respectively – very similar strengths with regards to Cu's coordination to the 6MR. The Cu forms a distorted square planer inside the 6MR in both frameworks, the addition of a H_2O coordination does not change this configuration. But the Cu-O bonds weakens in SSZ-13 and SAPO-34, the average Cu-O bond length is increased to 2.0152 and 2.1037Å respectively, see Tables 43 and 44. It is important to note, in SAPO-34, the Cu-O3 bond is on the boundary of bond-breaking with a long bond length of 2.4593Å, an indication of the strong H_2O coordination to Cu.

Table 43 (distances in Angstroms)

SSZ-13									
Before					**After**				
Cu-O1	Cu-O2	Cu-O3	Cu-O4	Spin on Cu	Cu-O1	Cu-O2	Cu-O3	Cu-O4	Cu-OH_2	Spin on Cu
1.9627	1.8989	2.0280	1.9790	0.75	1.9920	1.9289	2.1000	2.0399	2.0522	0.77

Table 44 (distances in Angstroms)

SAPO-34									
Before					**After**				
Cu-O1	Cu-O2	Cu-O3	Cu-O4	Spin on Cu	Cu-O1	Cu-O2	Cu-O3	Cu-O4	Cu-OH_2	Spin on Cu
1.9049	1.9519	1.9858	2.0207	0.74	1.9000	1.9847	2.4593	2.0706	1.9148	0.79

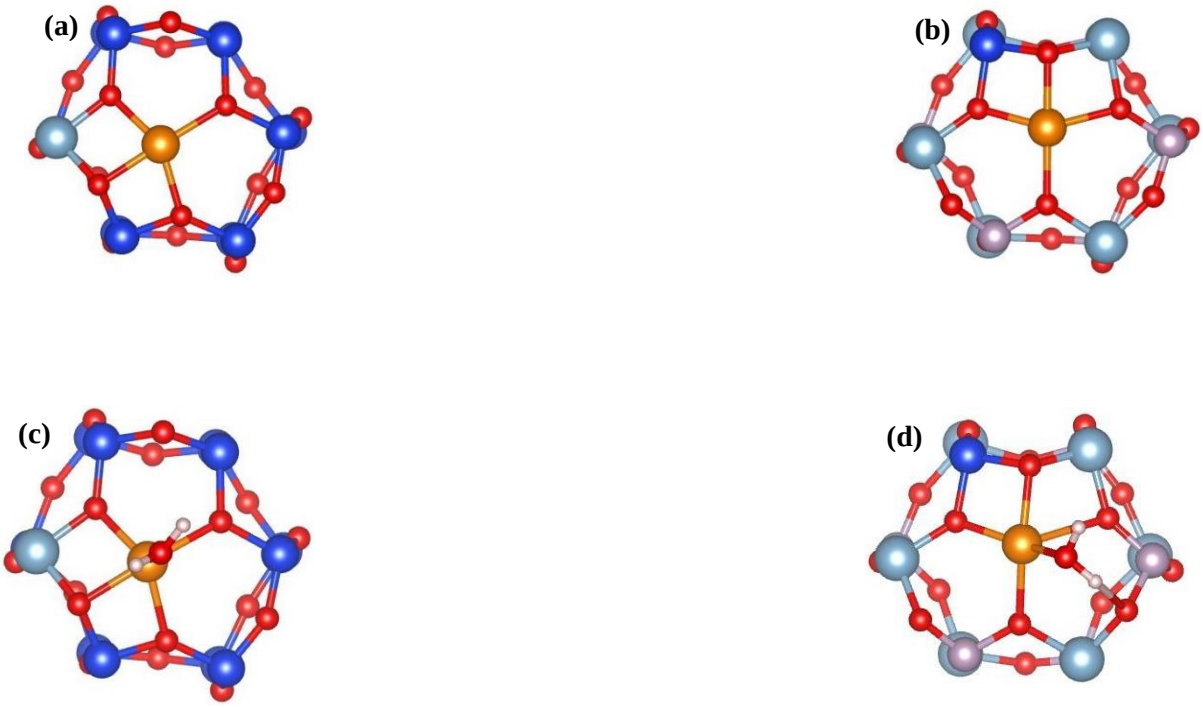

Figs. 54(a – d): (a – b) (001) view of the Cu inside the 6MR of site SI in the single configuration before H_2O coordination, and **(c – d)** after coordination.

In both frameworks the coordination of H_2O to Cu results in an elevation of the Cu from the plane of the 6MR as a result of the pulling force of H_2O on Cu. Prior to H_2O coordination the Cu was 0.4954 and 0.4533Å above the plane of the 6MR in SSZ-13 and SAPO-34 respectively – relatively flat geometries, and after H_2O adsorption the Cu rises from the 6MR plane by distances of 0.1845 and 0.3975Å respectively, see Tables 45. This increased in distances of Cu from the plane of 6MR is significant in both frameworks, especially in SAPO-34 which is approximately twice the increase observe in SSZ-13. The averaged Cu-O bond lengths upon coordination looks to agree well, since averaged Cu-O lengths in SAPO-34 are 0.0885Å greater than in SSZ-13. The Cu-O bond lengths are not directly proportional to the distance between the Cu and the 6MR plane, because the position of the 6MR plane is determined as a function of the T atoms' coordinates, since they are observed to be more static therefore gives an accurate account of the 6MR position. This is unlike the framework oxygen atoms which are either pushed upwards or pulled downwards upon coordination. Therefore, the Cu-O bond lengths would provide a partial indication of the position of Cu relative to the 6MR plane, as the framework oxygen atoms moves in sync with the Cu's behaviour.

The H_2O coordination to Cu in site SI is not observed in the GULP results despite the absence of dopant atoms in the 6MR (see Chapter 5.3). Instead, the H_2O molecules in both SSZ-13 and SAPO-34 are adsorbed on the 4MR framework adjacent to site SI. This difference in adsorption behaviour could be due to the presence of a single dopant atom in the 4MR, enabling a hydrogen atom on the H_2O molecule to form a hydrogen bond to it. However, it is more likely that the inclusion of crystal field splitting in CRYSTAL enables the H_2O molecule to coordinate in such a fashion, unlike in GULP where the coordination is driven largely by Coulombic electrostatic forces and the Buckingham potential.

Table 45 (distances in Angstroms)

	SSZ-13	**SAPO-34**
	Cu – plane of 6MR distance (Å)	Cu – plane of 6MR distance (Å)
Before	0.495408	0.453317
After	0.679872	0.850859
Difference	0.184464	0.397541

Figs. 55(a – d): (a – b) (110) view of the Cu inside the 6MR of site SI in the single configuration before H_2O coordination, and **(c – d)** after coordination.

5.4.2.1.2 Paired Si/Al atoms

The H_2O molecules can coordinate on the Cu inside the paired configurations like in the single, but as expected the strength of the coordination is weaker. The Cu-OH_2 distances are 2.1157 and 2.0303Å in SSZ-13 and SAPO-34, the coordination lengths approximately increased by 10% compared to the single configurations in both frameworks, see Tables 46 and 47.

Increased in Cu-OH_2 bond length is indication of a weaker coordination, this is because the Cu coordination to all four activated framework oxygen atoms in the 6MR results in a stronger Cu-O bonds, as indicated by the averaged Cu-O bond lengths of the bare paired configurations in SSZ-13 and SAPO-34. In the paired configurations, these averaged lengths are 1.9448 and 1.9551Å, which are significantly shorter than in the single configurations. The stronger Cu-O bonds in the paired configurations, is because all four oxygen atoms coordinated to the Cu are adjacent to the dopant atoms in the 6MR, therefore activated. Subsequently, these framework oxygen atoms feel more keenly the excess electronegative charge centred around the dopant atoms in SSZ-13 and SAPO-34, therefore acting as stronger ligands towards the Cu^{2+}.

In addition, the average weakening of the Cu-O bonds after H_2O coordination is less pronounced compared to in the single configuration. The averaged Cu-O bond lengths after H_2O coordination are 1.9809 and 2.0222Å for SSZ-13 and SAPO-34. This is a 0.036 and 0.067Å increased in Cu-O distance, note that the lengthening in SAPO-34 is approximately twice that of SSZ-13. In the single configuration, the increase in the Cu-O bond lengths are 0.048 and 0.138Å for SSZ-13 and SAPO-34. The change in the final Cu-O bond lengths between the single and paired is more significant for the SAPO-34.

The greater Cu-O lengthening after H_2O coordination in SAPO-34 and relatively similar averaged Cu-O bond lengths between single and paired configurations (0.036 and 0.048Å) in SSZ-13 is a result of the different angles of approach from H_2O in the two frameworks. In SAPO-34, the asymmetrical distribution of the two Si dopant atoms around the 6MR enables the H_2O to approach at an acute angle of 79˚. Looking at Fig. 56d, it is interesting to observe the H_2O is tilted towards the space between the two Si dopant atoms instead of on the other side of the 6MR. It is expected the H_2O would occupy the space away from the dopant atoms, this could be due an effect akin to the trans influence. Since, three of the four framework oxygen atoms coordinated to Cu^{2+} is activated. Taking into account the more ionic nature of AlPO, it is possible these oxygens are significantly strong σ donors, then the ligand trans to these oxygen atoms cannot donate electrons to the Cu^{2+} so well, resulting in a weaker interaction. This could force the H_2O molecule to approach the Cu at a position that is not trans to these oxygen atoms. However, in SSZ-13 all four framework oxygen atoms coordinated to the Cu are activated, consequently the excess electron density around the Cu could possibly be higher than in SAPO-34 resulting in a weaker H_2O coordination as indicated by the Cu-OH_2 bond lengths and the averaged Cu-O bond length.

In addition, for SSZ-13, the Al dopant atoms around the 6MR are symmetrically aligned and this forces the H_2O molecule to approach the Cu at a perpendicular fashion with respect to the 6MR. The similar adsorption orientations in the single and pair configurations ensures similar strengths of coordination with the Cu, and subsequent weakening of the Cu-O bonds within a small range of 0.036 – 0.048Å.

Table 46 (distances in Angstroms)

SSZ-13										
Before					**After**					
Cu-O1	Cu-O2	Cu-O3	Cu-O4	Spin on Cu	Cu-O1	Cu-O2	Cu-O3	Cu-O4	Cu-OH_2	Spin on Cu
1.9270	1.9627	1.9643	1.9250	0.78	1.9615	2.0011	2.0071	1.9538	2.1157	0.81

Table 47 (distances in Angstroms)

SAPO-34										
Before					**After**					
Cu-O1	Cu-O2	Cu-O3	Cu-O4	Spin on Cu	Cu-O1	Cu-O2	Cu-O3	Cu-O4	Cu-OH_2	Spin on Cu
1.9543	2.0312	1.9024	1.9325	0.78	2.0869	2.1037	1.9266	1.9717	2.0303	0.79

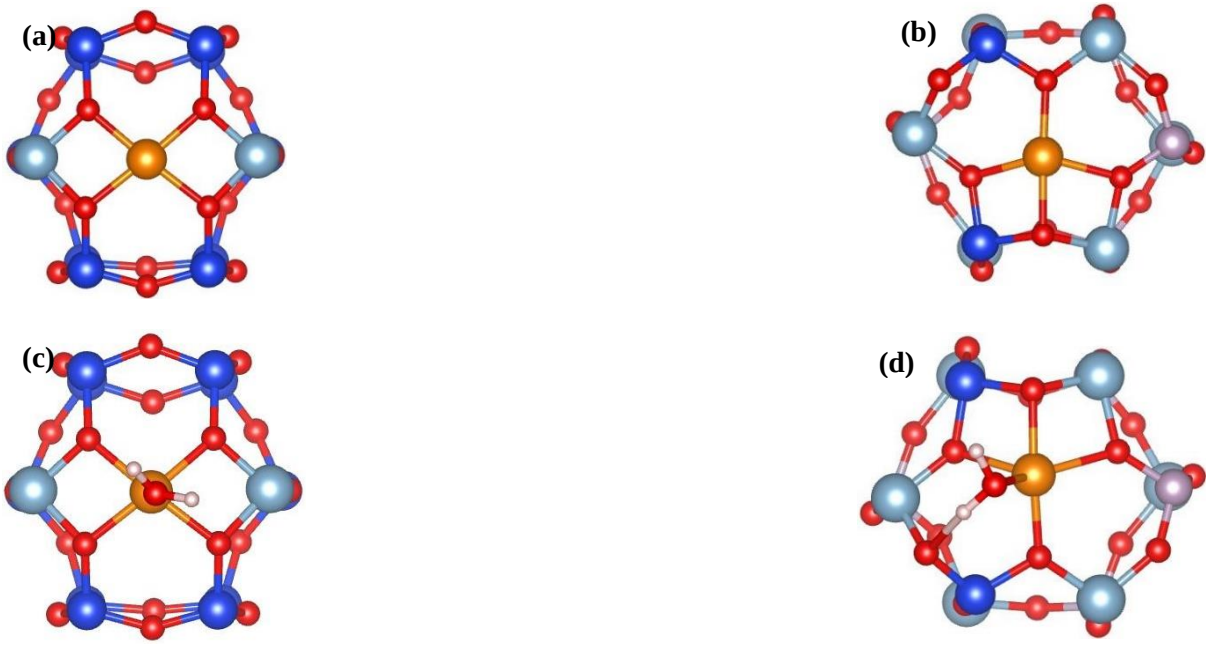

Figs. 56(a – d): (a – b) (001) view of the Cu inside the 6MR of site SI in the pair configuration before H_2O coordination, and **(c – d)** after coordination.

The distances between Cu and the 6MR decreased in both SSZ-13 and SAPO-34 upon H_2O coordination resulted in an increased in distance of Cu away from the 6MR plane, see Table 48. There is only a slight perceptible change for SSZ-13 at 0.1881Å in the paired and 0.1845Å in the single, since both adsorption configurations have the H_2O molecule perpendicular to the 6MR. SAPO-34 experienced approximately a decrease by half, this

significant change is because of the change in H_2O orientation during coordination with Cu from single to pair, thereby affecting the strength of H_2O adsorption.

The Cu distance to the plane of 6MR provides an indication of the strength of the pulling force exerted by the H_2O molecule on the Cu. Likewise, it gives a measure of the strength of the Cu coordination to the 6MR plane. The Cu to 6MR plane distances before H_2O adsorption in SAPO-34 and SSZ-13 are shorter in the pair than the single configurations, in good agreement with the shorter Cu-O bond lengths observed in the pair configurations as mentioned prior.

Table 48 (distances in Angstroms)

	SSZ-13	**SAPO-34**
	Cu – plane of 6MR distance (Å)	Cu – plane of 6MR distance (Å)
Before	0.481647	0.414643
After	0.669732	0.689385
Difference	0.188085	0.207734

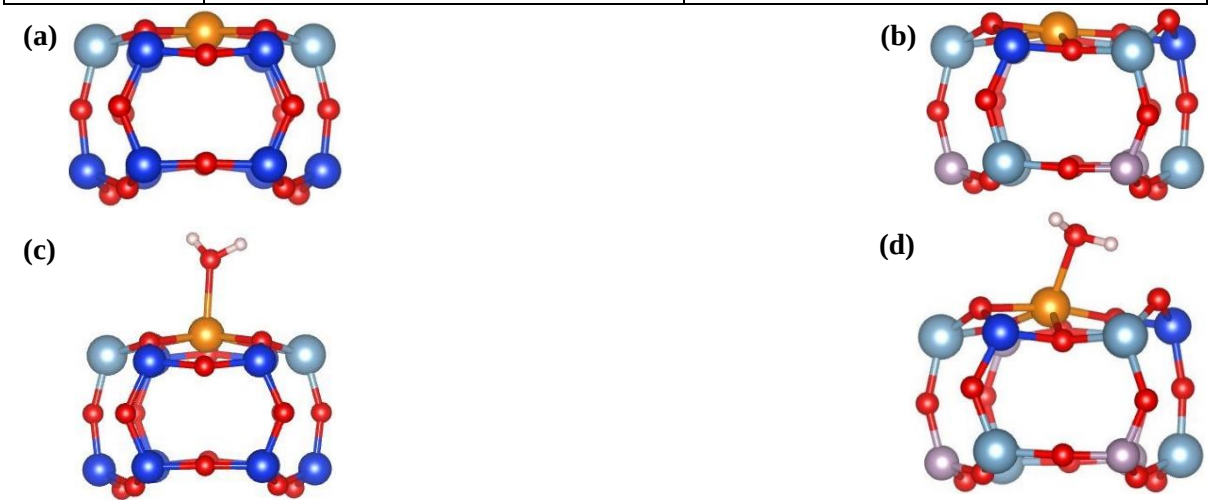

Figs. 57(a – d): (a – b) (110) view of the Cu inside the 6MR of site SI in the pair configuration before H_2O coordination, and **(c – d)** after coordination.

5.4.2.1.3 Two H_2O molecules – Single Si/Al atoms

With two H_2O molecules inside the single configuration we observe in both SSZ-13 and SAPO-34, the displacement of Cu from the 6MR. In both frameworks the two H_2O molecules are coordinated to the Cu of similar strengths, see Tables 49 and 50, breaking Cu's distorted square planar geometry inside the 6MR. The two weakest Cu-O bonds are broken in the process which are the bonds formed by non-activated framework oxygen atoms as indicated by Cu-O bond lengths. The resulting configuration has Cu bonded to two of the activated framework oxygen atoms in the 6MR, but pulled above the 6MR into the large cage by the coordination of the two H_2O molecules, see Figs. 58(a – b).

The resulting configuration looks to be relatively stable as indicated by the strong coordination bonds observed with Cu, in SSZ-13 and SAPO-34 the bond lengths either from the activated framework oxygen atoms or H_2O molecules are below 2.0Å. This shows that the

displacement of Cu from the 6MR in site SI is possible, considering the site was observed to be the equilibrium extra-framework site in CHA, due to energetic and steric factors.

Table 49 (distances in Angstroms)

SSZ-13									
Before					**After**				
Cu-O1	Cu-O2	Cu-O3	Cu-O4	Spin on Cu	Cu-O1	Cu-O2	Cu-O1H_2	Cu-O2H_2	Spin on Cu
1.9627	1.8989	2.0280	1.9790	0.75	1.9293	1.9460	1.9545	1.9144	0.76

Table 50 (distances in Angstroms)

SAPO-34									
Before					**After**				
Cu-O1	Cu-O2	Cu-O3	Cu-O4	Spin on Cu	Cu-O1	Cu-O2	Cu-O1H_2	Cu-O2H_2	Spin on Cu
1.9049	1.9519	1.9858	2.0207	0.74	1.9960	1.8933	1.9123	1.9800	0.78

Figs. 58(a – b): (001) view of the Cu inside the 6MR of site SI in the single configuration after coordination with two H_2O molecules.

The distance between Cu and the plane of 6MR shows a substantial increased after coordination with the two H_2O molecules, see Table 51. In SSZ-13, the Cu is pulled from the plane of the 6MR by a distance of 1.1468Å and in SAPO-34 by 1.1301Å. Showing that the Cu has been dislocated from the 6MR plane in both frameworks, see Figs. 59(a – b). The pull exerted on Cu is significantly greater than that observe in the one H_2O molecule calculation, see Table 45. Confirming the strength of the combined pulling force exerted by two H_2O molecules. It is plausible that increasing the number of H_2O molecules to four in order to aid a square planar geometry around the Cu^{2+} when coordinated, the Cu would be completely dislocated from the 6MR. However, this would involve the breaking of the Cu-O bonds with the activated framework oxygen atoms which are strong σ-donors.

Table 51 (distances in Angstroms)

	SSZ-13	**SAPO-34**
	Cu – plane of 6MR distance (Å)	Cu – plane of 6MR distance (Å)
Before	0.495408	0.453317
After	1.642201	1.583387
Difference	1.146793	1.130070

Figs. 59(a – b): (110) view of the Cu inside the 6MR of site SI in the single configuration after coordination with two H_2O molecules.

5.4.2.1.4 Two H_2O molecules – Pair Si/Al atoms

When increasing the number of H_2O molecules available to be coordinated in the pair configurations; in SSZ-13 the symmetric Al-O-Si-O-Si-Al sequence only enables coordinative space for one H_2O molecule to attack, and the other H_2O molecule occupies space in the large cage in between the 8MR and the first H_2O molecule, see Fig. 60a. The secondary H_2O molecule is strongly hydrogen bonded to the first with a bond distance of 1.68Å, and weakly bonded to the framework oxygen atoms in the 8MR (2.29 and 2.33Å).

On the other hand, in SAPO-34 the unsymmetrical arrangement of Si dopant atoms around the 6MR allows both H_2O molecules to simultaneously coordinate to the Cu. It is important to note that the two H_2O molecules are coordinated to the Cu trans to each other, in order to avoid significantly more π-back donation when trans to the activated framework oxygen atoms. The H_2O molecules achieve differing coordination strengths to the Cu, see Table 53. It is the H_2O molecule that is nearest to the Si dopant atoms that have the weaker coordination to Cu, this is because of the electrostatic repulsion between the electronegative oxygen atom on H_2O and the background negative charge centred around the Si atoms. This is responsible for a reduction in strength by 0.2347Å compared to the H_2O molecule on the other side of the 6MR.

In SSZ-13 the Cu-O bond length is 2.0659Å which is similar to in length to the calculation containing one H_2O molecule at 2.1157Å as expected. However, in SAPO-34 the ability to have two H_2O molecules coordinated to Cu resulted in one of the coordination bond to be stronger than in the one H_2O molecule calculation, 1.9418Å for the former and 2.0303Å for the latter. This is because with one H_2O molecule coordinated to the Cu, SAPO-34 maintains a distorted square planar geometry inside the 6MR. However, when two H_2O molecules are coordinated this geometry is broken, only three Cu-O bonds are present. Since the excess density around the Cu would be less than with four Cu-O bonds, enabling stronger coordination to the H_2O molecules without significant π-back donation.

Table 52 (distances in Angstroms)

SSZ-13									
Before					**After**				
Cu-O1	Cu-O2	Cu-O3	Cu-O4	Spin on Cu	Cu-O1	Cu-O2	Cu-O3	Cu-O4	Cu-OH_2	Spin on Cu
1.9270	1.9627	1.9643	1.9250	0.78	1.9613	2.0149	2.0195	1.9765	2.0659	0.83

Table 53 (distances in Angstroms)

SAPO-34										
Before					**After**					
Cu-O1	Cu-O2	Cu-O3	Cu-O4	Spin on Cu	Cu-O1	Cu-O2	Cu-O3	Cu-$O1H_2$	Cu-$O2H_2$	Spin on Cu
1.9543	2.0312	1.9024	1.9325	0.78	2.0427	2.0427	1.9351	1.9418	2.1775	0.81

Figs. 60(a – b): (001) view of the Cu inside the 6MR of site SI in the pair configuration after inclusion of two H_2O molecules.

In SSZ-13, despite the coordination of only one H_2O molecule on Cu, the overall pull felt by Cu is greater than in the one H_2O molecule calculation, since Cu is pulled away from the plane of the 6MR by a distance of 0.2583Å compared to 0.1881Å with only one H_2O molecule present within the vicinity. This indicates that the permanent dipole of the non-coordinated H_2O molecule might be active in exerting a slight pull on the Cu. It is possible the additional pull felt by Cu is due to the increased strength in bonding with the coordinated H_2O molecule, since the Cu-OH_2 bond length is 2.0659Å compared to 2.1157Å in the one H_2O molecule calculation. Considering the pull on Cu in the two H_2O molecules calculation inside the single configuration was calculated at 0.1845Å with a Cu-OH_2 bond length of 2.0522Å – a similar coordination strength to the H_2O coordination in the two H_2O molecules calculation for the pair configuration. It can be deduced that the additional pull felt Cu is from the non-coordinated H_2O molecule.

The distance between Cu and the 6MR is significantly larger in the SAPO-34, this is not surprising because two H_2O molecules are coordinated to the Cu unlike in SSZ-13. The distance from the 6MR is 0.6100Å – approximately two and a half times that observe in SSZ-13. The distance pulled by the two coordinated H_2O molecules in the pair configuration is greater than the one H_2O molecule coordinated inside the single. It is interesting to observe the difference in behaviour of the framework oxygen atoms in the 6MR between SSZ-13 and SAPO-34, in the former the oxygen atoms are relatively flat, but in the latter the oxygen atoms rises up like edges indicating a more flexible framework behaviour in the SAPO-34. This difference is only observed in the pair configurations, since in the single both frameworks have oxygen atoms that moves relative to the Cu atom. In SSZ-13, the inclusion of the second Al dopant atom in a symmetric fashion seems to "fix" the oxygen atoms in the 6MR in place.

Table 54 (distances in Angstroms)

	SSZ-13	**SAPO-34**
	Cu – plane of 6MR distance (Å)	Cu – plane of 6MR distance (Å)
Before	0.481647	0.414643
After	0.739896	1.024620
Difference	0.258250	0.609977

Figs. 61(a – b): (110) view of the Cu inside the 6MR of site SI in the pair configuration after inclusion of two H_2O molecules.

Comparing the GULP and CRYSTAL calculations inside site SI, the behaviour of the H_2O molecules are relatively different. This is because, in GULP the H_2O molecules adsorb onto the framework with higher frequency instead of coordinating to the Cu^{2+}, and the coordination to the Cu^{2+} when present is weak. Whilst in CRYSTAL, the H_2O molecules are coordinated to the Cu^{2+} unless of dopant effect as in the pair configuration for SSZ-13 with two H_2O molecules in the vicinity.

This discrepancy in H_2O behaviour between the two methods is due to the difference in calculating the interaction between H_2O molecules and the Cu^{2+}. In GULP, this interaction is described by a Buckingham potential to model the oxygen atom on a H_2O molecule with the Cu^{2+}. Despite, the strong electrostatic attractive force between the two opposite charge as determined by Coulomb's Law. The *A* repulsive term in the Buckingham potential for the Cu-OH_2 interaction is relatively high at 712.80eV, much higher than that for the Buckingham

potential between hydrogen atoms on H_2O and the framework oxygen atoms (396.27eV). Subsequently, in GULP we will observe the greater tendency of H_2O molecules to adsorb on the frameworks in SSZ-13 and SAPO-34 instead of coordinating to Cu^{2+}.

In CRYSTAL, since Cu^{2+} interaction with the permanent dipole of the H_2O molecule is largely determined by electrostatic forces. The hybrid DFT method used in our calculations is be able to accurately model the Coulomb's interactions as determined by exchange and correlation interactions.

5.4.2.2 Site SI energy

5.4.2.2.1 Single Si/Al atoms

The adsorption energy for the adsorption of a single H_2O molecule onto Cu^{2+} in site SI is -1.31 and -1.38eV at SSZ-13 and SAPO-34 respectively, see Table 55. The adsorption energy for SAPO-34 is -0.07eV more favourable. This is because the strength of adsorption in SAPO-34 is stronger than in SSZ-13, as indicated by the Cu-OH_2 bond lengths, see Table 43. The bond strength was as a result of the differing angle of approach made by the H_2O molecule, since in SAPO-34 the H_2O molecule approaches in an acute away in order to distant away from the Al dopant atom.

Table 55 (Energy in -eV)

SSZ-13					**SAPO-34**				
E_{Zeol+H_2O}	E_{Zeol}	E H_2O	Rel. E	Ads. E	E_{AlPO+H_2O}	E_{AlPO}	E H_2O	Rel. E	Ads. E
475047.86	472969.38	2077.16	472970.69	1.31	477118.05	475039.51	2077.16	475040.89	1.38

5.4.2.2.2 Pair Si/Al atoms

The adsorption energies in the pair configurations decreased relative to the single, see Table 56. This is because of the more favourable bare Cu-framework energy, since the addition of a second dopant atom in the 6MR results in a stronger Cu coordination to the framework oxygen atoms in the 6MR. The number of activated oxygen atoms in the 6MR increases from two to four and in SSZ-13 all four are coordinated to Cu. These activated oxygen atoms would be strong σ-donor, this explains the lower adsorption energy of -1.00eV. In SAPO-34, three of the four activated oxygens are coordinated to Cu, therefore the state of Cu in the 6MR is less secured in terms of strength of Cu-O bonding relative to SSZ-13. Subsequently, the adsorption energy is more favoured in SAPO-34

Table 56 (Energy in -eV)

SSZ-13					**SAPO-34**				
E_{Zeol+H_2O}	E_{Zeol}	E H_2O	Rel. E	Ads. E	E_{AlPO+H_2O}	E_{AlPO}	E H_2O	Rel. E	Ads. E
475049.32	472972.16	2077.16	472972.16	1.00	477119.29	475040.85	2077.16	475042.13	1.27

5.4.2.2.3 Two H_2O molecules – Single Si/Al atoms

Upon the adsorption of two H_2O molecules on Cu inside the single configuration, it is the SSZ-13 that achieved the lower adsorption energy by -0.10eV, see Table 57. The strength of Cu-OH_2 coordination for both H_2O molecules in SSZ-13 is on average stronger than SAPO-34, as indicated by the bond lengths, see Tables 49 and 50. This could possibly explain the more favourable adsorption energy in SSZ-13 compared to SAPO-34, since both frameworks have the same dopant configuration and the adsorption geometries of the H_2O molecules are identical, see Figs. 58(a – b) and Figs. 59(a – b).

Table 57 (Energy in -eV)

SSZ-13					**SAPO-34**				
E_{Zeol+H_2O}	E_{Zeol}	E H_2O	Rel. E	Ads. E	E_{AlPO+H_2O}	E_{AlPO}	E H_2O	Rel. E	Ads. E
477126.65	472969.38	4154.33	472972.33	2.95	479196.68	475039.51	4154.33	475042.36	2.85

5.4.2.2.4 Two H_2O molecules – Pair Si/Al atoms

SAPO-34 has significantly the more favourable adsorption energy by -0.47eV, see Table 58. The symmetric placement of the Al dopant atoms in the 6MR prevented an additional H_2O molecule to coordinate with the Cu, due to the electrostatic repulsion. However, in SAPO-34 there is coordinative space for two H_2O molecules to coordinate with the Cu, due to the ordering of the Si dopant atoms in the 6MR. This would explain the large difference in adsorption energy between the two frameworks.

Table 58 (Energy in -eV)

SSZ-13					**SAPO-34**				
E_{Zeol+H_2O}	E_{Zeol}	E H_2O	Rel. E	Ads. E	E_{AlPO+H_2O}	E_{AlPO}	E H_2O	Rel. E	Ads. E
477127.44	472972.16	4154.33	472973.11	1.95	479197.60	475040.85	4154.33	475043.28	2.42

5.4.2.3 Site SII configuration

5.4.2.3.1 SSZ-13

In the GULP water calculations due to the poorly built Hessian matrix during the minimization step, this restricted the number of H_2O molecules that we were able to model especially in site SII calculations, since no zeolitic stabilization will be provided to the Cu^{2+} atom. We observe from a brute force approach in building the GULP calculations database as a function of extra-framework sites and dopant configurations, that site SII in the large cage is an energy maximum. Subsequently, Cu^{2+} does not reside inside site SII, however, in our CRYSTAL calculations we witness the stabilization of Cu^{2+} inside the large cage by providing six H_2O molecules around the metal centre in an octahedral fashion to promote stabilization, see Figs. 62(a – b).

The Cu-OH_2 bond lengths are listed in Table 59 and are within the range of 1.92 – 2.20Å. We are able to observe the Jahn – Teller effect by deduction of the bond lengths, this is expected considering the d^9 electronic configuration in Cu(II) results in an odd number of electrons in the e_g orbitals. This tetragonal distortion is observed as a result of the orbital degeneracy of $d_{x^2-y^2}$ and d_{z^2}, and the Jahn – Teller effect will distort this degeneracy in order to achieve a lower ground state electronic energy. In this case here, this results in the compression of the two axial bonds and the elongation of the four equatorial bonds.

It is more common to observe axial elongation instead of equatorial because this weakens two bonds instead of four. Since the distortion is a function of energetics, this indicates that in this case two of the three electrons in Cu(II) occupies the $d_{x^2-y^2}$ orbital instead of the d_{z^2}.

The H_2O molecules are oriented in an alternative fashion between horizontal and vertical alignment to avoid steric clashes between the hydrogen atoms with the neighbouring H_2O. In addition, the overall position of the $[Cu(OH_2)_6]^{2+}$ complex inside the large cage is shifted closer to one side of the framework. This ensures the H_2O molecules can interact with the zeolitic framework via hydrogen bonding; the H_2O molecules maximizes this exposure by adjusting the hydrogen atoms in the direction of the framework oxygen atoms.

This adsorption geometry would not have been observed in GULP, because the electronic effects in tetragonal distortion of Jahn – Teller is a significant factor in achieving the equilibrium energy. Whilst, in GULP the potential energy is only as a function of the nuclear coordinates determined in this case by Coulomb's Law and the Buckingham potential, to model the Cu-OH_2 interactions.

Table 59 (distances in Angstroms)

SSZ-13						
Cu-O1H_2	Cu-O2H_2	Cu-O3H_2	Cu-O4H_2	Cu-O5H_2	Cu-O6H_2	Spin on Cu
2.19974	2.05848	2.10231	2.00748	1.92443	1.96998	0.85

Figs. 62(a – b): (a) (110) and **(b)** (001) views of the $[Cu(OH_2)_6]^{2+}$ complex inside the large cage of site SII in SSZ-13.

5.4.2.3.2 SAPO-34

The AlPO framework does not from first inspection affect the behaviour of the $[Cu(OH_2)_6]^{2+}$ complex compared with in SSZ-13. The Cu^{2+} is stabilized inside the large cage by the octahedral arrangement of the H_2O molecules. The Jahn – Teller tetragonal distortion is also observed in SAPO-34, indeed the same distortion as in SSZ-13 occurred – axial compression and equatorial elongation, see Table 60.

The overall position of the $[Cu(OH_2)_6]^{2+}$ complex moves nearer to the framework inside the large cage in order to achieve hydrogen bonding between framework oxygen atoms and the H_2O molecules, like in SSZ-13, see Figs. 63(a – b).

Table 60 (distances in Angstroms)

SAPO-34						
Cu-O1H_2	Cu-O2H_2	Cu-O3H_2	Cu-O4H_2	Cu-O5H_2	Cu-O6H_2	Spin on Cu
2.01214	2.13175	2.01126	2.26327	1.91414	1.97230	0.87

Figs. 63(a – b): (a) (110) and **(b)** (001) views of the $[Cu(OH_2)_6]^{2+}$ complex inside the large cage of site SII in SAPO-34.

5.4.2.4 Site SII energy

The adsorption energies were not calculated for the site SII calculations, since when the Cu^{2+} is situated inside SII, it is reduced to Cu^{+}. This is dictated by looking at the spin magnetic moment of Cu (see Chapter 5. 2. 1). Since, we are unable to calculate the absolute equilibrium energy values of the bare Cu^{2+}-exchanged frameworks, we compared the relative stabilities of the $[Cu(OH_2)_6]^{2+}$ complex in SSZ-13 and SAPO-34 by looking at the relative energies, see Table 61. In addition, we deduced the energy contribution per H_2O molecule in the complex and compared this against the Cu-O bonds (energy per bond) belonging to the framework, when Cu^{2+} occupies sites SI and SIV. In doing so, we are to gain an insight into the energetic preference of Cu^{2+} between H_2O ligands and framework O atoms in either SSZ-13 or SAPO-34.

The calculation of relative energy was observed in equation 49 of Chapter 5.3. It gives an indication of the energy of a bare Cu^{2+}-exchanged framework and any residing energy from the interaction between the H_2O molecules and the Cu^{2+} and with the framework. On average, the equilibrium energies of a Cu-SAPO-34 configuration is -2070.23eV lower in energy compared to Cu-SSZ-13 (taken from an average of the framework configurations used). The difference in relative energies between SSZ-13 and SAPO-34 is: -472976.45eV - -475045.85eV = -2069.43eV. Considering the averaged difference in equilibrium energies between Cu-SSZ-13 and Cu-SAPO-34 is -2070.23eV, the difference in relative energies between the two frameworks is -2069.43eV – a 0.81eV discrepancy. This shows strongly that the difference in relative energies between the frameworks is largely due to the different chemical compositions between SSZ-13 and SAPO-34, and not because of a specific difference in H_2O interactions inside the frameworks.

Looking at Table 61, and inspecting the energy per H_2O or Cu-O bond (framework), it is Cu^{2+} coordinated to the framework O atoms which are the more energetically favourable in either SSZ-13 or SAPO-34. This is especially evident when inside the 8MR windows of site SIV, since the energy contribution per Cu-O bond is pronouncedly twice the magnitude of that for a Cu-OH_2 bond. Subsequently, comparing the absolute energies of the systems of a $Cu(II)(OH_2)_6$ and Cu^{2+} in sites SI and SIV of SSZ-13 and SAPO-34, it is that latter which are favoured by a minimum threshold of -2.25eV. This indicates without additional energy of at least approximately 2eV from the surrounding environment, H_2O molecules are

thermodynamically unlikely to dislodge Cu^{2+} from their sitting sites in SI and SIV of SSZ-13 or SAPO-34.

Table 61 (Energy in -eV)

SSZ-13					**SAPO-34**				
$E_{Zeol+H2O}$	**E_{H2O}**	**Rel. E**	**$E_{Zeol\ in\ SI}$**	**$E_{Zeol\ in\ SIV}$**	**$E_{AlPO+H2O}$**	**E_{H2O}**	**Rel. E**	**$E_{AlPO\ in\ SI}$**	**$E_{AlPO\ in\ SIV}$**
485439.41	12462.98	472976.43	472979.10	472979.30	4787508.83	12462.98	475045.85	475049.06	475048.10
No. of H_2O	6		4	3	6			4	3
E per H_2O or Cu-O bond (framework)	79174.31		118244.83	157659.70	78829.41			118762.26	158349.37

5.4.2.5 Site SIII configuration

5.4.2.5.1 SSZ-13

We observed in Chapter 5.2.4, the ability of Cu^{2+} to occupy inside D6R of site SIII in SSZ-13 and SAPO-34 for specific dopant configurations. This occurs, when the dopant atoms are symmetrically arranged to occupy both 6MR rings in the D6R. The Cu^{2+} is coordinated to two of the activated oxygen framework atoms – the stronger σ-donation from these oxygen atoms would result in a stronger ligand-field splitting effect experienced by the Cu^{2+}. This would promote the Jahn-Teller tetragonal distortion, achieving a lower energy in the system.

The small size of a H_2O molecule with a molecule diameter of approximately 2.75Å means that within a given situation, the H_2O molecule would be able to fit inside the D6R and possibly dislodge or disrupt the Cu^{2+} coordination in site SIII. The resulting configuration has the H_2O molecule sitting inside the D6R, and the Cu^{2+} is moved into the plane of 6MR. Subsequently, the presence of H_2O molecule in the D6R displaces the Cu^{2+} in site SIII into SI. The Cu^{2+} undergoes a transformation in coordination from an octahedral inside site SIII, to a square-planar inside SI, see Tables 62a and b.

Table 62a

SSZ-13						
Before						
Cu-O1	Cu-O2	Cu-O3	Cu-O4	Cu-O5	Cu-O6	Spin on Cu
2.0377	2.0367	2.4278	2.2681	2.4197	2.2659	0.83

Table 62b

SSZ-13					
After					
Cu-O1	Cu-O2	Cu-O3	Cu-O4	Cu-OH_2	Spin on Cu
2.1254	1.9402	2.004	2.0486	2.0312	0.81

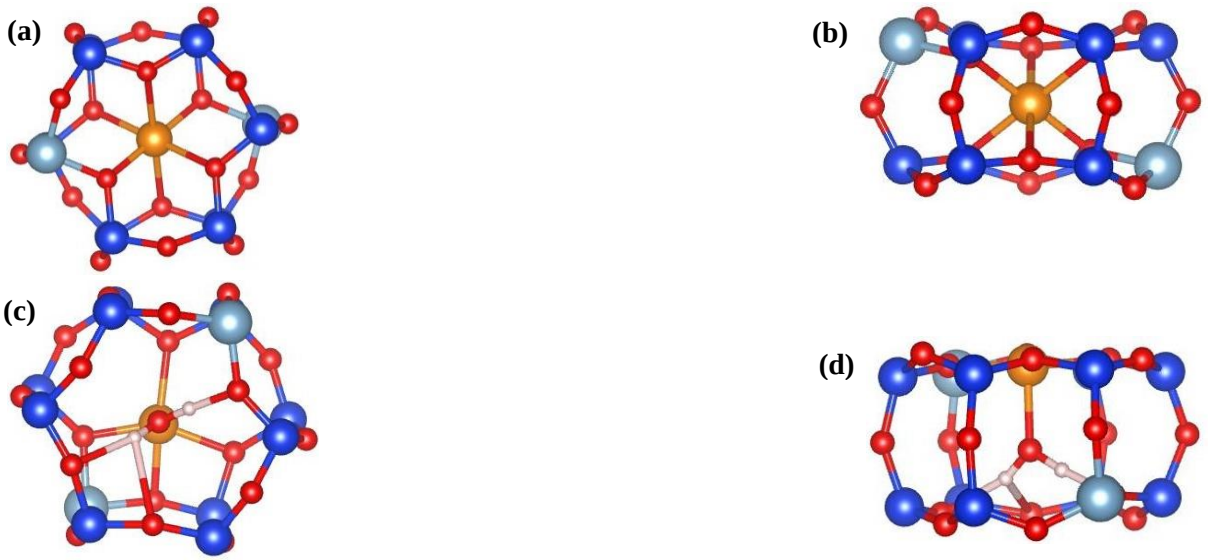

Figs. 64(a – d): (a) (001) and **(b)** (110) views of Cu^{2+} inside site SIII before H_2O inclusion, and after **(c)** – **(d)**.

Fig. 64(d) shows clearly the occupation of the H_2O molecule inside the centre of the D6R, pushing Cu^{2+} atom into the adjacent 6MR plane. The H_2O molecule is able to form hydrogen bonds with the framework oxygen atoms in the other 6MR, these bonds are within the range of 1.50 – 2.34Å. As expected, the Cu^{2+} is coordinated stronger to framework oxygen atoms in the 6MR in relation to when inside the D6R.

5.4.2.5.2 SAPO-34

Upon placing a H_2O molecule inside the D6R, this displaces the Cu^{2+} from the centre of the D6R into the plane of 6MR like in the SSZ-13 framework. The Cu^{2+} loses the octahedral coordination from the framework oxygen atoms, and when inside the 6MR plane it forms a square planar coordination inside the 6MR window, in addition to the coordination from the H_2O molecule from below, see Figs. 65(c – d). The coordination inside the 6MR in both frameworks are similar in terms of number of Cu-O bonds, and the averaged bond lengths are 2.0667 and 2.0296Å for SAPO-34 and SSZ-13 respectively.

Table 63a

SAPO-34						
Before						
Cu-O1	Cu-O2	Cu-O3	Cu-O4	Cu-O5	Cu-O6	Spin on Cu
2.2915	2.3026	2.3786	2.3823	1.9964	1.9960	0.69

Table 63b

SAPO-34					
After					
Cu-O1	Cu-O2	Cu-O3	Cu-O4	Cu-OH_2	Spin on Cu
2.0427	1.9769	1.8977	2.3493	1.9458	0.66

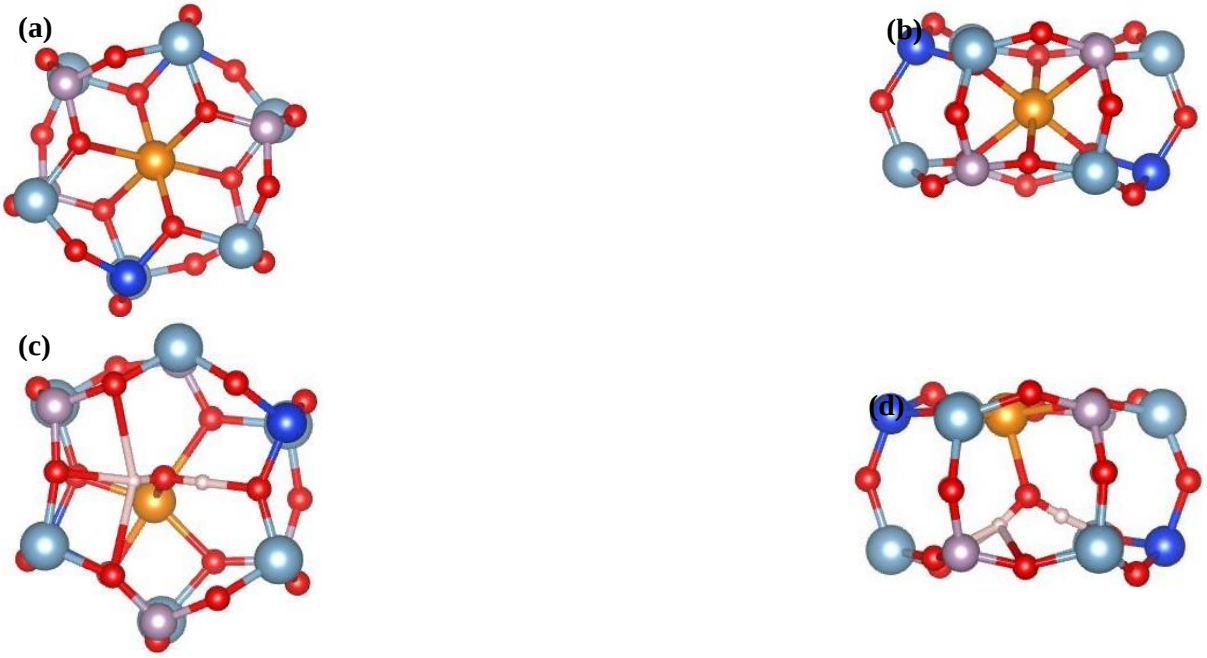

Figs. 65(a – d): (a) (001) and **(b)** (110) views of Cu^{2+} inside site SIII before H_2O inclusion, and after **(c)** – **(d)**.

5.4.2.6 Site SIII energy

The energies for site SIII configurations in SSZ-13 and SAPO-34 are observed in Table 64, the adsorption energy for SSZ-13 is significantly more favourable compared to SAPO-34 by -0.21eV. This is evident with the shorter averaged Cu-O bond lengths in SSZ-13 when Cu^{2+} is inside the 6MR, by a distance of 0.04Å. However, it is possible the more ionic nature of the SAPO-34 framework is less favourable with H_2O molecule interaction. This explains the reversal of adsorption energy favourability between SSZ-13 and SAPO-34 in the site SIII configurations, since the H_2O molecule resides inside the D6R in close proximity with the framework. Unlike in the site SI configurations where the H_2O molecule is in the large cage at a relatively far distance from the framework in SSZ-13 and SAPO-34, as a result the framework interaction with H_2O molecule is less of a pronounced effect. Instead, the ability of the framework to adopt more strenuous positions due to H_2O adsorption on the Cu^{2+} is more important.

The H_2O molecule has a permanent dipole moment of 1.84Debye, this is a relatively strong dipole moment. Yet, the iconicity of SAPO-34 as revealed by Cora *et al*[186] with Mulliken population analysis is greater than in a conventional zeolite framework, like SSZ-13. The interaction of H_2O molecule in SSZ-13 would be more favoured, because despite the permanent dipole in H_2O, the H_2O molecule is a neutral covalently bonded molecule. This is in good agreement with the results in GULP calculations of water calculations.

Table 64 (Energy in -eV)

SSZ-13					**SAPO-34**				
$E_{Zeol+}H_2O$	E_{Zeol}	E H_2O	Rel. E	Ads. E	$E_{AlPO+}H_2O$	E_{AlPO}	E H_2O	Rel. E	Ads. E
475048.47	472969.45	2077.16	472971.31	1.86	487508.83	475039.79	2077.16	475041.44	1.65

5.4.2.7 Site SIV configuration

5.4.2.7.1 Single Al/Si atoms

In the GULP calculations, we were able to observe that the 8MR in site SIV is able to fit both the Cu^{2+} atom and a single H_2O molecule inside its plane; this was shown to be a highly favourable energetic configuration, especially in comparison to the H_2O molecule vacating outside of the 8MR (sitting inside large cage), see Chapter 5.3. In our CRYSTAL calculations, we were able to reproduce the configurations of H_2O inside the plane of the 8MR, coordinated to the Cu^{2+} atom in site SIV, see Figs. 66(a – d).

The H_2O molecule is coordinated strongly to the Cu^{2+} with a coordination length of 1.8488Å, additional stabilization is provided by hydrogen bonding to the framework oxygen atoms in the 8MR, these are between distances of 1.7174 and 1.7780Å indicating strong adsorption of the H_2O molecule to the SSZ-13 framework. On average, the coordination of H_2O molecule to the Cu^{2+} weakens the Cu-O bonding to the framework as evident by the lengthening of the Cu-O bonds from 1.9158 to 1.9868Å. See Table 65. This is expected,

because the increased electron density around the metal centre from the H_2O coordination results in back-donation to the Cu-O antibonding orbitals.

Similarly, in the SAPO-34 situation, the H_2O molecule is able to coordinate inside the 8MR of SIV and bond with the Cu^{2+} with a distance of 1.8726Å, see Figs. 67(c – d). The original location of the Cu^{2+} is not inside the plane of the 8MR, but just of outside of it. This is because, the Cu^{2+} is able to coordinate with the SiO_4^{4-} tetrahedra outside of the 8MR instead of the one inside of the 8MR. This configuration is possible, most likely because of the iconicity in the AlPO framework enabling greater flexibility in the framework atoms movement relative to each other as evident by the framework oxygen atom being pulled out to coordinate with the $Cu^{2+,}$ see Figs. 67(a – b).

The Cu-OH_2 coordination distance is slightly greater in SAPO-34 compared to SSZ-13, because the Cu^{2+} atom is further away in the former, since it occupies a space just outside of the 8MR plane. Comparing tables 23 and 24, where the averaged Cu-O bond lengths in SSZ-13 is 1.9868Å against 2.0123Å in SAPO-34, the longer Cu-O bond lengths in SAPO-34 is counter-intuitive when taking into account the Cu-OH_2 distances. It is expected the shorter Cu-OH_2 distance is an indication of stronger coordination, subsequently a lengthening (weakening) of the Cu-O bonds in the framework would be observed. However, the longer Cu-O distances in SAPO-34 is not a direct evidence of a stronger H_2O coordination to the Cu^{2+}, but due to the Cu^{2+} not inside the 8MR plane like in SSZ-13.

Table 65 (distances in Angstroms)

SSZ-13								
Before				**After**				
Cu-O1	Cu-O2	Cu-O3	Spin on Cu	Cu-O1	Cu-O2	Cu-O3	Cu-OH_2	Spin on Cu
1.9770	1.9039	1.8664		2.1080	1.9012	1.9512	1.8488	0.75

Table 66 (distances in Angstroms)

SAPO-34									
Before					**After**				
Cu-O1	Cu-O2	Cu-O3	Cu-O4	Spin on Cu	Cu-O1	Cu-O2	Cu-O3	Cu-OH_2	Spin on Cu
1.8964	1.8840	2.4295	1.9505		2.1543	1.8924	1.9901	1.8726	0.78

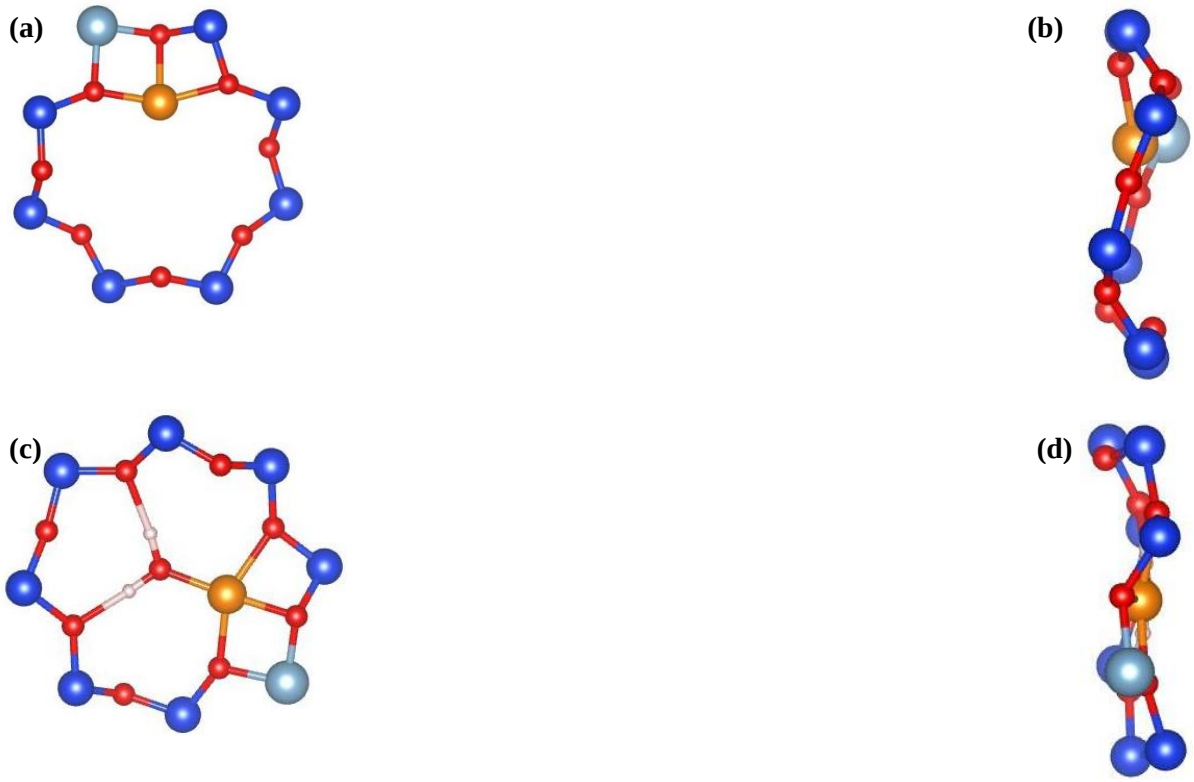

Figs. 66(a – d): (a) (001) and **(b)** (110) views of Cu^{2+} inside site SIV before H_2O inclusion, and after **(c)** – **(d)**.

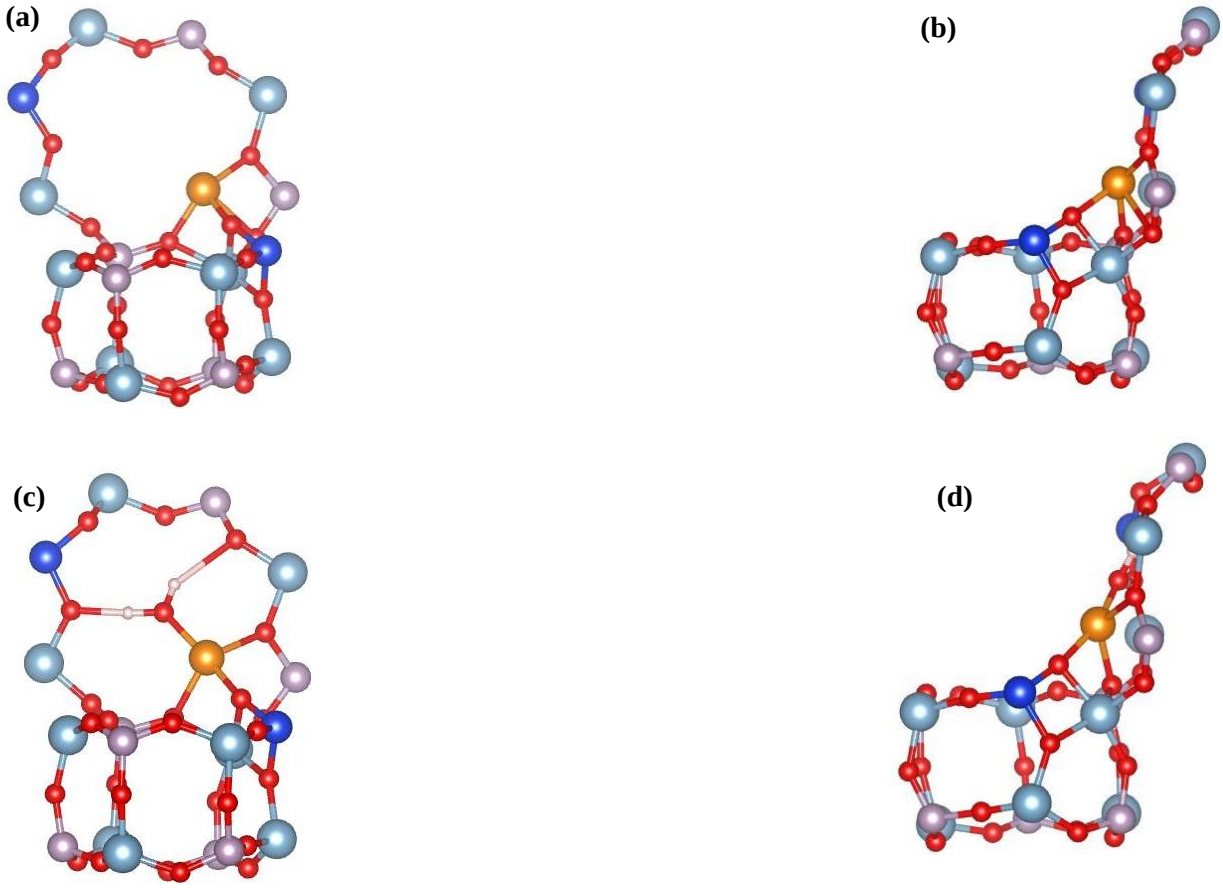

Figs. 67(a – d): (a) (001) and **(b)** (110) views of Cu^{2+} inside site SIV before H_2O inclusion, and after **(c)** – **(d)**.

5.4.2.7.2 Paired Al/Si atoms

To confirm if the 8MR in site SIV is a favourable location for the H_2O adsorption, the initial position of the H_2O molecule is placed inside the large cage, directly opposite the concerned 8MR window. This is a direct replica of the methodology used in the GULP calculations. In the GULP results, we were able to observed that the H_2O does not necessarily have to migrate inside the plane of the 8MR to achieve an equilibrium optimization. However, when the H_2O molecule is able to migrate into the 8MR plane, this is deduced to be energetically the most favoured configuration.

In this sub-set of CRYSTAL calculations in addition to investigating the effect of including a secondary dopant atom inside site SIV, we are able to observe the migration of H_2O from the original location in the large cage at a distance of 2.35 and 2.56Å from the Cu^{2+} inside the 8MR for SAPO-34 and SSZ-13 respectively, see Figs. 68(a – b) and Figs. 69(a – b). Tables 67 and 68 which lists the Cu-O bond distances before and after geometry optimization for SSZ-13 and SAPO-34 respectively shows the weakening of the Cu-O bonds inside the 8MR framework, and the strengthening of the Cu-OH_2 coordination. It is possible to explain the migration of the H_2O molecule into the plane of the 8MR via bond making, the H_2O molecule gains stabilization from hydrogen bonding with framework oxygen atoms inside the 8MR and the coordination with the Cu^{2+}, this aids a distorted square planar geometry.

See Figs. 68(a – d) and 69(a – d), the change in the H_2O location from the large cage to inside the 8MR plane. This is consistent in both SSZ-13 and SAPO-34, unlike in the GULP calculations which shows the H_2O molecule rarely occupying the plane of the 8MR window inside the frameworks. As mentioned previously, this discrepancy with the GULP results is due to the high repulsive *A* term found in the Buckingham potential used to model the Cu^{2+}-OH_2 interaction, which is nearly twice as high compared to the Cu^{2+}-zeolite/AlPO interaction. This could explain the absence of H_2O molecules occupying the plane of the 8MR in close proximity with Cu^{2+} in the GULP results.

Table 67 (distances in Angstroms)

SSZ-13									
Before					**After**				
Cu-O1	Cu-O2	Cu-O3	Cu-OH_2	Spin on Cu	Cu-O1	Cu-O2	Cu-O3	Cu-OH_2	Spin on Cu
2.1282	1.9043	1.9429	2.5596		2.1276	1.9048	1.9420	1.8824	

Table 68 (distances in Angstroms)

SAPO-34									
Before					**After**				
Cu-O1	Cu-O2	Cu-O3	Cu-OH_2	Spin on Cu	Cu-O1	Cu-O2	Cu-O3	Cu-OH_2	Spin on Cu
1.9878	1.8999	2.0914	2.3510		1.9892	1.8994	2.0922	1.8389	

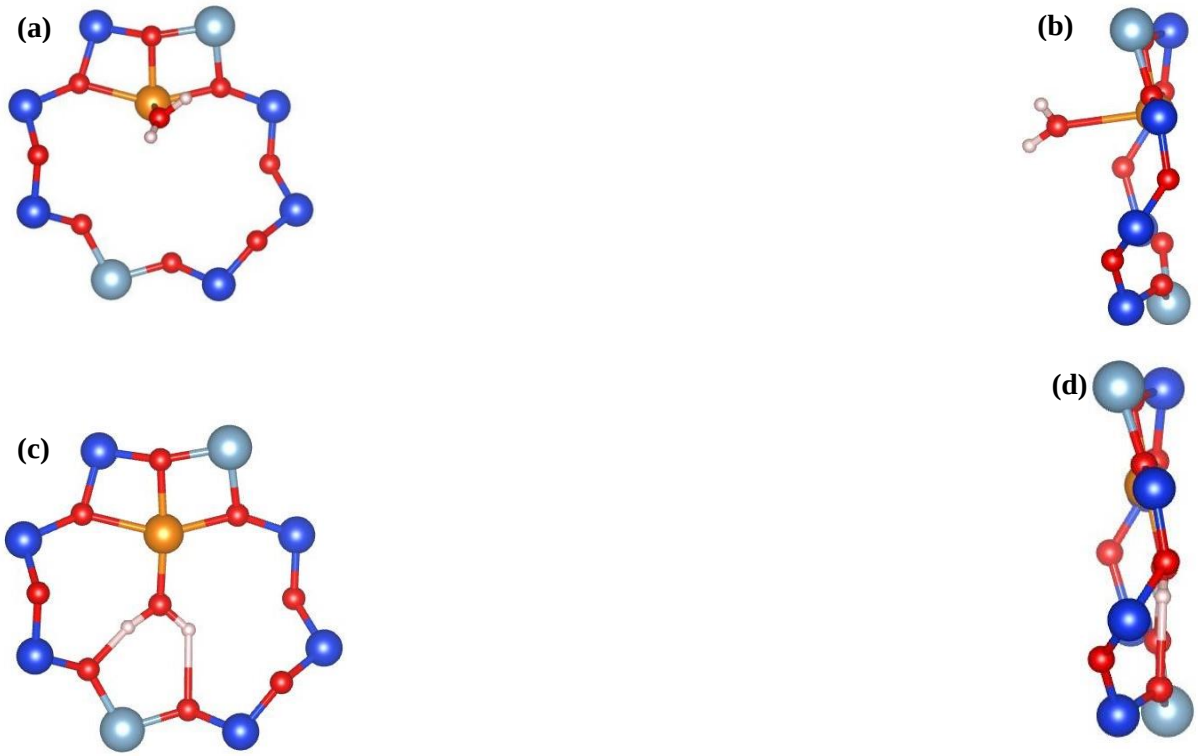

Figs. 67(a – d): (a) (001) and **(b)** (110) views of Cu^{2+} inside site SIV before H_2O migration, and after **(c)** – **(d)**.

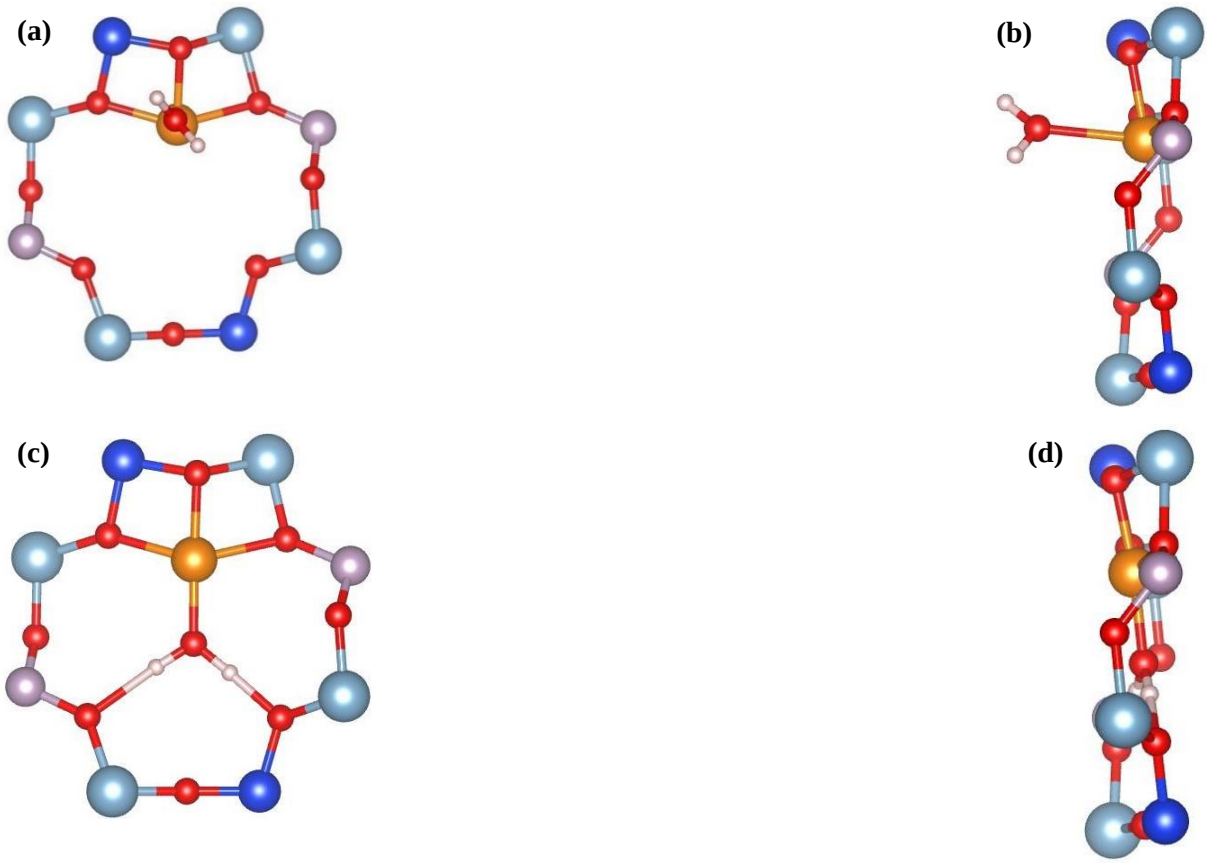

Figs. 68(a – d): (a) (001) and **(b)** (110) views of Cu^{2+} inside site SIV before H_2O migration, and after **(c)** – **(d)**.

In both paired configurations, due to the distance between the dopant atoms inside 8MR framework the Cu^{2+} is unable to coordinate to both the dopant atoms simultaneously, as a result, the Cu^{2+} is coordinated to only dopant atom. Because both dopant atoms are identical in their environment there is no selective preference for Cu^{2+} to coordinate one over another. However, in the AlPO framework we can build a Si-O-P-O-Si sequence inside the 8MR framework, see Figs. 69(a – b). This enables Cu^{2+} to coordinate to both the Si dopant atoms, ensuring a stronger bond the AlPO framework. Table 68 list the Cu-O bond distances for this particular framework configuration in SAPO-34.

The H_2O adsorption relative to the Si-O-P-O-Al-O-P-Si configuration is identical; the H_2O molecules migrates inside the 8MR plane and coordinates to the Cu^{2+} forming a square-planar geometry, see Figs. 69(a – d). However, the averaged change in Cu-O distances before and after H_2O is more pronounced with a 0.039Å difference compared to 0.0006Å in the prior. This is despite, the longer Cu-OH_2 coordinate distance in the Si-O-P-O-Si configuration. The longer Cu-OH_2 coordination distance is a direct indication of a weaker coordination; the higher electron density in the Cu^{2+}'s orbitals due to the excess negative charge from the two Si dopant atoms results in a back-donation into the empty Cu-OH_2 antibonding orbital.

An interesting observation, is that Cu-O bonding in the pre- and post- H_2O adsorption in the Si-O-P-O-Al-O-P-Si configuration are very similar in bond strengths on the basis of the averaged Cu-O bond lengths. This indicates that the H_2O adsorption has less of a pronounced effect compared to in the Si-O-P-O-Si configuration. From first inspection, the difference in averaged Cu-O bond lengths change could be due to the difference in pre-H_2O Cu-O bonding.

In Si-O-P-O-Si configuration, the averaged Cu-O bond length is 1.8723Å and in Si-O-P-O-Al-O-P-Si this is longer at 1.9930Å. The shorter, thereby stronger Cu-O bond lengths in Si-O-P-O-Si configuration because of coordination to two activated framework oxygen atoms. Upon H_2O coordination, the Cu^{2+} would experience a greater configurational change in the Si-O-P-O-Si sequence, because of the originally stronger Cu^{2+} coordination to the framework.

It is possible the original location of the H_2O molecule could have an effect, since the H_2O molecule was initially docked inside 8MR plane within a distance of 1.7198Å inside the Si-O-P-O-Si configuration. Subsequently, an additional calculation was carried out for the Si-O-P-O-Al-O-P-O-Si configuration with the H_2O molecule inside the 8MR plane within a 1.4855Å proximity of Cu^{2+}. The post-H_2O adsorption averaged Cu-O bond length is identical to the calculation with H_2O initially docked out-of-plane of the 8MR, at 1.9930Å.

Table 69 (distances in Angstroms)

SAPO-34									
Before					**After**				
Cu-O1	Cu-O2	Cu-O3	$Cu-OH_2$	Spin on Cu	Cu-O1	Cu-O2	Cu-O3	$Cu-OH_2$	Spin on Cu
1.8975	1.8880	1.8315	1.7198		1.9497	1.9022	1.8834	1.9184	

Figs. 69(a – b): (a) (001) and **(b)** (110) views of Cu^{2+} inside site SIV with H_2O adsorption.

5.4.2.7.3 Two H_2O molecules – Paired Si/Al atoms

In both SSZ-13 and SAPO-34, the presence of two H_2O molecules within the vicinity of site SIV showed only one H_2O molecule is able to fit inside the 8MR window. The second H_2O molecule occupies the large cage, but is directly coordinated to the Cu^{2+} and off-centred in order to gain zeolitic stabilization from the framework edge inside the large cage via hydrogen bonding, see Figs. 70 and 71(a – d).

In SSZ-13, the change in the averaged Cu-O bond distances before and after the coordination of the two H_2O molecules is an 0.089Å increased in length. Compared to the single H_2O adsorption, see Table 68, the change is very minor at 0.0003Å. This is expected, since the presence of two coordinated H_2O molecules would have a more pronounced effect on the Cu^{2+} configuration compared to a single H_2O molecule. Similarly, in SAPO-34 the averaged change in Cu-O bond length is 0.1490Å when two H_2O molecules are coordinated to the Cu^{2+} against 0.0006Å in the single H_2O adsorption. The presence of a second H_2O molecule results in a greater effect on the Cu-O bonding inside the 8MR window. As expected, Cu^{2+} coordination to the 8MR framework is weaker when two H_2O molecules are coordinated to the Cu^{2+} compared to a single H_2O. The H_2O molecule inside the 8MR plane forms the stronger bond to the Cu^{2+}, compared to the H_2O in the large cage on the basis of bond distances in Tables 70 and 71, in both tables the second H_2O molecule in the large cage is labelled H_2O2.

In terms of coordination, the inclusion of the second H_2O molecule resulted in the same adsorption configurations in both frameworks. An important observation is the inability of site SIV to include the second H_2O molecule inside the plane of the 8MR window, this is due to the limited capacity of the 8MR window to fit both H_2O molecules and the Cu^{2+} without introducing unfavoured steric effects.

Table 70 (distances in Angstroms)

SSZ-13											
Before						**After**					
Cu-O1	Cu-O2	Cu-O3	Cu-$O1H_2$	Cu-$O2H_2$	Spin on Cu	Cu-O1	Cu-O2	Cu-O3	Cu-$O1H_2$	Cu-$O2H_2$	Spin on Cu
2.1276	1.9048	1.9420	1.8238	2.5596		2.2520	1.9202	2.0699	1.8290	2.0366	

Table 71 (distances in Angstroms)

SAPO-34											
Before						**After**					
Cu-O1	Cu-O2	Cu-O3	Cu-$O1H_2$	Cu-$O2H_2$	Spin on Cu	Cu-O1	Cu-O2	Cu-O3	Cu-$O1H_2$	Cu-$O2H_2$	Spin on Cu
1.8999	2.0914	1.9878	1.8387	2.3510		1.9295	2.4946	2.0019	1.8655	1.9707	

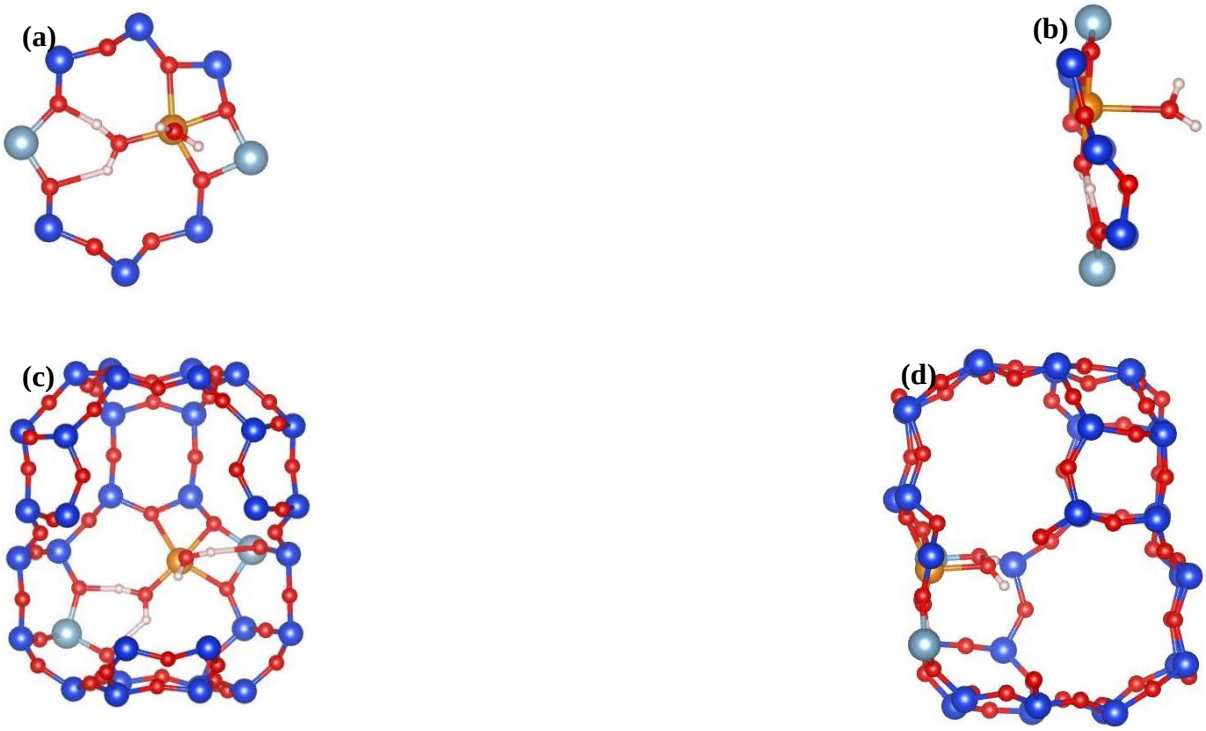

Figs. 70(a – d): SSZ-13, **(a)** (001) and **(b)** (110) views of Cu^{2+} inside site SIV with two nearby H_2O molecules before and after geometry optimization, **(c)** - **(d)**.

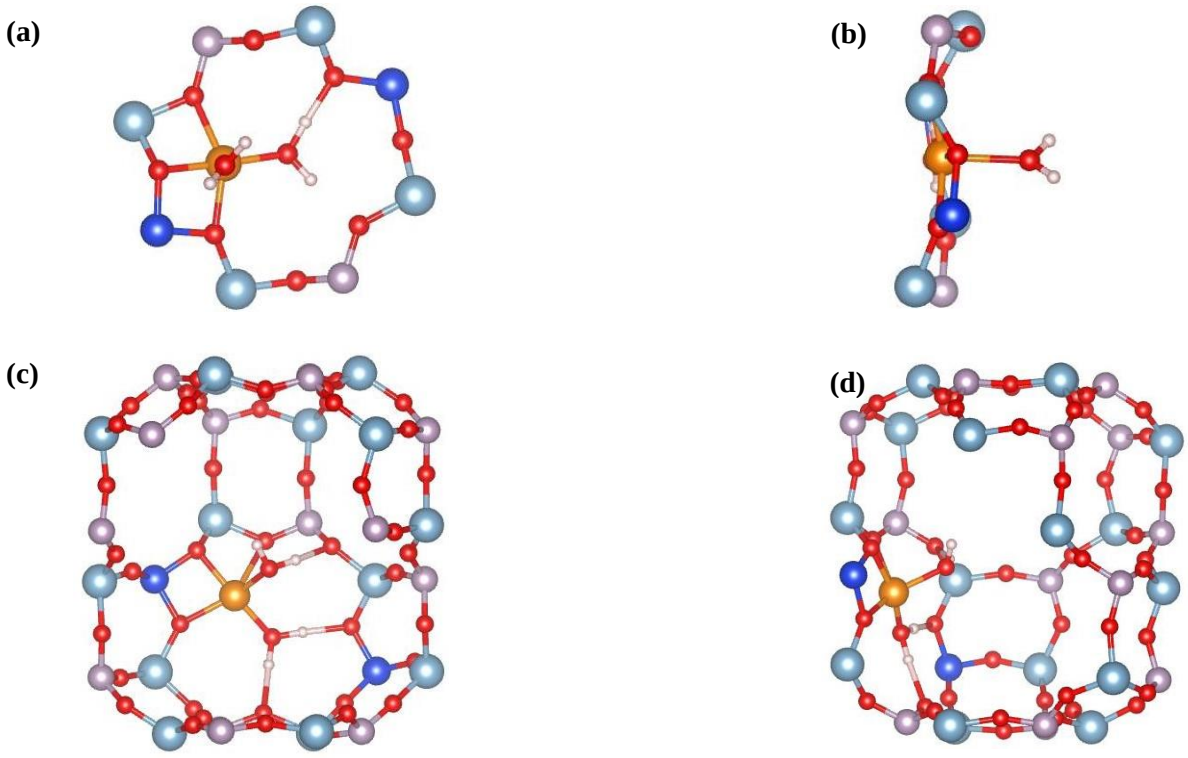

Figs. 71(a – d): SAPO-34, **(a)** (001) and **(b)** (110) views of Cu^{2+} inside site SIV with two nearby H_2O molecules before and after geometry optimization **(c)** - **(d)**.

5.4.2.8 Site SIV energy

5.4.2.8.1 Single Al/Si atoms

The adsorption energy of a H_2O molecule in SAPO-34 is 0.04eV more favourable compared to SSZ-13. Considering in SAPO-34, the Cu^{2+} is out of the plane of 8MR window, the difference in adsorption energy between the two frameworks could be predominantly as a function of the change in locations of Cu^{2+} than the different chemical composition between a zeolite and AlPO. In both situations, the H_2O is inside the 8MR window adsorbed to the respective framework via two hydrogen bonds each, in SSZ-13 these are measured at 1.7174 and 1.7780Å in lengths, and for SAPO-34 at 1.6426 and 2.2297Å. In SAPO-34, the individual hydrogen bonds are one strong and one weak. This substantial difference in SAPO-34 between the two hydrogen bonds with H_2O molecule is due to the displacement of the Cu^{2+} atom out of the 8MR window; the H_2O molecule is slightly out of the 8MR window plane in order to coordinate with the Cu^{2+}, see Figs. 67(c – d).

Table 72 (Energy in -eV)

SSZ-13					**SAPO-34**				
E_{Zeol+H_2O}	E_{Zeol}	E H_2O	Rel. E	Ads. E	E_{AlPO+H_2O}	E_{AlPO}	E H_2O	Rel. E	Ads. E
475048.35	472968.27	2077.16	472971.19	2.92	477117.76	475037.64	2077.16	475040.60	2.96

5.4.2.8.2 Paired Al/Si atoms

In the paired configurations concerning the same ordering of Si/Al sequence inside the 8MR, the adsorption energy of H_2O in SAPO-34 is more favourable by -0.12eV, see Table 73. This is similar to the adsorption energies in single configurations, the exception is in the paired the difference in energies is three times that observed prior, -0.12eV against -0.04eV. This substantial change in adsorption energy difference between the frameworks, is possibly due to the unexpected position of Cu^{2+} inside the SAPO-34 single configuration. Despite in the single configurations, adsorption in SAPO-34 is energetically more favourable than SSZ-13, the difference in adsorption energy could have been decreased by the Cu^{2+} occupying the space just outside of the 8MR in SAPO-34.

However, as the Si sequence ordering in SAPO-34 changes from Si-O-P-O-Al-O-P-Si to Si-O-P-O-Si the adsorption energy of H_2O decreases from -3.23eV to -2.05eV, see Table 32. This highlights the stability of the Cu^{2+} configuration in the Si-O-P-O-Si sequence as evident by a -1.43eV lower in energy between the Cu^{2+}-bare SAPO-34 frameworks of different Si sequences. This indicates a stronger coordination between Cu^{2+} and the 8MR framework in the Si-O-P-O-Si configuration, because of the presence of two strong σ-donors between the two nearby Si dopant atoms, thereby preventing a less favoured coordination of H_2O onto Cu^{2+} compared to in the Si-O-P-O-Al-O-P-Si configuration.

Table 73 (Energy in -eV)

SSZ-13					**SAPO-34 (Si-O-P-O-Al-O-P-Si)**				
E_{Zeol+H_2O}	E_{Zeol}	E H_2O	Rel. E	Ads. E	E_{AlPO+H_2O}	E_{AlPO}	E H_2O	Rel. E	Ads. E
475048.38	472968.11	2077.16	472971.21	3.11	475048.38	475038.60	2077.16	475041.83	3.23

Table 74 (Energy in -eV)

SAPO-34 (Si-O-P-O-Si)				
E_{AlPO+H_2O}	E_{AlPO}	E H_2O	Rel. E	Ads. E
477119.25	475040.03	2077016	475042.09	2.05

5.4.2.8.3 Two H_2O molecules – Paired Si/Al atoms

As two H_2O molecules are coordinated to the Cu^{2+} inside the 8MR the absolute values of adsorption energy expectedly increased from 3.11 and 3.23eV with a single H_2O molecule to 4.38 and 4.54eV for SSZ-13 and SAPO-34 respectively. In good agreement with the single H_2O molecule situations, the adsorption energy of SAPO-34 for two H_2O molecules is -0.16eV more favoured against the SSZ-13.

On the whole, the energetic trend observed for H_2O adsorption in site SIV is reflected in the prior investigated site of SI. This seems to indicate from our CRYSTAL calculations, that the SAPO-34 framework is more favourable for hosting H_2O molecules interactions, this could be due to the greater flexibility in the SAPO-34 framework and/or the more ionic quality of the AlPO framework might be favoured

Table 75 (Energy in -eV)

SSZ-13					**SAPO-34 (Si-O-P-O-Al-O-P-Si)**				
E_{Zeol+H_2O}	E_{Zeol}	E H_2O	Rel. E	Ads. E	E_{AlPO+H_2O}	E_{AlPO}	E H_2O	Rel. E	Ads. E
477126.82	472968.11	4154.33	472972.49	4.38	479197.47	475038.60	4154.33	475043.14	4.54

Summary 5.4: CRYSTAL water calculations

The CRYSTAL water calculations of SSZ-13 and SAPO-34 in general showed subtle differences in the H_2O adsorption configurations on the Cu^{2+} when residing in site SI. This discrepancy between the adsorption configurations is caused by the available dopant sitting around the 6MR window, and the flexibility of the framework to host the H_2O molecules. Subsequently, the adsorption energy is influenced by these varied adsorption configurations between SSZ-13 and SAPO-34. For the single H_2O adsorption on the single-dopant configuration; inside the SAPO-34 the H_2O molecule is coordinated directly to the Cu^{2+} but the H_2O molecule is tilted at an acute angle towards the 6MR plane, enabling a hydrogen bond with the framework oxygen atom on the 6MR window. This is not observed with SSZ-13, instead the H_2O is perpendicular towards the 6MR, and only coordinated to the Cu^{2+}. This is because, the 6MR window inside SAPO-34 is pushed upwards the H_2O molecule unlike in SSZ-13, see Table 45. Thus, the adsorption energy is more favoured for a SAPO-34 compared to SSZ-13 by 0.7eV.

The above trend is reversed as two H_2O molecules are adsorbed onto the single-dopant configuration inside site SI, the adsorption energy for SSZ-13 is -0.1eV favoured. In both frameworks, the Cu^{2+} is lifted away from the 6MR window, and partially displaced. For the paired dopant configurations inside site SI, the adsorption energy is more favoured for SAPO-34, this is because the dopant sitting around the 6MR favours the H_2O approach without charge repulsion, see Figs. 56(a – d). The pull of Cu^{2+} away from the 6MR is less pronounced with two H_2O molecules within the vicinity, as expected due to the presence of the additional dopant atom inside the 6MR. However, the SAPO-34 adsorption energy is more favoured by -0.47eV, because of absence of electrostatic repulsion between the incoming H_2O molecules and the site SI framework since the spacing of the Si atoms allows for a coordinative area.

The $Cu^{2+}(H_2O)_6$ complex was computed inside the large cage of site SII for both SSZ-13 and SAPO-34, it showed that unlike in the GULP calculations – the H_2O molecules arranged in an octahedral around the Cu^{2+} metal centre stabilizes the configuration. This is due to the inclusion of crystal-field splitting inside the CRYSTAL calculations. In addition, comparison of the energies between H_2O ligands and framework oxygen atom ligands, showed the latter is more favoured.

In comparison with site SI, the adsorption of H_2O on site SIV is more favoured, because the 8MR window is large enough to fit both the H_2O molecule and the Cu^{2+} inside. Whilst the proximity of the framework with H_2O allows strong hydrogen bonds to be formed, further resulting in a stronger adsorption configuration. In general, the SAPO-34 obtains the more favoured adsorption energy compared to SSZ-13 inside both single- and paired-dopant configurations. However, the sequence of the dopant sitting inside the 8MR cannot be dismissed, see Table 74. On the whole H_2O adsorption in SAPO-34 is more favoured due to Si dopant atoms sitting sequence, and the flexibility of the framework in contrast with the GULP results. However, this is possibly a simplify picture, as the topology of the site and the dopant configuration are key parameters in determining the favourability of an admolecule adsorption in these systems.

The stability of site SIV as an acid site was not observed in GULP, in general the discrepancy between GULP and CRYSTAL is in the former H_2O molecules were unlikely to coordinate to the Cu^{2+}, and instead would adsorb onto the framework instead. In CRYSTAL,

we see that the Cu^{2+}-OH_2 coordination is a prominent feature in the H_2O adsorption configurations, this particularly to prop up crystal-field splitting to ensure the absence of degeneracy in d^9 electronic configuration is satisfied.

5.5 CRYSTAL calculations of NH_3 adsorption

In a SCR reaction the use of NH_3 as the reducing agent is currently the most effective method in reducing NO_x in diesel engines, because only a stoichiometric amount of NH_3 is needed for the complete reduction of NO_x. Subsequently, these set of calculations is focused on the study of NH_3 behaviour in the frameworks of SSZ-13 and SAPO-34 as a function of Cu(II) in the two most stable extra-framework sites, 6MR in SI and 8MR in SIV.

The aim in this chapter is to investigate the adsorption of NH_3 molecule on Cu-SSZ-13 and –SAPO-34 via a periodic density functional study with the CRYSTAL14 package. Currently, ab initio studies in the literature have investigated adsorbates interaction in metal-exchanged zeolites with a range of computational techniques. These are focused on the adsorption of small molecules including NO, NO_2, O_2, NH_3, H_2O and SO_2, but not specifically on Cu-SSZ-13 or –SAPO-34. Sierralta *et al* performed adsorption studies of NO, NO_2, O_2, NH_3 and $_{SO2}$ over metal-exchanged ZSM-5 with a 3T cluster model[1]. Whilst, Hafner *et al*[23] studied NO adsorption on Cu and Co exchanged SAPO-34 with a periodic DFT method. Other studies included Sodupe and coworkers combined ONIOM and periodic calculations approach in the comparison of NH_3 and H_2O in a metal-free acidic chabazite[1]. This involved a negatively charged CHA framework and an ammonium cation, and a HCHA fragment for H_2O adsorption. In consideration of these literature studies and an absence of a full ab initio comparison of NH_3 adsorption in Cu-SSZ-13 and –SAPO-34, the current results are expected to be relevant and insightful.

The atomistic aims from this particular study is to: (i) understand the adsorption of NH_3 in terms of configurational and energetic factors in extra-framework sites SI and SIV, (ii) to determine the difference in NH_3 adsorption between the two sites SI and SIV, (iii) compare the difference in effect between a zeolite and AlPO framework on NH_3 adsorption, (iv) look at the effect in the number of dopant atoms in the extra-framework on NH_3 adsorption and (v) to investigate if the presence of NH_3 molecule(s) would displace Cu from the equilibrium SI site.

5.5.1 Computational procedure

As mentioned previously, the quantum chemical calculations performed are based on a periodic DFT method in the CRYSTAL14 package. The hybrid functional PBE0 and an additional 10% Hartree–Fock exact exchanged was used, as justified in Chapter 5.2.1. The initial positions of the NH_3 molecules are docked directly above the Cu(II) located in sites SI or SIV, and the orientation of the NH_3 molecules has the nitrogen atom pointing towards the Cu(II) within the range of 1.56 – 2.06 Å. Considering the permanent dipole moment in NH_3 the described orientation ensures the optimum interaction between the negatively charged nitrogen atom and Cu(II) cation.

The bare Cu-exchanged zeolite and AlPO frameworks were first optimized in GULP then subsequently optimized in CRYSTAL to enable inclusion of the electronic effects before the docking of the NH_3 molecules. Geometry optimization calculations were performed to determine the lowest energetic equilibrium structures of NH_3 adsorption in both SSZ-13 and SAPO-34. In this only the atomic coordinates were optimized.

In order to take into account the dopant effect on NH_3 adsorption distinct Al/Si configurations were adopted described as single Al/Si atom and paired Al/Si atoms respectively. For a single Al/Si atom configuration one dopant atom is present in the 6MR and

8MR frameworks of sites SI and SIV respectively, where the Cu occupies. In the paired case two dopants atoms are situated in the 6MR and 8MR frameworks of sites SI and SIV respectively. Subsequently, for each sites SI and SIV Cu occupies in the SSZ-13 and SAPO-34 frameworks, there is a single Al/Si atom and corresponding paired Al/Si atoms configuration.

5.5.2 Results

5.5.2.1 Site SI configuration

A NH_3 molecule was docked onto Cu^{2+} in the 6MR position at site SI with a single Al/Si atom in framework site. This was repeated with Al/Si atom pairs in the same 6MR position. For the first set of calculations, in both SSZ-13 and SAPO-34, two Al and Si atoms are doped per unit cell respectively. This gives a Si: Al ratio of 17:1 for SSZ-13 and Al: P: Si ratio of 9: 8: 1 for SAPO-34.

The Al and Si configuration for both frameworks are identical with unpaired Al/Si atoms in different (6MR) rings – single Al/Si atoms, see Figs. 72(a – b). The Cu atom sits in one of these 6MR rings, a site SI location.

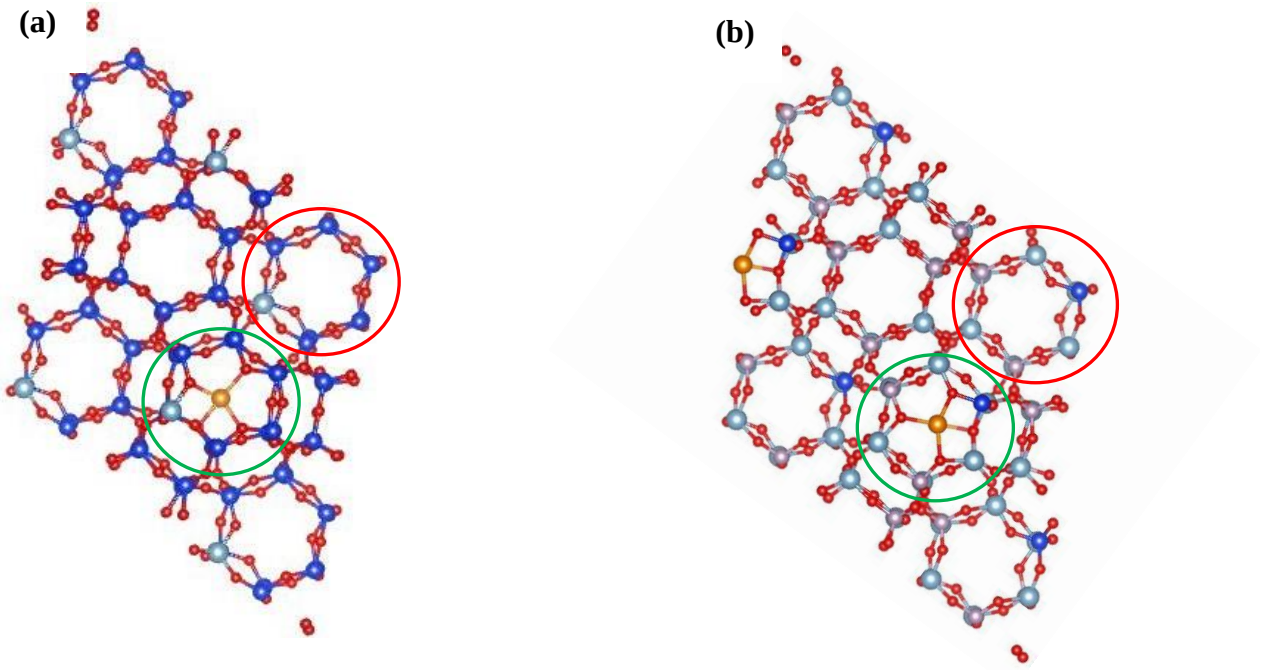

Figs. 72(a – b): **Left**, SSZ-13 unit cell. **Right**, SAPO-34 unit cell. Circled green is the 6MR with a single Al/Si atom and the Cu^{2+} sitting in site SIc. Circled red is the other single Al/Si atom in a distinct 6MR, SIe.

In the second set of calculations, the Si: Al and Al: P: Si ratios of both SSZ-13 and SAPO-34 are the same as the prior at 17:1 and 9: 8: 1 respectively. However, the locations of the Si/ Al atoms are paired in the same 6MR, see Figs. 73(a – b).

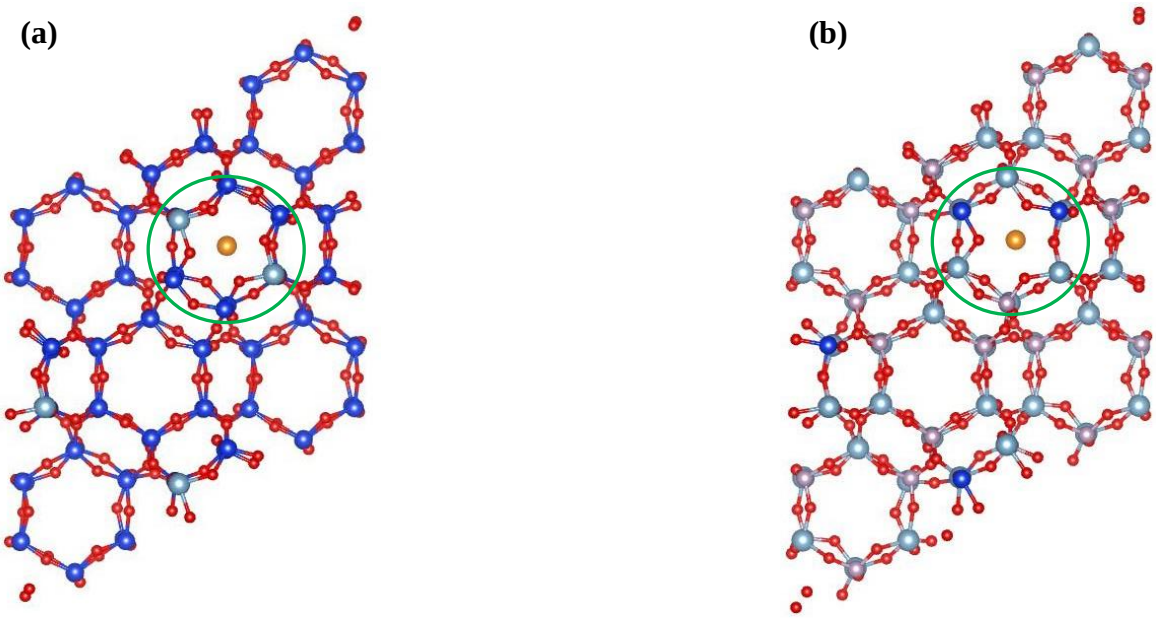

Figs. 73(a – b): **Left**, SSZ-13 unit cell. **Right**, SAPO-34 unit cell. Circled green is the 6MR with paired Al/Si atoms and the Cu^{2+} sitting in site SIc.

5.5.2.1.1 Single Si/Al atoms

In both SSZ-13 and SAPO-34, the NH_3 molecule coordinates to the Cu(II) via the N atom with Cu-N bond distances of 1.9519 and 1.9502Å respectively, as shown in Tables 76 and 77. The effect of NH_3 coordination results in a weakening of the Cu bonding to the zeolite and AlPO framework, this is evident with the lengthening of individual Cu-O bond distances after NH_3 coordination. This could be due to the adverse effect from weaker back-donation of the Cu^{2+} d-orbitals to the empty p-orbitals on the framework O atoms. Before coordination, the spin on Cu^{2+} is 0.75 and 0.74 for SSZ-13 and SAPO-34 respectively, after which it increased to 0.79 and 0.78. Indicating a lessening of the spin localization onto the neighbouring framework oxygen atoms. The SSZ-13 and SAPO-34 configurations of NH_3-Cu(II) in SI are shown in Figs. 74(a – b).

The approach of NH_3 in both SSZ-13 and SAPO-34 is at an acute angle of 67˚ with respect to the 6MR plane, away from the dopant atoms, Al and Si respectively. Due to the differences in valences between Si and Al in a zeolite, the introduction of a framework Al creates a negative charge in the lattice. Similarly in an AlPO the presence of a framework Si atom in place of P results in a negative charge. Subsequently, an electrostatic repulsion comes into focus when NH_3 is within the vicinity of AlO_4^{5-} or SiO_4^{4-} tetrahedra of SSZ-13 and SAPO-34 respectively.

Table 76 (distances in Angstroms)

SSZ-13										
Before					**After**					
Cu-O1	Cu-O2	Cu-O3	Cu-O4	Spin on Cu	Cu-O1	Cu-O2	Cu-O3	Cu-O4	Cu-N	Spin on Cu
1.9627	1.8989	2.0280	1.9790	0.75	2.0075	1.9154	2.0703	2.4640	1.9519	0.79

Table 77 (distances in Angstroms)

SAPO-34										
Before					**After**					
Cu-O1	Cu-O2	Cu-O3	Cu-O4	Spin on Cu	Cu-O1	Cu-O2	Cu-O3	Cu-O4	Cu-N	Spin on Cu
1.9049	1.9519	1.9858	2.0207	0.74	1.9141	2.0049	2.4674	2.0731	1.9502	0.78

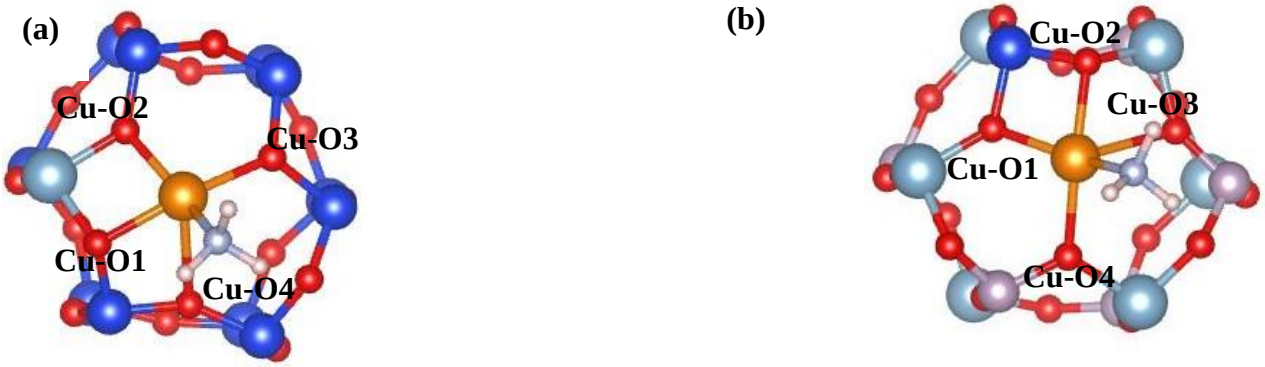

Figs. 74(a – b): **Left**, Cu-NH_3 configuration in SSZ-13. **Right**, Cu-NH_3 in SAPO-34.

Table 78 lists the distance of Cu from the plane of 6MR in site SI, before and after coordination with NH_3. In SSZ-13 and SAPO-34, the Cu is pulled further away from the plane of the 6MR framework by distances of 0.410327 and 0.426829Å respectively. Before NH_3 coordination, the Cu position relative to the plane of the 6MR is further away in SSZ-13 compared to SAPO-34, at 0.495408 and 0.453317Å respectively. This is could be due to the greater iconicity of the framework oxygen atoms in SAPO-34, acting as a better coordinating ligand to the Cu^{2+}, therefore pulling the Cu atom closer. However, during NH_3 coordination, in both SSZ-13 and SAPO-34, the Cu atom is pulled away from the plane of the 6MR, but the distance from the 6MR plane is slightly greater in SAPO-34 by 0.016502Å. Inspecting the averaged Cu-O bond lengths in SSZ-13 and SAPO-34 upon NH_3 adsorption, they are 2.1143

and 2.1149Å respectively. The similar averaged Cu-O bond lengths is in good agreement with the Cu to plane of 6MR distances.

Upon NH_3 adsorption, the Cu-O4 and Cu-O3 bonds in SSZ-13 and SAPO-34 respectively can be noted as bond-breaking due to the large bond lengths. Since, the bond distances are 2.4640 and 2.4674Å. In both cases, the framework oxygen atoms, O4 and O3 in SSZ-13 and SAPO-34 are directly below the approach of the NH_3 molecule, see Figs. 74(a – b).

Table 78 (distances in Angstroms)

	SSZ-13	**SAPO-34**
	Cu – plane of 6MR distance	Cu – plane of 6MR distance
Before	0.495408	0.453317
After	0.905736	0.880146
Difference	0.410327	0.426829

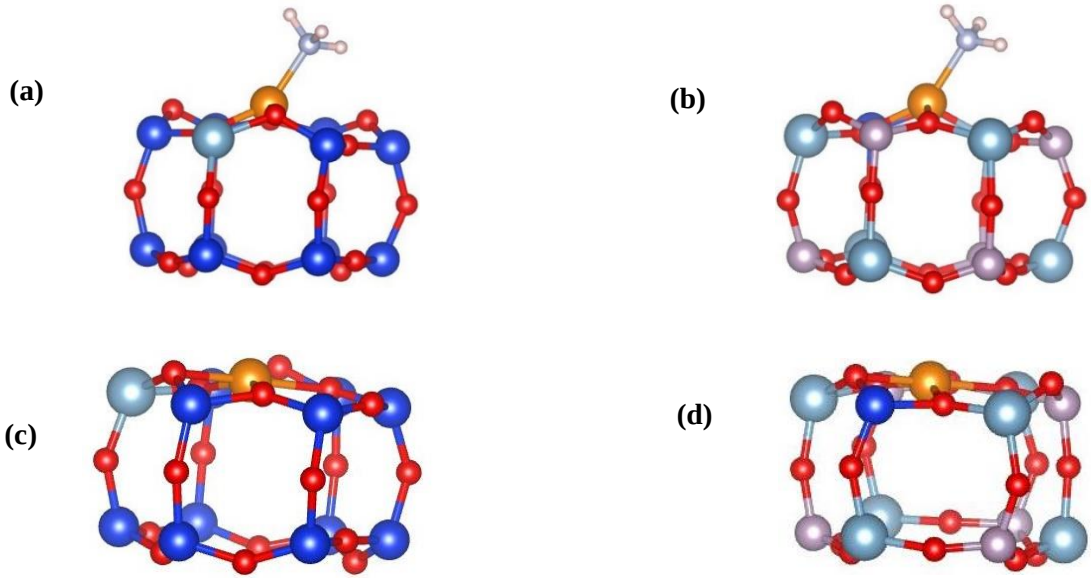

Figs. 75(a – b): **Left**, Cu-NH_3 configuration in SSZ-13. **Right**, Cu-NH_3 in SAPO-34. **(a - b)** Upon coordination with NH_3 and **(c - d)** without.

5.5.2.1.2 Paired Si/Al atoms

Similarly, for the paired Si/Al configurations, the Cu-O bond distances increased upon adsorption with the NH_3 molecule for both SSZ-13 and SAPO-34, see Tables 79 and 80. However, the observed weakening of the Cu-O bonds are lesser in the paired configurations. This is evident in SSZ-13 with an absent of the Cu-O4 bond breaking observed in the single configuration. The averaged distances for SSZ-13 before and after NH_3 adsorption was 1.945 and 1.992Å respectively; a 0.05Å lengthening of the Cu-O bond lengths due to NH_3 coordination. The SAPO-34 experienced a greater lengthening effect before and after adsorption, the averaged Cu-O distances were 1.9550 and 2.092Å respectively showing an increase of 0.14Å. The Cu-O3 bond breaking distance was also observed in SAPO-34 at 2.4772Å. In the single Si/Al configurations for both SSZ-13 and SAPO-34, the increased in

average Cu-O distance upon NH_3 adsorption was 0.15Å. This highlights that the paired Al configuration in SSZ-13 has a significant effect in the Cu coordination to the 6MR. Unlike for the paired Si configuration in SAPO-34 which does not have the same pronounced effect, instead the introduction of a secondary Si atom in the 6MR results in a weak perceptible change in the Cu-O bond lengths.

The Cu-N bond lengths is an indicator of the strength of the NH_3 adsorption, and inversely the coordination strength of Cu to the 6MR frameworks in SSZ-13 and SAPO-34. In both situations, single and paired Si/Al configurations, the SSZ-13 forms the longer Cu-N bonds compared to SAPO-34, see Tables 76, 77, 79 and 80. The inclusion of the additional Si/Al atom in the 6MR for paired configurations resulted in a decreased C-N bond distances as expected, indicating weaker NH_3 adsorption on Cu inside a paired configuration. This was observed for both SSZ-13 and SAPO-34. However, the Cu-N bond length in SAPO-34 is substantially shorter than SSZ-13 in the paired configurations. This is due to the change in NH_3 coordinating approach to the Cu in the latter.

Unlike in the single dopant configuration case, a paired Al configuration in SSZ-13 results in the NH_3 approaching the Cu in a perpendicular fashion. This is because of the uniform distribution of the Al atoms around the 6MR framework, since the Al dopants are opposite each in a symmetrical fashion round the 6MR. However, in SAPO-34, this is not observed, instead the NH_3 approaches the 6MR plane with an angle of 67˚ - same as in the single dopant configuration. See Figs. 76(a – b). In an AlPO framework the composition is made of alternating AlO_4^{5-} and PO_4^{3-} tetrahedra, the constraint of Si substitution for P results in a paired Si configuration in an asymmetrical fashion. As a result a Si-O-Al-O-Si sequence is achieved this enables NH_3 to attack Cu at an acute angle in order to minimise the electrostatic repulsion between the negative charge around the Si atoms and the lone pair on nitrogen. This indicates that the position of the secondary Si atom in the 6MR site is important in influencing the coordination of NH_3.

Table 79 (distances in Angstroms)

SSZ-13										
Before					**After**					
Cu-O1	Cu-O2	Cu-O3	Cu-O4	Spin on Cu	Cu-O1	Cu-O2	Cu-O3	Cu-O4	Cu-N	Spin on Cu
1.9270	1.9627	1.9643	1.9250	0.78	2.021	1.9633	1.9668	2.018	2.098	0.81

Table 80 (distances in Angstroms)

SAPO-34										
Before					**After**					
Cu-O1	Cu-O2	Cu-O3	Cu-O4	Spin on Cu	Cu-O1	Cu-O2	Cu-O3	Cu-O4	Cu-N	Spin on Cu
1.9543	2.0312	1.9024	1.9325	0.78	2.0025	1.9354	2.4772	1.9518	1.9706	0.76

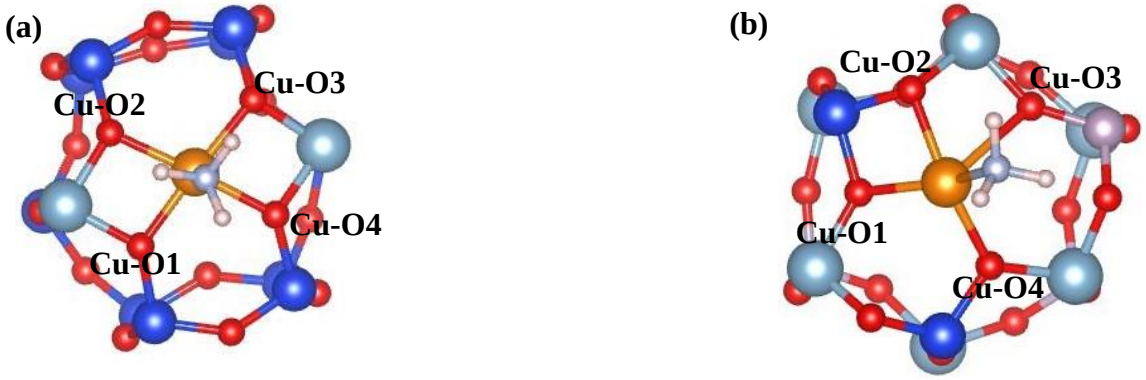

Figs. 76(a – b): **Left**, Cu-NH_3 configuration in SSZ-13. **Right**, Cu-NH_3 in SAPO-34.

The Cu distances from the plane of the 6MR increased after NH_3 adsorption as expected, see Table 81. In addition, the proximity of the Cu to the 6MR plane upon NH_3 adsorption is closer for both SSZ-13 and SAPO-34 in the paired configurations, compared to the single dopant configuration. This indicates the strength of the secondary dopant present. For SSZ-13, the presence of the second dopant leads to a near two times decreased in Cu distance from the 6MR plane, 0.41Å (Table 78) in the single and 0.23Å (Table 81) for the double configuration. However, SAPO-34 does not experience the same effect, there is a minor decreased between 0.43 and 0.39Å, but not the magnitude as observed in SSZ-13.

Inspecting Figs. 76(a –b) and 77(a –d), the framework oxygen atoms on the plane of the 6MR in SAPO-34 rises like edges. This is not observed in the SSZ-13, see Fig. 77a. Indicating the inherent framework flexibility in SAPO-34 compared to SSZ-13. This can be proposed as possible explanation to the similar Cu to plane of 6MR distances in both single and double SAPO-34 configurations. The ability of the SAPO-34 framework oxygen atoms in both single and double configurations to “follow” the Cu upon NH_3 adsorption.

In the SSZ-13 case, the inclusion of the secondary Al atom seems to remove the framework flexibility. This is observed by comparing Fig. 75a with Fig. 77a. In the latter, the framework oxygen atoms does not rise prominently like edges as for the single configuration. Subsequently, a more static configuration is observed in the paired SSZ-13 compared to the single. It is possible, because the more uniform coordination of Cu in the paired configuration is able to satisfy the activated oxygen atoms adjacent to Al dopant atoms more rigorously. Since, the all the activated oxygen are coordinated to the Cu in SSZ-13, but in SAPO-34 only three of the four activated oxygen atoms are coordinated to Cu due to the asymmetrical placement of the Si dopant atoms in the 6MR.

Table 81 (distances in Angstroms)

	SSZ-13	**SAPO-34**
	Cu – plane of 6MR distance (Å)	Cu – plane of 6MR distance (Å)
Before	0.481647	0.414643
After	0.713219	0.807159
Difference	0.231572	0.392517

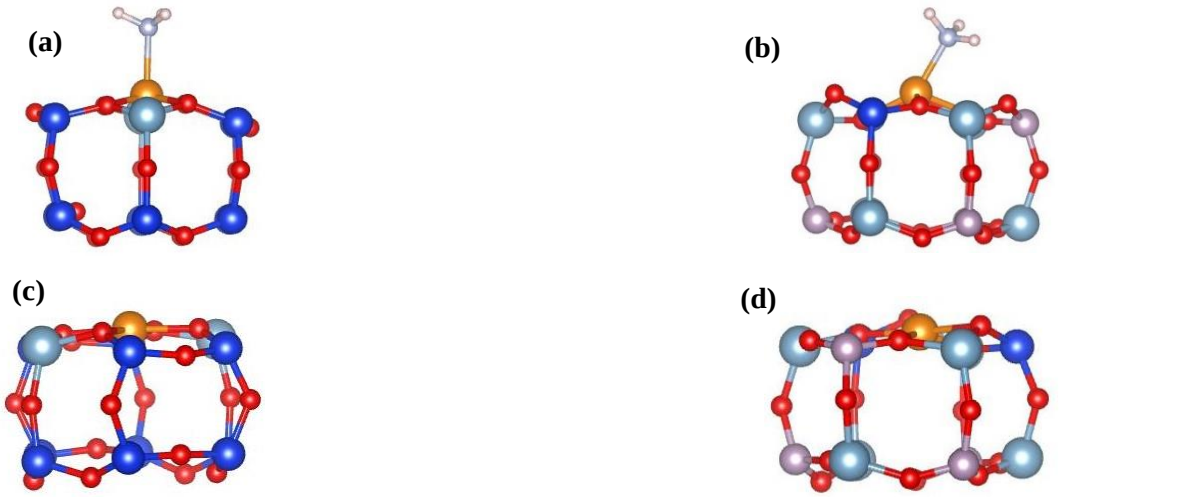

Figs. 77(a – d): Left, SSZ-13 and **right**, SAPO-34. **(a - b)** Upon coordination with NH3 and **(c - d)** without.

5.5.2.1.3 Two NH_3 molecules

In SSZ-13, introducing an additional NH_3 molecule into the single configuration of site SI results in a strong coordination to Cu from both the NH_3 molecules of equal strength, see Table 82. The Cu-N bond strengths are similar to an individual NH_3 coordination to the Cu, see Table 72. The Cu compensate for the coordination of two NH_3 molecules with the breaking of two Cu-O bonds in the 6MR. The resulting geometry has Cu displaced from the 6MR into the large cage oriented above the Al dopant atom, but coordinated to two of the activated framework oxygen atoms with two other NH_3 molecules coordination on the other side, see Fig. 78a and c.

An identical adsorption geometry is observed for SAPO-34, the Cu is pulled away from the plane of the 6MR by the coordination to two NH_3 molecules. The strengths of the C-N bonds are marginally different as indicated by the distances listed in Table 83. Two of the Cu-O bonds not coordinated to the activated oxygen atoms adjacent to the dopant atom have resulted in bond breaking like in SSZ-13. The Cu is oriented like a hinge above the Si dopant atom in the 6MR, see Fig. 78b and d.

Table 82 (distances in Angstroms)

SSZ-13 (Two NH_3 molecules)						
After						
Cu-O1	Cu-O2	Cu-O3	Cu-O4	Cu-N1	Cu-N2	Spin on Cu
1.9569	1.9467	N/A	N/A	1.9685	1.9685	0.74

Table 83 (distances in Angstroms)

SAPO-34 (Two NH_3 molecules)						
After						
Cu-O1	Cu-O2	Cu-O3	Cu-O4	Cu-N1	Cu-N2	Spin on Cu
2.0000	1.9167	N/A	N/A	1.9464	1.9863	0.74

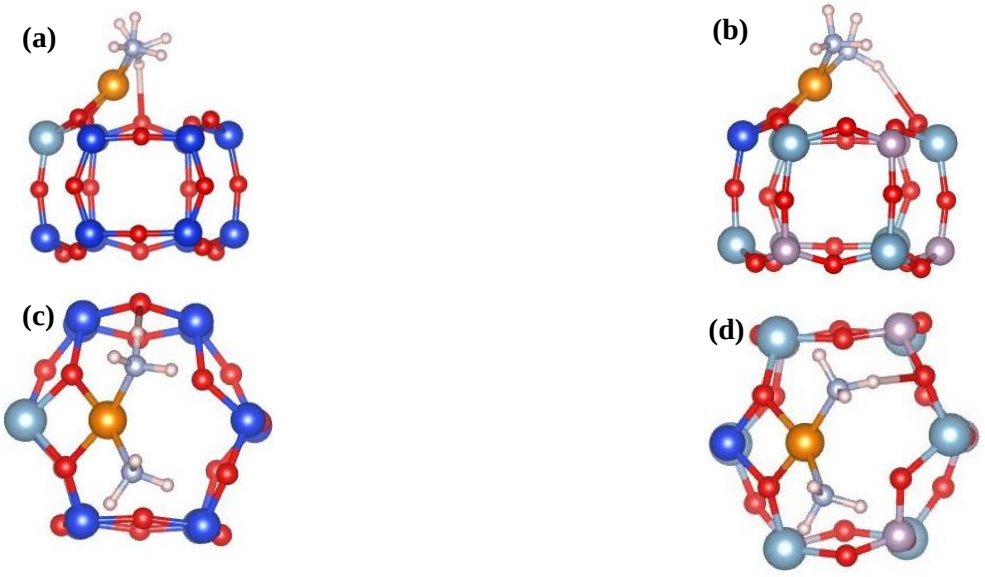

Figs. 78(a – d): Left, SSZ-13 and **right**, SAPO-34. **(a - b)** Top view of coordination with two NH_3 molecules and **(c - d)** side view.

5.5.2.2 Site SI energy

5.5.2.2.1 Single Si/Al atoms

The adsorption energies for both SSZ-13 and SAPO-34 are -2.01 and -1.97eV respectively, listed in Table 84. Comparing both, the adsorption energy in SAPO-34 is less favoured by 0.04eV. This relatively small energetic difference between the two frameworks is reflected by the similar Cu-NH_3 adsorption configurations in site SI.

In the single configurations, the NH_3 adsorption on site SI in both SSZ-13 and SAPO-34 possess the same NH_3 approach towards the Cu via an acute angle of 67˚, see Figs. 74(a – b) and Figs. 75(a – b). Subsequently, the coordination of NH_3 to Cu is of similar strengths as indicated by the Cu-N bond lengths of 1.95Å in both frameworks. The only discrepancy

between the adsorption configurations is the Cu in SSZ-13 is pulled further away from the plane of the 6MR compared to SAPO-34 as a result of NH_3 coordination, see Table 78. This is a possible indicator of a perceptibly favourable NH_3 adsorption within the SSZ-13 framework, which is reflected in the adsorption energies.

Table 84 (Energy in -eV)

SSZ-13					**SAPO-34**				
$E_{Zeol+NH_3}$	E_{Zeol}	E NH_3	Rel. E	Ads. E	$E_{AlPO+NH_3}$	E_{AlPO}	E NH_3	Rel. E	Ads. E
474507.11	472969.38	1535.71	472971.40	2.01	476577.19	475039.51	1535.71	475041.47	1.97

5.5.2.2.2 Paired Si/Al atoms

For the paired configurations, the adsorption energies are listed in Table 85. Interestingly, the pattern is reversed compared to the single configurations. The adsorption of NH_3 is more favourable by 0.32eV for the paired configuration of SAPO-34. The significant difference in adsorption energies between the paired SSZ-13 and SAPO-34 configurations is due to two factors. Firstly, the equilibrium energy of the paired Al dopants in SSZ-13 (E_{zeol}) is more stable in contrast to the single configuration by 1.78eV, compared to SAPO-34 with 1.35eV. This attributes to a 0.0004% lowering of the energy in SSZ-13, which is greater than in SAPO-34 with 0.0003%.

Secondly, the inclusion of the secondary dopant atom in the 6MR results in a geometrical factor, because in the SSZ-13, due to the spacing between the two Al atoms the NH_3 does not have an acute angle of approach to coordinate to the Cu. But in SAPO-34, the Si atoms are asymmetrically arranged this enables the NH_3 to approach at an acute angel to avoid the negatively charged dopant atoms. This is likely to be a significant factor in influencing the adsorption energy difference we observe.

However, as expected, increasing the number of dopant atoms in the occupied 6MR from one to two leads to a decreased in the adsorption energy for both SSZ-13 and SAPO-34. From -2.01 to -1.42eV and -1.97 to -1.74eV for SSZ-13 and SAPO-34 respectively, the change in favourability for NH_3 adsorption is more pronounced for the zeolite at 0.59eV than the AlPO at 0.23eV. The change in adsorption energy for SSZ-13 is more than twice that for SAPO-34. This is because, in SAPO-34 the change from a single to paired configurations does not affect the NH_3 acute angle approach in coordinating the Cu, see Fig. 76b and 77b. In SSZ-13, the NH_3 approaches in a perpendicular fashion with the negatively charged Al dopant atoms on either side of the 6MR (Fig. 76a and 77a), this would result in a relatively energetically strained state - as observed in the adsorption energies.

Table 85 (Energy in -eV)

SSZ-13					**SAPO-34**				
$E_{Zeol+NH_3}$	E_{Zeol}	E NH_3	Rel. E	Ads. E	$E_{AlPO+NH_3}$	E_{AlPO}	E NH_3	Rel. E	Ads. E
474508.30	472971.16	1535.71	472972.59	1.42	476578.31	475040.85	1535.71	475042.60	1.74

5.5.2.2.3 Two NH_3 molecules

The adsorption energies for two NH_3 molecules in SSZ-13 and SAPO-34 are -3.94 and -3.89eV respectively, see Table 11. Taking into account the adsorption energies for an individual NH_3 molecule are -2.01 and -1.97eV for SSZ-13 and SAPO-34, see Table 9, the adsorption energies for two NH_3 molecules is approximately twice the values of an individual one. The large energetic favourability in the coordination of two NH_3 molecules indicates that the displacement of Cu from site SI would not be a rare event. It is plausible that with the coordination of a third and fourth NH_3 molecule, the Cu would be completely displaced from the 6MR in site SI since this compensate for the loss of the two remaining Cu-O bonds. This is despite the discovery of site SI as the energetic equilibrium location for Cu(II) in SSZ-13 and SAPO-34. However, as shown in the CRYSTAL calculations of H_2O molecules this displacement of Cu is specific to the single configuration because in the paired, the Cu coordination to all four of the activated oxygen atoms in SSZ-13 and SAPO-34 prevents the dislocation of Cu from the 6MR.

The Cu displacement observed as a result of coordination with two NH_3 molecules is unlikely to occur in the 8MR of site SIV. This is because, the first NH_3 molecule would sit inside the 8MR and the second would coordinate to the Cu from the large cage. GULP and CRYSTAL calculations of H_2O molecules in site SIV shows that the 8MR can fit only one H_2O molecule. The relative similar sizes and dipoles of NH_3 and H_2O would indicate a similar outcome for NH_3. As a result, the NH_3 molecules are located in different positions and would not exert a uniform pull on the Cu like in site SI.

Table 86 (Energy in -eV)

SSZ-13					**SAPO-34**				
$E_{Zeol+NH_3}$	E_{Zeol}	E NH_3	Rel. E	Ads. E	$E_{AlPO+NH_3}$	E_{AlPO}	E NH_3	Rel. E	Ads. E
476044.75	472969.38	3071.43	472973.33	3.94	478114.82	475039.51	3071.43	475043.39	3.89

5.5.2.3 Site SIV configuration

A NH_3 molecule was docked onto Cu^{2+} in the 8MR position at site SI with a single Al/Si atom in framework site. This was repeated with Al/Si atom pairs in the same 8MR position. As per for the SI calculations, in both SSZ-13 and SAPO-34, two Al and Si atoms are doped per unit cell respectively. This gives a Si: Al ratio of 17:1 for SSZ-13 and Al: P: Si ratio of 9: 8: 1 for SAPO-34.

Al/Si dopant distances are controlled for the SSZ-13 and SAPO-34 configurations giving identical dopant configurations in both the single and paired situations as in previously (SI case). The Cu sits in the 8MR, labelled site SIV. The distances between the dopants follows an Al-O-Si-O-Si-O-Si-Al and a Si-O-Al-O-P-O-Al-Si sequence in SSZ-13 and SAPO-34 respectively, see Figs. 79(a – d). In addition, Fig. 8e shows a paired configuration in SAPO-34 with a Si-O-Al-O-Si sequence inside the 8MR. This enables the Cu^{2+} to coordinate to both the Si atoms inside the 8MR. The close proximity of the Si dopants in ensures that Cu is able to form bonds to the activated oxygen atoms adjacent to both the Si atoms.

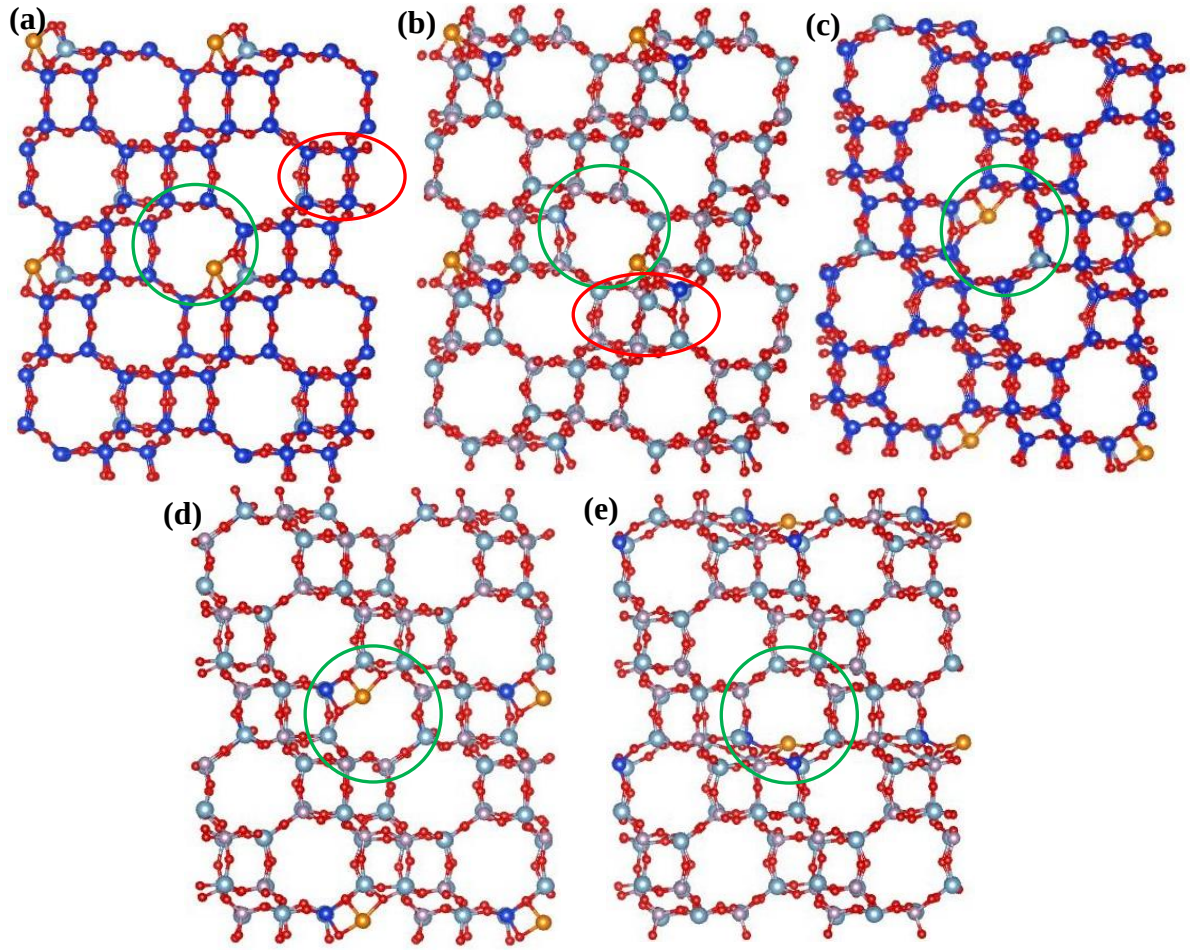

Figs. 79(a – e): **Left**, SSZ-13 unit cell. **Right**, SAPO-34 unit cell. **(a – b)** Circled green is the 8MR with a single Al/Si atom and the Cu^{2+} sitting in site SIVa. Circled red is the other single Al/Si atom in a 6MR, SIc. **(c – e)** Circled green is the 8MR with a paired Al/Si atoms and the Cu^{2+} in site SIVa.

5.5.2.3.1 Single Si/Al atoms

Looking at Figs. 80a – b, a significant difference in the Cu configuration is observed between the SSZ-13 and SAPO-34. In the AlPO situation, the Cu resides in the 8MR but it does not coordinate with the Si dopant in the 8MR, instead it coordinates with the Si dopant in the adjacent 6MR, see Fig. 80b. This peculiar configuration enables the Cu to form four bonds, three within the 8MR framework and an additional one with the Si atom in the 6MR. The Cu does not sit inside the plane of the 8MR like in SSZ-13, but it is adjacent to it. The location of the Cu in between sites (SI and SIV) in the AlPO framework is possible due to the relative inherent flexibility. The framework Al atom directly below the Cu is compressed downwards relative to the 6MR plane, enabling the Cu to coordinate with the activated oxygen atoms around the nearest Si dopant. The bond lengths are listed in Table 88.

For SSZ-13, a conventional Cu configuration is adopted in the 8MR. The Cu coordinates to the Al dopant in the 8MR forming three bonds, two of similar lengths (1.90 and 1.87Å) and one longer at 1.98Å, see Table 12. Compared to zeolite, the ability of the AlPO framework to flex due to the inherent iconicity of the bonding[186] enables a wider range of configurations, especially concerning the site SIV case, since the larger aperture of the 8MR relative to 6MR accommodates greater variation in Cu configurations as observed in Figs. 80a –b.

Upon NH_3 adsorption, the NH_3 molecule is small enough in size to fit inside the 8MR coordinating to Cu perpendicular to rest of the Cu-O bonds. In SSZ-13 the Cu-N bond length is 1.89Å and in SAPO-34 this is 1.91Å. This is due to the differences in locations for Cu between the two frameworks; the final NH_3 adsorption locations also differ. In SSZ-13, the NH_3 sits slightly out of the plane of the 8MR, compared to in SAPO-34 the NH_3 is inside of the plane. This is because in the latter, the Cu is not found inside the plane of the 8MR, therefore the NH_3 sits further inside the 8MR in order to achieve coordination. As a result, the Cu-N bond in SAPO-34 is 0.1Å longer. See Figs. 80(c – d). The adsorption of NH_3 exerts an influence on Cu coordination to the zeolite and AlPO frameworks, as expected. In SSZ-13, all three Cu-O coordination increases in length, listed in Table 87. The SAPO-34 loses the Cu-O3 coordination, whilst the other Cu-O bonds to the 8MR framework (Cu-O1 and Cu-O2) increases in length. However, the Cu-O4 bond decreases in length by an incremental amount of 0.003Å. This indicates that in both frameworks an overall weakening of the Cu coordination to the 8MR is observed. This is in good agreement with the site SI situation. In addition to the weakening of the Cu-O bonds, another effect due to NH_3 adsorption in SAPO-34 is in contrast to before NH_3 adsorption, the framework Al atom below the Cu is less compressed since the Cu is pulling away in order to coordinate with the NH_3 inside the 8MR.

Compared to NH_3 in site SI, the different topology of site SIV including the larger dimensions of an 8MR means we do not observe the adsorption of NH_3 on Cu(II) via an acute angle. The ability of the NH_3 to coordinate directly to the Cu(II) unhindered in site SIV unlike in site SI indicates that site SIV is a stronger acidic site compared to SI. In addition, the hydrogen atoms on the NH_3 molecule is able to form hydrogen bonds with framework oxygen atoms in the 8MR, ensuring stabilization of NH_3 within the frameworks via zeolitic interaction. In SSZ-13, two hydrogen bonds are formed between NH_3 and the 8MR framework with lengths of 1.96 and 2.05Å. For SAPO-34, one hydrogen bond is formed with the activated oxygen atom inside the 8MR at a distance of 1.96Å. This is absent in the SI configuration, since the NH_3 is located in the large cage without nearby framework. Both these factors, the unhindered

coordination to Cu and hydrogen bonding inside the 8MR would indicate a favoured NH_3 adsorption in sites SIV. This is confirmed in the adsorption energy analysis, see Tables 84 and 92.

Table 87 (distances in Angstroms)

SSZ-13										
Before					**After**					
Cu-O1	Cu-O2	Cu-O3	Cu-O4	Spin on Cu	Cu-O1	Cu-O2	Cu-O3	Cu-O4	Cu-N	Spin on Cu
1.9770	1.9039	1.8664	N/A	0.69	2.0879	1.9130	1.9388	N/A	1.8861	0.69

Table 88 (distances in Angstroms)

SAPO-34										
Before					**After**					
Cu-O1	Cu-O2	Cu-O3	Cu-O4	Spin on Cu	Cu-O1	Cu-O2	Cu-O3	Cu-O4	Cu-N	Spin on Cu
1.8840	1.9505	2.4294	1.8964	0.79	2.0018	2.1438	N/A	1.8932	1.9060	0.79

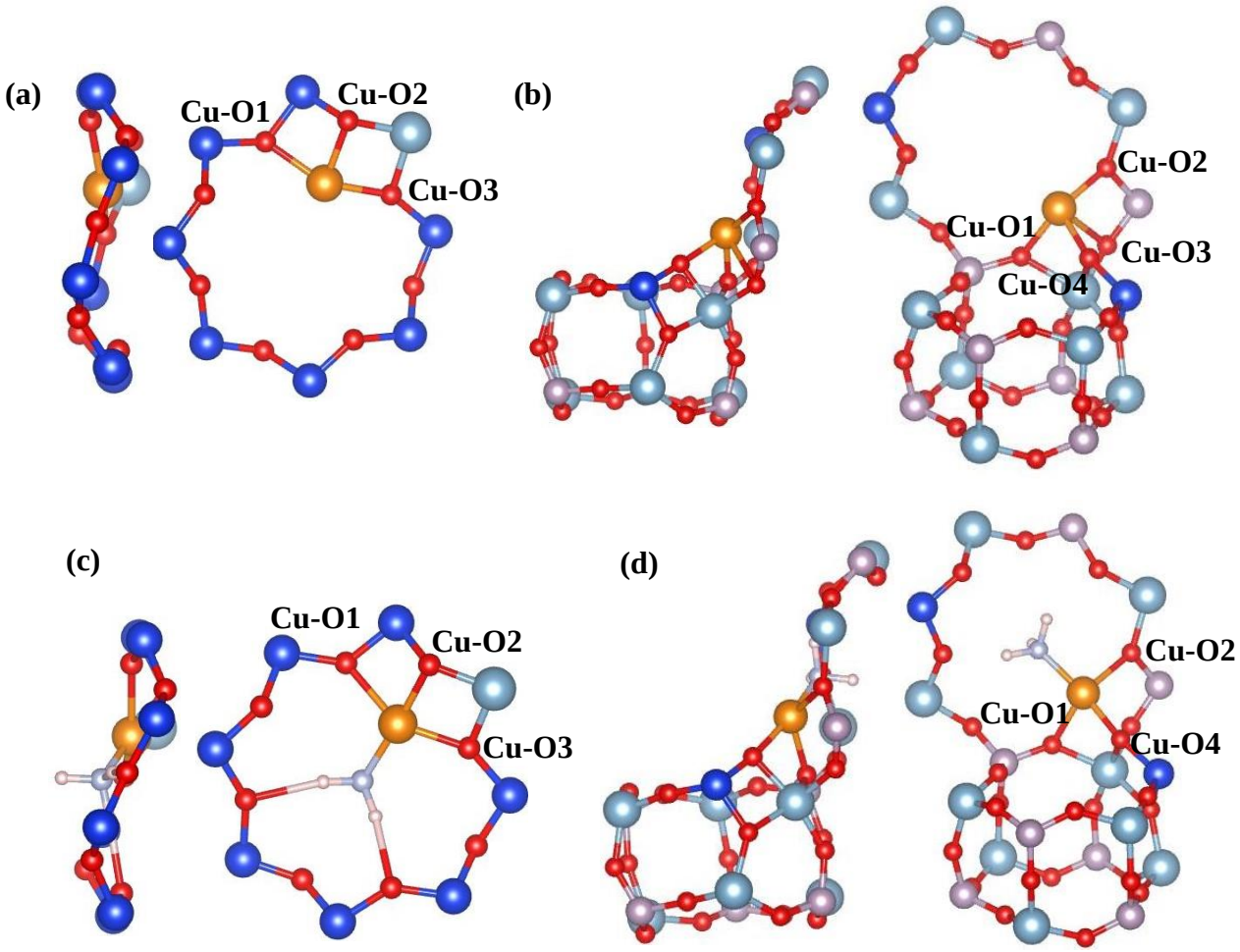

Figs. 80(a – d): **Left**, Cu-SSZ-13. **Right**, Cu-SAPO-34. Before, (**a – b)** and after NH_3 adsorption, (**c – d)**.

5.5.2.3.2 Paired Si/Al atoms

The paired Si/Al configurations resulted in identical Cu configurations for SSZ-13 and SAPO-34. Concerning SAPO-34, the placement of two Si dopant atoms in the same SIV site removes the competition for Cu to coordinate between the Si-doped 8MR or the adjacent Si-doped 6MR site. However, in the Si-O-Al-O-P-O-Al-Si sequence paired configuration since the diameter of the 8MR is 7.37Å, the Cu is too small in size to simultaneously coordinate to both the Si/Al dopant atoms in the 8MR site. As a result, the Cu can only coordinate to one, see Figs. 81a – b. The Si-O-Al-O-Si paired configuration has Cu^{2+} coordinated to both the Si dopant atoms, because the distance between the two Si dopant atoms are only one aluminium tetrahedral away from each other, see Figs. 81e. NH_3 adsorption between these two paired configurations in SAPO-34 is expected to differ, due to the difference in Si dopant configuration. The bond lengths listed in Tables 89, 90 and 91 show lengths in the range of 1.85 – 2.15Å, with SSZ-13 forming the longer bond lengths with an upper limit of 0.05Å against SAPO-34.

After NH_3 adsorption, the NH_3 coordinates in a similar fashion as observed with the single Si/Al configurations see Figs. 81d – f. As expected, the NH_3 adsorption weakens the Cu's coordination to the framework. In both SSZ-13 and SAPO-34, the NH_3 forms similar bond strengths to the Cu on the basis of their Cu-N bond lengths of 1.87 and 1.89Å respectively for the paired configurations with the same distances between the dopants atom. However, for the Si-O-Al-O-Si paired sequence, the Cu-N bond distance is longer at 1.93Å. This indicates a weaker NH_3 adsorption and the Cu-O bonds is shorter than that in the Si-O-Al-O-P-O-Al-Si configuration; a subsequent stronger Cu coordination to the 8MR. This shows the influence of the distribution and distances of the dopant atoms in a framework. In general, the 8MR is large enough to afford both the Cu and NH_3 to reside inside without any steric constraints, indicating a possible equilibrium location for NH_3 adsorption during the de-NO_x cycle.

The presence of a secondary dopant atom in the 8MR enables hydrogen bonding between the NH_3 molecule and uncoordinated activated framework oxygen atoms. In SSZ-13, two hydrogen bonds are formed with these oxygen atoms adjacent to the second Al dopant, one at length of 1.73Å and another at a more distant 2.22Å. The SAPO-34 configurations similarly are able to form two hydrogen bonds, in the Si-O-Al-O-P-O-Al-O-Si configuration however, only one of these is coordinated to the activated oxygen with a distance of 1.76Å and the other is at 1.97Å. The Si-O-Al-O-Si configuration achieves two hydrogen bonds but at longer distances of 2.47 and 2.31Å. Compared to the single configurations, the additional influence of hydrogen bonding with dopant atoms in the 8MR would result in a more favoured NH_3 adsorption energy in the paired configurations with the exception of the SAPO-34 paired Si-O-Al-O-Si configuration, see Tables 89 and 90.

Table 89 (in Angstroms)

SSZ-13										
Before					**After**					
Cu-O1	Cu-O2	Cu-O3	Cu-O4	Spin on Cu	Cu-O1	Cu-O2	Cu-O3	Cu-O4	Cu-N	Spin on Cu
2.0017	1.9009	1.8977	N/A	0.72	2.1246	1.9133	1.9394	N/A	1.8734	0.68

Table 90 (in Angstroms)

SAPO-34 (Si-O-Al-O-P-Al-O-Si pair)										
Before					**After**					
Cu-O1	Cu-O2	Cu-O3	Cu-O4	Spin on Cu	Cu-O1	Cu-O2	Cu-O3	Cu-O4	Cu-N	Spin on Cu
1.9591	1.8953	1.8897	N/A	0.68	2.0739	1.9084	1.9753	N/A	1.8851	0.66

Table 91 (in Angstroms)

SAPO-34 (Si-O-Al-O-Si pair)										
Before					**After**					
Cu-O1	Cu-O2	Cu-O3	Cu-O4	Spin on Cu	Cu-O1	Cu-O2	Cu-O3	Cu-O4	Cu-N	Spin on Cu
1.8975	1.8880	1.8315	N/A	0.67	1.9624	1.9023	1.8923	N/A	1.9300	0.72

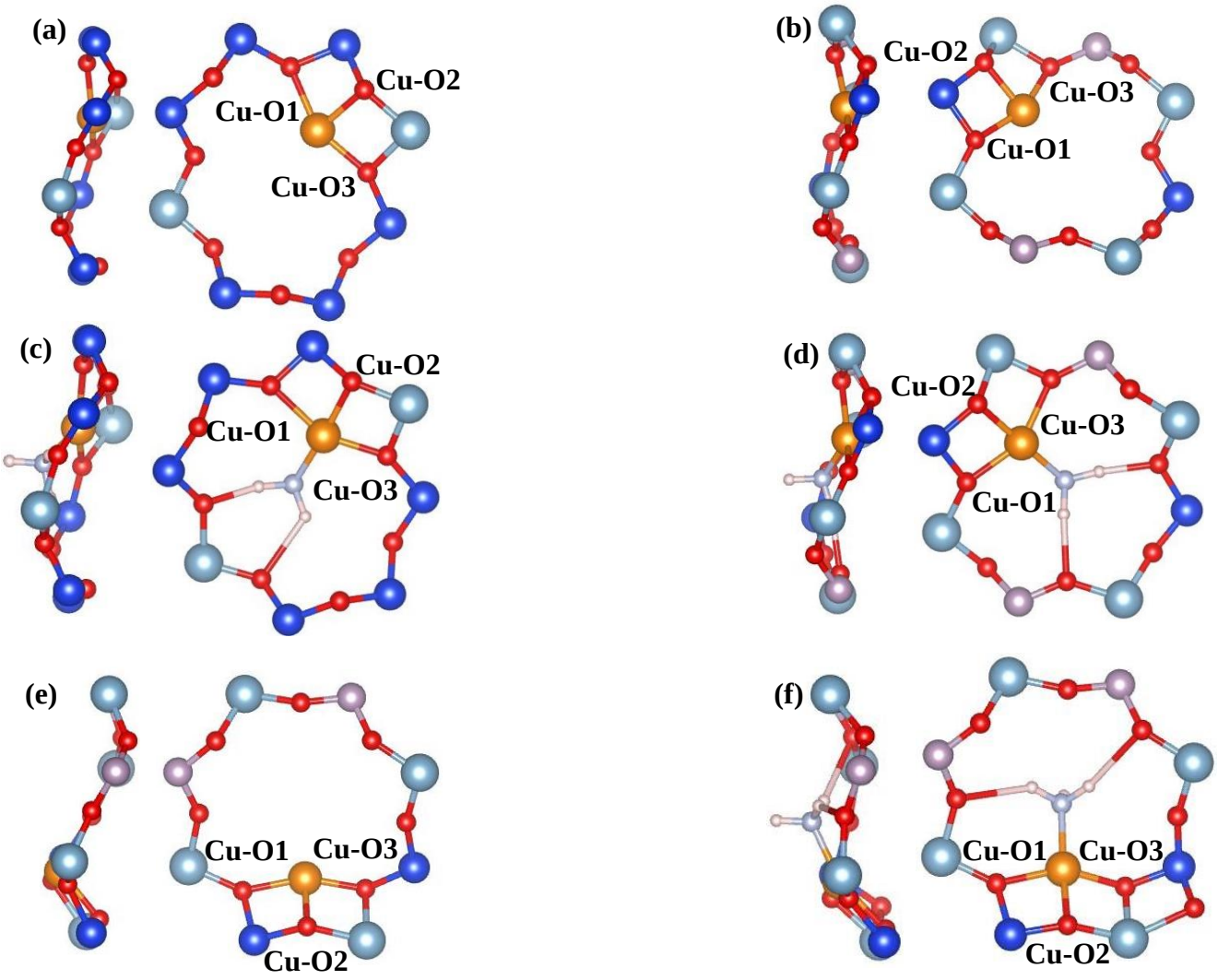

Figs. 81(a – f): Before **(a – b)** and after **(c – d)** NH_3 adsorption in pair configurations of SSZ-13 and SAPO-34 (Si-O-Al-O-P-O-Al-Si). Before **(e)** and after **(f)** NH_3 adsorption in Si-O-Al-O-Si pair configuration.

5.5.2.4 Site SIV energy

5.5.2.4.1 Single Si/Al atoms

The adsorption energies of NH_3 in both SSZ-13 and SAPO-34 are -3.24 and -3.32eV respectively, see Table 92. This is approximately two and a half times more favourable compared to NH_3 adsorption in site SI, see Table 84. In addition, adsorption in the SAPO-34 is more favourable by 0.08eV, this trend was also observed with site SI. Site SI has been found to be geometrically the equilibrium location for Cu adsorption, as a result NH_3 adsorption on Cu in SI would be energetically less favourable compared to SIV.

NH_3 adsorption is favoured in site SIV compared to SI, because as mentioned above Cu in the site SI is the favoured equilibrium, therefore NH_3 adsorption would weaken the Cu's coordination to the 6MR resulting in a destabilizing state. In addition, the larger aperture of the 8MR enables NH_3 to fit inside with the Cu, this allows a greater coordination between NH_3 and Cu as evident with the listed Cu-N bonds of 1.89 and 1.91Å for SSZ-13 and SAPO-34 respectively against 1.95Å for both in sites SI. The close proximity of the NH_3 to the framework

oxygen atoms in the 8MR enables greater stabilization with the formation of hydrogen bonds. This would have also contributed to the lower adsorption energy in site SIV.

Table 92 (Energy in -eV)

SSZ-13					**SAPO-34**				
$E_{Zeol+}NH_3$	E_{Zeol}	E NH_3	Rel. E	Ads. E	$E_{AlPO+}NH_3$	E_{AlPO}	E NH_3	Rel. E	Ads. E
474507.22	472968.27	1535.71	472971.51	3.24	476576.67	475037.64	1535.71	475040.96	3.32

5.5.2.4.2 Paired Si/Al atoms

The equilibrium energies of the bare Cu-SSZ-13 and Cu-SAPO-34 are near identical to that in the single configurations at -472968 and -475039eV respectively, see Tables 92 and 93. This is because as observed in Figs. 81a – b, the Cu only coordinates to one of the dopant atom within the vicinity of the 8MR. Therefore, the stabilization energy expected from the coordination with the additional dopant atom in a paired configuration is redundant. However, the influence of the secondary dopant in the 8MR comes into effect with NH_3 adsorption as observed in the adsorption energies indicating a more acidic environment. The paired SAPO-34 (Si-O-Al-O-P-O-Al-Si) configuration is lower in adsorption energy by -0.11eV, and the paired SSZ-13 is more favoured by –0.10eV. The lowering of the adsorption energy by approximately -0.1eV in the paired configurations, is due to additional stabilization of the activated framework oxygen atoms adjacent to the secondary dopant atom in the 8MR. This is provided by hydrogen bonding with the hydrogen atoms on the NH_3 molecule, where at least one of the activated oxygen atoms is hydrogen bonded, see Figs. 81(c – f).

SAPO-34 is 0.09eV lower in adsorption energy compared to SSZ-13, this is a similar difference in magnitude with both the frameworks in the single configurations (see Table 92). In both frameworks, the averaged Cu-O bond lengths are 1.99Å and the Cu-N coordination was at 1.87 and 1.89Å for the zeolite and AlPO respectively. As such, in terms of physical parameters there is only minor discrepancy between the two frameworks. The 0.09eV difference in adsorption energy is due to the chemical composition of the AlPO and the attributed more ionic composition. This seems to enable the AlPO framework to accommodate more favourably a NH_3 molecule adsorption. In general, the NH_3 adsorption is more favoured in sites SIV compared to sites SI. For the paired configurations, NH_3 adsorption in site SIV of frameworks SAPO-34 and SSZ-13 is 1.69 and 1.92eV more favoured respectively. Whilst in the single configurations, this difference is smaller but adsorption in sites SIV in SAPO-34 and SSZ-13 is lower by 1.35 and 1.23eV. The decrease in difference from the paired to single configurations is two-fold; for former the secondary dopant atom in the 8MR enables stabilization of the adjacent activated oxygen atoms, but this dopant atom in the 6MR results in a stronger Cu coordination to the framework and discourages NH_3 adsorption. As a result, the difference in adsorption energy between the paired configurations of sites SIV and SI is significantly greater.

The SAPO-34 (Si-O-Al-O-Si) paired configuration has an adsorption energy of -2.55eV, this 0.88eV higher energy compared to the Si-O-Al-O-P-O-Al-Si configuration, see Tables 93 and 94. This shows that the acidity of a site is intimately related to the distances between the dopant atoms. Since, in the Si-O-Al-O-Si configuration the Cu is able to simultaneously coordinate to both sets of activated oxygen atoms around the Si dopant atoms. This results in a stronger Cu coordination to the 6MR framework as evident by the shorter Cu-O bonds, in both before and after NH_3 adsorption relative to the Si-O-Al-O-P-O-Al-O-Si configuration, see Tables 90 and 91. Consequently, the equilibrium energy of the bare Cu-SAPO-34 for the Si-O-Al-O-Si sequence is 1.43eV lower in energy against the Si-O-Al-O-P-O-Al-O-Si configuration.

Despite the higher adsorption energy of -2.55eV relative to the other configurations in site SIV studied, it is still more favoured than NH_3 adsorption in sites SI. This is attributed to the favoured topology of the 8MR enabling close coordination of NH_3 to the Cu and formation of strong hydrogen bonds to the framework oxygen atoms in site SIV.

Table 93 (Energy in -eV)

SSZ-13					**SAPO-34 (Si-O-Al-O-P-O-Al-O-Si)**				
$E_{Zeol+}NH_3$	E_{Zeol}	E NH_3	Rel. E	Ads. E	$E_{AlPO+}NH_3$	E_{AlPO}	E NH_3	Rel. E	Ads. E
474507.16	472968.11	1535.71	472971.44	3.34	476577.75	475038.60	1535.71	475042.03	3.43

Table 94 (Energy in -eV)

SAPO-34 (Si- O-Al-O-Si)				
$E_{AlPO+}NH_3$	E_{AlPO}	E NH_3	Rel. E	Ads. E
476578.30	475040.03	1535.71	475042.59	2.55

Summary 5.5: CRYSTAL NH_3 calculations

In general, NH_3 adsorption is similar with H_2O adsorption, for the single-dopant configurations in site SI, an individual NH_3 molecular adsorption was shown to coordinate to the Cu^{2+} in both SSZ-13 and SAPO-34 in parallel fashion. The NH_3 approaches the Cu^{2+} residing in site SI at an angle to the 6MR plane, titled away from the dopant atom situated inside the 6MR. This is reflected by the adsorption energies computed, which showed a 0.04eV discrepancy, see Table 84.

For the paired-dopant configurations; adsorption of NH3 differs between SSZ-13 and SAPO-34, due to the varied sequencing of the two dopant atoms around 6MR window. In SSZ-13, the two Al atoms are symmetrically aligned opposite each other, but in SAPO-34 they are not, see Figs. 76(a – b). This means that in SAPO-34, there is a coordinative space for the Cu^{2+} to attack without experiencing electrostatic repulsion. This was observed in the H_2O calculations, indicating the dopant configuration is an important parameter to be considered when evaluating the feasibility of admolecules adsorption.

Co-adsorption of two NH_3 molecules inside a single-dopant configuration resulted in the Cu^{2+} atom partially displaced from the 6MR, see Figs. 78(a – d). This observation was also found in the H_2O calculations, in both set of calculations it is the adsorption energy inside SSZ-13 that is slightly favoured, see Table 86. A hypothesis for this is the greater stability achieved with the prior single NH_3 adsorption inside the SAPO-34, before the addition of a second NH_3 molecule.

Site SIV is the optimum site for NH_3 adsorption, see Tables 92 and 93, as similarly observed in the H_2O calculations. This indicates that in general, the 8MR window in site SIV is the acid site for admolecules adsorption, due to the large aperture of the 8MR to fit the Cu^{2+} atom and an admolecule, whilst fostering a distorted square-planar geometry around the Cu^{2+} metal centre. Like in the H_2O calculations, SAPO-34 and SSZ-13 achieved similar adsorption energies across the sites SI and SIV investigated between one to two NH_3 molecules. Inside the SIV subset calculations, the SAPO-34 indicated a more favourable framework for NH_3 adsorption, however, as evident in Table 94 this is very sensitive to the dopant sequencing.

Chapter 6 Conclusion

Recent work as showcased in this report has firstly been based on locating the favoured extra-framework sites of Cu^{2+} ions in SSZ-13 and SAPO-34 via a systematic method, this was determined by calculating the equilibrium energies of 620 Cu/dopant configurations in SSZ-13 and 340 in SAPO-34 using force-fields method in GULP. The results showed that sites SI is the most favoured sites for Cu^{2+}, followed by sites SIV, while both sites SIII and SIV are maxima.

CRYSTAL DFT calculations based on PBC were performed to reproduce and verify the findings from the GULP work, it confirmed that sites SI is indeed the favoured location of Cu^{2+} for SSZ-13 and SAPO-34. Site SI is 0.96eV lower in energy than site SIV, with an active Al atom present in each site for SSZ-13. Whilst in SAPO-34, the same energetic pattern was observed with a magnitude of 0.92eV A new site SV, has been determined as plausible site for Cu^{2+}, adjacent to 4MR structures which is 3.7eV higher in energy compared to a site SI in SAPO-34 and 3.1eV greater than a SI in SSZ-13. In addition, migration profile studies in CRYSTAL showed that the site SIIIs in SSZ-13 and SAPO-34 are local energy minima for a specific dopant configuration in contrast to our GULP and current literature findings.

Linear regression models were built with the aim of understanding and determining the relationship between the proximity of dopant atoms to Cu^{2+} atom in both SSZ-13 and SAPO-34 frameworks. This is the first step towards an analytical approach in building a structure-property relationship model in the Cu-CHA framework system. In general, it was observed that the proximity of the dopant atoms to the Cu^{2+} metal centre is one of the main parameters for influencing the overall energy of the system.

H_2O molecules were modelled both in GULP and CRYSTAL, for the latter method in both SSZ-13 and SAPO-34, site SIV was shown to be the most promising in hosting H_2O molecules on the basis of adsorption energies. In GULP, the H_2O molecules behaved more dynamically and were not observed to be ideal coordinating ligands with Cu^{2+}, instead non-specific interaction with the framework walls in both SSZ-13 and SAPO-34 was favoured.

NH_3 adsorption in CRYSTAL was performed, and like the H_2O adsorption, site SIV was found to be energetically more favourable in both frameworks. This indicates that site SIV could be a plausible active site in the de-NO_x reaction mechanism. Comparing the adsorption of small adsorbate molecules, it was shown that SAPO-34 is a more favourable framework for the host of H_2O and NH_3 in terms of adsorption energies, indicating a more reactive catalyst for the de-NO_x reaction. However, this is a simplify view, since the dopant configuration was found to be a key factor in influencing the acidity of an extra-framework site for admolecule adsorption.

Chapter 7 Further work

The study of the stability of dopant concentrations in SSZ-13 and AlPO-34, and its effect on Cu extra-framework sites, using periodic DFT calculations should be continued, as this was shown to be a key parameter in the determining the equilibrium energy of the systems and likewise the acidity of an extra-framework site for admolecules adsorption, regardless of framework composition.

Initiate adsorption studies of simple admolecules that are found in the reaction of mixture during the de-NO_x reaction on the Cu sites, these would include the reducing agent NH_3 and N_2, which makes up 78.09% of the air mixture which would be found inside the catalytic converters. Compare Cu location and adsorption energies in SSZ-13 and SAPO-34 with respect to these admolecules. The next step in elucidating an atomistic mechanism of the de-NO_x reaction is to initiate the transition state search for the crucial elementary steps of the reaction mechanism, such as to study co-adsorbed molecules relevant for the elementary steps of the reaction mechanism like NO_3NH_4.

A missing piece from the current work, is to address the importance of Cu nuclearity – precisely, comparing isolated Cu ions and dimeric clusters on the adsorption chemistry. This would provide a comprehensive insight of the system from the perspective of covering all the variables that would affect the system and the activity with respect to the de-NO_x reaction.

Bibliography

(1) Y. Mao, H-F. Wang, P. Hu, *Int. J. Quantum. Chem.*, 2014, **115**, 618-630.
(2) F. Liu, Y, Yu, H. He, *Chem. Commun.*, 2014, **50**, 8445-8463.
(3) H. Hamada, M. Haneda, *Appl. Catal. A Gen.,* 2012, **421**, 1-13.
(4) M. F. Fu, C. T. Li, P. Lu, L. Qu. M. Y. Zhang, Y. Zhou. M. G. Yu, Y. Fang, *Catal. Sci. Technol.,* 2014, **4**, 14-25.
(5) B. Guan, R. Zhan, H. Lin, Z. Huang, *Appl. Them. Eng.,* 2014, **66**, 395-414.
(6) G. L. Bauerle, S. C. Wu, K. Nobe, *Ind. Eng. Chem. Prod. Res. Dev.,* 1978, **17**, 117-122.
(7) S. Brandenberger, O. Krocher, A. Tissler, R. Althoff, *Cat. Rev. – Sci. Eng.,* 2008, **50**, 492-531.
(8) M. Iwamoto, H. Furukawa, Y. Mine, F. Uemura, S-i. Mikuriya, S. Kagawa, *J. Chem. Soc., Chem. Commun.,* 1986, 1272-73.
(9) S. Sato, Y. Yu-u, H. Yahiro, N. Mizuno, M. Iwamoto, *Appl. Catal.,* 1991, **70**, L1-L5.
(10) S. Sato, H. Hirabayashi, H. Yahiro. N. Mizuno, M. Iwamoto, *Catal. Lett.,* 1992, **12**, 193-9.
(11) J. H. Kwak, R. G. Tonkyn, D. H. Kim, J. Szanyi, C. H. F. Peden, *J. Catal.,* 2010, **275**, 187-190.
(12) T. Yu, T. Hao, D. Q. Fan, J. Wang, M. Q. Shen, W. Li, *J. Phys. Chem. C,* 2014, **118**, 6565-75.
(13) D. E. Doronkin, M. Casapu, T. Gunter, O. Muller, R. Frahm, J. D. Grunwaldt, *J. Phys. Chem. C*, 2014, **118**, 10204-12.
(14) M. P. Ruggeri, T. Selleri, M. Colombo, I. Nova, E. Tronconi, *J. Catal.*, 2014, **311**, 266-270.
(15) O. Mihai, C. R. Widyastuti, S. Andonova, K. Kamasamudram, J. H. Li, S. Y. Joshi, N. W. Currier, A. Yezerets, L. Olsson, *J. Catal.,* 2014, **311**, 170-181.
(16) C. Yan, H. Cheng, Z. Yuan, S. Wang, *Environ. Technol.,* 2014, **36**, 169-177.
(17) L. Ma, Y. S. Cheng, G. Cavataio, R. W. McCabe, L. X. Fu, J. H. Li, *Appl. Catal. B. Environ.,* 2014, **156**, 428-437.
(18) M. P. Ruggeri, I. Nova, E. Tronconi, *Top. Catal.,* 2013, **56**, 109-113.
(19) J. J. Xue, X. Q. Wang, G. S. Qi, J. Wang, M. Q. Shen, W. Li, *J. Catal.,* 2013, **297**, 56-64.
(20) P.S. Metkar, M. P. Harold, V. Balakotaiah, *Chem. Eng. Sci.,* 2013, **87**, 51-66.
(21) D. Wang, L. Zhang, K. Kamasamudram, W. S. Epling, *ACS Catal.,* 2013, **3**, 871-881.
(22) U. Deka, I. Lezcano-Gonzalez, B. M. Weckhyusen, A. M. Beale, *ACS Catal.*, 2013, **3**, 413-427.
(23) F. Göltl, J. Hafner, *J. Chem. Phys.,* 2012, **136**, 64501-17.
(24) B. F. Mentzen, G. Bergeret, *J. Phys. Chem. C.,* 2007, **111**, 12512-16.
(25) C. Lamberti, S. Bordiga, M. Salvaggio, G. Spoto, A. Zecchina, F. Geobaldo, G. Vlaic, M. Bellatreccia, *J. Phys. Chem. B.,* 1997, **101**, 344-360.
(26) K. Pierloot, A. Delabie, C. Ribbing, A. A. Verbreckmoes, R. A. Schoonheydt, *J. Phys. Chem. B,* 1998, **102**, 10789-98.
(27) A. Delabie, K. Pierloot, M. H. Groothaert, R. A. Schoonheydt, L. G. Vanquickenborne, *Eur. J. Inorg. Chem.,* 2002, **2002**, 515-530.
(28) S. Bordiga, D. Scarano, G. Spoto, A. Zecchina, C. Lamberti, C. O. Arein, *Vibr. Spectrosc.*, 1993, **5**, 69-74.
(29) S. Bordiga, E. Garrone, C. Lamberti, A. Zecchina, C. O. Arean, V. B. Kazansky, L. M. Kustov, *J. Chem. Soc. Faraday. Trans.,* 1994, **90**, 3367-3372.

(30) K. Pierloot, A. Delabie, M. H. Groothaert, R. A. Schoonheydt, *Phys. Chem. Chem. Phys.*, 2001, **3**, 2174-2183.
(31) J. Howard, J. M. Nichol, *J. Chem. Soc. Faraday. Trans.* 1989, **85**, 1233-1244.
(32) S. Kieger, G. Delahay, B. Coq, B. Neveu, *J. Catal.*, 1999, **183**, 267-280.
(33) M. Iwamoto, S. Yokoo, K. Sakai, S. Kagawa, *J. Chem. Soc., Faraday Trans.,* 1981, **77**, 1629-38.
(34) S. Kieger, G. Delahay, B. Coq, *Appl. Catal. B: Environ.*, 2000, **25**, 1-9.
(35) M. Iwamoto, H. Hamada, *Catal. Today,* 1991, **10**, 57-71.
(36) J. H. Kwak, H. Zhu, J. H. Lee, C. H. F. Peden, J. Szanyi, *Che. Commun.*, 2012, **48**, 4758-4760.
(37) J. H. Kwak, D. Tran, S. D. Burton, J. Szanzyi, J. H. Lee, C. H. F. Peden, *J. Catal.*, 2012, **287**, 203-209.
(38) D. W. Fickel, R. F. Lobo, *J. Phys. Chem. C*, 2010, **114**, 1633-1640.
(39) D. W. Fickel, E. D'Addio, J. A. Lauterbach, R. F. Lobo, *Appl. Catal. B: Environ.*, 2011, **102**, 441-448.
(40) P. G. Blakeman, E. M. Burkholder, H-Y. Chen, J. E. Collier, J. M. Fedeyko, H. Jobson, R. R. Rajaram, *Catal. Today,* 2014, **231**, 56-63.
(41) U. Deka, I. Lezcano-Gonzalez, S. J. Warrender, A. L. Picone, P. A. Wright, B. M. Weckhuysen, A. M. Beale, *Microporous Mesoporous Mater.*, 2013, **166**, 144-152.
(42) F. Göltl, R. E. Bulo, J. Hafner, P. Sautet, *J. Phys. Chem. Lett.*, 2013, **4**, 2244-49.
(43) I. Lezcano-Gonzalez, U. Deka, H. E. van der Bij, P. Paalanen, B. Arstad, B. M. Weckhuysen, A. M. Beale, *Appl. Catal. B: Environ.*, 2014, **154-155**, 339-349.
(44) J. H. Kwak, T. Varga, C. H. F. Peden, F. Gao, J. C. Hanson, J. Szanyi, *J. Catal*., 2014, **314**, 83-93.
(45) A. A. Verma, S. A. Bates, T. Anggara, C. Paolucci, A. A. Parekh, K. Kamasamudram, A. Yezerets, J. T. Miller, W. N. Delgass, W. F. Schneider, F. H. Ribeiro, *J. Catal.*, 2014, **312**, 179-190.
(46) J. Xue, X. Wang, G. Qi, J. Wang, M. Shen, W. Li, *J. Catal.*, 2013, **297**, 56-64.
(47) L. Wang, W. Li, G. Qi, D. Weng, *J. Catal.,* 2012, **289**, 21-29.
(48) J.-S. McEwen, T. Anggara, W. F. Schneider, V. F. Kispersky, J. T. Miller, W. N. Delgass, F. H. Ribeiro, *Catal. Today*, 2012, **184**, 129-144.
(49) J. Gale, *J. Chem. Soc., Faraday. Trans.,* 1997, **93(4)**, 629-637.
(50) H. Bosch, F. Janssen, *Catal. Today*, 1988, **2**, 369-532.
(51) K. Skalska, J. S. Miller, S. Ledakowicz, *Sci. Total Environ.*, 2010, **408**, 3976-3989.
(52) L. J. Muzio, G. C. Quartucy, *Prog. Energy Combust. Sci.*, 1997, **23**, 233-266.
(53) S. Sillman, *Atmos. Environ*., 1999, **33**, 1821-1845.
(54) D. C. Carslaw, S. D. Beevers, *Atmos. Environ.,* 2004, **38**, 3585-94.
(55) R. Kartenbuch, K. H. Becker, J. A. G. Gomes, J. Kleffmann, J. C. Lorzer, M. Spittler, P. Wiesen, R. Ackermann, A. Geyer, U. Platt, *Atmos. Environ.,* 2001, **35**, 3385-3394.
(56) M. A. Gomez-Garcia, V. Pitchon, A. Kiennemann, *Environ. Int.,* 2005, **31**, 923-32.
(57) J. Van Durme, J. Dewulf, C. h. Leys, H. Van Langenhove, *Appl. Catal. B-Environ.,* 2008, **78**, 324-333.
(58) Z. Wang, J. Zhou, Y. Zhu, Z. Wen, J. Liu, L. Cen, *Process Technol.,* 2007, **88**, 817-23.
(59) Y. Zeldovich, *Acta Physicochimica USSR,* 1946, **21**, 577-628.
(60) S. M. Shahed, H. K. Newhall, *Combust. Flame,* 1971, **17**, 131-37.

(61) J. Blauwens, B. Smets, J. Peeters, *J. Combust. Inst.*, 1977, **16**, 1055-62.
(62) A. Tomita, *Fuel Process Technol.*, 2001, **71**, 53-70.
(63) M. T. Javed, N. Irfan, B. M. Gibbs, *J. Environ. Manage.,* 2007, **83**, 251-289.
(64) R. Rodenhausen, *Environ. Prog.*, 2004, **18**, 260-6.
(65) A. G. Chmielewski, *Radiat. Phys. Chem.,* 2007, **76**, 1480-4.
(66) J. Wang, C. h. Wu, J. Chen, H. Zhang, *J. Chem. Eng.,* 2006, **121**, 45-9.
(67) W. Yang, H. Hsing, Y. Yang, J. Shyng, *J. Hazard. Mater.,*2007, **148**, 653-9.
(68) S. Devahasdin, C. h. Fan, K. Li, D. H. Chen, *J. Photochem. Photobiol. A,* 2003, **156**, 161-70.
(69) L. Wang, H. Chen, M-H. Yuan, S. Rivillon, E. H. Klingenberg, J. X. Li, R. T. Yang, *Appl. Catal. B: Environ.,* 2014, **152-153**, 162-171.
(70) W. Held, A. Koenig, T. Richter, L. Puppe, SAE Paper 900496*,* 1990.
(71) M. Iwamoto, H. Yahiro, S. Shundo, Y. Yu-u, N. Mizuno, Shokubai*,* 1990, **32**, 430.
(72) J. Kašpar, P. Fornasiero, M, Graziani, *Catal. Today.*, 1999, **50**, 285-298.
(73) E. Fridell, M. Skoglundh, B. Westerberg, S. Johansson, G. Smedler, *J. Catal.,* 1999, **183**, 196-209.
(74) L. Li, N. Guan, *Microporous Mesoporous Mater.*, 2009, **117**, 450-457.
(75) A. König, W. Held, T. Richter, *Top. Catal.*, 2004, **28**, 99-103.
(76) M. Li, Y. Yeom, E. Weitz, W. M. H. Sachtler, *J. Catal.,* 2005, **235**, 201-8.
(77) J. M. Thomas, R. Raja, D. W. Lewis, *Angew. Chem. Int. Ed.*, 2005, **44**, 6456-6482.
(78) M. Richter, R. Eckelt, B. Parlitz, R. Fricke, *Appl. Catal. B: Environ.,* 1998, **15**, 129-146.
(79) I. Bull, R. S. Boorse, W. M. Jaglowski, G. S. Koermer, A. Moini, A. J. Patchett, W. M. Xue, P. Burk, J. C. Dettling, M. T. Caudle, U.S. Patent 0,226,545, 2008.
(80) S. I. Zones, U.S. Patent 4,544,538, 1985.
(81) S. I. Zones, T. L. Yuen, S. J. Miller, U.S. Patent 6,709,644, 2004.
(82) J. M. Fedeyko, H.-Y. Chen, T. H. Ballinger, E. C. Weigert, H.-L. Chang, J. P. Cox, P. J. Andersen, SAE Technical Paper 2009-01-0899, 2009.
(83) M. Calligaris, G. Nardin, *Zeolites*, 1982, **2**, 200-204.
(84) J. Dedecek, B. Wichterlova, P. Kubat. *Microporous Mesoporous Mater.,*1999, **32**, 63-71.
(85) A. F. Gualtieri, E. Passaglia, *Eur. J. Mineral.,* 2006, **18**, 351-9.
(86) C. R. A. Catlow, J. M. Thomas, *Chem. Phys. Lett.,* 1992, **188**, 320-5.
(87) L. J. Smith, A. Davidson, A. K. Cheetham, *Catal. Lett.,* 1997, **49**, 143-6.
(88) R. Gounder, E. Iglesia, *Chem. Commun.,* 2013, **49**, 3491-3509.
(89) D. Wang, L. Zhang, K. Kamasamudram, W. S. Epling, *ACS. Catal.*, 2013, **3**, 871-81.
(90) R. Q. Long, R. T. Yang, *J. Catal.*, 2002, **207**, 224-231.
(91) P. M. Ruggeri, A. Grossale, I. Nova, E. Tronconi, H. Jirglova, Z. Sobalik, *Catal. Today*, 2012, **184**, 107-114.
(92) M. Rivallan, G. Ricchiardi, S. Bordiga, A. Zecchina, *J. Catal.*, 2009, **264**, 104-116.
(93) S. P. Metkar, V. Balakotaiah, P. M. Harold, *Catal. Today*, 2012, **184**, 115.
(94) J. Szanyi, T. M. Paffett, *J. Catal*., 1996, **164**, 232.
(95) F. Poignant, J. L. Freysz, M. Daturi, J. Saussey, *J. Catal. Today*, 2001, **70**, 197.
(96) M. Iwasaki, H. Shinjoh, *Phys. Chem. Chem. Phys.,* 2010, **12**, 2365.
(97) M. Rivallan, G. Ricchiardi, S. Bordiga, A. Zecchina, *J. Catal*., 2009, **264**, 104.
(98) M. Iwasaki, H. Shinjoh, *Phys. Chem. Chem. Phys*., 2010, **12**, 2365.

(99) A. Desikusumastuti, T. Staudt, M. Happel, M. Laurin, J. Libuda, *J. Catal*., 2008, **260**, 315.
(100) M. Rivallan, G. Ricchiardi, S. Bordiga, A. Zecchina, *J. Catal*., 2009, **264**, 104.
(101) M. Colombo, I. Nova, E. Tronconi, App. Catal. B, 2012, **111**, 433.
(102) M. Ahrens, O. Marie, P. Bazin, M. Daturi, *J. Catal*., 2010, **271**, 1.
(103) M. Iwasaki, H. Shinjoh, *Phys. Chem. Chem. Phys.,* 2010, **12**, 2365.
(104) C. Ciardelli, I. Nova, E. Tronconi, D. Chatterjee, B. Bandl-Konrad, M. Weibel, B. Krutzsh, *Appl. Catal. B*, 2007, **70**, 80
(105) M. Iwasaki, H. Shinjoh, *Appl. Catal. A*, 2010, **390**, 71
(106) P. M. Ruggeri, A. Grossale, I. Nova, E. Tronconi, H. Jirglova, Z. Sobalik, *Catal. Today*, 2012, **184**, 107.
(107) Y. H. Yeom, J. Henao, M. J. Li, W. M. H. Sachtler, E. Weitz, *J. Catal.*, 2005, **231**, 181.
(108) C. Ciardelli, I. Nova, E. Tronconi, D. Chatterjee, B. Bandl-Konrad, *Chem. Commun.*, 2004, **23**, 2718.
(109) I. Nova, C. Ciardelli, E. Tronconi, D. Chatterjee, B. Bandl-Konrad, *Catal. Today*, 2006, **114**, 3.
(110) M. J. Li, J. Henao, Y. Yeom, E. Weitz, W. M. H. Sachtler*, Catal. Lett*., 2004, **98**, 5.
(111) A. Grossale, I. Nova, E. Tronconi, D. Chatterjee, M. J. Weibel, *Catal.*, 2008, **256**, 312.
(112) I. Nova, C. Ciardelli, E. Tronconi, D. Chatterjee, B. Bandl-Konrad, *Catal. Today*, 2006, **114**, 3.
(113) H. Y. Chen, Q. Sun, B. Wen, Y. H. Yeom, E. Weitz, W. M. H. Sachtler, *Catal. Today*, 2004, **96**, 1.
(114) I. Malpartida, O. Marie, P. Bazin, M. Daturi, X. Jeandel, *Appl. Catal. B*, 2012, **113**, 52.
(115) M. Koebel, M. Elsener, M. Kleemannm, *Catal. Today*, 2000, **59**, 335-345.
(116) M. Devadas, O. Krocher, M. Elsener, A. Wokaun, N. Soger, M Pfeifer, Y. Demel, L. Mussmann, *Appl. Catal. B*, 2006, **67**, 187-196.
(117) M. Koebel, M. Elsener, G. Madia, SAE Technical Paper, 2001 – 01-3625, 2001.
(118) T. Curtin, *Environmental Catalysis*, Taylor and Francis, New York, 2005.
(119) H. Peace, B. Owen, D. W. Raper, *Sci. Total Environ.,* 2004, **334**, 347-357.
(120) E. Jacob, R. Muller, A. Schneeder, T. Cartus, R. Dreisbach, H. Mai, M. Paulus, J. Spengler, *In Motortechnische Zeitschrift* 2006, 67.
(121) A.E. Van Diepen, M. Makkee, J.A. Moulijn, *Environmental Catalysis*, Imperial College Press, London, 1999.
(122) K. Boulouchos, O. Krocher, T. Lutz, *Auto & Technik* 2005, 28–32.
(123) R.M. Heck, R.J. Farrauto, S.T. Gulati, *Catalytic Air Pollution Control*, Wiley Intersciences, New York, 2002.
(124) A. Martinez-Arias, J.C. Conesa, M. Fernandez-Garcia, J.A. Anderson, *In Supported Metals in Catalysis*, Imperial College Press, London, 2005.
(125) P. L. T. Gabrielsson, *Top. Catal*., 2004, **28**, 177-184.
(126) B.H. Engler, *Chem. Ing. Tech*. 1991, **63 (4)**, 298–312.
(127) N. Haug, B. Scharer, *Operating Experiences with the SCR Technology*, 1991, **51 (11),** 389–394.
(128) G. Busca, L. Lietti, G. Ramis, F. Berti, *A Review. Appl. Catal.* B, 1998, **18 (1–2)**, 1–36.
(129) E. Jakob, G. Emmerling, A. Doring, U. Graf, M. Harris, B. Hupfeld, VDI Fortschritt-Berichte Band Nr. 348, Dusseldorf, May, 1998.

(130) M. Devadas, G. Piazzesi, O. Krocher, A. Wokaun, In International Symposium on Air
Pollution Abatement Catalysis, Krakow, September, 2005.
(131) M. Devadas, O. Krocher, M. Elsener, A. Wokaun, N. Soger, M. Pfeifer, Y. Demel, L. Mussmann, *Appl. Catal. B*, 2006, **67 (3–4),** 187–196.
(132) M. E. Davis, *Nature*, 2002, **417**, 813-821.
(133) M. T. Weller, *Inorganc Materials Chemistry*, Oxford University Press, New York, 1994
(134) C. S. Cundy, P. A. Cox, *Micropor. Mesopor. Mat.*, 2005, **82**, 1-78.
(135) M. Bevilacqua, T. Montanari, E. Finocchio, G. Busca, *Catal. Today*, 2006, **116**, 132.
(136) D. Klukowski, P. Balle, B. Geiger, S. Wagloehner, S. Kureti, B. Kimmerle, A. Baiker, J. D. Grunwaldt, *Appl. Catal. B,* 2009, **93**, 185.
(137) J. Dedecek, L. Capek, P. Sazama, Z. Sobalik, B. Wichterlova, *Appl. Catal. A*, 2011, **391**, 244.
(138) M. Zamadics, X. Chen, L. Kevan, *J. Phys. Chem.*, 1992, **96**, 2653-7.
(139) B. R. Goodman, C. K. Haas, W. F. Schneider, J. B. Adams, *Catal. Lett.*, 2000, **68**, 85-93.
(140) S. I. Zones, *J. Chem. Soc., Faraday Trans.*, 1991, **87**, 3709-3716.
(141) W. D. Fickel, R. Lobo, *J. Phys. Chem. C*, 2010, **114**, 1633-1640.
(142) L. Wang, W. Li, G. S. Qi, D. Weng, *J. Catal.*, 2012, **289**, 21-29.
(143) S. Brandenberger, O. Kröcher, A. Tissler, R. Althoff, *Appl. Catal. B: Environ.*, 2010, **95**, 348–357.
(144) S. Brandenberger, O. Kröcher, A. Tissler, R. Althoff, *Appl. Catal. A: Gen.,* 2010, **373**, 168–175.
(145) K. Otto, M. Shelef, J.T. Kummer, *Phys. Chem*., 1970, **74 (13)**, 2690–2698.
(146) Q. Sun, Z.X. Gao, H.Y Chen, W.M.H. Sachtle, *J. Catal.* 2001, **201 (1),** 89–99.
(147) K. Rahkamaa-Tolonen, T. Maunula, M. Lomma, M. Huuhtanen, R.L. Keiski, *Catal. Today*, 2005, **100 (3–4)**, 217–222.
(148) G. Delahay, D. Valade, A. Guzman-Vargas, B. Coq, *Appl. Catal. B*, 2005, **55 (2)**, 149–155.
(149) H.Y. Huang, R.Q. Long, R.T. Yang, *Appl. Catal. A*, 2002, **235 (1–2)**, 241–251.
(150) R.Q. Long, R.T. Yang, *J. Catal.*, 2002, **207 (2),** 224–231.
(151) R.Q. Long, R.T. Yang, *J. Catal.,* 1999, **188 (2)**, 332–339.
(152) G. Piazzesi, M. Devadas, O. Krocher, M.Elsener, A. Wokaun, *Catal. Commun.*, 2006, **7 (8)**, 600–603.
(153) L.J. Lobree, I.C. Hwang, J.A Reimer, A.T. Bell, *J. Catal.*, 1999, **186 (2)**, 242–253.
(154) K. Hadjiivanov, H. Knozinger, B. Tsyntsarski, L. Dimitrov, *Catal. Lett*., 1999, **62 (1)**, 35–40.
(155) K. Hadjiivanov, J. Saussey, J.L. Freysz, J.C. Lavalley, *Catal. Lett*., 1998, **52 (1–2),** 103–108.
(156) T.E. Hoost, K.A. Laframboise, K. Otto, *Catal. Lett.,* 1995, **33 (1–2),** 105–116.
(157) M. Koebel, G. Madia, F. Raimondi, A. Wokaun, *J. Catal*., 2002, **209 (1)**, 159–165.
(158) K. Hadjiivanov, H. Knozinger, B. Tsyntsarski, L. Dimitrov, *Catal. Lett*., 1999, **62 (1),** 35–40.
(159) Y.H. Yeom, J. Henao, M.J. Li, W.M.H. Sachtler, E. Weitz, *J. Catal.*, 2005, **231 (1)**, 181–193.
(160) J. Despres, M. Koebel, O. Krocher, M. Elsener, A. Wokaun, *Microporous Mesoporous Mater.*, 2003, **58 (2)**, 175–183.

(161) Y.H. Yeom, B. Wen, W.M.H. Sachtler, E. Weitz, *J. Phys. Chem. B*, 2004, **108 (17)**, 5386–5404.
(162) G. Madia, M. Koebel, M. Elsener, A. Wokaun, *Ind. Eng. Chem. Res.,* 2002, **41 (16)**, 4008–4015.
(163) V.H. Veley*, J. Am. Chem. Soc.,* 1903, **83,** 736–749.
(164) M. Koebel, M. Elsener, G. Madia, *Motorechnische Zeitschrift*, 2001, **62**, 166–175.
(165) R.Q. Long, R.T. Yang, *Catal. Lett.,* 2002, **78 (1–4),** 353–357.
(166) Y.J. Li, J.N. Armor, *Appl. Catal. B*, 1997, **13 (2),** 131–139.
(167) R.Q. Long, R.T. Yang, *Chem. Commun*., 2000, **17**, 1651–1652.
(168) E.M. El-Malki, R.A. van Santen, W.M.H. Sachtler, *J. Catal.*, 2000, **196 (2)**, 212–223.
(169) M. Kogel, V.H. Sandoval, W. Schwieger, A. Tissler, T. Turek, *Chem. Eng. Technol*., 1998, **21 (8)**, 655–658.
(170) B. Coq, M. Mauvezin, G. Delahay, J.B. Butet, S. Kieger, *Appl. Catal. B*, 2000, **27 (3)**, 193–198.
(171) J.A.Z. Pieterse, S.Booneveld, R.W. van den Brink, *Appl. Catal. B*, 2004, **51 (4)**, 215–228.
(172) H. Sjovall, L. Olsson, E. Fridell, R.J. Blint, *Appl. Catal. B*, 2006, **64 (3–4),** 180–188.
(173) R. Moreno-Tost, J. Santamaria-Gonzalez, E. Rodriguez-Castellon, A. Jimenez-
Lopez, M.A. Autie, E. Gonzalez, M.C. Glacial, C.D. Pozas, *Appl. Catal. B*, 2004, **50 (4),** 279–288.
(174) F. Radtke, R.A. Koppel, A. Baiker, *Catal. Today*, 1995, **26 (2)**, 159–167.
(175) M. Mauvezin, G. Delahay, F. Kisslich, B. Coq, S. Kieger, *Catal. Lett*., 1999, **62 (1)**, 41–44.
(176) B. G. Dick, A. W. Overhauser, *Phys. Rev.*, 1958, **112**. 90.
(177) N. M. Harrison, in Computational Materials Science, NATO Science Series III, ed. R. Catlow, E. Kotomin, IOS Press, Amsterdam, 1st edn, 2003, vol. 187, ch. 3, pp. 45-71.
(178) P. Hohenberg, W. Kohn, *Phys. Rev.*, 1964, **136**, B864-71.
(179) W. Kohn, L. J. Sham, *Phys. Rev.*, 1965, **140**, A1133-38
(180) J. D. Gale, N. J. Henson, *J. Chem. Soc. Faraday Trans.,* 1994, **90**, 3175-9.
(181) G.S. Qi, R.T. Yang, *Appl. Catal. B*, 2005, **60 (1–2)**, 13–22.
(182) P. Forzatti, L. Lietti, *Chem. Rev.,* 1996, **3 (1),** 33–51.
(183) S.C. Wood, *Chem. Eng. Prog.*, 1994, **90 (1)**, 32–38.
(184) R. Delahay,; S. Kieger,; N. Tanchoux,; P. Trens,; B. Coq, *Appl. Catal. B*, 2004, **52 (4),** 251–257.
(185) M. Li, Y. Yeom, E. Weitz, W.M.H. Sachtler, *Catal. Lett*., 2006, **112 (3–4)**, 129–132.
(186) F. Cora, M. Alfredsson, G. Mallia, D. S. Middlemiss, W. C. Mackrodt, R. Dovesi, R. Orlando, *Struct. Bond.*, **113**, 171-232.
(187) D. D. Johnson, *Phys. Rev. B*, 1988, **38**, 12807-12813.
(188) D. W. Lewis, A. R. Ruiz-Salvador, N. Almora-Barrios, A. Gomez, M. Mistry, *Mol. Simul.*, 2002, **28:6-7**,649-661.
(189) F. M. Higgins, N. H. de Leeuw, S. C. Parker, *J. Mater. Chem.*, 2002, **12**, 124-131.